A Bare Hull Upright Trimmed Resistance Prediction for High Performance Sailing Yachts

Niels Kleijweg

TUDelft

Delft
University of
Technology

Challenge the future

A Bare Hull Upright Trimmed Resistance Prediction for High Performance Sailing Yachts

by

Niels Kleijweg

to obtain the degree of Master of Science
at the Delft University of Technology,
to be defended publicly on Monday June 20, 2016 at 2:00 PM.

An electronic version of this thesis is available at `http://repository.tudelft.nl/`.

Faculty of Mechanical, Maritime and Materials Engineering (3mE), Delft University of Technology

TUDelft

Preface

Over the past four decades, extensive research was conducted on the Delft Systematic Yacht Hull Series (DSYHS) by the Ship Hydromechanics Laboratory of the Delft University of Technology to determine the hydrodynamic forces and moments acting on sailing yacht hulls. From that research, regression formulas for these forces and moments were derived. These regressions make it possible to predict the hydrodynamic forces and moments acting on arbitrary yachts. Over the years, new individual series were added to the DSYHS to keep up with the developments in yacht design. After the last extension of the DSYHS more than ten years ago, the developments have not stopped. New research in the form of this MSc thesis is conducted on the hydrodynamic forces acting on modern yacht hulls. The aim of this research is to improve the velocity prediction of modern high performance yachts.

Writing my thesis on a subject so close to my personal interest and passion has been a true privilege. I am ever thankful for getting the opportunity and the freedom to do what I really wanted to do.

I would like to express my sincere gratitude towards the people involved with my thesis. First and foremost, to my supervisors, Dr. ir. Lex Keuning and Prof. dr. ir. René Huijsmans for their valuable criticism and patience. I would also like to thank Dr. ir. Marc Gerritsma and Dr. ir. Robert Hekkenberg for being the other two members of my thesis committee. Furthermore, I would like to sincerely thank the staff of the Ship Hydromechanics Laboratory for their assistance, advise and company during my research.

On a more personal note, I would like to sincerely thank my parents and my grandparents for their everlasting support in all my pursuits.

Niels Kleijweg
Delft, June 2016

Abstract

The technological developments in sailing yacht design and construction over the past fifteen years are tremendous. As a result of these developments, the present methods for the velocity prediction of sailing yachts are less applicable to recent high performance yacht designs. The accuracy of the velocity prediction suffers from this in some extent. In order to improve the velocity prediction of contemporary yachts from a hydrodynamic perspective, a new bare hull upright trimmed resistance prediction for modern high performance yachts, to be used in velocity prediction programs (VPPs), has been derived in this thesis.

VPPs are used extensively for the design of sailing yachts, from racing yachts to recreational yachts. Velocity predictions are used to compare candidate designs and to optimize hull shapes, appendages, and the dimensions of rigs and sails. Furthermore, they are used to determine ratings for individual yachts. A VPP predicts the velocity of a yacht for various wind strengths and wind directions by finding an equilibrium between hydrodynamic forces acting on the hull and aerodynamic forces acting on the sails.

VPPs generally rely on the regressions derived from the Delft Systematic Yacht Hull Series (DSYHS) for the estimation of the hydrodynamic forces and moments acting on sailing yacht hulls. The DSYHS is a collection of different systematic series of yacht hulls. The DSYHS contains in total almost sixty different hulls. Extensive research was conducted on the DSYHS to determine the hydrodynamic forces and moments acting on the hulls. Regression formulas for these forces and moments were derived from that research. These regression formulas are based on hydrostatic parameters of yacht hulls. This makes it possible to predict the hydrodynamic forces and moments acting on an 'arbitrary' yacht. The regressions of the DSYHS are presumably the most accurate formulations for the prediction of hydrodynamic forces and moments acting on yachts.

Since the beginning of the research on the DSYHS in 1973, the design of sailing yachts has changed dramatically. Over the years, new individual series were added to the DSYHS to keep up with the developments in yacht design. After the last extension of the DSYHS more than ten years ago, the most pronounced developments in yacht design are the straight vertical bows, the wide transoms, the very small overhangs aft and the very light displacement hulls. Furthermore, the contemporary designs carry above the waterline their maximum beam all the way aft. These developments contribute to the ever increasing speed potential of the newer designs.

As a results of these developments, the DSYHS is no longer representative of today's high performance yacht designs. The regression formulas derived from the DSYHS are therefore less applicable to recent hull shapes. The accuracy of the velocity prediction of modern high performance yachts suffers from this in some extent. The developments in yacht design and the limitations of the regressions of the DSYHS for the velocity prediction of contemporary high performance yachts formed the motivation for the present study.

The aim of this study was to improve the velocity prediction of modern high performance sailing yachts from a hydrodynamic perspective. Improving the prediction of the bare hull upright trimmed resistance was a promising method to realize this. To this end, a new systematic series of contemporary high performance yacht hulls has been created. A TP52-design was used as the parent model for this series. This systematic series contains 21 different hull shapes. The new series is representative of a wide range of today's high performance yachts. The regression formulas derived from this new series cover a wider speed range and a different range of hydrostatic parameters than those of the DSYHS.

The hydrodynamic forces acting on the models in this new series have been determined with computational fluid dynamics (CFD). The upright trimmed resistance of the models has been determined for eight speeds, from Froude numbers 0.25 up to 0.95. Trimmed means that a trimming moment of the driving force and the crew's weight is applied to the yacht. The driving force acting on a sailing yacht is the resultant aerodynamic force acting on the sails in parallel to the yacht's velocity. Its point

of application is the centre of effort (CoE) of the sails. All the models have been tested for exactly the same CoE height. The upright trimmed resistance of every model at every speed has been determined for three different trimming moments of the crew's weight. These three moments correspond to typical crew configurations during sailing.

To establish the reliability and the accuracy of the numerical results presented in this thesis, a Verification & Validation (V&V) analysis has been performed. A grid refinement study has been performed to assess the uncertainty of the numerical results for the parent hull of the systematic series. For validation, the numerical results for the parent hull have been compared to the results of resistance measurements. The corresponding comparison errors for the resistance values are between -2.9 and -8.6 percent of the experimental results. Validation is successful from a programmatic standpoint. For the purpose of deriving regressions for the upright trimmed resistance prediction in VPPs, the approach of validating numerical results at a level below 10 percent is considered to be reasonable and acceptable. The performance of the numerical flow solver and the accuracy of the numerical results are satisfying. Confidence in the numerical results of the systematic series exists.

The resistance forces acting on the models in the new systematic series have been used to derive new regression formulas for the estimation of the bare hull upright trimmed resistance based on hydrostatic parameters of yacht hulls. Five different regressions for the upright trimmed residuary resistance of the bare hull have been derived: a regression for the minimum resistance of the three crew positions, three regressions for the resistance of each individual crew position, and a regression incorporating the influence of the trimming moment of the crew's weight on the resistance. All the expressions can be easily implemented in existing VPPs, because they contain only hydrostatic parameters and no terms involving the trimming moment of the driving force. For a high performance sailing yacht with a full crew, the regressions for the minimum resistance is preferred, because this represents the optimum performance of the yacht. The other regressions can be used for different crew configurations or other ranges of trimming moments.

The derived regressions provide an accurate resistance prediction for models covered by the new systematic series. Even for models (slightly) outside the parameter range covered by this series or models with different design characteristics than the characteristic hull shapes in this series, the prediction can be quite accurate. The regressions seem to be stable, robust and not too sensitive to variations in the input parameters. The applicability of the derived regressions to the velocity prediction of modern high performance sailing yachts with existing VPPs has been illustrated. The obtained polar diagram seemed very reasonable.

The new regressions for the upright trimmed resistance are a good first step to improve the velocity prediction of modern high performance sailing yachts. For accurate velocity predictions of these yachts, it is still necessary to improve the prediction of the other resistance components as well. The motivation is still that the regressions of the DSYHS are less applicable to modern high performance yacht designs due to the range of parameters contained within the DSYHS and the limited speed range of the DSYHS. Of course, the applicability of the aerodynamic models used in VPPs to high performance yachts need to be assessed as well and improved if necesarry.

Contents

List of Symbols

Latin Letters

$(1+k)$	Form factor	$[-]$
A_W	Waterplane area	$[m^2]$
A_X	Maximum sectional area	$[m^2]$
$A_{X_{20}}$	Maximum sectional area under 20 degrees heel	$[m^2]$
B_{OA}	Beam overall	$[m]$
B_{WL}	Beam of the waterline	$[m]$
$B_{WL_{20}}$	Beam of the waterline under 20 degrees heel	$[m]$
$B_{WL\phi}$	Beam of the waterline under heel	$[m]$
C	CFL number, or Courant number	$[-]$
C_b	Block coefficient	$[-]$
C_f	Friction coefficient calculated with the ITTC 1957 Model-Ship Correlation Line [16]	$[-]$
C_p	Prismatic coefficient	$[-]$
C_w	Waterplane area coefficient	$[-]$
C_x	Maximum sectional area coefficient	$[-]$
$C_{x_{20}}$	Maximum sectional area coefficient under 20 degrees heel	$[-]$
$C_{x\phi}$	Maximum sectional area coefficient under heel	$[-]$
$\text{Cov}(X_1, X_2)$	Covariance between the two random variables X_1 and X_2	
E	comparison error	$[N]$
$\text{E}[X]$	Expected value, or mean, of random variable X	
F_S	Safety factor	$[-]$
F_x	Resistance in CFD computation	$[N]$
$F_x{}^*$	Resistance in CFD computation used as reference for comparison	$[N]$
F_z	Vertical force in CFD computation	$[N]$
Fn	Froude number, $Fn = V/\sqrt{gL_{WL}}$	$[-]$
g	Gravitational acceleration	$[m/s^2]$
h_i	Typical cell size	$[m]$
k	Coverage factor	$[-]$
k	Turbulent kinetic energy	$[m^2/s^2]$
KM_L	Longitudinal metacentric height	$[m]$
L_{OA}	Length overall	$[m]$
L_{ref}	Reference length	$[m]$
L_{WL}	Length of the waterline	$[m]$
$L_{WL_{20}}$	Length of the waterline under 20 degrees heel	$[m]$
$L_{WL\phi}$	Length of the waterline under heel	$[m]$
LCB	Longitudinal position of the centre of buoyancy measured from $^1/_2 L_{WL}$, positive forward	$[m]$
$LCB_\%$	Longitudinal position of the centre of buoyancy expressed in percentage of L_{WL} measured from $^1/_2 L_{WL}$; i.e. $LCB/L_{WL} \cdot 100$	$[\% L_{WL}]$
LCB_{fp}	Longitudinal position of the centre of buoyancy measured from the forward perpendicular (fp)	$[m]$

LCF	Longitudinal position of the centre of flotation measured from $1/2L_{WL}$, positive forward	$[m]$
$LCF_\%$	Longitudinal position of the centre of flotation expressed in percentage of L_{WL} measured from $1/2L_{WL}$; i.e. $LCF/L_{WL} \cdot 100$	$[\%L_{WL}]$
LCF_{fp}	Longitudinal position of the centre of flotation measured from the forward perpendicular (fp)	$[m]$
LCG_{fp}	Longitudinal position of the centre of gravity measured from the forward perpendicular (fp)	$[m]$
M_y	Moment about the centre of gravity (CoG) in direction of the y-axis, in CFD computation	$[Nm]$
M_θ	Longitudinal trimming moment about the CoG	$[Nm]$
$M_{\theta_{CREW}}$	Longitudinal trimming moment of the crew's weight about the CoG	$[Nm]$
$M_{\theta_{SAILS}}$	Longitudinal trimming moment of the driving force about the CoG	$[Nm]$
$\mathrm{MSE}(T)$	Mean squared error of estimator T	
n_g	Number of grids in the dataset	$[-]$
N_i	Number of cells	$[-]$
$N_i{}^*$	Expected number of cells	$[-]$
p	Observed order of grid convergence	$[-]$
p	Pressure	$[Pa]$
$\bar{r}$	Best estimate of measurand R	$[N]$
r_i	Refinement factor	$[-]$
$r_i{}^*$	Expected refinement factor	$[-]$
R	Convergence ratio of the grid triplet of the fine, medium and coarse grid	$[-]$
R	Measurand	$[N]$
R^2	Coefficient of determination	$[-]$
$\bar{R}^2$	Adjusted coefficient of determination	$[-]$
R_{f_m}	Frictional resistance at model scale, $L_{WL} = 2.00\,m$	$[N]$
R_{f_p}	Frictional resistance at prototype scale, $L_{WL} = 10.00\,m$	$[N]$
R_{F_h}	Frictional resistance of the bare hull	$[N]$
R_I	Induced resistance	$[N]$
R_k	Convergence ratio	$[-]$
R_{r_m}	Residuary resistance at model scale, $L_{WL} = 2.00\,m$	$[N]$
R_{r_p}	Residuary resistance at prototype scale, $L_{WL} = 10.00\,m$	$[N]$
R_{R_h}	Residuary resistance of the bare hull	$[N]$
R_{R_k}	Residuary resistance of the keel	$[N]$
$R_{R\theta_h}$	Upright trimmed residuary resistance of the bare hull	$[N]$
R_t	Resistance of the model determined with the experimental method	$[N]$
R_{t_m}	Total resistance at model scale, $L_{WL} = 2.00\,m$	$[N]$
R_{t_p}	Total resistance at prototype scale, $L_{WL} = 10.00\,m$	$[N]$
$R_{t_{strip}}$	Resistance of the turbulence-stimulating strips	$[N]$
R_T	Total upright resistance	$[N]$
R_{T_h}	Bare hull upright resistance	$[N]$
$R_{T\theta}$	Total upright trimmed resistance	$[N]$
$R_{T\theta_h}$	Upright trimmed resistance of the bare hull	$[N]$
$R_{T\theta\phi}$	Total trimmed resistance under heel	$[N]$
$R_{T\theta\phi\beta}$	Total trimmed resistance under heel and leeway	$[N]$

$R_{T\phi}$	Total resistance under heel	$[N]$
$R_{T\phi h}$	Resistance of the bare hull under heel	$[N]$
$R_{T\phi\beta}$	Total resistance under heel and leeway	$[N]$
R_{V_k}	Viscous resistance of the keel	$[N]$
R_{V_r}	Viscous resistance of the rudder	$[N]$
Re	Reynolds number	$[-]$
S_c	Wetted surface of the canoe body	$[m^2]$
$S_{c_{20}}$	Wetted surface of the canoe body under 20 degrees heel	$[m^2]$
$S_{c\phi}$	Wetted surface of the canoe body under heel	$[m^2]$
t	Time	$[s]$
T_c	Draft of the canoe body	$[m]$
$T_{c_{20}}$	Draft of the canoe body under 20 degrees heel	$[m]$
$T_{c\phi}$	Draft of the canoe body under heel	$[m]$
u_c	Combined standard experimental uncertainty	$[N]$
u_i	Cartesian velocity component	$[m/s]$
u_i	Standard experimental uncertainty	$[N]$
u_τ	Wall-friction velocity	$[m/s]$
U_R	Expanded experimental uncertainty for measurand R	$[N]$
U_V	Validation uncertainty	$[N]$
U_ϕ	Estimate of the discretization uncertainty	
U_{ϕ_1}	Estimate of the discretization uncertainty of the finest grid	$[N]$
U_{ϕ_4}	Estimate of the discretization uncertainty of the medium grid	$[N]$
V	Velocity	$[m/s]$
V_m	Velocity at model scale, $L_{WL} = 2.00\,m$	$[m/s]$
V_{ref}	Reference velocity	$[m/s]$
V_Ω	Volume of the computational domain	$[m^3]$
$\mathrm{Var}(X)$	Variance of random variable X	
w_i	Weights for the different grids used in the weighted least-squares minimization of the error estimator	$[-]$
x_i	Cartesian coordinate	$[m]$
X	Random variable	
y	Distance to the wall	$[m]$
y_1	Distance between the wall and the nearest node	$[m]$
y_1^+	Wall coordinate associated with the first node near the wall	$[-]$
y^+	Wall coordinate	$[-]$
z	Heave	$[m]$
z_{CoE}	Height of the CoE above the waterline	$[m]$
$z_{CoE_{eff}}$	Height of the effective CoE above the waterline	$[m]$

Greek Letters

α	Constant	$[-]$
α	Scale factor	$[-]$
α_1	Constant	$[-]$
α_2	Constant	$[-]$
β	Leeway angle	$[°]$
$\Delta_\%$	Percentage change	$[\%]$
Δ_c	Displacement of the canoe body	$[kg]$
Δ_ϕ	Data range parameter	$[N]$

δ_1	Estimator of the discretization error	$[N]$
δ_2	Estimator of the discretization error	$[N]$
δ_{12}	Estimator of the discretization error	$[N]$
δ_{RE}	Estimator of the discretization error	$[N]$
$\Delta R_{F\phi_h}$	Change in frictional resistance of the bare hull due to heel	$[N]$
$\Delta R_{R\theta_h}$	Change in residuary resistance of the bare hull due to the trimming moment of the driving force	$[N]$
$\Delta R_{R\phi_h}$	Change in residuary resistance of the bare hull due to heel	$[N]$
$\Delta R_{R\phi_k}$	Change in residuary resistance of the keel due to heel	$[N]$
ϵ	Dissipation rate of turbulent kinetic energy, or turbulence dissipation rate	$[J/(kg \cdot s)]$
ϵ_ϕ	Discretization error	
ϵ_{ϕ_1}	Discretization error of the finest grid	$[N]$
ϵ_{ϕ_4}	Discretization error of the medium grid	$[N]$
θ	Pitch angle	$[°]$
μ	Dynamic viscosity	$[Pa \cdot s]$
μ_t	Eddy viscosity, or turbulent viscosity	$[Pa \cdot s]$
ν	Kinematic viscosity, $\nu = \mu/\rho$	$[m^2/s]$
ν_t	Turbulent kinematic viscosity, $\nu_t = \mu_t/\rho$	$[m^2/s]$
ρ	Density	$[kg/m^3]$
ρ_m	Density at model scale, $L_{WL} = 2.00\,m$	$[kg/m^3]$
ρ_p	Density at prototype scale, $L_{WL} = 10.00\,m$	$[kg/m^3]$
$\rho(X_1, X_2)$	Correlation coefficient of random variables X_1 and X_2	$[-]$
σ	Standard deviation	
σ_{RE}	Standard deviation of the non-weighted least-squares minimization of error estimator δ_{RE}	$[N]$
σ_{RE}^W	Standard deviation of the weighted least-squares minimization of error estimator δ_{RE}	$[N]$
τ	Global time step	$[s]$
τ_W	Wall shear stress	$[Pa]$
ϕ	Heel angle	$[°]$
ϕ_0	Estimate of the exact solution	$[N]$
ϕ_1	Resistance computed on the finest grid	$[N]$
ϕ_4	Resistance computed on the medium grid	$[N]$
ϕ_{exact}	Exact solution	$[N]$
ϕ_i	Any integral or other functional of the local flow quantity under consideration	
ϕ_{LS}	Discrete value of the least-squares fit corresponding to ϕ_i	$[N]$
ω	Specific turbulence dissipation rate, or turbulence frequency, $\omega = \epsilon/k$	$[1/s]$
∇_c	Volume of displacement of the canoe body	$[m^3]$

Subscripts

c	Canoe body
h	Bare hull
k	Keel
r	Rudder
RE	Richardson extrapolation

WL	Waterline
β	With leeway angle
θ	Trimmed
ϕ	Under heel

Acronyms

ASM	Algebraic stress model
ASME	American Society of Mechanical Engineers
CFD	Computational fluid dynamics
CFL	Courant-Friedrichs-Lewy
CoE	Centre of effort
CoG	Centre of gravity
DNS	Direct numerical simulation
DSYHS	Delft Systematic Yacht Hull Series
EASM	Explicit algebraic stress model
fp	Forward perpendicular
FVM	Finite-volume method
GCI	Grid Convergence Index
ITTC	International Towing Tank Conference
JCGM	Joint Committee for Guides in Metrology
IMS	International Measurement System
LES	Large-eddy simulation
MARIN	Maritime Research Institute Netherlands
RANS	Reynolds-averaged Navier-Stokes
SST	Shear stress transport
SYRF	Sailing Yacht Research Foundation
TP52	Transpac 52
VOF	Volume of fluid
VPP	Velocity prediction program
V&V	Verification & Validation

List of Figures

List of Tables

1

Introduction

The speed of sailing yachts has always fascinated people involved in the sailing community. It is probably the most talked-about topic when it comes to yachts. Not only on the water or on the shore after sailing, but also in design offices. Those people always feel the desire to sail faster and faster. The technological developments in yacht design and construction over the past decades are tremendous. These developments contribute to the ever increasing speed potential of the newer yacht designs. For the design of sailing yachts and especially high performance yachts, the speed potential is the dominant factor.

The velocity of sailing yachts is predicted with velocity prediction programs (VPPs). A VPP predicts the velocity of a yacht for various wind strengths and wind directions by finding an equilibrium between hydrodynamic forces acting on the hull and aerodynamic forces acting on the sails. The predicted velocity of a yacht at different true wind angles for different true wind speeds is visualized in a polar diagram. VPPs are used extensively for the design of almost every sailing yacht, from racing yachts to recreational yachts. Velocity predictions are used to compare candidate designs and to optimize hull shapes, appendages, and the dimensions of rigs and sails. Furthermore, they are used to determine ratings, or handicaps, for individual yachts. These ratings allow yachts of different sizes and with different characteristics to race each other with an equal chance to win, at least that is the intention.

For existing racing yachts, the predicted polar diagrams are used, in combination with full-scale performance measurements taken during sailing, to calculate the optimum sail combinations for specific sailing conditions. They can also be used to calculate the optimum route based on a meteorological forecast. Full-scale measurements are generally used to increase the accuracy of the velocity predictions of these racing yachts. This is useful for the optimization of hull shapes, appendages, rigs, sails, and the way they are sailed. Unfortunately, these are generally isolated private efforts, exclusively done by racing teams with large budgets. Measured data is not publicly available for research, because this would give opponents insight in the performance of the yacht. They are trying to be the fastest and stay the fastest for a reason.

The velocity prediction of sailing yachts with VPPs relies on a set of expressions, as function of the hydrostatic parameters of yachts, for the estimation of the hydrodynamic forces acting on them. VPPs generally use the regressions derived from the Delft Systematic Yacht Hull Series (DSYHS) for the estimation of the hydrodynamic forces and moments acting on yachts. The DSYHS is a collection of different systematic series of yacht hulls. Each individual series contains a parent model and a number of systematic variations of this parent model. The DSYHS contains seven of these series and in total almost sixty different yacht hulls. Extensive research was conducted on the DSYHS to determine the hydrodynamic forces and moments acting on the hulls, such as the upright resistance, the resistance under heel and the yaw moment. All the models in the DSYHS were tested with a consistent measurement set-up and procedure at the Ship Hydromechanics Laboratory of the Delft University of Technology over the years. The DSYHS is presumably the largest consistent systematic series of yacht hulls tested.

Regression formulas for the hydrodynamic forces and moments were derived from these tests. These regression formulas are based on hydrostatic parameters of yacht hulls. This makes it possible

to predict the hydrodynamic forces and moments acting on an 'arbitrary' sailing yacht. The regressions of the DSYHS are presumably the most famous and the most accurate formulations for the prediction of hydrodynamic forces and moments acting on yachts.

Since the beginning of the extensive research on the DSYHS by Gerritsma and Moeyes [13] in 1973, the design of sailing yachts has changed dramatically. Over the years, new individual series were added to the DSYHS to keep up with the developments in yacht design. After the last extension of the DSYHS more than ten years ago, the developments have not stopped. The most pronounced developments in yacht design since then are the straight vertical bows, the wide transoms, the very small overhangs aft and the very light displacement hulls. Furthermore, the contemporary designs carry above the waterline their maximum beam all the way aft. These developments contribute to the ever increasing speed potential of the newer yacht designs. Modern high performance yachts are capable of sailing in a semi-displacement mode for a wide range of conditions. Maximum speeds up to Froude number 0.85 are the rule rather than the exception. To give an impression, Froude number 0.85 corresponds for a full-scale Transpac 52 (TP52) with a waterline length of almost 16 metres to 21 knots.

The developments in yacht design over the last years are significant. As a result, the DSYHS is no longer representative of today's high performance yacht designs. Recent designs may not be fully covered by the hull shapes within the DSYHS. The regression formulas derived from the DSYHS can therefore be less applicable to contemporary hull shapes. The accuracy of the velocity prediction of modern high performance yachts will suffer from this in some extent.

The developments in yacht design and the possible limitations of the regressions of the DSYHS for the velocity prediction of contemporary high performance yachts form the motivation for the present study. Furthermore, there is very few published research on modern yachts available. Most of the research is conducted as isolated private efforts for very small series of high performance yachts or for individual racing yachts. Research is not published, because other design offices and opponents would benefit from this. From the sailing yacht world, there is a (strong) desire to expand the publicly available database of hydrodynamics of yacht hulls with modern designs. This current database consists primarily of the DSYHS. For the design of sailing yachts and the determination of ratings of individual yachts, there is a need to improve the velocity prediction of modern yachts.

This study aims therefore at improving the velocity prediction of modern high performance yachts from a hydrodynamic perspective. A promising method for the improvement of the velocity prediction of modern sailing yachts from a hydrodynamic perspective is to improve the prediction of the two largest bare hull resistance components. This approach is followed in the present study. As a result of the developments in sailing yacht design, it is found necessary to create a new systematic series of contemporary high performance yacht hulls. A modern TP52-design is used as the parent model for this series. The new series is representative of a wide range of today's high performance yachts. The hydrodynamic resistance forces acting on the models in the new systematic series are used to derive new regression formulas for the estimation of resistance forces based on hydrostatic parameters of yacht hulls. These formulations can be used in existing VPPs.

Structure of this thesis

Since the regressions of the DSYHS are presumably the most accurate formulations for the prediction of hydrodynamic forces and moments acting on sailing yachts, they form the starting point of the present study. A detailed description of the DSYHS is given in Chapter 2. The limitations of the DSYHS regressions for modern yachts are investigated. These limitations form the motivation for the present study. As a result of the developments in sailing yacht design, it is found necessary to create a new systematic series of contemporary yacht hulls in order to improve the velocity prediction of high performance yachts. The new systematic series is derived in Chapter 3. The bare hull resistance components of the parent hull are also discussed. The two largest bare hull resistance components of the parent hull are the main focus of this study. The conditions for which the hydrodynamic forces are determined, are discussed in Chapter 4.

For the velocity prediction of high performance yachts, a new resistance decomposition is proposed in Chapter 5. This decomposition is followed in the present study. The hydrodynamic resistance forces acting on the models in the systematic series are determined with computational fluid dynamics (CFD). The numerical method and the numerical results are discussed in Chapter 6. A grid refinement study

is performed to assess the numerical uncertainty in Chapter 7. The numerical results will be validated with the results of resistance measurements. Chapter 8 describes these resistance measurements and the assessment of the experimental uncertainties. The validation analysis is discussed in Chapter 9.

From the database of the new systematic series, which contains the resistance values for various hull forms and speeds, new expressions are derived for the estimation of the resistance components based on hydrostatic parameters of yacht hulls. A regression analysis is performed on the dataset to derive these expressions in Chapter 10. The applicability of the derived regressions to the velocity prediction of high performance yachts with existing VPPs is illustrated in that chapter. The conclusions and recommendations presented in Chapter 11 conclude this thesis.

2

Delft Systematic Yacht Hull Series

The Delft Systematic Yacht Hull Series (DSYHS) is a collection of different systematic series of sailing yacht hulls. Each individual series contains a parent model and a number of systematic variations of this parent model. The DSYHS contains seven of these series and in total almost 60 different yacht hulls. Extensive experimental research was conducted on the DSYHS to determine the hydrodynamic forces and moments acting on the hulls, such as the upright resistance, the resistance under heel and the yaw moment. The DSYHS is presumably the largest consistent systematic series of yacht hulls tested. Regression formulas for the hydrodynamic forces and moments were derived from the measurements. These regression formulas are based on the main dimensions and the hydrostatic coefficients of sailing yacht hulls. This makes it possible to predict the hydrodynamic forces and moments acting on an 'arbitrary' yacht. Velocity prediction programs (VPPs) generally rely on the regressions of the DSYHS for the estimation of the hydrodynamic forces and moments acting on a sailing yacht.

Within the DSYHS, the resistance of sailing yachts is decomposed into various components. This decomposition and the various resistance components are discussed in Section 2.1. The regression formulas derived from the DSYHS for these resistance components are also given in that section.

The hydrodynamic forces and moments acting on the models were determined with resistance measurements. All the models in the series were tested with a consistent measurement set-up and procedure at the Ship Hydromechanics Laboratory of the Delft University of Technology over the years. All the hydrodynamic forces and moments were extrapolated to a waterline length of ten metres. The hydrodynamic forces and moments at this scale were used in regression analyses to derive the regression formulas given in this chapter. The extrapolation of the measured resistance forces is described in Section 2.2.

The hydrostatic parameter range contained within the DSYHS determines the range of applicability of the derived regressions. The range of hydrostatic parameters contained within the DSYHS is summarized in Section 2.3. In order to asses the accuracy of the regressions, experimental results are compared with the resistance predicted with the regressions in Section 2.4. The limitations of the regressions are discussed in Section 2.5. These limitations form the motivation for the present study.

2.1. Resistance decomposition and regressions

The method by which the hydrodynamic resistance forces in the Delft Systematic Yacht Hull Series (DSYHS) have been decomposed in separate components is shown in Figure 2.1. Four different types of total resistance are defined in this figure. The total resistance mentioned in the block at the top of each column is equal to the sum of the resistance components of the other blocks in that column. This decomposition and the regression formulas for these components are summarized in this section.

The interest of the present study lies in the bare hull resistance components, and therefore, only these components will be discussed further after the four different types of total resistance are summarized. The bare hull resistance components are indicated with the grey-coloured blocks in Figure 2.1. The resistance components in the white-coloured blocks are not discussed in this thesis. For a thorough discussion of these components, the reader is referred to Keuning et al. [27,28]. According to the DSYHS decomposition, the bare hull resistance is modelled as the sum of the following five

components: the frictional resistance of the hull, the residuary resistance of the hull, the delta frictional resistance of the hull due to heel, the delta residuary resistance of the hull due to heel, and the delta residuary resistance due to the trimming moment of the driving force.

It should be noted that the decomposition of Figure 2.1 only holds in calm water. Since the present study deals solely with calm-water phenomena, added resistance in waves is not discussed. For a thorough discussion of added resistance in waves, the reader is referred to Keuning et al. [27,29].

The regressions of the DSYHS are based on hydrostatic parameters of sailing yacht hulls. This makes it possible to predict the hydrodynamic forces and moments acting on an arbitrary sailing yacht. VPPs generally rely on the regressions of the DSYHS for the estimation of the hydrodynamic forces and moments acting on a sailing yacht hull.

The regressions of the DSYHS are presumably the most accurate formulations for the prediction of hydrodynamic forces and moments acting on yacht hulls. Even for modern yachts, the DSYHS regressions are the most accurate prediction method as was shown by Raymond [40]. Careful selection of hydrostatic coefficients, the construction of the regressions while keeping the physics involved in mind, and the large database of the DSYHS resulted in accurate, robust and stable regressions that are still relatively simple. Due to the large parameter range contained within the DSYHS, the regressions are applicable to a large variety of sailing yacht designs. Sections 2.3, 2.4 and 2.5, and the work of Huetz [14] supports these findings.
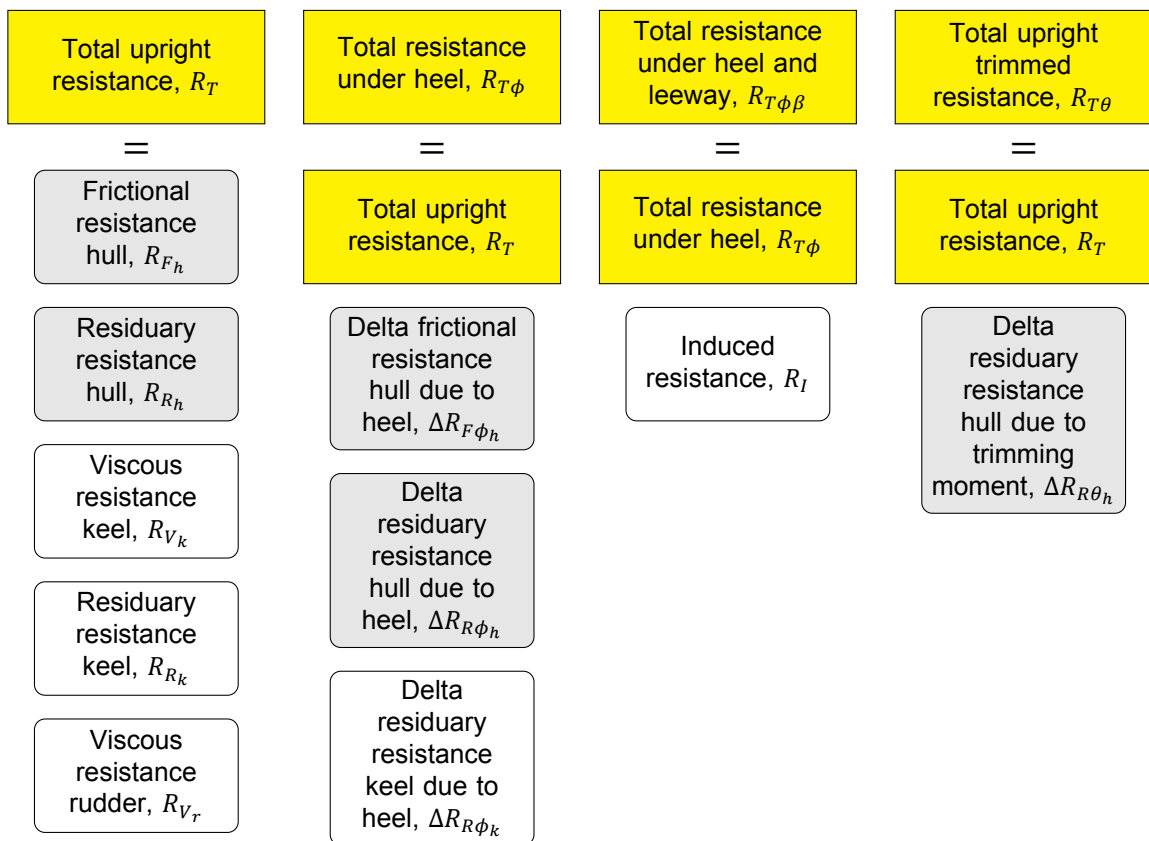
Figure 2.1: Resistance decomposition used for the DSYHS. Figure adapted from Keuning and Sonnenberg [27]. There are four different types of total resistance used in this decomposition. The total resistance mentioned in the block at the top of each column is equal to the sum of the resistance components of the other blocks in that column. The resistance components in the grey-coloured blocks are the bare hull resistance components.

2.1.1. Total resistance

There are four different types of total resistance — resistance of the hull with its appendages — defined in the resistance decomposition, shown in Figure 2.1: the total upright resistance, the total resistance under heel, the total resistance under heel and leeway, and the total upright trimmed resistance. Their

definitions are given in this subsection. Please note that throughout this thesis, the trimmed condition and the untrimmed condition imply nothing more than whether or not longitudinal trimming moments of the driving force and the crew's weight are applied to the yacht. In both conditions, the yacht is free to heave and pitch.

The driving force acting on a sailing yacht is the resultant aerodynamic force acting on the sails in parallel to the yacht's velocity. Its point of application is the centre of effort (CoE) of the sails. In steady-state conditions, the driving force is equal to the resistance. Obviously, the driving force and the resistance are antiparallel vectors.

Total upright resistance
The total upright resistance of the hull with its appendages is defined by

$$R_T = R_{F_h} + R_{R_h} + R_{V_k} + R_{R_k} + R_{V_r}, \tag{2.1}$$

where R_T is the total upright resistance, R_{F_h} is the frictional resistance of the bare hull, R_{R_h} is the residuary resistance of the bare hull, R_{V_k} is the viscous resistance of the keel, R_{R_k} is the residuary resistance of the keel, and R_{V_r} is the viscous resistance of the rudder. Only the bare hull resistance components are discussed further in this thesis. The resistance components of the rudder and the keel are not of interest for this study. For a thorough discussion of these resistance components, the reader is referred to Keuning and Sonnenberg [27].

Total resistance under heel
The total resistance under heel is defined by

$$R_{T\phi} = R_T + \Delta R_{F\phi_h} + \Delta R_{R\phi_h} + \Delta R_{R\phi_k}, \tag{2.2}$$

where $R_{T\phi}$ is the total resistance under heel, $\Delta R_{F\phi_h}$ is the change in frictional resistance of the bare hull due to heel, $\Delta R_{R\phi_h}$ is the change in residuary resistance of the bare hull due to heel, and $\Delta R_{R\phi_k}$ is the change in residuary resistance of the keel due to heel.

Total resistance under heel and leeway
The total resistance under heel and leeway is defined by

$$R_{T\phi\beta} = R_{T\phi} + R_I, \tag{2.3}$$

where $R_{T\phi\beta}$ is the total resistance under heel and leeway, and R_I is the induced resistance. The induced resistance is related to the side force generation of the hull with its appendages when sailing with leeway. The induced resistance is not decomposed into separate components for the hull, the keel and the rudder, because the side force generation and the associated induced resistance depend heavily on the interaction between the hull and its appendages. The induced resistance is not discussed in this thesis due to this strong coupling between the hull and its appendages. For a thorough discussion of the induced resistance and the side force generation, the reader is referred to Keuning et al. [27,28].

Total upright trimmed resistance
The total upright trimmed resistance of the hull with its appendages is defined by

$$R_{T\theta} = R_T + \Delta R_{R\theta_h}, \tag{2.4}$$

where $R_{T\theta}$ is the total upright trimmed resistance, and $\Delta R_{R\theta_h}$ is the change in residuary resistance of the bare hull due to the trimming moment of the driving force. The trimming moment of the driving force influences the trim angle of the yacht and thereby its sinkage and resistance. This trimming moment results always in a more bow-down attitude of the yacht compared to when this trimming moment is not applied.

2.1.2. Bare hull upright resistance
The bare hull upright resistance consists of the frictional resistance of the hull and the residuary resistance of the hull; i.e.

$$R_{T_h} = R_{F_h} + R_{R_h}, \tag{2.5}$$

where R_{T_h} is the bare hull upright resistance, R_{F_h} is the frictional resistance of the bare hull, and R_{R_h} is the residuary resistance of the bare hull.

Frictional resistance hull

Within the DSYHS, the frictional resistance of the bare hull is determined by

$$R_{F_h} = \frac{1}{2}\rho V^2 S_c C_f, \tag{2.6}$$

where ρ is the density of water, V is the velocity, S_c is the wetted surface of the canoe body, and C_f is the friction coefficient calculated with the International Towing Tank Conference (ITTC) 1957 Model-Ship Correlation Line [16]:

$$C_f = \frac{0.075}{(\log_{10} Re - 2)^2}. \tag{2.7}$$

Within the DSYHS, the Reynolds number, Re, is defined by

$$Re = \frac{0.7 L_{WL} \cdot V}{\nu}, \tag{2.8}$$

where L_{WL} is the length of the waterline, and ν is the kinematic viscosity of water. $0.7 L_{WL}$ is used as the characteristic length in the Reynolds number. This length was originally chosen for Series 1 of the DSYHS to allow for the particular waterline profiles of these models and the corresponding flow field to be captured in the Reynolds number. According to Keuning and Sonnenberg [27], for the more modern hull shapes after Series 1, a characteristic length of $0.9 L_{WL}$ seems to be more appropriate. Nevertheless, for consistency, $0.7 L_{WL}$ is used as the characteristic length throughout the entire DSYHS. This influences the residuary resistance as well.

The expression for the frictional resistance of the bare hull in the DSYHS is based on the ITTC 1957 expression for the frictional resistance [16]. Compared to the ITTC, no form factor is used for the DSYHS; $(1 + k) = 1$ for the DSYHS in the ITTC procedure. As a result, the influence of the hull shape on the frictional resistance is incorporated in the residuary resistance.

According to Keuning and Sonnenberg [27], the derivation of a formulation for the form factor, as function of the main dimensions and the hydrostatic coefficients of yacht hulls, from the results of the DSYHS was impossible. The absence of such a formulation made it impossible to establish the form factor for an arbitrary sailing yacht. Moreover, Keuning and Sonnenberg show that the form factors, derived from Prohaska's plots, for the hull shapes within the DSYHS are generally small; for Series 1 up to 4 the form factor satisfies $1.03 \leq (1 + k) \leq 1.07$ in all but two extreme cases. No form factor was therefore used in the formulation of the frictional resistance for the DSYHS.

Residuary resistance hull

According to Keuning and Katgert [25], the residuary resistance of the hull can be approximated by

$$\frac{R_{R_h}}{\rho g \nabla_c} = a_0 + \frac{\nabla_c^{1/3}}{L_{WL}}\left(a_1 \frac{LCB_{fp}}{L_{WL}} + a_2 C_p + a_3 \frac{\nabla_c^{2/3}}{A_W} + a_4 \frac{B_{WL}}{L_{WL}} + a_5 \frac{LCB_{fp}}{LCF_{fp}} + a_6 \frac{B_{WL}}{T_c} + a_7 C_x\right), \tag{2.9}$$

where g is gravitational acceleration, ∇_c is the volume of displacement of the canoe body, a_i are the coefficients of the regression, LCB_{fp} is the longitudinal position of the centre of buoyancy measured from the forward perpendicular (fp), C_p is the prismatic coefficient, A_W is the waterplane area, B_{WL} is the beam of the waterline, LCF_{fp} is the longitudinal position of the centre of flotation measured from the fp, T_c is the draft of the canoe body, and C_x is the maximum sectional area coefficient. The definitions of the hydrostatic coefficients are given in Appendix A. The coefficients, a_0 up to a_7, were determined for Froude numbers 0.15 up to 0.75 with increments of 0.05 and are listed in Table B.2.

2.1.3. Bare hull resistance under heel

The bare hull heeled resistance consists of the upright resistance of the hull, the delta frictional resistance of the hull due to heel and the delta residuary resistance of the hull due to heel; i.e.

$$R_{T\phi_h} = R_{T_h} + \Delta R_{F\phi_h} + \Delta R_{R\phi_h}, \tag{2.10}$$

where $R_{T\phi_h}$ is the bare hull resistance under heel, $\Delta R_{F\phi_h}$ is the change in frictional resistance of the bare hull due to heel, and $\Delta R_{R\phi_h}$ is the change in residuary resistance of the bare hull due to heel.

Delta frictional resistance due to heel

According to Keuning and Sonnenberg [27], the change in frictional resistance of the hull due to heel is solely attributed to a change in wetted area of the yacht hull; i.e.

$$\Delta R_{F\phi_h} = \frac{1}{2}\rho V^2 C_f (S_c - S_{c\phi}), \tag{2.11}$$

where $S_{c\phi}$ is the wetted area of the canoe body under heel.

Delta residuary resistance due to heel

According to Keuning and Katgert [26], the change in residuary resistance of the bare hull due to heel can be approximated by

$$\frac{\Delta R_{R\phi_h}}{\rho g \nabla_c} = b_0 + b_1 \left(\frac{B_{WL\phi}}{T_{c\phi}} - \frac{B_{WL}}{T_c} \right) + b_2 (C_{x\phi} - C_x) + b_3 \frac{L_{WL\phi}}{L_{WL}}, \tag{2.12}$$

where b_i are the coefficients of the regression, $B_{WL\phi}$ is the beam of the waterline under heel, $T_{c\phi}$ is the draft of the canoe body under heel, $C_{x\phi}$ is the maximum sectional area coefficient under heel, and $L_{WL\phi}$ is the length of the waterline under heel. The coefficients, b_0 up to b_3, were determined for Froude numbers 0.15 up to 0.45 with increments of 0.05 and are listed in Table B.3.

2.1.4. Bare hull upright trimmed resistance

The bare hull upright trimmed resistance, $R_{T\theta_h}$, is defined by

$$R_{T\theta_h} = R_{T_h} + \Delta R_{R\theta_h}, \tag{2.13}$$

where $\Delta R_{R\theta_h}$ is the change in residuary resistance of the bare hull due to the trimming moment of the driving force. According to Keuning and Sonnenberg [27], the change in residuary resistance of the bare hull due to the trimming moment of the driving force can be approximated by

$$\frac{\Delta R_{R\theta_h}}{M_\theta / (KM_L \cdot \tan 1°)} = T_0 + T_1 \frac{L_{WL}}{B_{WL}} + T_2 \frac{B_{WL}}{T_c} + T_3 \frac{A_W}{\nabla_c^{2/3}} + T_4 LCB_\% + T_5 LCF_\%, \tag{2.14}$$

where T_i are the coefficients of the regression, M_θ is the longitudinal trimming moment of the driving force, KM_L is the longitudinal metacentric height, $LCB_\%$ is the longitudinal position of the centre of buoyancy expressed in percentage of L_{WL} measured from $1/2L_{WL}$, and $LCF_\%$ is the longitudinal position of the centre of flotation expressed in percentage of L_{WL} measured from $1/2L_{WL}$. The coefficients, T_0 up to T_5, were determined for Froude numbers 0.25 up to 0.60 with increments of 0.05 and are listed in Table B.4.

For the trimming moment of the driving force about the yacht's CoG, the following expression is used in the DSYHS:

$$M_\theta = 0.65 L_{WL} R_{T_h}, \tag{2.15}$$

where $0.65 L_{WL}$ is the assumed CoE height of the sails, and R_{T_h} is the bare hull upright resistance.

2.2. Extrapolation of resistance forces

The hydrodynamic forces and moments acting on the models of the DSYHS were determined with resistance tests in the #1 and #2 towing tanks of the Ship Hydromechanics Laboratory at the Delft University of Technology over the years. The waterline lengths of the models used in these tests were 1.6 metres for Series 1 and 2.0 metres for the other series. All the hydrodynamic forces and moments were extrapolated to a prototype scale with a waterline length of ten metres. The hydrodynamic forces and moments at this scale were used in regression analyses to derive the regressions of the DSYHS. The resistance forces of the bare hull were extrapolated as described in this section. The described method can be used to extrapolate the resistance to 'any' scale.

The measured resistance of the model is decomposed into a frictional resistance and a residuary resistance; i.e.

$$R_{t_m} = R_{f_m} + R_{r_m}, \tag{2.16}$$

where R_{t_m} is the total resistance at model scale, R_{f_m} is the frictional resistance at model scale, and R_{r_m} is the residuary resistance at model scale. The fictional resistance of the model follows Equation (2.6):

$$R_{f_m} = \frac{1}{2}\rho_m V_m{}^2 S_c C_f, \tag{2.17}$$

where ρ_m is the density at model scale, V_m is the model speed, and C_f is the friction coefficient of ITTC 1957 Model-Ship Correlation Line, determined by Equation (2.7). The Reynolds number needed for determining C_f is again based on a waterline length of $0.7L_{WL}$ and can be determined by Equation (2.8). For the same reasons as described in Subsection 2.1.2, no form factor is used for the frictional resistance.

As a consequence of this estimation of the frictional resistance, the residuary resistance contains the wave-making resistance, the viscous pressure resistance and maybe a (small) part of the frictional resistance. The wave-making resistance depends especially on the Froude number while the viscous pressure resistance and the frictional resistance depend especially on the Reynolds number. This introduces some (small) errors in the extrapolation procedure.

The residuary resistance of the model can now be determined from combining Equations (2.16) and (2.17). The residuary resistance is scaled under the assumption that the residuary resistance coefficients at model scale and at prototype scale are the same. Hence, it follows that

$$R_{r_p} = \frac{\rho_p}{\rho_m}\alpha^3 R_{r_m}, \tag{2.18}$$

where R_{r_p} is the residuary resistance at prototype scale, ρ_p is the density at prototype scale, and α is the scale factor between the waterline lengths of the two scales. The frictional resistance, R_{f_p}, at prototype scale can be determined from Equations (2.6), (2.7) and (2.8). The total resistance, R_{t_p}, at prototype scale is now given by

$$R_{t_p} = R_{f_p} + R_{r_p}. \tag{2.19}$$

2.3. Parameter range contained within the DSYHS

The DSYHS is a collection of different systematic series of sailing yacht hulls. Each individual series contains a parent model and a number of systematic variations of this parent model. The DSYHS contains seven of these series and in total almost 60 different hulls. The hydrostatic parameters of the 55 models of Series 1 up to 4, 6 and 7 are listed in Table B.1. The lines plans of some of the models are depicted in Appendix C.

Over the years, a large variety of sailing yacht designs was incorporated in the DSYHS. Series 1 is based on the Standfast 43, which was a successful Admiral's Cupper in 1970. The parent hull of this series is Sysser 1. The 22 hull shapes within Series 1 were tested in the 1970s. In 1983, a new parent hull, Sysser 25, was introduced for Series 2 and 3 to reflect the changing trends in yacht design. Within Series 3, emphasis was placed on very light displacement hulls and larger length-to-beam ratios.

To keep up with the developments in sailing yacht design, a new parent hull, Sysser 44, was added to the DSYHS in 1995. Sysser 44 is a 40-feet International Measurement System (IMS)-design. Series 6 and 7 were added after the year 2000. The three hull shapes of Series 6 are based on Sysser 44 and were specifically added to create more variation in the maximum sectional area coefficient contained within the DSYHS. The three hull shapes of Series 7 are based on Sysser 25. The goal of Series 7 was to incorporate the characteristics of maxi and mega yachts. These yachts had smaller beam-to-length ratios in combination with small displacement-to-length ratios than was contained within the DSYHS at that time.

The hydrostatic parameter range contained within the DSYHS determines the range of applicability of the regressions. Series 1 up to 4 contain together 49 models and were used to derive the regressions given by Keuning and Sonnenberg [27]. The regression for the change in residuary resistance of the bare hull due to the trimming moment, Equation (2.14), was derived from these 49 models. The hydrostatic parameter range for these series is given in Table 2.1. The maximum, minimum and mean values, and the standard deviation are listed for each parameter.

The regressions derived by Keuning and Katgert [25,26] are based on the 55 models of Series 1 up to 4, 6 and 7. The regression for the residuary resistance of the hull, Equation (2.9), and the regression for the change in residuary resistance of the bare hull due to heel, Equation (2.12), were derived from these 55 models. The parameter range for these series is given in Table 2.2. The maximum, minimum and mean values, and the standard deviation are listed for each parameter.

As a result of this large variety in hull shapes contained within the DSYHS, a very wide range of possible yacht designs is being covered by the DSYHS. Nevertheless, it may be necessary to expand the DSYHS once more with a new series of modern yacht designs.

Table 2.1: The parameter range contained within Series 1 up to 4 of the DSYHS. The regression for the change in residuary resistance of the bare hull due to the trimming moment of the driving force, Equation (2.14), is based on this range.

	$\frac{LCB_{fp}}{L_{WL}}$	C_p	$\frac{\nabla_c^{2/3}}{A_W}$	$\frac{B_{WL}}{L_{WL}}$	$\frac{LCB_{fp}}{LCF_{fp}}$	$\frac{\nabla_c^{1/3}}{L_{WL}}$	C_x	$\frac{B_{WL}}{T_c}$
Maximum	0.582	0.599	0.265	0.366	1.002	0.230	0.777	19.38
Minimum	0.500	0.522	0.079	0.200	0.920	0.120	0.646	2.46
Mean	0.533	0.555	0.173	0.289	0.962	0.182	0.695	6.22
σ	0.019	0.018	0.048	0.039	0.022	0.035	0.048	3.63
σ [%Mean]	3.54	3.33	27.9	13.8	2.26	19.4	6.82	59.4

Table 2.2: The parameter range contained within Series 1 up to 4, 6 and 7 of the DSYHS. The regression for the residuary resistance of the hull, Equation (2.9), and the regression for the change in residuary resistance of the bare hull due to heel, Equation (2.12), are based on this range.

	$\frac{LCB_{fp}}{L_{WL}}$	C_p	$\frac{\nabla_c^{2/3}}{A_W}$	$\frac{B_{WL}}{L_{WL}}$	$\frac{LCB_{fp}}{LCF_{fp}}$	$\frac{\nabla_c^{1/3}}{L_{WL}}$	C_x	$\frac{B_{WL}}{T_c}$
Maximum	0.582	0.599	0.265	0.366	1.002	0.230	0.790	19.38
Minimum	0.500	0.519	0.079	0.170	0.920	0.120	0.646	2.46
Mean	0.535	0.553	0.172	0.282	0.962	0.180	0.700	6.12
σ	0.019	0.019	0.046	0.044	0.021	0.034	0.049	3.45
σ [%Mean]	3.58	3.49	26.8	15.6	2.15	19.0	7.00	56.5

2.4. Comparison of the regressions with experimental results

In order to asses the accuracy of the regressions for the bare hull resistance, the resistance computed with these regressions is compared with experimental results. A comparison of the resistance values for the upright untrimmed condition, the upright trimmed condition and the heeled untrimmed condition is given in this section. The comparison is made at prototype scale, $L_{WL} = 10.00\ m$.

Ten models of the DSYHS are used in this comparison: Syssers 25, 28, 33, 39, 44, 47, 61, 62, 72 and 73. The lines plans and the hydrostatic parameters of all these Syssers are given in Appendix C. These Syssers were tested with the standard measurement method of the DSYHS in one of the two towing tanks of the Ship Hydromechanics Laboratory at the Delft University of Technology over the years. The standard measurement method of the DSYHS was specifically developed by the Ship Hydromechanics Laboratory for resistance measurements of sailing yacht models. For an explanation of this experimental method, the reader is referred to Katgert and Den Ouden [24].

The differences between the resistance estimated with the DSYHS regressions and the measured resistance for the upright untrimmed, upright trimmed and heeled untrimmed conditions are listed in Table B.5. These comparison errors E are given as a percentage of the extrapolated experimental results. Some exceptions excluded, the DSYHS regressions reasonably — $|E| \leq 10\%$ — predict the resistance of these ten Syssers. The resistance of the upright untrimmed condition is the most accurately predicted. For Syssers 25, 28, 39 and 44, the resistance prediction is accurate with differences between $\pm 7.5\%$.

Even for the Syssers with the more 'extreme' parameters compared to the mean values of the parameter range contained within the DSYHS, e.g. Syssers 39, 71 and 72, the prediction is reasonable. For Sysser 39, the prediction is accurate with differences between $\pm 6\%$. For Syssers 71 and 72, the difference between the resistance predicted by the regressions and the resistance measured in the towing tank is within -0.1% and +16.8% for the upright resistance, and within -1.8% and +13.9% for the trimmed resistance. This illustrates that the regressions of the DSYHS are applicable to a large variety of sailing yacht designs.

This comparison also indicates that the resistance of the more traditional hull shapes, i.e. the hull shapes of Series 1 up to 4, is better predicted than the resistance of the more recent hull shapes of Series 7. This is not that strange since Series 1 up to 4 contain together 49 models while Series 7 contains only three models. The more traditional hull shapes are stronger represented in the DSYHS. This suggests that the resistance of modern sailing yachts, which have considerably different design characteristics than the traditional hull shapes of the DSYHS and have similar beam-to-length and displacement-to-length ratios as Sysser 72 and 73, may not be accurately predicted by the DSYHS regressions. As said before, Series 7 was specifically created to introduce smaller beam-to-length ratios in combination with small displacement-to-length ratios than was contained within the DSYHS at that time.

2.5. Limitations of the DSYHS regressions

As stated before, a very wide range of possible sailing yacht designs is being covered by the DSYHS. In order to keep up with the trends and developments in sailing yacht design, it may be necessary to expand the DSYHS once more with a new series of contemporary yacht designs. After the last extension of the DSYHS, the most pronounced developments in yacht design are the straight vertical bows, the wide transoms and the very light displacement hulls. Furthermore, the contemporary designs carry above the waterline their maximum beam all the way aft. These changes in sailing yacht design are significant and may have led to the situation where recent designs of yacht hulls are not longer fully covered by the hull shapes within the DSYHS. The regression formulas derived from the DSYHS can therefore be less applicable to the contemporary hull shapes. The accuracy of the velocity prediction for modern high performance sailing yachts will suffer from this in some extent. Moreover, these developments contribute to the ever increasing speed potential of the newer designs.

The limitations of the regressions of the DSYHS for modern high performance sailing yachts are discussed in this section. They form the motivation for the present study.

2.5.1. Speed range

An obvious limitation of the use of the regression formulas, derived from the DSYHS, for the purpose of velocity prediction of modern high performance yachts is the speed range covered by the series. The speeds range within the DSYHS covers Froude numbers from 0.15 up to 0.75. Some of the regressions cover only Froude numbers up to 0.45. Modern high performance yachts are capable of reaching higher speeds than Froude number 0.75. For the velocity prediction of these yachts, regression formulas for the hydrodynamic forces and moments up to Froude number 0.95 are desirable.

2.5.2. Parameter range
Another limitation of the use of the regression formulas, derived from the DSYHS, for the purpose of velocity prediction of modern yachts is the big difference in hull design between modern hull shapes and 'traditional' hull shapes. Contemporary hull shapes distinguish themselves from the traditional hull shapes of the DSYHS by their straight vertical bows, wide transoms, very long waterlines compared to the overall length, very light displacement hulls, relatively small beam-to-length ratios of the waterline, small displacement-to-length ratios and relatively small displacement-to-waterplane area ratios. Moreover, the contemporary designs carry above the waterline their maximum beam all the way aft. The differences between modern and traditional hull shapes become very obvious if, for instance, the lines plans of Sysser 25 and Sysser 85, shown in Figures C.1 and C.13, respectively, are compared with each other. The main dimensions and the hydrostatic coefficients of modern sailing yachts may not be fully covered by the parameter range contained within the DSYHS.

In order to put these thoughts in perspective, a comparison between the hydrostatic parameters of the modern Sysser 85 and the parameter range contained within the DSYHS is made. The parameter range of the DSYHS is given in Table 2.2. Sysser 85 resembles a modern Transpac 52 (TP52) racing yacht design. The lines plan and the hydrostatic parameters of Sysser 85 are given in Appendix C. Sysser 85 does not belong to the DSYHS.

A comparison of its parameters with the parameter range of the DSYHS is given in Table 2.3. This comparison shows that the parameters of this hull shape fall entirely within the range of the DSYHS. Although all its parameters lie within the parameter range of the DSYHS, the difference between some of its parameters and the mean value of the parameters in the DSYHS is larger than the standard deviation of the parameter in the DSYHS. This holds for the displacement-to-waterplane area ratio, the beam-to-length ratio of the waterline, the longitudinal centre of buoyancy-to-longitudinal centre of flotation ratio and the displacement-to-length ratio. The deviation of these parameters from the mean value of the DSYHS coincides perfectly with the differences between the traditional hull shapes of the DSYHS and modern hull shapes. This suggests that the regression formulas derived from the DSYHS are less applicable to recent hull shapes. The DSYHS is no longer representative of today's high performance yacht designs.

Table 2.3: The parameters of Sysser 85 and the parameter range contained within the DSYHS, given in Table 2.2.

	$\frac{LCB_{fp}}{L_{WL}}$	C_p	$\frac{\nabla_c^{2/3}}{A_W}$	$\frac{B_{WL}}{L_{WL}}$	$\frac{LCB_{fp}}{LCF_{fp}}$	$\frac{\nabla_c^{1/3}}{L_{WL}}$	C_x	$\frac{B_{WL}}{T_c}$
Maximum	0.582	0.599	0.265	0.366	1.002	0.230	0.790	19.38
Sysser 85, TP52	0.539	0.543	0.122	0.205	0.940	0.131	0.683	6.92
Minimum	0.500	0.519	0.079	0.170	0.920	0.120	0.646	2.46
Mean	0.535	0.553	0.172	0.282	0.962	0.180	0.700	6.12
σ	0.019	0.019	0.046	0.044	0.021	0.034	0.049	3.45

2.5.3. Resistance prediction
In order to asses the accuracy of the regressions of the DSYHS for contemporary high performance sailing yacht designs, the predicted resistance of a modern design is compared with experimental results. The comparison is made at prototype scale, $L_{WL} = 10.00\ m$. A comparison of the total resistance values for the upright untrimmed condition, the upright trimmed condition and the heeled untrimmed condition for Sysser 85 is given. Sysser 85 was tested with the standard measurement method of the DSYHS in the #1 towing tank of the Ship Hydromechanics Laboratory at the Delft University of Technology in the year 2010. For an explanation of this experimental method, the reader is referred to Katgert and Den Ouden [24].

The bare hull resistance calculated with the DSYHS regressions and the bare hull resistance measured in the towing tank for the upright untrimmed, upright trimmed and heeled untrimmed conditions are depicted in Figure 2.2. In Table B.5, the bare hull resistance calculated with the DSYHS regressions is given as a percentage change from the extrapolated experimental results. The DSYHS regressions mostly underpredict the resistance of Sysser 85. This holds for the upright, trimmed and heeled conditions. The difference between the resistance predicted by the regressions and the resistance measured in the towing tank is within -15.9% and +1.9%.

For the residuary resistance, the relative discrepancy between the regressions and the experimental results is larger. For the upright residuary resistance, this discrepancy is within -28.4% and +3.1% for Froude numbers up to 0.60, as can be seen in Table B.6. For Froude numbers after 0.60, the upright residuary resistance is accurately predicted by the DSYHS regressions. Some exceptions excluded, the change in residuary resistance due to the trimming moment of the driving force and the change in residuary resistance due to heel is poorly predicted by the regressions of the DSYHS. Excluding Froude number 0.25 for which the discrepancies are by far the largest, the differences are within -39.7% and -4.4%.

The large discrepancies in residuary resistance are significant. Together with the relatively large differences in bare hull resistance, they will definitely influence the accuracy of the performance prediction of this TP52-design. One of the reasons for these relatively large differences in total resistance and residuary resistance between the regressions of the DSYHS and the experimental results may be the deviation of the hydrostatic parameters of Sysser 85 from the mean value of the parameter range contained within the DSYHS.

A comparison between the accuracy of the resistance prediction for models belonging to the DSYHS, discussed in Section 2.4, and the accuracy of the resistance prediction for Sysser 85, not belonging to the DSYHS, suggests that the regressions of the DSYHS predict the resistance of the models belonging to the DSYHS more accurately.

2.5.4. Conclusions
After the last extension of the DSYHS, the most pronounced developments in sailing yacht design are the straight vertical bows, the wide transoms, the very light displacement hulls and the very long waterlines compared to the overall length. Above the waterline, the contemporary designs carry their maximum beam all the way aft. These changes in sailing yacht design are significant and have led to the situation where recent designs of sailing yacht hulls are less accurately covered by the hull shapes within the DSYHS. The regression formulas derived from the DSYHS are therefore less applicable to recent hull shapes. The accuracy of the velocity prediction of modern high performance sailing yachts will suffer from this in some extent. Moreover, these developments contribute to the ever increasing speed potential of the newer designs. The DSYHS is no longer representative of today's high performance yacht designs. As a result of the developments in yacht design, it is found necessary to create a new systematic series of modern high performance yacht hulls. The regressions derived from this new series should cover a wider speed range and a different range of main dimensions and hydrostatic coefficients than those of the DSYHS.

Based on a similar analysis for an IMOCA 60, Huetz [14] also suggests that new regressions are necesarry to improve the velocity prediction of recent designs, especially for the influence of heel and trim on the bare hull resistance.
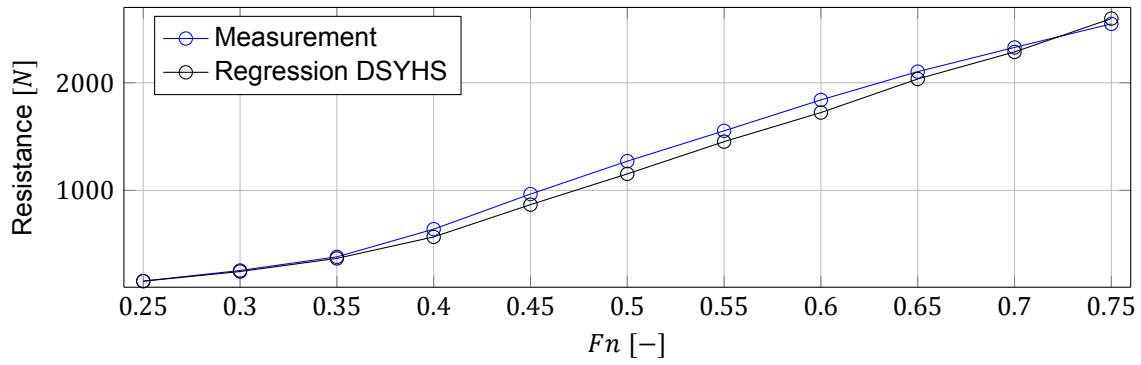
(a) Bare hull upright resistance.
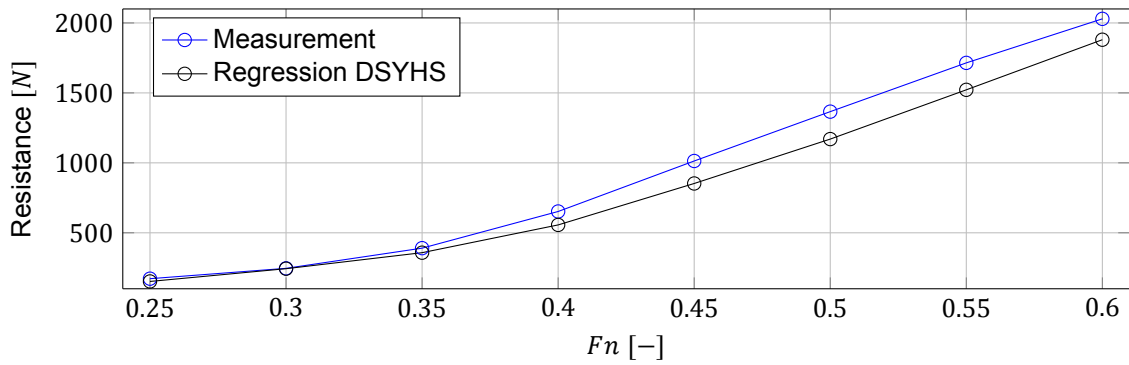
(b) Bare hull upright trimmed resistance.
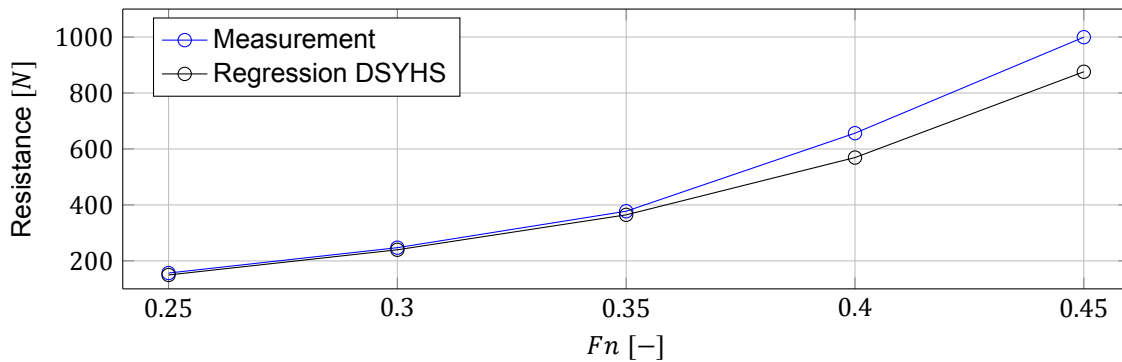
(c) Bare hull resistance under 20 degrees heel.
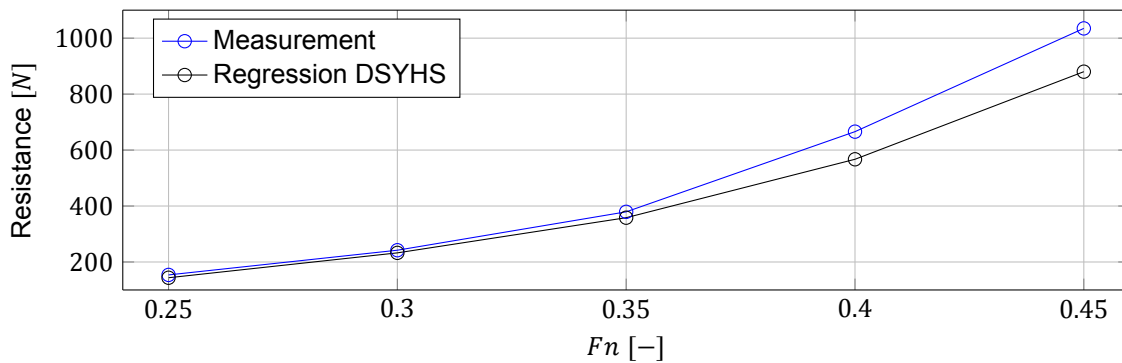
(d) Bare hull resistance under 30 degrees heel.

Figure 2.2: The resistance calculated with the DSYHS regressions and the measured resistance for Sysser 85 with a waterline length of ten metres for the upright untrimmed, upright trimmed and heeled untrimmed conditions.

3

New systematic series

As a result of the developments in sailing yacht design, it is necessary to create a new systematic series of contemporary yacht hulls, in order to improve the velocity prediction of modern high performance yachts. The regressions derived from this new series should cover a wider speed range and a different range of hydrostatic parameters than those of the DSYHS. The new series should be representative of a wide range of today's high performance yacht designs.

Within this study, a new systematic series of high performance sailing yacht hulls is derived. A modern TP52-design is used as the parent model of this new series. The parent hull is selected in Section 3.1. From this parent hull, a number of relevant hull shapes is derived. The chosen systematic variations and the used transformation methods are discussed in Section 3.2. The variations of the parent model are chosen such that the new series covers the wide range of modern yacht designs as much as possible. The derived systematic series and the models it contains, are presented in Section 3.3.

The hydrodynamic forces acting on the models in this new series are not determined with experimental research in the towing tank as was done for the DSYHS, but are calculated with computational fluid dynamics (CFD). A thorough discussion of this numerical method is given in Chapter 6. The test conditions for which the hydrodynamic forces are determined, are given in Chapter 4. The hydrodynamic forces acting on the models are used to derive new regressions for the bare hull resistance in Chapter 10.

Determining the upright untrimmed resistance, the resistance under heel and the upright trimmed resistance of the models, and deriving new regressions for all the bare hull resistance components is beyond the scope of this study. Consequently, a choice has to be made between these resistance components. This choice will be based on an assessment of the bare hull resistance components of the parent hull in Section 3.1.

3.1. Parent hull

For the new systematic series of modern high performance yacht hulls, a parent hull has to be selected. A choice was made to select a not-too-extreme design in order for the new systematic series to be widely applicable. A modern racing yacht design was tested for various speeds and heel angles in the towing tank of the Ship Hydromechanics Laboratory at the Delft University of Technology in the year 2010. This model, Sysser 85, was selected to be the parent hull of the new systematic series.

Sysser 85 was designed by the Ship Hydromechanics Laboratory in the year 2010. The model is based on Sysser 28 of the DSYHS and was designed to the characteristics and main dimensions of a Transpac 52 (TP52). According to modern high performance sailing yacht designs, Sysser 85 has a straight vertical bow, a wide transom, a very light displacement hull, a very long waterline compared to its overall length, and it carries above the waterline its maximum beam all the way aft. Sysser 85 satisfies the TP52 class rules [45]. Sysser 85 is not an existing TP52 and was never added to the DSYHS. The lines plan of Sysser 85 is depicted in Figure C.13. The main dimensions and the hydrostatic parameters of the parent hull of the new systematic series, at full scale, are listed in Table 3.1.

Table 3.1: Main dimensions and hydrostatic parameters of
Sysser 85, a TP52-design, at full scale.

L_{OA}	$[m]$	15.85	LCF_{fp}	$[m]$	8.94
L_{WL}	$[m]$	15.60	S_c	$[m^2]$	36.59
B_{WL}	$[m]$	3.19	A_X	$[m^2]$	1.01
B_{OA}	$[m]$	4.41	A_W	$[m^2]$	34.22
T_c	$[m]$	0.462	C_b	$[-]$	0.371
∇_c	$[m^3]$	8.56	C_p	$[-]$	0.543
Δ_c	$[kg]$	8780	C_x	$[-]$	0.683
LCB_{fp}	$[m]$	8.40	C_w	$[-]$	0.687

3.1.1. Bare hull resistance components

Determining the bare hull upright untrimmed resistance, the bare hull resistance under heel and the bare hull upright trimmed resistance of the models in the new systematic series, and deriving new regressions for all the bare hull resistance components is beyond the scope of the present study. Consequently, a choice has to be made between these resistance components. A promising method for the improvement of the velocity prediction of modern sailing yachts from a hydrodynamic perspective is to improve the prediction of the two largest bare hull resistance components. An assessment of the relative importance of the bare hull resistance components is therefore necessary. The bare hull resistance components of the parent hull, derived from experimental results with the resistance decomposition shown in Figure 2.1, are examined in this subsection.

Sysser 85 was tested with the standard measurement method of the DSYHS in the #1 towing tank of the Ship Hydromechanics Laboratory at the Delft University of Technology in the year 2010. For an explanation of this experimental method, the reader is referred to Katgert and Den Ouden [24]. The bare hull upright resistance, the bare hull upright trimmed resistance, and the bare hull resistance under 20 and 30 degrees were measured. The resistance values obtained from these tests are extrapolated to a waterline length of ten metres with the method discussed in Section 2.2. The resistance values at this scale are used in this comparison of the bare hull resistance components.

Following the resistance decomposition method of the DSYHS, shown in Figure 2.1, the bare hull upright trimmed resistance consists of the bare hull upright untrimmed resistance and the change in residuary resistance of the bare hull due to the trimming moment of the driving force. The bare hull resistance under heel consists of the bare hull upright untrimmed resistance, and the change in residuary and frictional resistance due to heel.

The resistance for the upright untrimmed, upright trimmed and heeled untrimmed conditions, as well as the delta resistance components, of Sysser 85 are plotted in Figure 3.1. For the trimmed and heeled conditions, the bare hull upright untrimmed resistance is by far the largest component of the resistance. It covers 85 to 104 percent of the bare hull trimmed resistance and 90 to 106 percent of the bare hull resistance under heel. For the higher Froude numbers, the delta residuary resistance due to the trimming moment of the driving force is considerably larger than the delta resistance due to heel.

The upright untrimmed resistance and the delta resistance due to the trimming moment of the driving force seem to be the two most important bare hull resistance components for the velocity prediction of Sysser 85. This especially holds for the higher Froude numbers, where the upright untrimmed resistance and the delta resistance due to the trimming moment of the driving force are the largest bare hull resistance components. The upright untrimmed resistance is the dominant resistance component at all the speeds. Improving the prediction of the upright untrimmed resistance and the delta resistance due to the trimming moment by deriving new regressions, from the new systematic series, for these components is therefore a promising method to improve the velocity prediction of modern TP52-like yacht designs from a hydrodynamic perspective. The upright untrimmed resistance and the delta resistance due to the trimming moment of the driving force are therefore the main focus of this study.
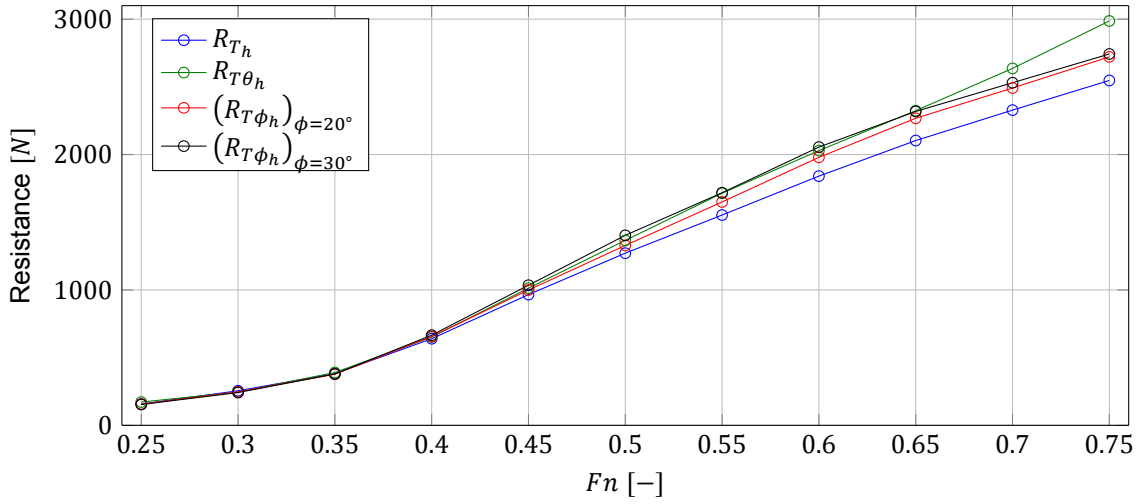
(a) Bare hull resistance.
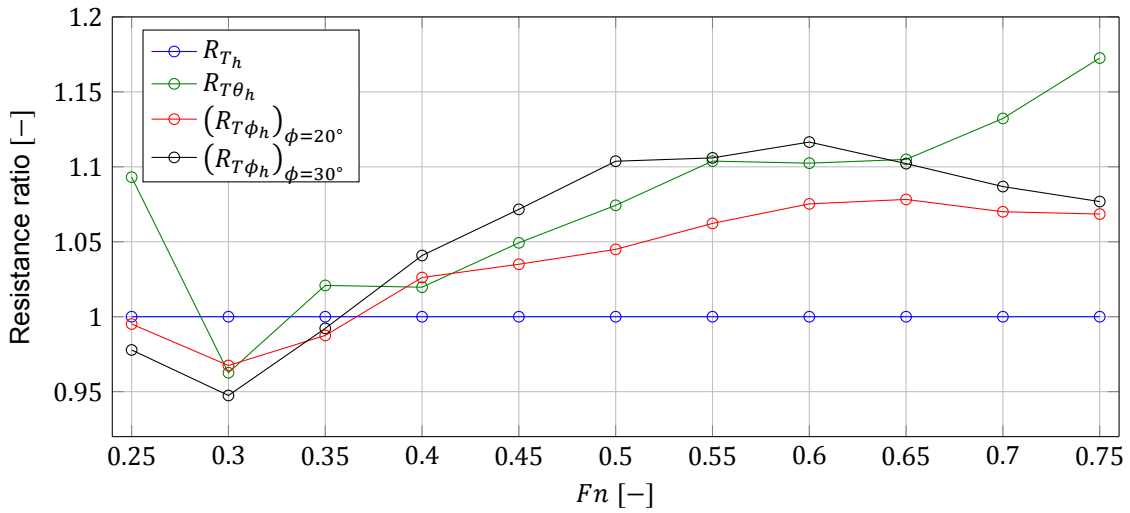
(b) Resistance ratio with respect to the bare hull upright untrimmed resistance.
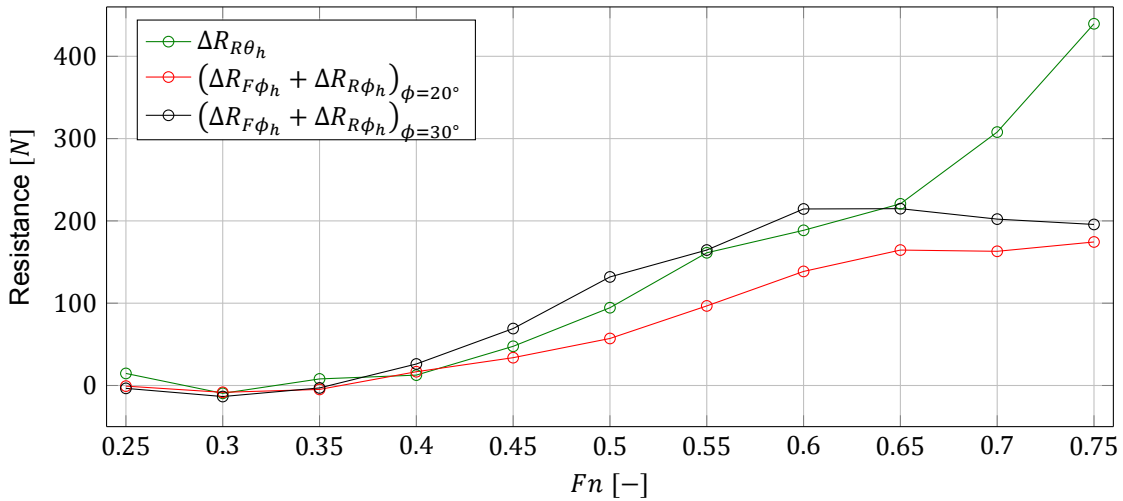
(c) Delta resistance components.

Figure 3.1: The bare hull resistance and the delta resistance components of Sysser 85 with a waterline length of ten metres for the upright untrimmed, upright trimmed and heeled untrimmed conditions, derived from resistance measurements.

3.2. Variations

In order to derive relations between the hydrodynamic forces and the geometries of various hull shapes, a systematic series of different hull shapes is created. The new systematic series of modern high performance yacht hulls should cover a wide range of hydrostatic parameters in order to be widely applicable. The new series should be representative of a wide range of today's high performance yacht hulls. Since the available computation time is limited, the number and the type of variations have to be chosen wisely. The varied parameter is expected to have a significant influence on the hydrodynamic forces. Moreover, the variation in the parameter is large enough to find a noteworthy change in the hydrodynamic forces. In order to uncouple the influence of the different hydrostatic parameters on the hydrodynamic forces, only the specific parameter under consideration should be changed while keeping all the other parameters constant. A large systematic series will enhance the quality, robustness and stability of the derived regressions. The new systematic series is derived taking all these considerations into account.

Before deriving the new systematic series, the variations between the models are chosen in Subsection 3.2.1. After the variations are selected, the hull shapes in the systematic series can be constructed by means of the transformation methods discussed in Subsection 3.2.2. The derived systematic series is presented in the next section.

3.2.1. Selected variations

A new bare hull upright trimmed resistance prediction is derived from a new systematic series of high performance yacht hulls in this study. In order to derive the new systematic series specifically for this goal, use is made of the regressions of the DSYHS derived by Keuning et al. [25,27]. These references give expressions for the bare hull upright resistance and the delta residuary resistance due to the trimming moment of the driving force. These two regressions are given by Equations (2.9) and (2.14) of this thesis. These expressions are a perfect way to identify the hydrostatic parameters that are expected to have a significant influence on the upright trimmed resistance. Variations in these parameters are used to construct the systematic series.

Following these two regressions of the DSYHS, the new systematic series is focussed on variations in displacement-to-length ratio, beam-to-length ratio, beam-to-draft ratio, longitudinal centre of buoyancy-to-length ratio, longitudinal centre of buoyancy-to-longitudinal centre of flotation ratio, prismatic coefficient, maximum sectional area coefficient, and displacement-to-waterplane area ratio. The expected influence of these parameters on the resistance is discussed below. A description of the variations applied to the 21 models of the new series is given in Table 3.2. The range of variations is also listed there. All the models have the same waterline length.

The displacement-to-length ratio, $\nabla_c^{1/3}/L_{WL}$, also called the slenderness ratio, expresses the fineness of a hull. Its influence on the resistance is pretty obvious. More displacement for a given waterline length generally increases the resistance. A lower displacement-to-length ratio leads to a reduction of the intensity of the generated waves and consequently to a reduction in wave-making resistance. It also reduces the viscous pressure resistance. This resistance component and the wave-making resistance are part of the residuary resistance. The displacement-to-length ratio is expected to be the dominant parameter for the residuary resistance.

The beam-to-length ratio, B_{WL}/L_{WL}, is also an important factor for the resistance of sailing yachts. In general, for a given waterline length and displacement, a larger waterline beam increases the wetted surface and therefore the frictional resistance. For the higher speeds in upright condition, it may reduce the resistance due to generation of more dynamic lift. For a given length and displacement, a yacht with a smaller beam-to-length ratio generally sails faster on close-hauled courses while a yacht with a larger beam-to-length ratio is faster on broad reach courses. In general, the wider yacht has a higher resistance under heel and leeway, a poorer seakeeping behaviour and a larger added resistance in waves for wave encounter angles between 180 degrees (head waves) and 90 degrees (beam waves), i.e. on courses between close-hauled and beam reach.

The beam-to-length ratio is an important factor especially for the resistance at the higher speeds. It was originally introduced into the regressions of the DSYHS based on its importance for the resistance of planing motorboats. For planing motorboats, the length-to-beam ratio of the part of the hull remaining

in the water determines the aspect ratio of that waterline and for a large part the generated lift and the resistance. Note that for a planing motorboat, its waterline beam remains almost unchanged while its waterline length is highly influenced by the trim angle and the speed. Contrary to planing motorboats, sailing yachts at high speeds use a large part of their waterline length for the longitudinal stability needed to resist the trimming moment of the driving forces acting on the sails. The hydrostatic beam-to-length ratio is considered to be an important factor for the resistance of sailing yachts, especially at the higher speeds.

The beam-to-draft ratio, B_{WL}/T_c, expresses the proportions of the ship's sections. It effects the resistance in various ways. A larger beam-to-draft ratio implies a larger wetted surface for the same displacement and thus a higher frictional resistance. At the lower speeds, the wave resistance generally increases with increasing beam-to-draft ratio. The beam-to-draft ratio is closely related to the dead rise angle. A high beam-to-draft ratio implies a small dead rise angle, which is good for the planing abilities and the resistance at the higher speeds, but results in bad seakeeping behaviour and an increase in resistance at the lower speeds. A high beam-to-draft ratio implies a large deformation of the waterline shape under heel, which may negatively influence the resistance under heel.

In general, for smooth hulls with an almost constant beam-to-draft ratio over the entire waterline length, the beam-to-draft ratio of the waterline, B_{WL}/T_c, is highly correlated with the displacement-to-waterplane area ratio. In this case, a high beam-to-draft ratio implies a relatively light displacement hull with respect to its waterplane area. The beam-to-draft ratio is also likely to be highly correlated to the displacement-to-wetted surface area ratio.

The longitudinal centre of buoyancy-to-length ratio, LCB_{fp}/L_{WL}, defines the position of the longitudinal position of the centre of buoyancy. The longitudinal centre of buoyancy expresses the degree of concentration of the lengthwise distribution of the volume of displacement. The longitudinal centre of buoyancy-to-length ratio is also a measure for the centreline shape. It is an important factor for the pressure distribution along the hull and therefore for the intensity of the generated wave system. A centre of buoyancy ahead of the optimum position is likely to intensify the generated waves at the bow sections. A centre of buoyancy aft of the optimum position is likely to intensify the generated waves at the aft sections and can increase flow separation at the afterbody. An optimum LCB_{fp} has to be found together with an optimum prismatic coefficient, since both have a strong influence on the wave-making resistance and interact with each other. In general, the longitudinal centre of buoyancy should move aft with increasing speed. The variation in the optimum location of the centre of buoyancy is generally very small over the speed range.

The prismatic coefficient, C_p, defines the ratio between the volume of displacement and the extrusion of the maximum sectional area, A_X, along the waterline length;

$$C_p = \frac{\nabla_c}{A_X L_{WL}}. \tag{3.1}$$

A low prismatic coefficient indicates a relatively large maximum sectional area, concentrated displacement around the midship and thus slender ends at the bow and the stern. A high prismatic coefficient indicates an evenly distributed displacement along the waterline length with a lot of volume at the stern and the bow. The prismatic coefficient is an important factor for the wave-making resistance. Its influence on the resistance changes with speed. It is also associated with the interference between the waves generated at the bow and the waves generated at the stern. The displacement-to-length ratio, the prismatic coefficient and the centre of buoyancy are the most important parameters for the intensity and the shape of the generated wave systems at the bow and at the stern.

The optimum prismatic coefficient increases with the Froude number. An optimum prismatic coefficient together with an optimum position of the longitudinal centre of buoyancy should be specifically chosen for the desired speed range. In general, bluff — less streamlined — forebodies tend to increase the generated waves while bluff afterbodies tend to decrease them. A high prismatic coefficient with the centre of buoyancy far aft indicates a very bluff afterbody while the forebody is still relatively streamlined. With increasing speed, the optimum prismatic coefficient increases and the optimum centre of buoyancy moves aft. The associated fuller stern increase the viscous pressure resistance by lowering

the pressure at the afterbody due to the associated thicker boundary layer, possible flow separation and larger streamline curvature; thereby the pressure difference between the bow and the stern is increased, resulting in a higher viscous pressure resistance. However, the fuller stern generally reduces the wave-making resistance.

At the low speeds, the wave-making resistance is relatively small and the viscous pressure resistance is more important while at the higher speeds, the wave-making resistance dominates and the viscous pressure resistance is of less importance. A yacht optimized for high speeds has a relatively large prismatic coefficient with a centre of buoyancy moved relatively aft while a yacht optimized for low speeds has a relatively low prismatic coefficient with the centre of buoyancy relatively far forward.

The waterplane area-to-displacement ratio, $A_W/\nabla_c^{2/3}$, also called the loading factor, influences the resistance especially at the higher speeds. At the higher speeds, hydrodynamic lift is generated which reduces the resistance. The hydrodynamic lift is related to the hydrodynamic pressure acting on the hull and the horizontal surface of the hull. For a given pressure, the generated lift is proportional to this horizontal surface. This surface is highly correlated to the hydrostatic waterplane area. The waterplane area-to-displacement ratio is a measure for the trade-off between the hydrodynamic lift at the higher speeds and the yacht's weight. It gives an indication for the planing abilities of a yacht. The higher the ratio, the easier the hull shape should be able to plane. The loading factor was originally introduced into the regressions of the DSYHS based on its importance for the resistance of planing motorboats.

The longitudinal centre of buoyancy-to-longitudinal centre of flotation ratio, LCB_{fp}/LCF_{fp}, defines the longitudinal centre of flotation with respect to the longitudinal centre of buoyancy. This ratio is an important factor for the running trim and thereby also for the running sinkage of a yacht. The longitudinal centre of buoyancy is the point where the resultant hydrostatic buoyancy force acts on the yacht. The longitudinal centre of gravity is located above the centre of buoyancy. The longitudinal centre of flotation is the geometric centre of the waterplane area and the pivot point about which the sailing yacht trims. The longitudinal centre of flotation is correlated to the centre of effort of the hydrodynamic lift provided at the higher speeds. A higher LCB_{fp}/LCF_{fp} ratio therefore helps to trim bow up at the higher speeds, because it increases the arm between the gravity force and the resultant hydrodynamic lift. Trimming bow up may result in lower resistance and higher dynamic lift.

The maximum sectional area coefficient, C_x, is defined by

$$C_x = \frac{A_X}{B_{WL}T_c}.$$ (3.2)

It defines the fullness of the section with the maximum sectional area. A high coefficient indicates a boxy section shape. A low coefficient indicates more V-shaped sections. The maximum sectional area coefficient is expected to influence the residuary resistance at the lower speed and at the higher speeds.

3.2.2. Transformation methods
In order to apply the selected variations to the parent hull, different transformation methods are used. Variations in the beam-to-length ratio, the beam-to-draft ratio and the displacement-to-length ratio are obtained by uniformly stretching of the geometry in three directions. Stretching along the three axes is accomplished by multiplication of the coordinates of control points with three factors, one for each direction.

Variations in the prismatic coefficient are obtained by narrowing or widening of the model by uniformly stretching. The waterlines and the buttocks are then reshaped to obtain the same displacement, the same longitudinal centre of buoyancy-to-length ratio, the same longitudinal centre of buoyancy-to-longitudinal centre of flotation ratio and the desired prismatic coefficient. Variations in the maximum sectional area coefficient are obtained by altering the bilge radius and reshaping the sections.

Variations in the longitudinal centre of buoyancy-to-length ratio are obtained by shifting the sections to obtain the longitudinal distribution of sectional areas belonging to the desired longitudinal centre of buoyancy. Slight modifications of the sections and buttocks are necessary to obtain the desired variation. Variations in the longitudinal centre of buoyancy-to-longitudinal centre of flotation ratio are

obtained by altering the shape of the design waterline by widening or narrowing the waterline in the front and the back while keeping the same longitudinal centre of buoyancy. Slight modifications of the buttocks are necessary to obtain the desired longitudinal centre of buoyancy.

No effort is made to incorporate specific variations in the displacement-to-waterplane area ratio. A wide range of variations in this ratio is already present in the series as an inevitable consequence of the above-mentioned variations. Keeping this ratio constant for these above-mentioned variations was found to be impossible.

All the models have been faired and checked for smoothness.

3.3. Systematic series

Now the variations are selected, the new models can be derived from the parent hull with the described transformation methods. The lines plans and the hydrostatic parameters of the 21 models in the new series are given in Appendix C.3. The magnitude of the obtained variations deviates slightly from the numbers given in Table 3.2. The hydrostatic coefficients and ratios of the hull shapes in this series are listed in Table 3.3. The parameter range in the series is also given. This range differs from the parameter range of the DSYHS, listed in Table 2.2.

Table 3.2: Description of the new systematic series.

Model	Variations
Sysser 85	Parent hull.
Sysser 86	Same displacement as parent but 15% narrower and 15% deeper.
Sysser 87	Same displacement as parent but 15% wider and 15% shallower.
Sysser 88	Same beam-to-draft ratio as parent but a 15% higher displacement.
Sysser 89	Same beam-to-draft ratio as parent but a 15% lower displacement.
Sysser 90	Same beam-to-length ratio as parent but a 15% higher displacement and 15% deeper.
Sysser 91	Same beam-to-length ratio as parent but a 15% lower displacement and 15% shallower.
Sysser 92	Higher maximum sectional area coefficient (+7%).
Sysser 93	Lower maximum sectional area coefficient (-7%).
Sysser 94	Higher prismatic coefficient (+10%).
Sysser 95	Lower prismatic coefficient (-10%).
Sysser 96	Longitudinal centre of buoyancy moved aft by 4%. Longitudinal centre of flotation moved aft by 2%.
Sysser 97	Longitudinal centre of buoyancy moved forward by 4%. Longitudinal centre of flotation moved forward by 2%.
Sysser 98	Longitudinal centre of flotation moved aft by 2% while keeping the same longitudinal centre of buoyancy.
Sysser 99	Longitudinal centre of flotation moved forward by 2% while keeping the same longitudinal centre of buoyancy.
Sysser 100	Similar to Sysser 86 but then with 7.5% variation.
Sysser 101	Similar to Sysser 87 but then with 7.5% variation.
Sysser 102	Similar to Sysser 88 but then with 7.5% variation.
Sysser 103	Similar to Sysser 89 but then with 7.5% variation.
Sysser 104	Similar to Sysser 90 but then with 7.5% variation.
Sysser 105	Similar to Sysser 91 but then with 7.5% variation.

Table 3.3: Hydrostatic parameters of the hull shapes in the new systematic series. The maximum, minimum and mean values, and the standard deviation of the parameters are listed at the bottom of the table.

	$\frac{\nabla_c^{1/3}}{L_{WL}}$	$\frac{B_{WL}}{L_{WL}}$	$\frac{T_c}{B_{WL}}$	$\frac{LCB_{fp}}{L_{WL}}$	$\frac{LCB_{fp}}{LCF_{fp}}$	C_p	C_x	$\frac{\nabla_c^{2/3}}{A_W}$
Sysser 85	0.131	0.205	0.145	0.539	0.940	0.543	0.683	0.122
Sysser 86	0.131	0.175	0.195	0.537	0.938	0.544	0.684	0.142
Sysser 87	0.131	0.239	0.106	0.538	0.939	0.544	0.684	0.104
Sysser 88	0.137	0.220	0.144	0.539	0.939	0.544	0.684	0.125
Sysser 89	0.124	0.189	0.145	0.539	0.939	0.544	0.683	0.119
Sysser 90	0.137	0.205	0.166	0.539	0.939	0.543	0.683	0.134
Sysser 91	0.124	0.205	0.123	0.539	0.939	0.544	0.683	0.110
Sysser 92	0.133	0.203	0.146	0.540	0.940	0.539	0.726	0.126
Sysser 93	0.128	0.203	0.146	0.536	0.937	0.548	0.633	0.117
Sysser 94	0.131	0.184	0.161	0.539	0.939	0.603	0.677	0.128
Sysser 95	0.131	0.224	0.132	0.539	0.941	0.497	0.685	0.118
Sysser 96	0.131	0.206	0.142	0.560	0.956	0.545	0.677	0.121
Sysser 97	0.131	0.203	0.147	0.515	0.919	0.541	0.690	0.123
Sysser 98	0.131	0.205	0.144	0.540	0.921	0.550	0.679	0.120
Sysser 99	0.131	0.205	0.145	0.539	0.957	0.535	0.692	0.122
Sysser 100	0.131	0.190	0.168	0.539	0.940	0.543	0.684	0.132
Sysser 101	0.131	0.221	0.124	0.539	0.940	0.543	0.684	0.113
Sysser 102	0.134	0.212	0.144	0.539	0.940	0.543	0.684	0.124
Sysser 103	0.128	0.197	0.145	0.539	0.940	0.543	0.683	0.121
Sysser 104	0.134	0.205	0.155	0.539	0.940	0.543	0.684	0.128
Sysser 105	0.128	0.205	0.134	0.539	0.940	0.543	0.683	0.116
Maximum	0.137	0.239	0.195	0.560	0.957	0.603	0.726	0.142
Minimum	0.124	0.175	0.106	0.515	0.919	0.497	0.633	0.104
Mean	0.131	0.205	0.146	0.538	0.939	0.544	0.683	0.122
σ	0.003	0.014	0.018	0.007	0.008	0.017	0.015	0.008
σ [%Mean]	2.60	6.84	12.6	1.31	0.88	3.14	2.22	6.80

4
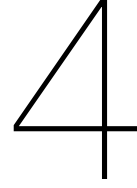
Test conditions

A new bare hull upright trimmed resistance prediction for modern high performance yachts will be derived from the new systematic series in Chapter 10. The bare hull upright trimmed resistance of the hull shapes in this series is determined for various speeds and applied trimming moments with computational fluid dynamics (CFD). The test conditions for which the hydrodynamic forces are determined, are discussed in this chapter. A summary of these conditions concludes this chapter.

4.1. Length scales

A TP52-design is used as the parent model for the new systematic series. A TP52 has an overall length of 15.85 metres and a waterline length of 15.60 metres. In the regression analysis discussed in Chapter 10, the waterline length in the new systematic series is the standard ten metres of the DSYHS. Three different scales of the waterline length are used in this thesis: model scale, prototype scale and full scale corresponding to $L_{WL} = 2.00\,m$, $L_{WL} = 10.00\,m$ and $L_{WL} = 15.60\,m$, respectively.

A choice has to be made to either use the prototype scale in the numerical simulations or to use the model scale in the simulations and to extrapolate the resistance to prototype scale with the method discussed in Section 2.2. Both approaches have their pros and cons. An obvious advantage of running simulations at model scale is the availability of data for validation, which can be obtained from resistance measurements in a towing tank. However, the obtained resistance values have to be extrapolated. This introduces uncertainties. Running the numerical simulations at prototype scale eliminates the need for extrapolation, but poses difficulties for the validation of the numerical results.

The lack of reliable prototype-scale or full-scale experimental resistance data makes it really difficult to validate the resistance values obtained from numerical simulations at these scales. Hence, the numerical simulations are performed at model scale only. The computed resistance is extrapolated to prototype scale using the extrapolation method discussed in Section 2.2. The resistance values at this scale are used in the regression analysis discussed in Chapter 10.

4.2. Longitudinal trimming moment

Determining the upright trimmed resistance requires a specification of the applied trimming moment. The longitudinal trimming moment about a sailing yacht's centre of gravity (CoG) consists of the trimming moment of the driving force and the trimming moment of the crew's weight;

$$M_\theta = M_{\theta_{SAILS}} + M_{\theta_{CREW}}, \tag{4.1}$$

where M_θ is the longitudinal trimming moment about the yacht's CoG, $M_{\theta_{SAILS}}$ is the longitudinal trimming moment of the driving force about the CoG, and $M_{\theta_{CREW}}$ is the longitudinal trimming moment of the crew's weight about the CoG. The CoG is assumed to be located at the design waterline above the centre of buoyancy. The definitions of the trimming moments of the driving force and the crew's weight are discussed in the following subsections.

4.2.1. Driving force

The driving force acting on a sailing yacht is the resultant aerodynamic force acting on the sails in parallel to the yacht's velocity. Its point of application is the centre of effort (CoE) of the sails. In steady-state conditions, the driving force is equal to the resistance. Obviously, the driving force and the resistance are antiparallel vectors. The resistance of the models in the systematic series are determined for steady-state conditions. The longitudinal trimming moment of the driving force about the yacht's CoG is therefore equal to the magnitude of the hydrodynamic resistance multiplied by the height of the CoE of the sails above the waterline.

The position of the centre of effort is derived from the maximum sail-plan of a TP52. Measurements of the sails are taken from the TP52 class rules [45] and are listed in Figure H.2. As a result of sail twist, the various jibs and the various spinnakers there is no such thing as one fixed CoE height. For a TP52, the CoE height is estimated to be $0.60L_{WL}$, which covers a wide range of sailing conditions. This height of the CoE is used throughout the entire systematic series.

With this assumption for the height of the CoE of the sails, the longitudinal trimming moment of the driving force is given by

$$M_{\theta_{SAILS}} = 0.60L_{WL} \cdot R_{T\theta_h},$$
(4.2)

where $0.60L_{WL}$ is the assumed CoE height, and $R_{T\theta_h}$ is the upright trimmed resistance of the bare hull. This CoE height is slightly different than the $0.65L_{WL}$ used in the DSYHS.

It should be noted that $0.60L_{WL}$ is used as the CoE height at model scale. The CoE height at the prototype scale and full scale differs from this, because the resistance force does not simply scale with the scale factor, between the waterline lengths, to the third power. The yacht at model scale has a relatively higher resistance due to viscous effects. Using $0.60L_{WL}$ at all the scales, with of course the corresponding waterline lengths, implies that the yacht at model scale is subjected to a relatively larger trimming moment than at a larger scale. Consequently, this discrepancy in trimming moment between the scales results in different trim, sinkage and resistance. Obviously, in order to extrapolate the resistance values from one scale to another, the attitude of the yacht should remain the same. This implies properly scaled trimming moments from one scale to the other. To obtain a similar attitude of the model at another scale, the trimming moment should be scaled with the scale factor to the fourth power.

The CoE height can therefore not be scaled with the scale factor only. The CoE height, z_{CoE}, at a particular scale should satisfy the following expression in order to obtain scale similarity between the different scales:

$$z_{CoE} = \frac{1.2R_{t_m}\alpha^4}{R_{t_p}},$$
(4.3)

where 1.2 is the CoE height at model scale, R_{t_m} is the resistance at model scale, α is the scale factor between the waterline lengths, and R_{t_p} is the resistance at that particular scale. For the larger scales, the centre of effort is higher than $0.60L_{WL}$ and varies with the speed. For Sysser 85, $0.60L_{WL}$ at model scale corresponds for prototype scale to $0.83L_{WL}$ at Froude number 0.25, $0.77L_{WL}$ at Froude number 0.35, $0.69L_{WL}$ at Froude number 0.45 and $0.68L_{WL}$ at Froude numbers 0.55 up to 0.85. This holds when no trimming moment of the crew's weight is applied.

4.2.2. Crew's weight

In general, a modern high performance yacht needs a large crew. The position of the crew on board greatly influences the performance of the yacht. The weight of the crew together with its position on board exert a trimming moment about the yacht's CoG. This trimming moment can greatly influence the performance of a sailing yacht, because it partly counteracts the bow-down trimming moment of the driving force. The resulting more bow-up attitude of the yacht reduces the resistance significantly at higher speeds due to more hydrodynamic lift while it increases the resistance at lower speeds significantly due to the intensified wave system generated at the stern and immersed transom effects, such as possible flow separation, larger streamline curvature at the edge of the transom, lowered pressure around this edge, and possible suction.

The resistance forces acting on modern yachts are generally very sensitive to trim at every speed. The sensitivity of the resistance to the trim angle, for a modern high performance yacht, is illustrated by Table D.1. This table gives the bare hull upright resistance of Sysser 85 at Froude numbers 0.25 up to 0.85 for three different fixed pitch angles, -1, 0, and +1 degrees, while being free to heave. Some exceptions excluded, the difference in resistance for the plus or minus one degree trim angle is about plus or minus 10 percent over the entire speed range compared to the resistance for the zero degree trim angle.

In real life, any crew would try to enhance the performance of a sailing yacht (during racing) by moving its weight to the optimum position. Excluding the weight of the crew, its position on board and thereby the trimming moment of the crew's weight leads to an underestimation of the performance of sailing yachts. In order to bear a close resemblance to real-life sailing conditions and to accurately predict the velocity of modern high performance sailing yachts, trimming moments of the crew's weight are included in the numerical simulations. These trimming moments can also be used to cover, for instance, movable ballast.

In order to determine the influence of the crew's weight and its position on board on the resistance, three crew positions and three corresponding trimming moments are defined for the numerical simulations. The trimming moments used in the simulations are based on the maximum weight of the crew for a TP52 and realistic crew positions during sailing. According to the TP52 class rules [45], the maximum mass of the crew during racing is 1130 kilograms.

A crew position with no trimming moment, called the 'crew CoG position', is defined to cover light wind conditions or sailing with a small crew. It is also useful for comparison with the DSYHS, for which no trimming moments of the crew's weight are used. For a TP52 with a full crew, this position is more or less the crew position for upwind sailing or broad reaching in low wind speeds. A 'crew back position' and corresponding trimming moment for broad reaching at high speeds is defined based on the maximum crew weight and typical crew configurations during sailing in these conditions. For the sake of illustration, a typical configuration of the crew on a TP52 during broad reaching at high speeds is shown in Figure 4.1. Another condition, called the 'crew middle position', is defined for intermediate conditions. The trimming moment for this position is half the moment for the crew back position.

An overview of the defined crew positions and the corresponding longitudinal trimming moments about the CoG of the models at full scale, prototype scale and model scale are given in Table 4.1. The moments at full scale are scaled with one over the scale factor to the fourth power, i.e. $1/\alpha^4$, to obtain the moments applied at model and prototype scale.

The trimming moment of the crew's weight can be translated into a shift in the longitudinal centre of gravity of the sailing yacht. Applying a trimming moment about the 'original' longitudinal centre of gravity, which is located above the hydrostatic centre of buoyancy, or using a shift in the longitudinal centre of gravity of the yacht to cover the effects of the weight of the crew and its position on board is, of course, equivalent. The longitudinal centre of gravity of a sailing yacht together with its crew can simply be determined by

$$LCG_{fp} = LCB_{fp} - \frac{M_{\theta_{CREW}}}{\nabla_c \rho g}, \tag{4.4}$$

where LCG_{fp} is the longitudinal position of the centre of gravity measured from the forward perpendicular (fp), LCB_{fp} is the original longitudinal centre of gravity, $M_{\theta_{CREW}}$ is the trimming moment of the crew's weight about the original CoG, and $\nabla_c \rho g$ is the yacht's weight. This longitudinal centre of gravity may be a good independent variable to cover the effects of the crew on the resistance and to facilitate interpolation of the resistance between the three crew positions in the regression analysis, discussed in Chapter 10.

4.2.3. Longitudinal trimming moment
With these definitions of the trimming moments of the driving and the crew's weight, the longitudinal trimming moment about a sailing yacht's CoG is defined by

$$M_\theta = 0.60 L_{WL} \cdot R_{T\theta_h} + M_{\theta_{CREW}}, \tag{4.5}$$

where $M_{\theta_{CREW}}$ is one of the three longitudinal trimming moments of the crew's weight from Table 4.1. These three formulations of the longitudinal trimming moment, M_θ, about the CoG are used in the numerical simulations and the remainder of this thesis.

The trimming moment of the driving force is applied in the numerical simulations by applying the resistance force, computed in the previous time step, at a height of $0.60L_{WL}$ above the CoG in the same horizontal direction as the ship's velocity. The trimming moment of the crew's weight is applied in the numerical simulation as a constant trimming moment about the CoG of the model.

4.2.4. Effective centre of effort
Another way to interpret the use of crew positions in the simulations is to translate the trimming moments of the driving force and the crew's weight into an 'effective' height of the CoE of the sails according to

$$z_{CoE_{eff}} = 0.60L_{WL} + \frac{M_{\theta_{CREW}}}{R_{T\theta_h}}, \tag{4.6}$$

where $z_{CoE_{eff}}$ is the height of the effective CoE. This effective CoE height is simply defined as the total longitudinal trimming moment divided by the resistance. It represents the height of the CoE of the sails if the total trimming moment, defined by Equation (4.5), is solely attributed to the trimming moment generated by the driving force. The trimming moment of the crew's weight partly counteracts the trimming moment of the driving force. The effective CoE height is therefore lower than the actual CoE height. This lower effective centre of effort covers the concept of reefing sails and applying more or less twist to a sail. Both reefing and twist alter the height of the CoE. The effective CoE height may be a good independent variable to cover the effects of the total trimming moment on the resistance and to facilitate interpolation of the resistance between the three crew positions in the regression analysis, discussed in Chapter 10.

The effective height of the CoE makes the set-up used in this study wider applicable. The range of trimming moments, used in the formulation of the new upright trimmed resistance prediction, covers more than the maximum sail area and the maximum crew weight of a TP52. Different crew positions and weight, reefing and twist are also covered by the derived regressions as long as they obey the range of trimming moments used in the regressions.

4.3. Speed range
The upright resistance of the models in the systematic series is determined for Froude numbers 0.25 up to 0.95 with increments of 0.10. This range of Froude numbers covers speeds from 6 knots up to 23 knots for a full-scale TP52. This is a realistic speed range for a TP52 in racing conditions. The velocities at full scale, prototype scale and model scale for this range of Froude numbers are listed in Table 4.2.

For the crew CoG position, the maximum speed is lowered to Froude number 0.85. At Froude number 0.95, the very high trimming moment of the driving force and the absence of a counteracting trimming of the crew's weight result for some of the models in a severe bow-down attitude. This bow-down attitude results in a very high resistance. Moreover, it makes convergence of the numerical simulations very hard and sometimes impossible. It is also not a realistic sailing condition. For all of the models, the crew CoG position does not result in the optimum resistance at this speed. The resistance for the other two crew positions is lower and sometimes significantly lower. It was therefore decided to exclude the simulation for the crew CoG position at Froude number 0.95 for all of the models.

4.4. Fluid properties
Different water properties are used for the different length scales. Fresh water is used at model scale while seawater is used at prototype scale and full scale. Following the ITTC standards for water properties [17], the density and the kinematic viscosity of fresh water at a water temperature of $17\ °C$ are $998.778\ kg/m^3$ and $1.08155 \cdot 10^{-6}\ m^2/s$, respectively. For seawater with a water temperature of $15\ °C$, the density and the kinematic viscosity are $1025.90\ kg/m^3$ and $1.18831 \cdot 10^{-6}\ m^2/s$, respectively. These water properties are used throughout this thesis.

In the numerical simulations, the properties of fresh water at a water temperature of $17\ °C$ are used. For the air in the numerical simulations, the density and the kinematic viscosity are $1.2\ kg/m^3$ and

Table 4.1: The three crew positions and corresponding longitudinal trimming moments of the crew's weight about the CoG at full scale, prototype scale and model scale. A minus sign indicates a bow-up trimming moment.

Crew position	Full scale $M_{\theta_{CREW}}$ [kNm]	Prototype scale $M_{\theta_{CREW}}$ [kNm]	Model scale $M_{\theta_{CREW}}$ [Nm]
CoG	0	0	0
Middle	-32.96	-5.57	-8.90
Back	-65.92	-11.13	-17.80

Table 4.2: Speed range used for the numerical simulations.

Fn [−]	Full scale V [m/s]	V [kt]	Prototype scale V [m/s]	V [kt]	Model scale V_m [m/s]
0.25	3.12	6.06	2.48	4.81	1.11
0.35	4.36	8.48	3.47	6.74	1.55
0.45	5.61	10.91	4.46	8.66	1.99
0.55	6.86	13.33	5.45	10.59	2.44
0.65	8.11	15.76	6.44	12.51	2.88
0.75	9.35	18.18	7.43	14.44	3.32
0.85	10.60	20.60	8.42	16.36	3.77
0.95	11.85	23.03	9.41	18.29	4.21

Figure 4.1: A typical crew configuration on a TP52 during broad reaching at high speeds. Picture from [33].

$1.54 \cdot 10^{-5} \ m^2/s$, respectively.

4.5. Summary of the test conditions

The models in the new systematic series are tested in upright condition without any appendages. No drift angles and no heel angles are used. The bare hull upright trimmed resistance of all the models in the new systematic series is determined with numerical simulations at model scale, $L_{WL} = 2.00 \ m$, at Froude numbers 0.25 up to 0.95 with increments of 0.10 for the three different crew positions and corresponding trimming moments defined in Table 4.1. Corresponding velocities are given in Table 4.2. For the crew CoG position, the maximum speed is lowered to Froude number 0.85. A centre of effort height of $0.60 L_{WL}$ is used for the point of application of the driving force.

The trimming moment of the crew's weight is applied about the CoG of the model, which is assumed to be located at the design waterline. All the models in the new systematic series are tested for the same trimming moments of the crew's weight. The trimming moment of the driving force is applied in the numerical simulations by applying the resistance force, computed in the previous time step, at a height of $0.60 L_{WL}$ above the CoG in the same horizontal direction as the ship's velocity. Fresh water of 17 degrees Celsius is used in the simulations.

The resistance values computed at model scale are extrapolated to prototype scale, $L_{WL} = 10.00 \ m$, with the method discussed in Section 2.2. At prototype scale, seawater with a water temperature of 15 degrees Celsius is used. The resistance values at this scale are used to derive new regressions for the upright trimmed resistance in Chapter 10.

5

Resistance decomposition

A resistance decomposition method is necesarry for the velocity prediction of sailing yachts, in order to account for all the different hydrodynamic resistance forces acting on a yacht. Since the hydrodynamic resistance decomposition used for the Delft Systematic Yacht Hull Series (DSYHS), shown in Figure 2.1, proved its value and accuracy over the years, the idea was to follow this decomposition method for the present study. As a result, the bare hull upright untrimmed resistance and the bare hull upright trimmed resistance have to be determined both; however, this is not strictly necesarry for the velocity prediction of sailing yachts. A slightly different resistance decomposition is therefore proposed in this chapter. This decomposition is followed in the present study.

Note that throughout this thesis, the trimmed condition and the untrimmed condition imply nothing more than whether or not longitudinal trimming moments of the driving force and the crew's weight are applied to the yacht. In both conditions, the yacht is free to heave and pitch.

For the DSYHS, the bare hull resistance forces were measured without corrections for the trimming moment of the driving forces. According to Keuning and Sonnenberg [27], "This is a customary routine in the testing of sailing yachts but particularly so when testing a systematic series of not actually designed yachts of which no sailplan is known". Only for the upright condition, additional resistance measurements were performed including correction moments for the driving force. This distinction between untrimmed and trimmed was also introduced for the DSYHS because of practical reasons. Trimmed resistance measurements for a predetermined height of the centre of effort (CoE) of the sails are tricky or at least require a number of iteration runs in order to apply the correct trimming moment, corresponding to the measured resistance, to the model. The required amount of tank testing for such an approach is quite prohibitive. On the other hand, untrimmed resistance measurements are fairly simple and do not require iteration runs. The untrimmed resistance multiplied by $0.65L_{WL}$ was used as the applied trimming moment in the trimmed condition. No iteration runs were performed for the trimmed conditions. As a result, the actual centre of effort is lower than the target centre of effort height of $0.65L_{WL}$, and the actual heights differ between the models in the DSYHS.

This distinction between untrimmed and trimmed resistance is no longer needed for numeral simulations, because it is now easily possible to determine the trimmed resistance of a sailing yacht for exactly the predetermined CoE height. Also the resistance under heel and leeway can be determined for this specific CoE height. Furthermore, it is now possible to test all the models in the systematic series for exactly the same CoE height. This is important for consistency in the systematic series and for deriving meaningful regression formulas. Determining the bare hull resistance components of the models for exactly the same CoE height seems more logical than determining these resistance components without including the influence of trimming moments of the driving forces. This is motivated by the fact that the hydrodynamic forces acting on yachts are always affected by trimming moments of the driving forces in reality. Including trimming moments for the determination of the bare hull resistance components is considered to have a closer resemblance with the physics involved in real-life sailing conditions and to be more accurate. Moreover, with the ever increasing speed potential of the newer yacht designs, the importance of including trimming moments for accurate resistance prediction of yachts in sailing conditions increases. The untrimmed resistance is redundant for the velocity

prediction of sailing yachts. A new resistance decomposition is therefore proposed in Figure 5.1. This decomposition is followed in the present study.

Obviously, a representative CoE height has to be chosen for the systematic series. It is unlikely that this assumed CoE height is equal to the actual CoE height of the constructed yacht. Furthermore, the CoE height is influenced by the trim of the sails and the various sails used. Nevertheless, it is very likely that the trimmed resistance calculated for the assumed CoE height is a lot closer to the actual resistance of the yacht than the untrimmed resistance using no CoE height. This holds for upright, heeled and leeway conditions.

The new resistance decomposition, shown in Figure 5.1, makes one adjustment to the resistance decomposition of the DSYHS, shown in Figure 2.1. In the new method, the bare hull upright resistance and the delta resistance due to the trimming moment are added together to form the bare hull upright trimmed resistance. No distinction between these two components is made any more. Compared to the method of the DSYHS, the upright untrimmed resistance is omitted from the new decomposition and is replaced by the upright trimmed resistance. The definitions of the residuary resistance components and the induced resistance change therefore (slightly) between both methods while the definitions of the frictional resistance components and the viscous resistance components remain unchanged. The new decomposition is believed to have a closer resemblance with the physics involved in real-life sailing conditions. This especially holds for the higher speeds. Determining the upright resistance in untrimmed condition is no longer necesarry. Only the upright trimmed resistance is therefore determined for the models in the new systematic series.

From a physical point of view, it is not strange to omit the bare hull upright untrimmed resistance from the resistance decomposition entirely and to replace it by the upright trimmed resistance. The hydrodynamic forces and moments acting on a sailing yacht are always affected by the trimming moment of the driving force in reality. Not including a trimming moment in the calculations of the various bare hull resistance components is physically less correct. Of course, for the lower speeds, omitting trimming moments does not significantly affect the resistance, because the trimming moment of the driving force is very small and does not significantly influence the trim angle of the yacht. For the higher speeds, the trimming moments are large and influence the trim angle and the resistance considerably. The resistance forces acting on modern yachts are generally very sensitive to trim at every speed. The importance of including trimming moments for accurate resistance prediction of yachts in sailing conditions increases with speed.

The sensitivity of the resistance to the trim angle, for a modern high performance yacht, is illustrated by Table D.1. This table gives the bare hull upright resistance of Sysser 85 at Froude numbers 0.25 up to 0.85 for three different fixed pitch angles, -1, 0, and +1 degrees, while being free to heave. Some exceptions excluded, the difference in resistance for the plus or minus one degree trim angle is about plus or minus 10 percent over the entire speed range compared to the resistance for the zero degree trim angle.

Of course, heel and leeway influence the magnitude of the trimming moment of the driving force. It seems reasonable to attribute these differences in trimming moment to the delta resistance component due to heel and the induced resistance.

From this new resistance decomposition, the need arises to update the regressions for the other residuary resistance components and the induced resistance as well, since there is a small difference in their definitions between the method of the DSYHS and the new method. Updating the regressions for the other bare hull residuary resistance components and the induced resistance is also preferable based on the limitations of the regressions of the DSYHS, as discussed in Section 2.5. However, updating all the regressions is outside the scope of this study. Despite that the other resistance components are not the focus of this study, they are needed for the velocity prediction of sailing yachts. To be able to use the new resistance decomposition method in a velocity prediction program, the regressions of the DSYHS are used for all the resistance components except for the new bare hull upright trimmed residuary resistance. The new regressions derived in Chapter 10 are used for that resistance. For now, it is assumed that between the decomposition of the DSYHS, shown in Figure 2.1, and the new decomposition, shown in Figure 5.1, the values of the delta residuary resistance components, the residuary resistance of the keel and the induced resistance are not changed significantly. The new decomposition and the decomposition of the DSYHS are used in Section 10.8 to calculate a velocity prediction of

a TP52-design.

The new resistance decomposition and the various resistance components are briefly discussed in the remainder of this chapter. The new bare hull upright trimmed resistance prediction is summarized in Appendix G.

Upright trimmed resistance of the bare hull

For the new resistance decomposition, a new upright trimmed residuary resistance of the bare hull is defined. Compared to the decomposition of the DSYHS, the bare hull upright trimmed residuary resistance, $R_{R\theta_h}$, is defined by

$$R_{R\theta_h} = R_{R_h} + \Delta R_{R\theta_h}, \tag{5.1}$$

where R_{R_h} is the residuary resistance of the bare hull defined by the decomposition of the DSYHS, and $\Delta R_{R\theta_h}$ is the change in residuary resistance of the bare hull due to the trimming moment of the driving force defined by the decomposition of the DSYHS. The new decomposition makes no distinction between the influence of R_{R_h} and $\Delta R_{R\theta_h}$ on the trimmed residuary resistance of the bare hull. New formulations are derived for the bare hull trimmed residuary resistance, $R_{R\theta_h}$, in Chapter 10.

The formulation for the frictional resistance of the bare hull remains unchanged between both methods. However, for the new decomposition a characteristic length of $0.9L_{WL}$ instead of $0.7L_{WL}$ is used for the Reynolds number. This characteristic length seems to be more appropriate for the modern hull shapes of the new systematic series. An explanation for this choice is given in Section 10.1. The Reynolds number is needed to estimate the friction coefficient.

The upright trimmed resistance of the bare hull, $R_{T\theta_h}$, is defined by

$$R_{T\theta_h} = R_{F_h} + R_{R\theta_h}, \tag{5.2}$$

where R_{F_h} is the frictional resistance of the bare hull defined by Equation (2.6).

Total upright trimmed resistance

The total upright trimmed resistance, $R_{T\theta}$, in the new decomposition is defined by

$$R_{T\theta} = R_{F_h} + R_{R\theta_h} + R_{V_k} + R_{R_k} + R_{V_r}, \tag{5.3}$$

where R_{F_h} is the frictional resistance of the bare hull, $R_{R\theta_h}$ is the upright trimmed residuary resistance of the bare hull, R_{V_k} is the viscous resistance of the keel, R_{R_k} is the residuary resistance of the keel, and R_{V_r} is the viscous resistance of the rudder. The regressions of the DSYHS are used for all these resistance components except for the new bare hull upright trimmed resistance. The regressions of the DSYHS are discussed in Chapter 2.

Total trimmed resistance under heel

The total trimmed resistance under heel, $R_{T\theta\phi}$, is defined by

$$R_{T\theta\phi} = R_{T\theta} + \Delta R_{F\phi_h} + \Delta R_{R\phi_h} + \Delta R_{R\phi_k}, \tag{5.4}$$

where $R_{T\theta}$ is the total upright trimmed resistance, $\Delta R_{F\phi_h}$ is the change in frictional resistance of the bare hull due to heel, $\Delta R_{R\phi_h}$ is the change in residuary resistance of the bare hull due to heel, and $\Delta R_{R\phi_k}$ is the change in residuary resistance of the keel due to heel. The regressions of the DSYHS are used for these three delta resistance components.

Total trimmed resistance with heel and leeway

The total trimmed resistance under heel and leeway, $R_{T\theta\phi\beta}$, is defined by

$$R_{T\theta\phi\beta} = R_{T\theta\phi} + R_I, \tag{5.5}$$

where $R_{T\theta\phi}$ is the total trimmed resistance under heel, and R_I is the induced resistance. The regressions of the DSYHS are used for the induced resistance.
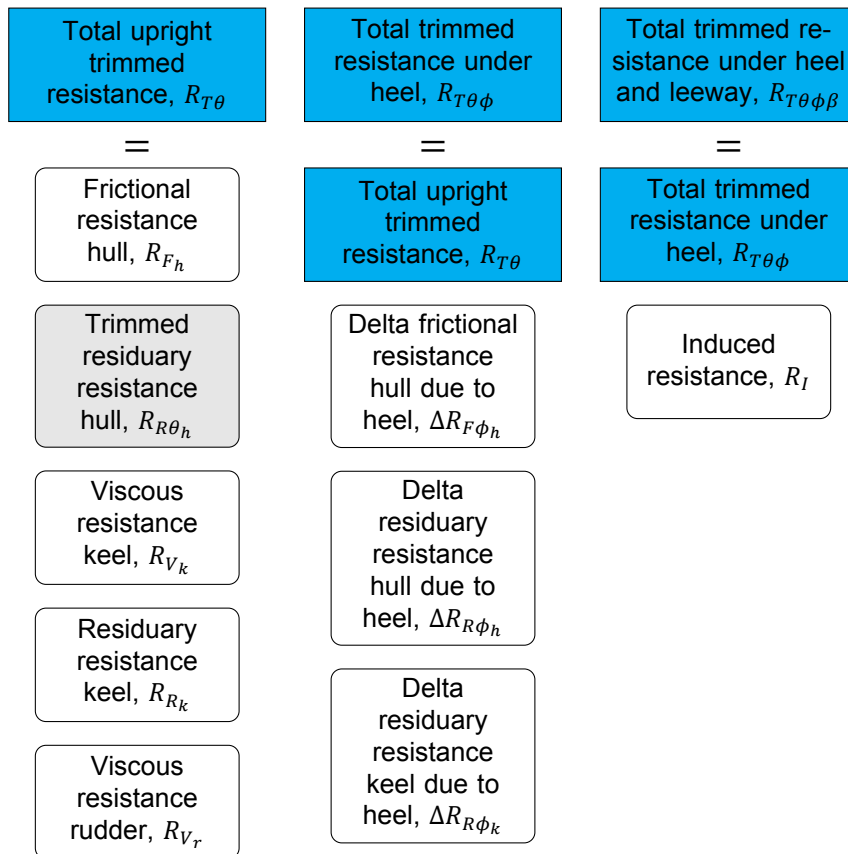
Figure 5.1: The new resistance decomposition. There are three different types of total resistance defined in this decomposition. The total resistance mentioned in the block at the top of each column is equal to the sum of the resistance components of the other blocks in that column. The components in the blue-coloured blocks and the grey-coloured block have a new formulation compared to the decomposition of the DSYHS, given Figure 2.1. For the trimmed residuary resistance of the bare hull in the grey-coloured block, a new regression formulation is derived in Chapter 10. For the resistance components in the white-coloured blocks, the regression formulations of the DSYHS are used for now.

<div style="text-align: right; font-size: 4em;">6</div>

Numerical method

The hydrodynamic forces acting on the models in the new systematic series are determined with computational fluid dynamics (CFD). The numerical simulations are performed using the ISIS-CFD flow solver [11] implemented in the commercial FINE™/Marine software package of NUMECA International [35]. This flow solver solves the unsteady incompressible Reynolds-averaged Navier-Stokes (RANS) equations with a finite-volume method (FVM). The theoretical background and the simulation settings are discussed in this chapter. For the interested reader or the reader less familiar with fluid dynamics, a more elaborate explanation of (computational) fluid dynamics is given in Appendix E. The numerical results are presented and discussed in Section 6.10. All the numerical simulations are performed following the test conditions discussed in Chapter 4.

From a scientific point of view, it is desirable to asses the quality and the credibility of numerical simulations. To establish the reliability and the accuracy of the numerical results, a Verification & Validation (V&V) analysis is performed. The verification analysis and the assessment of the numerical uncertainty are discussed in Chapter 7. The CFD results are validated with the results of resistance measurements in Chapter 9.

6.1. Governing equations

The flow field around a ship is likely to be partly or fully turbulent. In general, for turbulent flows in ship hydromechanics applications, the full Navier-Stokes equations are too complex to solve by direct numerical simulation (DNS) due to the very wide range of length scales of turbulent motion. By using modelling approaches, e.g. large-eddy simulation (LES) or the Reynolds-averaged Navier-Stokes (RANS) equations, solving turbulent motion can be greatly simplified by modelling instead of resolving all the scales of turbulent motion. For practical ship hydromechanics applications, LES is still too costly.

For the present study, the RANS equations are used, because they produce sufficiently accurate results for an acceptable required computation time. The numerical simulations are performed using the ISIS-CFD flow solver [11] implemented in the commercial FINE™/Marine software package of NU-MECA International [35]. This flow solver was developed by the Equipe Modélisation Numérique at the Ecole Centrale de Nantes. It solves the unsteady incompressible RANS equations with a finite-volume spatial discretization on three-dimensional unstructured meshes.

To derive the RANS equations, Reynolds averaging is applied to the Navier-Stokes equations to obtain the mean, or time-averaged, equations of fluid motion. Following Reynolds [41], in order to capture the randomly unsteady turbulent state of the flow, any flow quantity f is decomposed into a mean value, $\overline{f}$, and a fluctuating value, f'; i.e. $f = \overline{f} + f'$. For incompressible turbulent flow, fluctuations in the velocities, u_i, and the pressure, p, are expected; hence, $u_i = \overline{u}_i + u'_i$, and $p = \overline{p} + p'$. The

incompressible Reynolds-averaged Navier-Stokes equations in Cartesian coordinates are

$$\frac{\partial \overline{u}_i}{\partial x_i} = 0,$$ (6.1a)

$$\frac{\partial \overline{u}_i}{\partial t} + \overline{u}_j \frac{\partial \overline{u}_i}{\partial x_j} = -\frac{1}{\rho}\frac{\partial \overline{p}}{\partial x_i} + \nu \frac{\partial^2 \overline{u}_i}{\partial x_j{}^2} + g_i - \frac{\partial \overline{u'_i u'_j}}{\partial x_j},$$ (6.1b)

where u_i are the Cartesian velocity components, x_i are the Cartesian coordinates, t is the time, ρ is the density, p is the pressure, ν is the kinematic viscosity, and g_i is the gravitational acceleration. Subscripts i and j can have values 1, 2 or 3 and denote one of the three Cartesian coordinates, x_1, x_2 and x_3, and corresponding velocity components, u_1, u_2 and u_3. Note that as a consequence of Einstein notation, or Einstein summation convention, summation over the repeated index in a term is implied.

Equation (6.1a) is the Reynolds-averaged conservation of mass equation, or the Reynolds-averaged continuity equation. This equation is transformed into a pressure equation from which the pressure field is extracted in the ISIS-CFD flow solver. The reader is referred to Wesseling [46] for the mathematical details. Equation (6.1b) is one of the three Reynolds-averaged momentum equations.

6.1.1. Turbulence models

As a consequence of Reynolds-averaging the Navier-Stokes equations, an additional turbulence model is necessary to close the resulting equations. Many turbulence models were developed and proposed over the years. Selecting an appropriate turbulence model is all about balancing the desired accuracy against the computation time. For the present study, the large systemic series requires small computation times while keeping a sufficiently high accuracy.

According to the ITTC [18], $k - \omega$ two-equation turbulence models have shown to be able to yield accurate predictions in ship hydromechanics. They are by far the most applied turbulence models in this scientific field. A $k - \omega$ turbulence model is also used for the present study, because it produces sufficiently accurate results for an acceptable required computation time. $k - \omega$ two-equation turbulence models use a transport equation for the turbulent kinetic energy, k, and a transport equation for the specific turbulence dissipation rate, ω, to model the conservation of these two turbulence quantities. The turbulent kinetic energy and the specific turbulence dissipation rate calculated from the two transport equations are used to determine the Reynolds stresses.

Various $k - \omega$ two-equation turbulence models were developed and proposed over the years. For an accurate determination of the hydrodynamic forces in ship hydromechanics, two good options for turbulence modelling are the explicit algebraic stress model (EASM) $k - \omega$ two-equation turbulence model, Gatski and Speziale [12], and the shear stress transport (SST) $k - \omega$ two-equation turbulence model, developed by Menter [34]. Over the years, several changes were made to both turbulence models; therefore, various variations of both models exist. The principles of both models have not changed and are discussed in Appendix E.1.2. The EASM and the SST $k - \omega$ two-equation turbulence model are both implemented in the ISIS-CFD flow solver. The specific details of the turbulence models implemented in this flow solver are given in its theoretical manual [11].

The EASM turbulence model and the SST turbulence model differ in the way the Reynolds stress term is modelled. The SST $k - \omega$ model is a linear eddy-viscosity model and follows the Boussinesq hypothesis, or Boussinesq eddy-viscosity assumption. For complex turbulent flows characterized by intense vortices, the isotropic description of turbulence in the Boussinesq hypothesis probably results in inaccurate results. The EASM $k - \omega$ model uses a different approach for the modelling of the Reynolds stresses. Explicit algebraic stress models are derived from the six Reynolds stress equations. Compared to linear eddy-viscosity models, the Reynolds stresses in EASMs are modelled with additional (non-linear) terms that can include powers of the mean-velocity gradients or combinations of the mean strain-rate tensor and the mean rotation-rate tensor. This allows for an anisotropic description of turbulence. This anisotropic description enhances the modelling of vortices significantly compared to linear eddy-viscosity models.

According to NUMECA International [35], the SST $k - \omega$ model is the recommended turbulence model for all basic computations. According to them, the EASM $k - \omega$ turbulence model yields slightly better results for a reasonable extra computation time. A small test has been conducted to illustrates the

small differences between both turbulence models. Table F.1 gives the resistance values of Sysser 85 computed with the two turbulence models on the medium grid at Froude numbers 0.45 and 0.85. The resistance values are very similar and the comparison error is less than 1 percent between both methods. The EASM model gives a slightly higher resistance at both speeds.

For the lower Froude number, the computation time of the SST model is higher than that of the EASM model while for the higher Froude number it is the opposite. This is unexpected since the more complex EASM turbulence model is likely to have a longer computation time. Of course, this small test in not conclusive; therefore, the recommendations of NUMECA International [35] are followed, and the SST $k-\omega$ turbulence model, developed by Menter [34], is used for all the numerical simulations presented in this thesis. Moreover, this turbulence model is chosen, because it produces consistent and sufficiently accurate results for an acceptable required computation time. Complex turbulent flows characterized by intense vortices are not to be expected based on the smooth hull shapes, the unappended hulls and the fact that the resistance forces are determined in upright condition only, without any drift angles; therefore, it is probably not necessary to use the EASM model.

6.1.2. Free surface
For capturing of the free surface in the numerical simulations, the volume of fluid (VOF) method is used. The VOF method is a free-surface modelling technique, which is used to track and locate the interface between the two fluids — water and air — in a numerical simulation. These incompressible and non-miscible fluids are modelled in the governing equations through an effective density and an effective viscosity. For each grid cell, a volume fraction, c_i, is defined as the fraction of the cell that contains fluid i. With the absence of fluid i in a cell, $c_i = 0$. With the sole presence of fluid i in a cell, $c_i = 1$. For each cell, the volume fraction satisfies $0 \leq c_i \leq 1$. The sum of the volume fraction of water, c_1, and the volume fraction of air, c_2, satisfies one in each cell. Since a volume fraction between zero and one indicates the presence of a mixture of the two fluids in a grid cell, a specific definition of the free-surface location is required. As definition of the interface between the two fluids, a volume fraction of 0.5 is used.

The effective density and the effective viscosity are used in the governing equations to account for the presence of a mixture of the two fluids in a cell. The effective density, ρ, and the effective viscosity, ν, are defined by $\rho = c_1 \rho_1 + c_2 \rho_2$ and $\nu = c_1 \nu_1 + c_2 \nu_2$, respectively, where subscript 1 indicates water and subscript 2 indicates air.

The evolution of the volume fraction in a grid cell is governed by a convection equation that ensures movement of the interface with the velocity of the fluid. This equation is called the volume fraction equation.

6.2. Discretization
The important details of the spatial discretization and the temporal discretization of the unsteady incompressible RANS equations are discussed in this section. For the full mathematical details of the discretization of the governing equations and the numerical methods involved, the reader is referred to Wesseling [46] and the theoretical manual of the ISIS-CFD flow solver [11].

6.2.1. Spatial discretization
The unsteady incompressible RANS equations are solved with a finite-volume spatial discretization on three-dimensional unstructured meshes. The finite-volume method (FVM) subdivides the computational domain into a number of finite volumes, or control volumes. The equations are integrated over the control volumes. For each control volume, the discretized governing equations are solved to determine the flow quantities in each of the volumes. The additional transport equations for the turbulence quantities are discretized and solved similarly to the momentum equations. The volume fraction equation is discretized with a different discretization scheme than the momentum equations.

For the discretization of the convective fluxes in the momentum equations and the equations for turbulence modelling, the mixed-order AVLSMART discretization scheme [39] is used. The AVLSMART scheme uses a combination of the first-order accurate upwind differencing scheme and the third-order accurate QUICK scheme [32]. The third-order QUICK scheme is the base scheme of the AVLSMART scheme. Based on local flow conditions, the AVLSMART scheme switches between the QUICK scheme and the upwind differencing scheme in order to use the most appropriate scheme at that location. The

AVLSMART discretization scheme is limited to third-order accuracy.

The volume fraction equation is discretized with the mixed-order BRICS discretization scheme. The Blended Reconstruction Interface Capturing Scheme (BRICS) was developed by the Equipe Modélisation Numérique at the Ecole Centrale de Nantes [11] from other interface capturing schemes to improve the free-surface capturing. The BRICS scheme uses a combination of the first-order accurate upwind and downwind differencing schemes, and the second-order central differencing scheme. Hence, this discretization method is limited to second-order accuracy. The central differencing scheme is the base scheme of the BRICS scheme. Based on local flow conditions, it switches automatically between the three different schemes to the most appropriate scheme at that location. As a result, the BRICS scheme probably produces an order of accuracy lower than two.

For accurate free-surface capturing, a refinement of the grid around the free surface in the simulation is required. The grid cells do not need to deform when the free surface changes. Accurate free-surface capturing imposes strict requirements on the computational grid. These requirements are discussed in Section 6.4.

The finite-volume discretization methods used on the three-dimensional unstructured meshes in the FINE™/Marine flow solver are limited to third-order accuracy for the turbulence equations and the momentum equations, and to second-order accuracy for the volume fraction equation. They are likely to produce an order between one and two due to the various combinations of the first-order accurate upwind and downwind differencing schemes, the second-order central differencing scheme, and the third-order QUICK scheme used for the discretization of these equations.

6.2.2. Temporal discretization

The equations have to be discretized in time as well. The temporal discretization method used in the ISIS-CFD flow solver is complex and only the important details are briefly discussed here.

Fully implicit temporal discretization schemes are used for the discretization of the momentum equations and the turbulence transport equations. The volume fraction equation is not discretized with a fully implicit scheme. A second-order accurate, three-level scheme is used for the temporal discretization of the time derivatives in the governing equations. The continuity equation is transformed into a pressure equation from which the pressure field is extracted. This allows for solving the pressure and the velocity field separately and reduces thereby computation time.

After spatial discretization and temporal discretization, a system of non-linear and coupled equations for the discretized governing equations are obtained. The time-marching method used in the ISIS-CFD flow solver to solve this system of equations is based on a segregated algorithm, which solves the governing equations sequentially. This algorithm uses an iterative procedure at every time step to solve the system of non-linear equations.

Every iteration consists of the following steps: (1) the volume fraction equation is solved, and the effective density and the effective viscosity are updated; (2) the equations for turbulence modelling are solved; (3) the momentum equations are solved to obtain new predictions of the velocities; (4) the pressure equation is solved to obtain the new pressure field; (5) the velocity components are updated with the new pressure field; and (6) if the continuity equation is sufficiently satisfied, i.e. if the residuals are low enough or the maximum number of non-linear iterations per time step is reached, the solver advances to the next time step and updates the flow quantities. Else the solver goes back to step (1) and does another iteration. The number of non-linear iterations for each global time step is limited to five for the simulation described in this thesis.

To enhance the stability of the numerical simulations, under-relaxation is applied to control the update of computed flow quantities at each iteration step in the segregated algorithm. Under-relaxation reduces the update of a flow quantity in an iteration step and thereby dampens oscillations and instabilities in the solution. The computed change of a quantity in a iteration step is multiplied by an under-relaxation factor. The flow quantity from the previous iteration step is then updated with this reduced change to obtain the flow quantity for the present iteration step. As a consequence of the system of non-linear equations, under-relaxation is necesarry for stability. The default under-relaxation parameters of the ISIS-CFD flow solver are adequate for the numerical simulations described in this thesis and they are therefore used.

The stability of discretization schemes can depend on time step limitations and limitations on the Courant-Friedrichs-Lewy (CFL) number. The CFL number, or simply the Courant number, is defined as the ratio of the displacement of a fluid particle in one time step to the cell size in that direction; the Courant number in the direction of one of the three Cartesian coordinates, α, is defined by

$$c_\alpha = \frac{|u_\alpha|\tau}{h_\alpha}, \tag{6.2}$$

where c_α is the Courant number in direction α, τ is the time step, and h_α is the cell size in direction α. A Courant number for the three-dimensional case is obtained from summation over the three Courant numbers defined by this equation. For unstructured grids with arbitrary shaped cells, this definition of the Courant number is not really practical. The following definition of the Courant number, C, is therefore used in the numerical simulations:

$$C = \frac{F\tau}{V}, \tag{6.3}$$

where F is the total (positive) flux out of the grid cell, and V is the volume of the cell.

The momentum equations and the turbulence transport equations are discretized with fully implicit temporal discretization schemes. The stability of the discretization of these equations does not suffer from any time step restrictions or CFL number limitations. The volume fraction equation is not discretized with a fully implicit scheme. The discretization of the volume fraction equation suffers from CFL number limitations. Consequently, it cannot be used without a time step restriction. In order to reduce this restriction in time step and to speed up the numerical computations, a sub-cycling acceleration method was implemented for the volume fraction equation in the ISIS-CFD flow solver.

This sub-cycling method solves the volume fraction equation several times during one global time step. Solving the volume fraction equation at sub-time steps reduces the Courant number. In this way, a larger global time step is possible without compromising numerical stability. The method requires a target Courant number and a maximum number of sub-cycles. Sub-time steps are calculated accordingly. If the target Courant number is reached or the maximum number of sub-cycles is reached, the volume fraction equation is not solved again in that global time step.

Different time step laws are implemented in the ISIS-CFD flow solver. A simple uniform time law, which defines a constant global time step in the time-marching method, is used for the simulations described in this thesis. The default time step size is given by $\tau = 0.01 L_{ref}/V_{ref}$, where V_{ref} is the reference velocity and L_{ref} is the reference length, or the waterline length. This implies 100 global time steps for every cycle of flow along the hull.

The uniform time law used together with the sub-cycling acceleration method produces satisfying results. The sub-cycling acceleration allows for a larger global time step than the default global time step. The global time step with the sub-cycling acceleration method is adjusted to $\tau = 0.025 L_{ref}/V_{ref}$. Together with a target Courant number of 20, this global time step provides numerical stability and convergence for all the simulations. A maximum number of five sub-cycles is adequate to obtain a maximum Courant number very close to the target Courant number. The maximum number of non-linear iterations for each global time step in the segregated algorithm is five. These settings are used for all the numerical simulations conducted for the new systematic series.

6.2.3. Initial conditions

Suitable initial conditions are required for the governing equations. As initial condition either the body at rest, i.e. no fluid flow, or a converged simulation is used. From a converged simulation, the pressure field, the velocity field, the turbulence quantities and the residuals are used as initial conditions for the new simulation. Either way, the body is accelerated with a smooth acceleration profile to the desired forward speed in a period of one second.

A continuous progression from lower speeds to higher speeds is used. Consequently, a simulation for a particular Froude number is restarted from the converged simulation at its previous speed. Only for Froude numbers 0.25 and 0.65, the simulations are started with the body at rest, with no fluid flow. This is a consequence of the low-speed grid and the high-speed grid defined in the next section. For Froude number 0.65, a larger acceleration period of 1.75 seconds is used to suppress instabilities

during acceleration.

For the $k - \omega$ two-equation turbulence model, additional equations are solved. Consequently, suitable initial conditions are required. The following initial conditions for the turbulence quantities are used: $\nu_t = \nu \cdot 10^{-3}$, $\omega = V_{ref}/L_{ref}$, and $k = \nu_t \cdot \omega$.

6.3. Boundary layers

The governing equations and the computational mesh should ideally resolve all the significant properties of the flow. However, the modelling of turbulent boundary layers with CFD can be complex and challenging as a consequence of the various physical characteristics of turbulence and the high velocity gradients resulting from the no-slip condition at the wall. High gradients of turbulence quantities can also be present close to the wall. For the interested reader or the reader less familiar with fluid dynamics, a more elaborate discussion on turbulent boundary layers and scaling of the mean-velocity profile is given in Appendix E.2.

Two approaches can be taken with CFD to resolve the high gradients close to the wall. The first approach is to resolve the gradients with the governing equations and the equations for turbulence modelling all the way down to the viscous sublayer, with the no-slip condition applied at the wall. This requires a very high density of very small grid cells close to the wall, in order to capture the high gradients accurately.

Another approach is to use wall functions to capture the physical effects and the high gradients present in the viscous wall region. The idea of the wall-function approach is to not solve the governing equations close to the wall. Based on log-law relations, the boundary conditions at the wall are applied some distance away from the wall in the lower part of the log-law region. In this way, the governing equations and the equations for turbulence modelling do not need to be solved close to the wall. The wall functions are used to describe the mean-velocity profile and the profile of the turbulence quantities in between the wall and the location where the boundary conditions are applied. Wall functions are essentially log-law relations rewritten to incorporate the turbulence quantities k and ω. The reader is referred to [11,37,47] for more details. This wall-function approach is preferable to the other approach, because it greatly reduces the density of grid cells close to the wall and thereby the computation time.

With the wall-function approach, the first grid point normal to the wall should be located in the lower part of the log-law region. The log-law region starts roughly somewhere between $y^+ = 20$ and $y^+ = 200$, depending on the Reynolds number. y^+ is the distance from the wall expressed in viscous lengths, or wall units. This wall coordinate, y^+, is defined by Equation (E.5). The Reynolds number, Re, is defined by

$$Re = \frac{V_{ref} \cdot L_{ref}}{\nu}. \tag{6.4}$$

NUMECA International [35] suggests $30 \leq y_1^+ \leq 300$, depending on the Reynolds number. y_1^+ is the value of y^+ associated with the first node near the wall. At model scale — low-Reynolds-number flows —, y_1^+ is about 30 while at full scale — high-Reynolds-number flows —, y_1^+ can be as high as 300. According to NUMECA International [35], the correct y_1^+ can be estimated with

$$y_1^+ = \max\left\{30; \min\left\{30 + 270\frac{Re - 10^6}{10^9}; 300\right\}\right\}. \tag{6.5}$$

For the speed range used in the numerical computations, shown in Table 4.2, the suggested values of y_1^+ range from 30.3 for Froude number 0.25 to 31.8 for Froude number 0.95. Based on a truncated series solution of the Blasius equation, NUMECA International [35] proposes an estimate for the distance, y_1, between the wall and the first computation node, as function of y_1^+. This ensures that the first grid point normal to the wall is located in the lower part of the log-law region.

Exactly following the suggestions of NUMECA International for y_1^+ requires the generation of a grid for every Froude number. This eliminates the possibility to restart a computation for a particular Froude number from the converged simulation at its previous speed, because restarting is only possible on exactly the same grid. Restarting reduces computation times and grid-generation efforts. Since the idea is to run computations for a large systematic series, restarting of computations is necesarry. In order to remain as close as possible to the suggested y_1^+ values while keeping the benefits of

restarting computations from previous speeds, the speed range used in the numerical computations, listed in Table 4.2, is divided into a 'low-speed' range, $0.25 \leq Fn \leq 0.55$, and a 'high-speed' range, $0.65 \leq Fn \leq 0.95$. Only for Froude numbers 0.25 and 0.65, the simulations are started with the body at rest.

Two grids for every model in the systematic series are generated accordingly: a 'low-speed grid' and 'high-speed grid'. Both grids are nearly identical and differ in the boundary layer refinement only. A different y_1 value is used for the generation of the two grids. This results in a different cell size, only close to the wall, in wall-normal direction. All the other grid-generation settings are exactly the same between the two grids. As a result of the lower y_1 value, a high-speed grid contains approximately 5.5 percent more cells than its corresponding low-speed grid.

The suggested y_1^+ and corresponding y_1 values for Froude numbers 0.35 and 0.65 are the most appropriate to be used for the y_1 value in the generation of the low- and the high-speed grid, respectively. These y_1 values give the best range of y_1^+ values for the other speeds calculated on that grid. The ISIS-CFD flow solver offers robust wall functions that are not too sensitive to y_1^+ values and that can produce accurate results for values of y_1^+ outside the suggested range. Therefore, it is not an issue to use slightly different y_1^+ values than those suggested by NUMECA International [35].

To properly resolve the turbulent boundary layer, the grid should be sufficiently refined in order to contain the computed boundary layer. Moreover, the computed boundary layer should be covered by a minimum number of nodes in wall-normal direction. A viscous-layer refinement with eight cells in wall-normal direction is used. The grid cells should not be stretched too rapidly in wall-normal direction, in order to cover the highest regions of the outer layer accurately as well.

6.4. Free-surface modelling

For capturing the free surface in the numerical simulations, the volume of fluid (VOF) method is used. The VOF method is a free-surface modelling technique that is used to track and locate the interface between the two fluids — water and air — in the flow solver. Accurate free-surface capturing imposes strict requirements on the computational grid. Around the resolved free surface, the grid should be sufficiently refined to have enough nodes per wave height and per wavelength. The resolved free surface in the simulation should always be contained within the grid refinement.

In the grid-generation process, discussed in Section 6.8, a grid refinement is applied around the initial free surface. The initial free surface is located at $z = 0$ in the computational domain, depicted in Figure 6.1. The refinement should be large enough to cover the resolved waves. Important factors for accurate free-surface capturing are the height of this grid refinement and the properties of the refined cells. A highly anisotropic mesh is required in the free-surface region to have enough nodes per wave height and per wavelength. A cell size of $L_{WL}/8 \times L_{WL}/8 \times L_{WL}/1000$ in the region of the free surface is adequate. The aspect ratio of the refined cells is 125.

For accurate free-surface simulations, it is important that the resolved free surface in the simulation is contained within the grid refinement around the initial free surface. In order to obtain accurate, but not too costly computations, an 'optimum' height of the grid refinement has to be found. The 'optimum' settings for the generation of the refinement around the initial free surface are listed in Table 6.1.

A small test has been conducted to illustrate that compared to these optimum settings, increasing the height of the grid refinement around the initial free surface is not necessary. The resistance values of Sysser 85 at Froude numbers 0.45 and 0.85, computed on grids with the optimum height of the free-surface grid refinement and grids with a 25-percent thicker free-surface grid refinement, are listed in Table F.2. Again, a distinction between low- and high-speed grids is made, and therefore, four different grids are used in this comparison. At both speeds, the difference in computed resistance between the 'optimum' grid and the grid with the thicker refinement is negligible. However, the grids with the thicker free-surface grid refinement contain approximately 24 percent more cells.

6.5. Ship motions: heave and pitch

To obtain the equilibrium position of a ship in a simulation, i.e. the steady-state solution with equilibrium trim and equilibrium sinkage, two fundamentally different methods can be used. The first method is to couple the governing equations for the flow with Newton's second law of motion for the ship motions.

In order for this coupling to be stable, the time step has to comply with stability restrictions and should be relatively small. This small time step and the larger system of equations leads to an increase in computation time. In order to decrease the computation time and to relax the restriction in time step, another method was implemented in the FINE™/Marine flow solver [35].

This other method uses an ad hoc quasi-static approach for determining the equilibrium position of a ship in the simulation. Ship motions are imposed rather than solved with Newton's second law. There is no direct coupling between the motion equations and the governing equations. The quasi-static method assumes that ship motions change so slowly that therefore inertia forces are very small and can be ignored. The equilibrium position in the simulation is obtained from successive predictions of the position of the ship based on computed flow forces acting on the hull.

The ship's position is evaluated every 20 global time steps for $0.25 \leq Fn \leq 0.55$ and every 60 global time steps for $0.65 \leq Fn \leq 0.95$ to insure stable computations and to save computation time. After the evaluation, the position is smoothly updated to reach the new relaxed predicted position within 20 global time steps for $0.25 \leq Fn \leq 0.55$ and within 30 global time steps for $0.65 \leq Fn \leq 0.95$. This ensures stable computations and smooth transitions between predicted positions. Under-relaxation is used to relax the update of the motions and to enhance the stability of the simulations. For $0.25 \leq Fn \leq 0.55$ and $0.65 \leq Fn \leq 0.95$, under-relaxation factors of 0.20 and 0.30 are used, respectively. These under-relaxation factors are adequate for all the numerical simulations described in this thesis.

The quasi-static method remains stable even for larger time steps. This enables the use of the sub-cycling acceleration method for the volume fraction equation, discussed in Subsection 6.2.2. The quasi-static method can be used at all Froude numbers if the settings are changed accordingly. According to NUMECA International [35], the quasi-static approach produces the same results as the method with Newton's second law of motion as long as the approach is correctly used.

The sinkage and the trim of a model are calculated with respect to its centre of gravity. Its centre of gravity is located at the same longitudinal and transverse location as its hydrostatic centre of buoyancy. For simplicity, the centre of gravity is assumed to be located at the design waterline of the model.

6.5.1. Mesh deformation
As a result of ship motions — heave and pitch —, the computational mesh has to be deformed in order to follow the rigid-body motion in the numerical simulations. A body-fitted mesh is generated before the simulation. A weighted deformation method is used to translate the rigid-body motion into a deformation of the grid cells in this mesh. The grid cells located directly around the body exactly follow the body without being deformed. The cells further away from the body are stretched or compressed accordingly with a weighted deformation technique.

For accurate free-surface simulations, it is important to generate a body-fitted mesh with the rigid body in a position close to its finial position — equilibrium sinkage and trim. Otherwise, free-surface capturing may be negatively affected by ship motions. Since the free-surface grid refinement follows the rigid body through the grid-deformation method, the situation may occur that the resolved free surface around the transom and the bow is no longer contained within the free-surface grid refinement due to a too different equilibrium position of the ship compared to its position used for grid generation. This results in the loss of accuracy. A solution is to translate the rigid body into a position close to its finial position before generating the grid. However, since multiple simulations for different speeds are performed on one grid, which gives the possibility to restart computations from each other and thereby greatly reduces computation time, finding a common position close to all the equilibrium positions computed on the grid is difficult.

From Figures 6.3 and 6.4, which show the trim and the sinkage of Sysser 85 and Sysser 88 for the three crew positions, it follows that there are no common positions close to the final position of each individual simulation on the low-speed grid, $0.25 \leq Fn \leq 0.55$, and on the high-speed grid, $0.65 \leq Fn \leq 0.95$. The trim and the sinkage of the other models in the systematic series follow a similar trend as the trim and the sinkage of Syssers 85 and 88. For every model, the trim values, and also the sinkage values, differ a lot between speeds and crew positions. The only common thing is that at every speed and for every crew position the models tend to sink in. That is why the models are given an initial heave displacement of five millimetres before meshing. This ensures that for the converged solution the resolved free surface is contained within the free-surface grid refinement when

the model has reached its final position in the simulation. No initial pitch angle was applied before meshing, because no common value could be found.

6.6. Numerical ventilation

High-Froude-number simulations typically require special attention with respect to numerical ventilation phenomena on the hull. With the volume of fluid method, a mixture of air and water can be transported under the hull in a high-Froude-number simulation. The air trapped under the hull affects the wetted surface, the hydrodynamic forces, the trim and the sinkage. Numerical ventilation, or numerical streaking, is not a physical process and should be avoided. The likelihood of numerical ventilation increases with speed. The occurrence of numerical ventilation depends on the quality of the computational grid. At high speeds, numerical ventilation is almost impossible to prevent without additional streaking corrections. The ISIS-CFD flow solver uses a streaking correction to correct the volume fraction to physical values in the case of numerical ventilation. This streaking correction is used for the numerical simulation described in this thesis.

6.7. Computational domain

The computational domain is defined as a rectangular cuboid around the model, without the intersection of the cuboid and the model's geometry. The computational domain consists of nine surfaces: six faces of the cuboid and three surfaces of the model's geometry. The geometry of a model is defined by three surfaces: a deck, a transom and a hull. The computational domain should be large enough to capture the wake correctly, to not disturb the flow field around the model and to not influence the solution of the simulation. A computational domain that stretches one waterline length upstream, three waterline lengths downstream, one and a half waterline lengths to either side, one and a half waterline lengths below, and a half waterline length above the model is adequate for Froude numbers 0.25 up to 0.95.

For computation of upright resistance values without any leeway angels, the symmetry in flow field along the longitudinal axis of the model can be exploited. With the use of a symmetry boundary condition, only half of the computational domain is required. The port side of the model is used in the numerical simulations. The computational domain, used in the simulations described in this thesis, measures $5L_{WL} \times 1.5L_{WL} \times 2L_{WL}$. A schematic of this computational domain and the axes convention are depicted in Figure 6.1. The free surface is located at $z = 0$ in the domain and forms the interface between water and air. The model moves in positive x-direction.

Adequate boundary conditions have to be applied to the nine surfaces of the computational domain. The deck, the hull and the transom are all solid boundaries. The deck is considered to have negligible drag compared to the hydrodynamic resistance, and therefore, a slip boundary condition is prescribed to it. A no-slip boundary condition with wall functions is applied to the hull and the transom. To the face of the computational domain at $y = 0$, a symmetry boundary condition is applied. The other five faces of the computational domain are external boundaries. Hydrostatic-pressure boundary conditions are applied to the faces at $z = -1.5L_{WL}$ and $z = 0.5L_{WL}$. The hydrostatic pressure is updated in the numerical simulations with the position of the free surface. The fluid is free to flow across these two faces. Far-field boundary conditions are imposed on the three faces at $y = 1.5L_{WL}$, $x = L_{WL}$, and $x = -4L_{WL}$.

6.8. Computational grid

The unsteady incompressible RANS equations are solved with a finite-volume spatial discretization on three-dimensional unstructured meshes. The finite-volume method subdivides the computational domain into a number of control volumes. For each control volume, the discretized governing equations are solved to find the flow quantities in each of the volumes. Consequently, the computational domain has to be discretized, taking into consideration all the previously mentioned requirements on the computational grid.

The settings used for grid generation are briefly discussed in this section and are summarized in the middle column of Table 7.1. The grid generated with these settings is denoted the 'medium' grid. A medium grid contains typically about 0.86 million cells for the low-speed grid and 0.91 million cells for the high-speed grid. For every model in the systematic series, a low-speed grid and a high-speed

$(-4L_{WL}, 1.5L_{WL})$ $(L_{WL}, 1.5L_{WL})$

y

$(-4L_{WL}, 0)$ $(0,0)$ x $(L_{WL}, 0)$
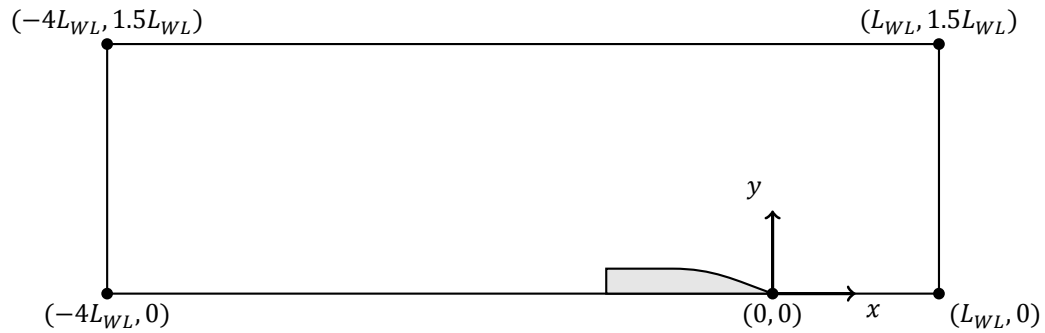
(a) View of the computational domain at $z = 0$. Port side of the ship is depicted. Coordinates of the points are given as (x, y).

$(-4L_{WL}, 0.5L_{WL})$ $(L_{WL}, 0.5L_{WL})$

z

Air

Free surface x

Water

$(-4L_{WL}, -1.5L_{WL})$ $(L_{WL}, -1.5L_{WL})$
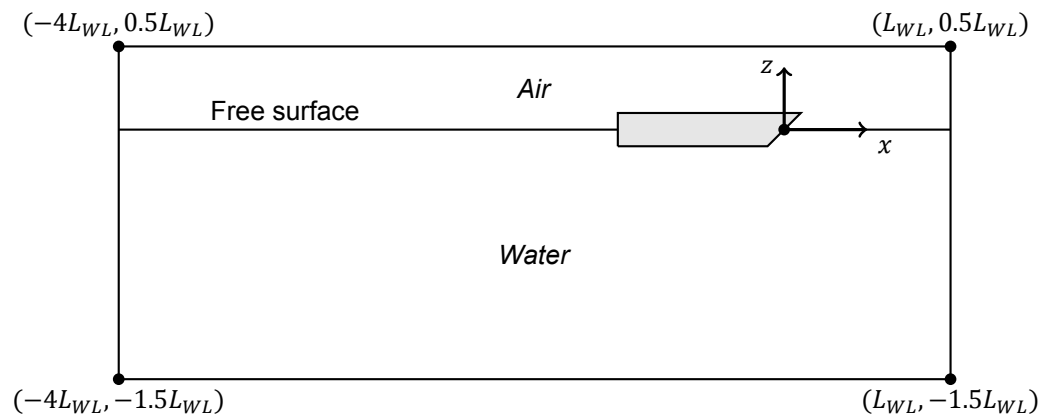
(b) View of the computational domain at $y = 0$. Coordinates of the points are given as (x, z).

Figure 6.1: Computational domain with ship movement in positive x-direction.

grid are generated with these settings. Computations for the three crew positions at a specific speed are performed on the same grid.

The computational domain of Figure 6.1 is subdivided into control volumes using the HEXPRESS™ grid generator of the FINE™/Marine software package. HEXPRESS™ generates body-fitted unstructured meshes. The advantage of unstructured meshes is that complex geometries can easily be meshed. The generated mesh is a full hexahedral mesh consisting solely of hexahedron cells.

The grid-generation process follows the following steps: (1) an initial mesh is generated based on the global cell size; (2) grid refinement is applied in certain regions to adapt the initial mesh to the ship's geometry and to facilitate accurate free-surface capturing; and (3) refinement for boundary layers is inserted on the selected solid surfaces using the desired y_1 value. An initial heave displacement of five millimetres is applied to the ship's geometry before meshing.

Optimization of the generated grid is performed automatically by HEXPRESS™ with the use of an optimization algorithm, in order to fix negative, concave, twisted or highly skewed cells. These cells are likely to pose robustness, stability and accuracy issues. All the generated grids contain no negative, concave, twisted or highly skewed cells. The quality of a generated grid also depends on the orthogonality, the aspect ratio and the expansion ratio of the grid cells. All the generated grids have a satisfying quality.

6.8.1. Initial mesh

The initial mesh of the computational domain is generated based on the global cell size. The computational domain of Figure 6.1 measures $5L_{WL} \times 1.5L_{WL} \times 2L_{WL}$, which corresponds to $10 \times 3 \times 4$ metres. This domain is subdivided along the Cartesian axes to create 20 cells in x-direction, 8 cells in y-direction and 8 cells in z-direction. The resulting computational mesh contains 1280 cells. The corresponding global cell size is $L_{WL}/4 \times 3L_{WL}/16 \times L_{WL}/4$, which corresponds to $0.50 \times 0.375 \times 0.50$

metres.

6.8.2. Surface refinement

Grid refinement is applied in certain regions to adapt the initial mesh to the ship's geometry and to facilitate accurate free-surface capturing. The three surfaces of the ship's geometry — deck, transom and hull — and the grid around the free surface have to be refined. The refinement of a cell with the HEXPRESS™ grid generator depends on the maximum number of refinements of an initial grid cell, the target cell size, the maximum aspect ratio of the cells, and the refinement diffusion. The cells are successively subdivided such that either the maximum number of refinements is reached or the geometrical criteria are met. Cells can be subdivided into two, four or eight cells. Cells are subdivided anisotropically as often as possible to limit the number of cells in the grid. The maximum aspect ratio is used to control the subdivision into two, four or eight cells. The refinement diffusion is used to ensure a sufficiently smooth transition between fine and coarse cell regions. A refinement diffusion of two means that when a cell is refined its directly neighbouring cells and the direct neighbours of the neighbouring cell are also refined. A global diffusion means that the refinement can be diffused throughout the entire grid.

The hull and the transom are the two surfaces where hydrodynamic forces (can) act on the ship. The grid at these surfaces has to be refined adequately. The hull and the transom are refined similarly. The deck is considered to have negligible drag compared to the hydrodynamic resistance, and therefore, fewer refinements are adequate for the deck. The grid refinement around the free surface was already discussed in Section 6.4. The surface refinement settings used to generate the medium grid are summarized in Table 6.1.

Some numerical tests have been conducted to illustrate that these refinement settings are adequate. Table F.3 gives the resistance values of Sysser 85 at Froude numbers 0.45 and 0.85 computed on three different grids: the medium grid, a grid with additional refinement of the hull compared to the medium grid, and a grid with additional refinement of the transom curve compared to the medium grid. The transom curve is the edge between the hull and the transom. Additional refinement of the transom curve can have a positive effect on the capturing of the wake at the transom. A distinction between low- and high-speed grids is made in this comparison.

The grid with additional refinement of the hull uses a maximum number of refinements of 7 instead of 6. The number of cells in the computational grid increases with 65 percent and 75 percent for the low- and the high-speed grid, respectively. At Froude numbers 0.45 and 0.85, the difference between the resistance computed on the medium grid and the resistance computed on the grid with the additional refinement of the hull is negligible.

The grid with the additional refinement of the transom curve uses a maximum number of refinements of 8 instead of 6. Only the cells next to the transom curve are additionally refined. The number of cells in the computational grid increases with approximately 7 percent compared to the medium grid. The difference in resistance is negligible at both speeds. These two test indicate that the refinement settings used for the medium grid are adequate.

6.8.3. Viscous layers

The hull and the transom are the two surfaces where hydrodynamic forces (can) act on the ship. Viscous layers have to be inserted in the grid at these surfaces in order to resolve the boundary layers correctly. The deck is considered to have negligible drag compared to the hydrodynamic resistance, and therefore, a slip boundary condition was prescribed. Consequently, no viscous layers have to be inserted at the deck.

A distinction between low- and high-speed grids was made in Section 6.3 based on the suggested values for y_1^+. The low- and the high-speed grid are nearly identical and differ in the boundary layer refinement only. A different y_1 value is used for the generation of both grids, which results in a different cell size in wall-normal direction. For the low-speed grid, $y_1 = 7.51 \cdot 10^{-4}\ m$. For the high-speed grid, $y_1 = 3.58 \cdot 10^{-4}\ m$. All other grid-generation settings are exactly the same.

To accurately resolve the boundary layer, the grid should be sufficiently refined with high-aspect-ratio cells close to the solid surface. The viscous layers are inserted into the grid by anisotropic refinement tangential to the solid surface. The dimension of a refined cell in streamwise direction is large compared to its dimension in wall-normal direction. The resolved boundary layer should be covered

by a minimum number of nodes in wall-normal direction. A viscous-layer refinement with eight cells in wall-normal direction is used. The grid cells should not be stretched too rapidly in wall-normal direction, in order to cover the highest regions of the outer layer accurately as well. A stretching ratio of 1.2 is used.

Table 6.1: The refinement settings for the surfaces in the computational domain, used to generate the medium grid with the HEXPRESS™ grid generator.

Surface	Number of refinements	Target cell size $[m]$	Maximum aspect ratio $[-]$	Refinement diffusion
Hull	6	$0 \times 0 \times 0$	2	*Global*
Transom	6	$0 \times 0 \times 0$	2	*Global*
Deck	4	$0 \times 0 \times 0$	2	*Global*
Free surface	8	$0.25 \times 0.25 \times 0.002$	128	4

6.9. Convergence

The numerical simulations are used to determine the hydrodynamic forces acting on a ship in a steady state. The resistance, the sinkage and the trim are the desired output quantities of a simulation. In order to ensure reliable convergence of the solution, the following convergence criteria are defined: all residuals should level out and the solution — forces, moments and motions — should not change any more. A convergence criteria describing the magnitude of the drop in residuals was found to be inadequate for the numerical simulations described in this thesis. Since most of the simulations are restarted from a converged simulation at a lower speed and the ship is smoothly accelerated to the new speed, the drop in residuals is very limited in the simulations. Most residuals drop only one order of magnitude during a simulation. The residuals of the converged solution of the restarted simulation are always a bit higher than the residuals of its previous simulation as a result of the increased speed.

The residuals of the three momentum equations for velocity components u, v and w, the pressure equation for the pressure p, and the transport equations for k and ω are monitored for every simulation. The convergence histories of forces, moments and motions are monitored as well. A typical convergence history of the residuals, forces, moments and motions of a computation at Froude number 0.55 is plotted in Figure 6.2. Computations at the other speeds follow this same typical convergence behaviour. Only for the computations at Froude numbers 0.25 and 0.65, the convergence history is slightly different, because these computations are started with the body at rest, i.e. no fluid flow. Consequently, the forces, moments, motions and residuals are all zero at the start of the simulation.

After the solution is considered to be converged, based on the defined convergence criteria, the simulation runs for at least 200 additional time steps. Small fluctuations are always present in the solution, even after the solution is considered to be converged. The final solution of a simulation is therefore obtained by averaging over the last 200 time steps of the simulation. For all the simulations, the standard deviation of the resistance over the last 200 time steps is less than 0.1 percent of the mean value.

In order to test the used convergence criteria, the simulations for Sysser 85 at Froude numbers 0.45 and 0.85 were restarted after they were considered to be converged. The resistance, sinkage and trim values for the converged solution and the solution after a doubling of the number of time steps in the simulation are listed in Table F.4. After the number of time steps had doubled, the resistance was only increased by 0.042‰ and 0.47‰ for Froude numbers 0.45 and 0.85, respectively. The changes in sinkage and trim are also negligible. These small differences strengthen the confidence in the selected convergence criteria.

6.10. Numerical results

For the sake of illustration, the upright trimmed resistance, and corresponding heave and pitch of Syssers 85 and 88 are shown in Figures 6.3 and 6.4. The other models in the systematic series have similar curves. The resistance curves and the motion curves have their expected typical shape. The difference in resistance between the crew positions also follows the expected behaviour. Typically, the resistance for the crew CoG position is the lowest at Froude numbers 0.25 and 0.35. At Froude
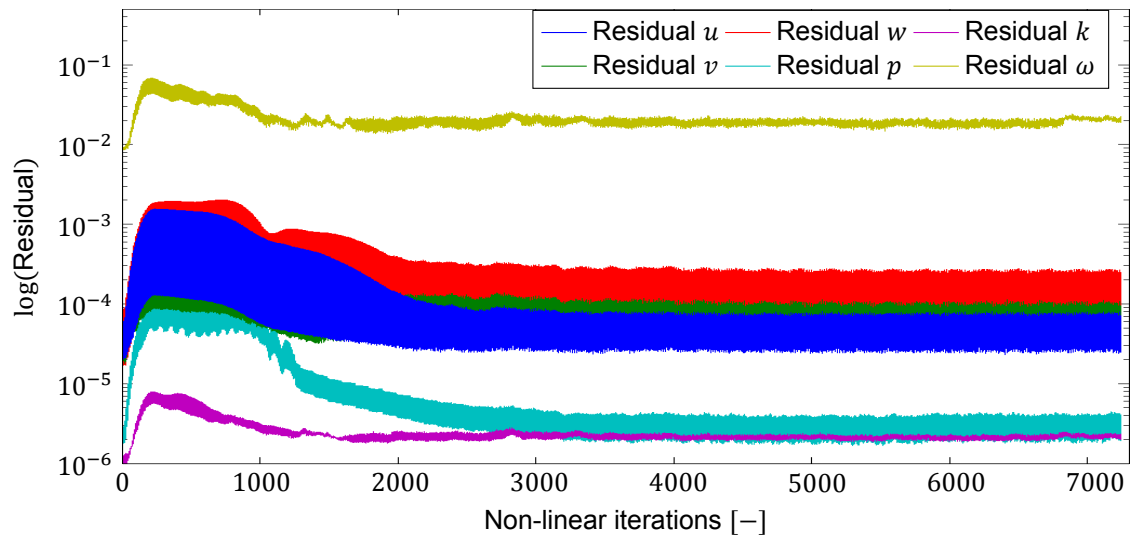
(a) History of the residuals of the three momentum equations, the pressure equation, and the two transport equations for k and ω.
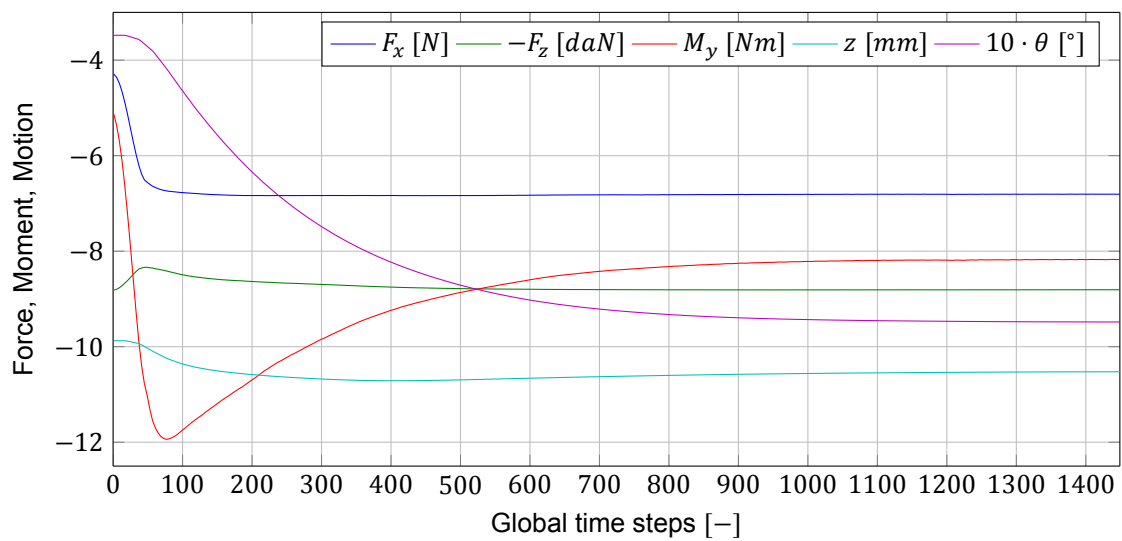
(b) Convergence of resistance F_x, vertical force F_z, moment M_y about the CoG, heave z, and pitch θ.

Figure 6.2: Convergence of a computation at Froude number 0.55.

number 0.45, the resistance for the crew middle position is the lowest. At the higher Froude numbers, the resistance for the crew back position is the lowest. At the lower speeds, the more bow-down attitude for the crew CoG position reduces the intensity of the wave system generated at the stern. It also results in a smoother flow field at the stern with less curved streamlines and less flow separation than for the other two crew positions. With increasing speed, the influence of these effects on the resistance becomes less important, because a more bow-up attitude increases the hydrodynamic lift and thereby decreases the resistance.

The minimum resistance of the three crew positions for every model in the systematic series is plotted as ratio to the minimum resistance for the parent hull, Sysser 85, in Figure 6.5. This allows for an easy comparison of the differences between the models. The found differences in resistance between the models in the systematic series are to be expected based on the applied variations. For instance, Sysser 89 has to the lowest resistance at all the speeds except at Froude number 0.25. Sysser 89 has the lowest displacement, a relatively low beam-to-length ratio and the same draft-to-beam ratio as the parent hull. Therefore, the resistance of Sysser 89 is likely to be the lowest. Sysser 91 has the same displacement as Sysser 89, but has a relatively low draft-to-beam ratio and the same beam-to-length ratio as the parent hull. Compared to Sysser 89 the resistance of Sysser 91 should be higher. Compared to the parent hull, the resistance of Sysser 89 should be lower. This is indeed the case.

Except for the parent hull, every model in the systematic series has its own antithesis. The systematic series contains for every selected variation a hull shape with an increase of the parameter and a hull shape with a decrease of the parameter. A description of the applied variations is given in Table 3.2. Most of the models and their antithesis have a mirrored behaviour in Figure 6.5 with respect to the parent hull. This does not hold for all of the models, because not all the variations have a linear relationship with the resistance. Syssers 96 and 97 show the most pronounced deviations from this mirrored behaviour. The variations applied to these models are related to the centre of buoyancy and the centre of flotation.

For the variations in displacement-to-length ratio, beam-to-length ratio and draft-to-beam ratio, hull shapes with intermediate variation were created. Sysser 86 up to Sysser 91 have 15-percent variation in a specific hydrostatic parameter compared to the parent hull. Sysser 100 up to Sysser 105 have 7.5-percent variation compared to the parent hull. Sysser 100 corresponds to Sysser 86; Sysser 101 corresponds to Sysser 87; and so on. The resistance ratio of the hull shape with the maximum variation to the parent hull, and the resistance ratio of the hull shape with the intermediate variation to the parent hull have a similar behaviour over the speed range, as can be seen in Figure 6.5. The shape of the curves is very similar. For most of these variations, the resistance ratio either increases or decreases (almost) linearly with increasing magnitude of the applied variation.

A seemingly strange thing happens for Sysser 97 at Froude number 0.95. Compared to the resistance of the parent hull, the resistance becomes all of a sudden relatively high. Based on the hull shape of this model, and the resistance curves and the motion curves for the three crew positions, this increase is not that strange. Sysser 97 has the longitudinal centre of buoyancy and the longitudinal centre of flotation relatively far forward. The position of the centre of buoyancy is pretty far ahead of the optimum position at this speed. This strongly intensifies the generated waves at the bow sections. Furthermore, this model has a relatively low centre of buoyancy-to-centre of flotation ratio, which makes it more difficult to trim bow up. This decreases the generated hydrodynamic lift and increases the sinkage and the resistance. As a consequence of the high resistance, the trimming moment of the driving force is also high and the model trims even more bow down.

Another seemingly strange thing happens for Sysser 94 at Froude number 0.35. Only at this speed, its resistance is higher than the resistance of the parent hull. Sysser 94 has a 10-percent higher prismatic coefficient than the parent hull. The three simulations for the three crew positions show the same behaviour compared to the resistance of the parent hull. An explanation could not be found.
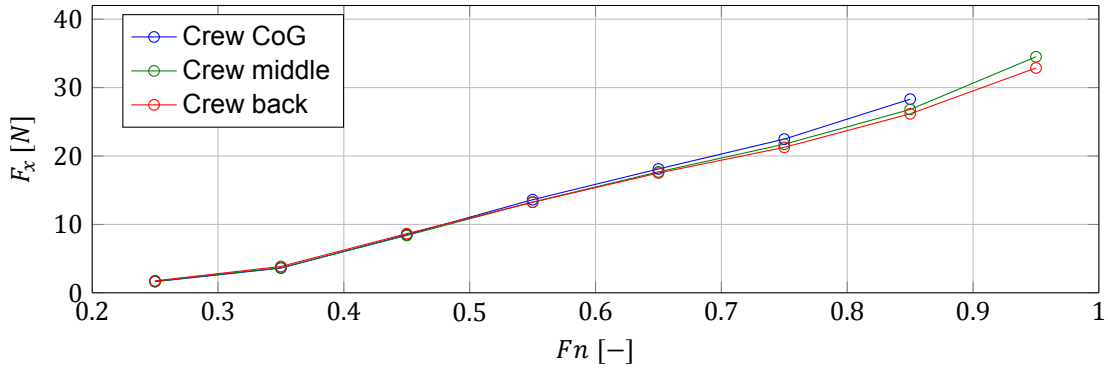
(a) Bare hull upright trimmed resistance for the three crew positions.
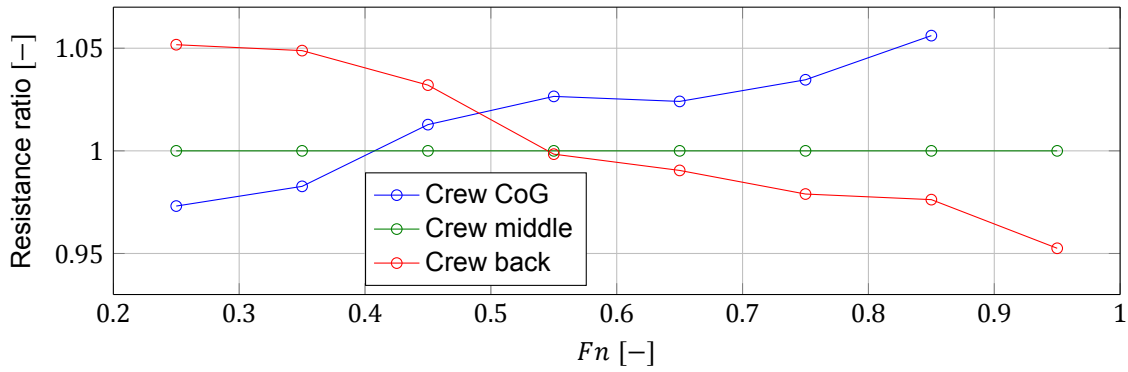
(b) Resistance ratio for the three crew positions, with respect to the resistance for the crew middle position.
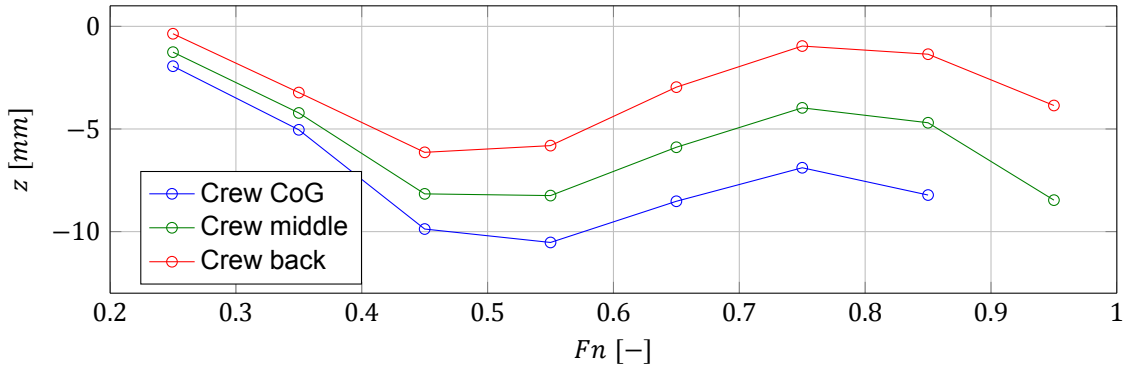
(c) Heave for the three crew positions.
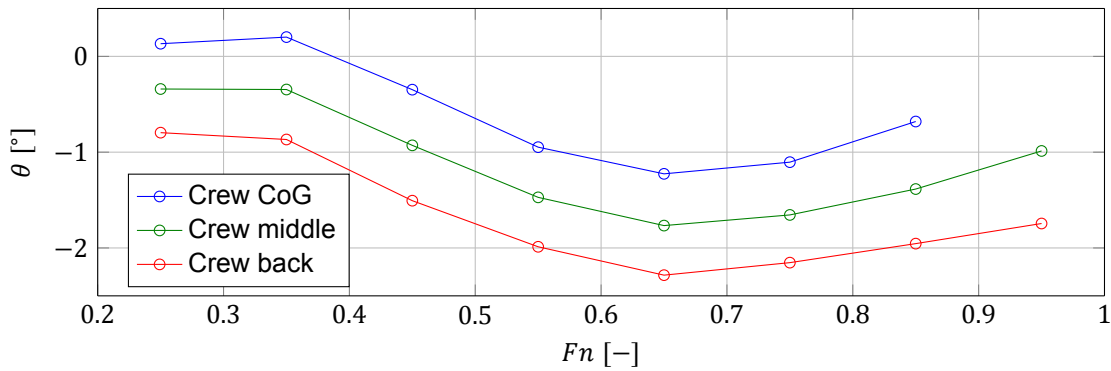
(d) Pitch for the three crew positions.

Figure 6.3: Numerical results of Sysser 85.
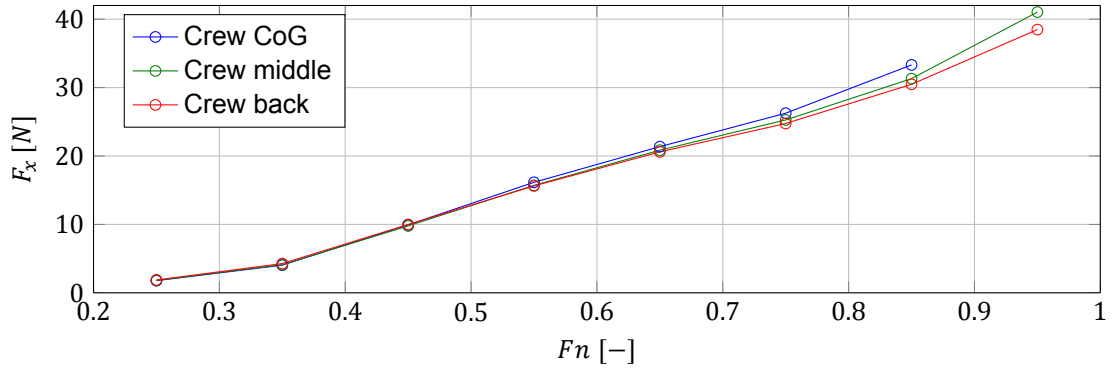
(a) Bare hull upright trimmed resistance for the three crew positions.
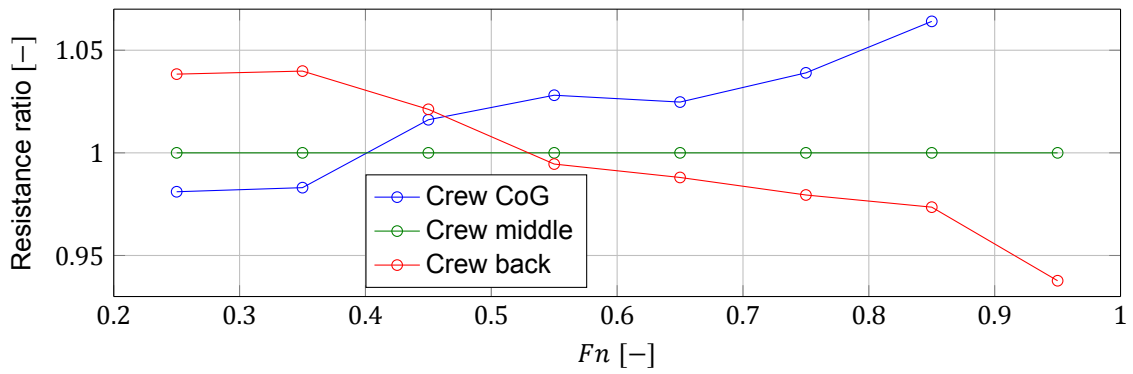
(b) Resistance ratio for the three crew positions, with respect to the resistance for the crew middle position.
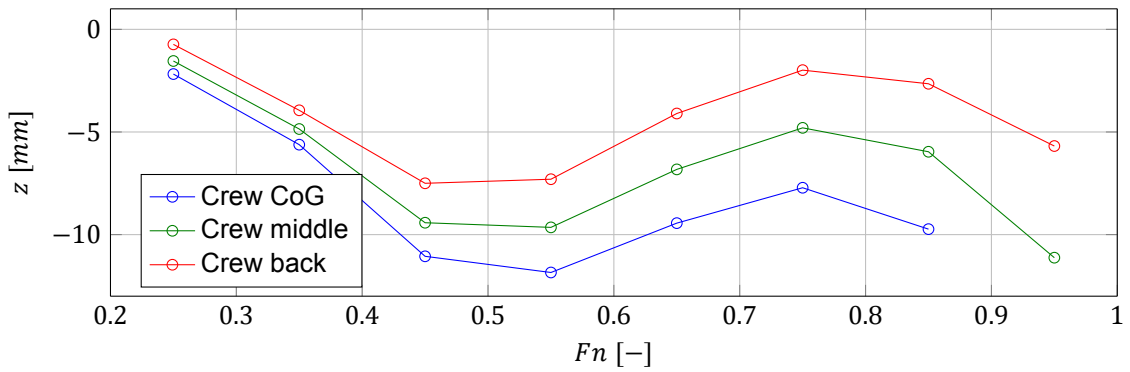
(c) Heave for the three crew positions.
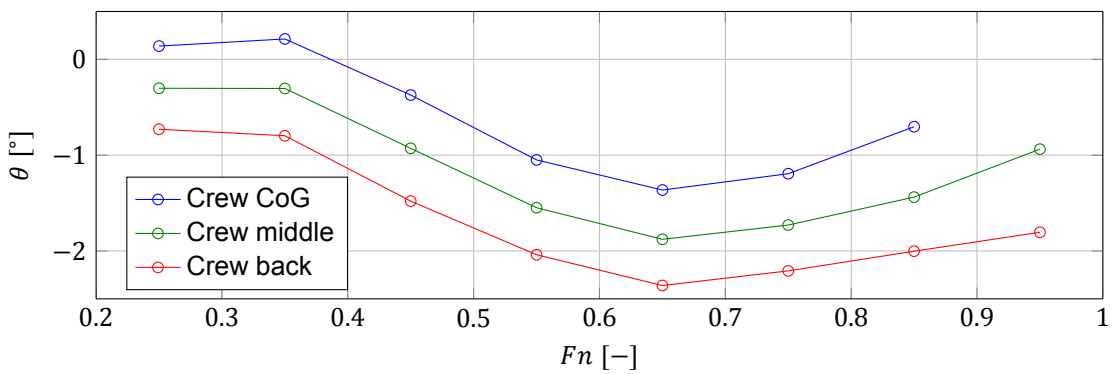
(d) Pitch for the three crew positions.

Figure 6.4: Numerical results of Sysser 88.
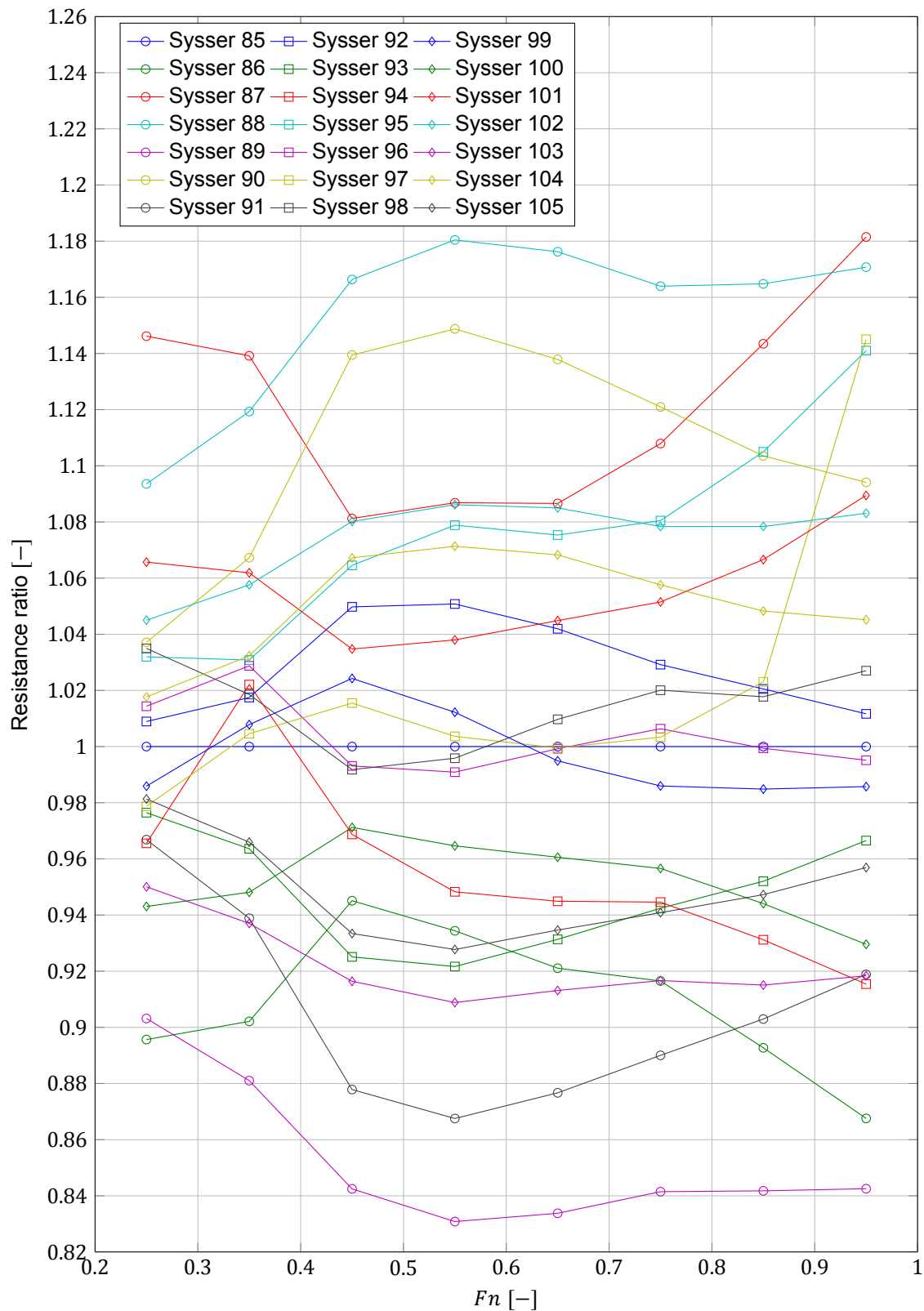
Figure 6.5: The minimum resistance of the three crew positions for every model in the systematic series as ratio to the minimum resistance for the parent hull, Sysser 85.

7

Numerical uncertainty

From a scientific point of view, it is desirable to asses the quality and the credibility of numerical simulations. To establish the reliability and the accuracy of the numerical results presented in this study, a Verification & Validation (V&V) analysis is performed. This V&V analysis is performed following the ITTC guidelines for uncertainty analysis in CFD [15]. The verification analysis is discussed in this chapter. Validation of the numerical results is discussed in Chapter 9.

According to Roach [43], verification is a purely mathematical procedure with the intention to show that *the equations are solved right*, whereas validation is an engineering practice with the intention to show that *the right equations are solved*. This implies that numerical errors and uncertainties belong to verification. On the other hand, modelling errors and uncertainties belong to validation. Validation consists of a comparison of numerical results and experimental results.

The different parts of the verification analysis are discussed in Section 7.1. From this discussion, it follows that the numerical error consists solely of the discretization error. The discretization error is determined with a grid refinement study. The procedure proposed by Eça and Hoekstra [9] is used for this assessment. Section 7.3 describes the estimation of the discretization error with this procedure. Section 7.4 describes the Eça and Hoekstra procedure for the estimation of the discretization uncertainty from this error.

The Eça and Hoekstra procedure is based on a systematic grid refinement study. This systematic refinement requires that the grids are geometrically similar and that the range of grid refinement is wide and fine enough to justify the use of a truncated power series expansion of the error. Obtaining geometric similarity between unstructured grids is a real challenge. The procedure used to obtain the series of refined grids is described in Section 7.2.

A distinction between including and excluding the influence of solving ship motions is made in this grid refinement study, because the quasi-static approach is used to obtain the equilibrium position of a ship in the simulation. With this approach, ship motions are imposed rather than solved at each time step. There is no direct coupling between the motion equations and the governing equations. This uncoupling may lead to unwanted scatter in the dataset of the refinement study, which results in an unexpected or strange order of convergence and unreliable uncertainty estimates. To accurately and reliably establish the observed order of grid convergence and the numerical uncertainty of the governing equations, two cases are investigated: one excluding the influence of solving ship motions in Section 7.6 and one including the influence of solving ship motions in Section 7.7. The reasoning behind this approach is discussed in more detail in Section 7.5. A comparison between both cases concludes this chapter.

The numerical uncertainty is determined for the parent hull of the systematic series on the low-speed grid at Froude number 0.45 and on the high-speed grid at Froude number 0.85. No trimming moment of the crew's weight is applied; i.e. the crew CoG position is used. These Froude numbers are selected because they both resemble 'extreme' flow conditions with distinctive and complex flow characteristics that may be hard to model numerically. Theoretically at Froude number 0.40, the wavelength of the wave generated at the bow becomes equal to the waterline length of the yacht. In that case, the wave crests generated at the bow coincides with the wave crests generated at the stern. This is coupled with a

large increase in wave-making resistance. In practice, this typically occurs at a (slightly) higher Froude number, because the distance between the location where the bow waves are generated and the location where the stern waves are generated is generally (slightly) higher than the nominal waterline length. The semi-displacement mode at Froude number 0.85 may also pose numerical difficulties due to complex flow phenomena. The complex flow phenomena and possible numerical difficulties at Froude numbers 0.45 and 0.85 are the reasons why they are selected for this grid refinement study.

An important distinction between errors and uncertainties has to be mentioned. Following Roache [44], an uncertainty defines an interval that should contain the exact solution with a certain degree of confidence; an error is defined as the difference between the numerical solution and the exact solution. Uncertainties are estimated as the absolute value of an error estimator multiplied by a factor of safety.

7.1. Verification

Following Roach [43], verification itself consists of two parts: code verification and solution verification. Code verification has to be done before solution verification. The purpose of code verification is to ensure that the numerical model and the equations are correctly implemented in and solved by the CFD solver. Solution verification assesses the numerical simulation uncertainty.

7.1.1. Code verification

Code verification involves meticulous testing of the computational code on benchmark cases presented in literature. This makes code verification very costly and time consuming. Hence, code verification is beyond the scope of the present study. Moreover, it is not necesarry, because use is made of the ISIS-CFD flow solver [11] implemented in the commercial FINE™/Marine software package of NUMECA International [35]. One of the benefits of using commercial CFD codes is that these codes are subjected to very extensive code verification exercises prior to release. For a code verification analysis of the ISIS-CFD flow solver, reference is made to Deng et al. [3]. A complete V&V analysis of the ISIS-CFD flow solver is given by Deng et al. [4].

7.1.2. Solution verification

Solution verification assesses the numerical simulation uncertainty. Following Roache [43,44], the ITTC [15], and Eça and Hoekstra [9], the numerical uncertainty is estimated as the absolute value of a numerical error estimator multiplied by a factor of safety. The numerical error is defined as the difference between the numerical solution and the exact solution. It consists of three parts: round-off errors, iterative errors and discretization errors.

Round-off errors

Round-off errors arise from the finite precision of computers. Its importance tends to increase with grid refinement. According to Eça and Hoekstra [9], round-off errors are generally suitable small due to the double-precision arithmetic used in numerical flow solvers. Round-off errors are considered to be negligible in the present refinement study based on the double-precision arithmetic used in the FINE™/Marine flow solver.

Iterative errors

Iterative errors are a consequence of the non-linearity of the system of partial differential equations solved in CFD. Various sources of non-linearity are present, e.g. the convective terms in the Reynolds-averaged Navier–Stokes equations and in the equations of the turbulence model. The iterative convergence error is defined as the difference between an intermediate solution and the solution converged as far as the accuracy of the computer permits. From a time and cost perspective, simulations are generally truncated close to this final solution. This introduces iterative errors.

For the estimation of the numerical error, it is convenient to neglect the influence of the iterative errors on the numerical error compared to the discretization error, because convergence to machine accuracy is very time consuming. Eça and Hoekstra [5] suggest as a rule of thumb that the iterative error should be two to three orders of magnitude smaller than the discretization error, in order to have a negligible influence on the estimation of the numerical uncertainty.

As said before in Section 6.9, after the solution is considered to be converged based on the defined convergence criteria, the simulation runs for at least 200 additional time steps. The final solution of a simulation is obtained by averaging over the last 200 time steps of the simulation. For all the performed simulations, the standard deviation of the resistance over the last 200 time steps is less than 0.1 percent of the mean value. For the numerical simulations performed in this grid refinement study, the standard deviation of the resistance is less than 0.03 percent of the mean value. Based on this very small standard deviation, the iterative convergence errors are assumed to be negligible. This very small standard deviation indicates that the used solution is very close to the solution converged as far as the machine accuracy permits, and thus iterative errors are very small.

Furthermore, in order to test the used convergence criteria, the simulations for Sysser 85 at Froude numbers 0.45 and 0.85 were restarted after they were considered to be converged. After the number of time steps had doubled, the resistance was only increased by 0.042‰ and 0.47‰ for Froude numbers 0.45 and 0.85, respectively, as was shown in Table F.4. This suggests that the assumed converged solution is very close to the to-machine-accuracy converged solution; it suggests that the iterative error is very small. Of course, this small test is not conclusive, but it nevertheless suggests a very small contribution of the iterative error on the numerical error compared to the discretization error determined in Sections 7.6 and 7.7, which is between 1.3 and 2.6 percent on the medium grid. For this refinement study, the iterative convergence errors are assumed to be negligible compared to the discretization error.

Discretization errors

Discretization errors are a consequence of the finite-volume method that is used for the spatial discretization of the governing equations. The governing equations are discretized into a system of algebraic equations which introduces a numerical error. The discretization error is defined as the difference between the numerical solution converged to machine accuracy and the exact solution. Unlike the round-off error and the iterative error, the relative importance of the discretization error decreases with grid refinement.

Numerical error

Under the assumption that the round-off errors and the iterative errors are indeed negligible compared to the discretization error, the numerical error consists solely of the discretization error. An accurate discretization error estimator is indispensable to obtain a reliable numerical uncertainty estimate. As reported by Eça and Hoekstra [10,6], using the established methods of Roache [43,44] and others for uncertainty estimation is found to be difficult in practical applications due to practical grid-density and geometric-similarity limitations. These practical limitations are likely to contribute to scatter and noise in the data [10,6]. Scatter and noise make it difficult to apply the power series expansion of the error, used in the established methods, to the database.

To avoid these limitations, the numerical uncertainty estimation procedure proposed by Eça and Hoekstra [9] is used. This method gives a number of possibilities for the numerical error estimation if the power series expansion of the error, used in the established methods, does not produce satisfying results. The Eça and Hoekstra method has a similar approach as the ITTC procedures [15] and American Society of Mechanical Engineers (ASME) procedures [1]. Klaij et al. [30] report on different practical test cases for which the numerical uncertainty is successfully and satisfyingly determined with the Eça and Hoekstra method. This method is also used at the Maritime Research Institute Netherlands (MARIN). The Eça and Hoekstra procedure was thoroughly tested for a variety of cases [7,8,9,30].

In the present refinement study, the numerical uncertainty is estimated with the Eça and Hoekstra procedure. The uncertainty is determined for Sysser 85 on the low-speed grid at Froude number 0.45 and on the high-speed grid at Froude number 0.85.

7.2. Grid generation for refinement study

Just like the established numerical uncertainty estimation methods, the Eça and Hoekstra procedure [9] is based on a systematic grid refinement study. This systematic refinement requires that the used grids are geometrically similar and that the range of grid refinement is wide and fine enough to justify the use of a truncated power series expansion of the error, i.e. to give a single dominant term in the power series expansion. Geometric similarity is satisfied when the grid refinement ratio, which is defined as

the ratio of the cell sizes between two grids, is constant in the entire computational domain, and when the properties of the grid cells, e.g. aspect ratio, skewness and orthogonality, are unaffected.

Unfortunately, it is a real challenge to obtain geometric similarity for a series of refined unstructured grids. According to Eça and Hoekstra [6], the lack of geometric similarity between the grids is a main contributor to scatter in the data of a refinement study. Great care has to be taken in order to satisfy the geometric-similarity constraint as much as possible when generating the refined grids.

For each grid in the refinement study, a typical cell size, h_i, is defined by

$$h_i = \sqrt[3]{\frac{V_\Omega}{N_i}},$$

(7.1)

where V_Ω is the volume of computational domain, and N_i is the number of cells of that particular grid. The subscript i can have values 1, 2, 3, 4, 5 and 6, and stands for the finest, finer, fine, medium, coarse and coarser grid, respectively. The refinement factor, r_i, between two successive grids is defined by

$$r_i = \frac{h_{i+1}}{h_i}.$$

(7.2)

When generating a refined grid, the refinement ratio should be chosen carefully. Ratios close to one are undesirable, since changes in the solution will be very small. In general, the refinement ratio is advised to be two. However, for practical ship hydromechanics applications this refinement ratio is often too large due to practical grid-density limitations. A refinement factor of two introduces no additional numerical error source. With a refinement factor other than two, interpolation to a common location is required to compute solution changes. This introduces interpolation errors. Evaluation methods for interpolation errors are given by Roache [43].

For this refinement study, a refinement ratio of $\sqrt[3]{2}$, resulting in a doubling of the amount of cells from one grid to the other, is used. A refinement factor of two is way too large and practically infeasible, because it results in an octupling of the amount of cells from one grid to the other. The interpolation errors are assumed to be negligible compared to the discretization error.

7.2.1. grid-generation approach

In order to construct geometrically-similar unstructured grids with the HEXPRESS™ mesh generator, the refinement factors have to be chosen very carefully. This is a consequence of the dependence of the grid generator on integers to specify the initial number of cells in each direction, the number of viscous layers and the refinement diffusion. These integers have to be scaled for some surfaces in order to obtain geometrically similar grids. Choosing the refinement ratios carefully results again in integers and not in rational numbers. Rational numbers have to be rounded otherwise. Rounding of rational numbers to integers contributes to the lack of geometric similarity between the grids. Based on the integer numbers used for the generation of the medium grid, the following refinement ratios are used: 2.00, 1.50, 1.25, 1.00, 0.75 and 0.50. These refinement ratios are defined with the typical cell size of the medium grid as the reference size. The typical amount of cells in the refined grids is 7, 3, 2, 0.9, 0.4 and 0.1 million.

In order to create unstructured grids with HEXPRESS™ that satisfy the geometric-similarity constraint as much as possible, some of the settings of the grid generator, mentioned in Section 6.8, have to be adapted accordingly. The initial mesh size has to be scaled with one over the refinement factor. This changed initial mesh size ensures that the cells at the hull, the transom and the deck are scaled automatically and accordingly. Therefore, changing the settings for the hull, the transom and the deck, given in Table 6.1, is not necesarry. For these surfaces, the target cell size is namely zero. Keeping the number of refinements and the global refinement diffusion the same ensures that the cells of the changed initial mesh are refined similarly to the cells of the original mesh. This results in geometrically similar cells.

For the grid refinement around the initial free surface, the settings for the target cell size and the refinement diffusion, given in Table 6.1, have to be changed. The target cell size has to be scaled with one over the refinement factor. As a consequence of the changed cell size, the height of the grid

refinement around the initial free surface is scaled automatically with one over the refinement factor. To avoid this unwanted change in the height of the free-surface grid refinement, the refinement diffusion has to be multiplied by the refinement factor. This ensures that compared to the reference grid, the height of the grid refinement around the initial free surface is unchanged.

For the viscous layers, the first layer thickness, which determines the cell size normal to the solid surface, has to be adapted to ensure geometrically similar cells in the boundary layer. Since the initial mesh size is scaled with one over the refinement factor, the first layer thickness in the boundary layer has to be scaled similarly. This preserves the aspect ratio, the skewness and the orthogonality of the cells in the viscous layers. To avoid the change in thickness of the viscous-layer refinement, the number of layers has to be multiplied by the refinement factor.

In order to obtain numerical simulations with similar numerical properties concerning convergence and stability, the global time step has to be changed for each grid as well. The most important factor to ensure similar numerical simulations is the Courant number, which is defined similarly to Equation (6.2) by

$$c_i = \frac{|u|\tau_i}{h_i},$$
(7.3)

where c_i is the Courant number on grid i, and τ_i is the global time step on grid i. Under the assumption that the change in flow velocities between the grids is very small, the change of the typical cell size has to be counteracted by a similar change in the global time step. This ensures that the Courant number in the simulations remains more or less constant between the different grids. In this way, the numerical properties of the simulations are more or less preserved between the grids.

From the generated grids, which are given further on in this section, it follows that despite the effort made for the generation of the refined grids, the observed number of cells after grid generation differs from the expected number of cells. As a consequence, the observed refinement factor also differs from the expected refinement factor. In order to keep the Courant number in the simulations more or less constant, the global time step is scaled with one over the observed refinement factor instead of one over the expected refinement factor. The settings used for motion solving, discussed in Section 6.5, are adapted for every grid to the different global time step.

The above-mentioned settings for the generation of geometrically-similar unstructured grids with HEX-PRESS™ are summarized in Table 7.1.

7.2.2. Refined grids
The number of cells and the refinement factors of the twelve grids — six low-speed grids and six high-speed grids — created with the above-mentioned grid-generation approach are listed in Table 7.2. The expected refinement ratio r_i^*, the expected number of cells N_i^*, the observed refinement ratio r_i and the observed number of cells N_i are listed in this table. The observed values are the actual values obtained after grid generation. The first thing that strikes from this table is the difference between the expected number of cells and the observed number of cells. Despite this sometimes relatively big difference, the grids, with the exception of the coarser grid, are satisfactorily geometrically similar. Mesh properties, e.g. the aspect ratio, the skewness and the orthogonality of the cells, are reasonably preserved between the different grids. A series of grid topologies of the refined grids is shown in Figure 7.1. A part of the cross section of each grids at midship is depicted in this figure. The grids all have a similar block-like structure.

The coarser grid is omitted from the refinement study because of the lack of geometric similarity with the rest of the grids. Moreover, the computation results on the coarser grid are outliers in the refinement study.

7.3. Discretization error estimation
Eça and Hoekstra [9] propose a procedure for the estimation of the numerical uncertainty of any integral or local flow quantity, based on grid refinement studies. This method tries to avoid the limitations encountered with established uncertainty estimation procedures applied to practical ship hydromechanics applications. Scatter in a dataset, arising from practical grid-density and geometric-similarity limitations

Table 7.1: Settings used for the generation of geometrically-similar unstructured grids with HEXPRESS™, and the global time step used for the simulations. Listed are the settings for the medium grid from Sections 6.2 and 6.8, and Table 6.1. The settings for the refined grid are based on the settings for the medium grid and are scaled with the refinement factor. Note that there are two different grid refinement ratios used in this table, namely, the expected ratio, $r_i{}^*$, used for the grid generation and the observed ratio, r_i, used for the simulation settings. Both ratios are given for each grid in Table 7.2.

	Medium grid	Refined grid
Initial mesh		
Cell size $[m]$	$L_{WL}/4 \times 3L_{WL}/16 \times L_{WL}/4$	$(L_{WL}/4 \times 3L_{WL}/16 \times L_{WL}/4)/r_i{}^*$
Hull, transom, deck		
Target cell size $[m]$	$0 \times 0 \times 0$	*Unchanged*
Number of refinements	6 and deck 4	*Unchanged*
Refinement diffusion	*Global*	*Unchanged*
Free surface		
Target cell size $[m]$	$0.25 \times 0.25 \times 0.002$	$(0.25 \times 0.25 \times 0.002)/r_i{}^*$
Number of refinements	8	*Unchanged*
Refinement diffusion	4	$4r_i{}^*$
Viscous layers		
Low-speed grid: y_1 $[m]$	$7.51 \cdot 10^{-4}$	$7.51 \cdot 10^{-4}/r_i{}^*$
High-speed grid: y_1 $[m]$	$3.58 \cdot 10^{-4}$	$3.58 \cdot 10^{-4}/r_i{}^*$
Number of layers	8	$8r_i{}^*$
Time step		
Global time step $[s]$	$0.025L_{WL} / V$	$0.025L_{WL} / (V\, r_i)$

Table 7.2: Properties of the different grids used in the grid refinement study. $r_i{}^*$ and $N_i{}^*$ are the expected values before grid generation while r_i and N_i are the observed values after grid generation. Refinement ratios are defined with the typical cell size of the medium grid as the reference size. $\Delta_\% = (N_i - N_i{}^*)/N_i{}^* \cdot 100$.

	i	$r_i{}^*$	Low-speed grids				High-speed grids			
			$N_i{}^*$	r_i	N_i	$\Delta_\%$	$N_i{}^*$	r_i	N_i	$\Delta_\%$
		$[-]$	$[-]$	$[-]$	$[-]$	$[\%]$	$[-]$	$[-]$	$[-]$	$[\%]$
Coarser	6	0.50	107859	0.60	186579	73.0	113517	0.59	186579	64.4
Coarse	5	0.75	364025	0.80	437550	20.2	383120	0.78	438776	14.5
Medium	4	1.00	862875	1.00	862875	0	908136	1.00	908136	0
Fine	3	1.25	1685303	1.26	1738538	3.2	1773703	1.27	1870953	5.5
Finer	2	1.50	2912203	1.45	2628983	-9.7	3064959	1.46	2818703	-8.0
Finest	1	2.00	6903000	1.92	6139829	-11.1	7265088	1.91	6312510	-13.1

(a) Coarser grid

(b) Coarse grid

(c) Medium grid

(d) Fine grid

(e) Finer grid

(f) Finest grid
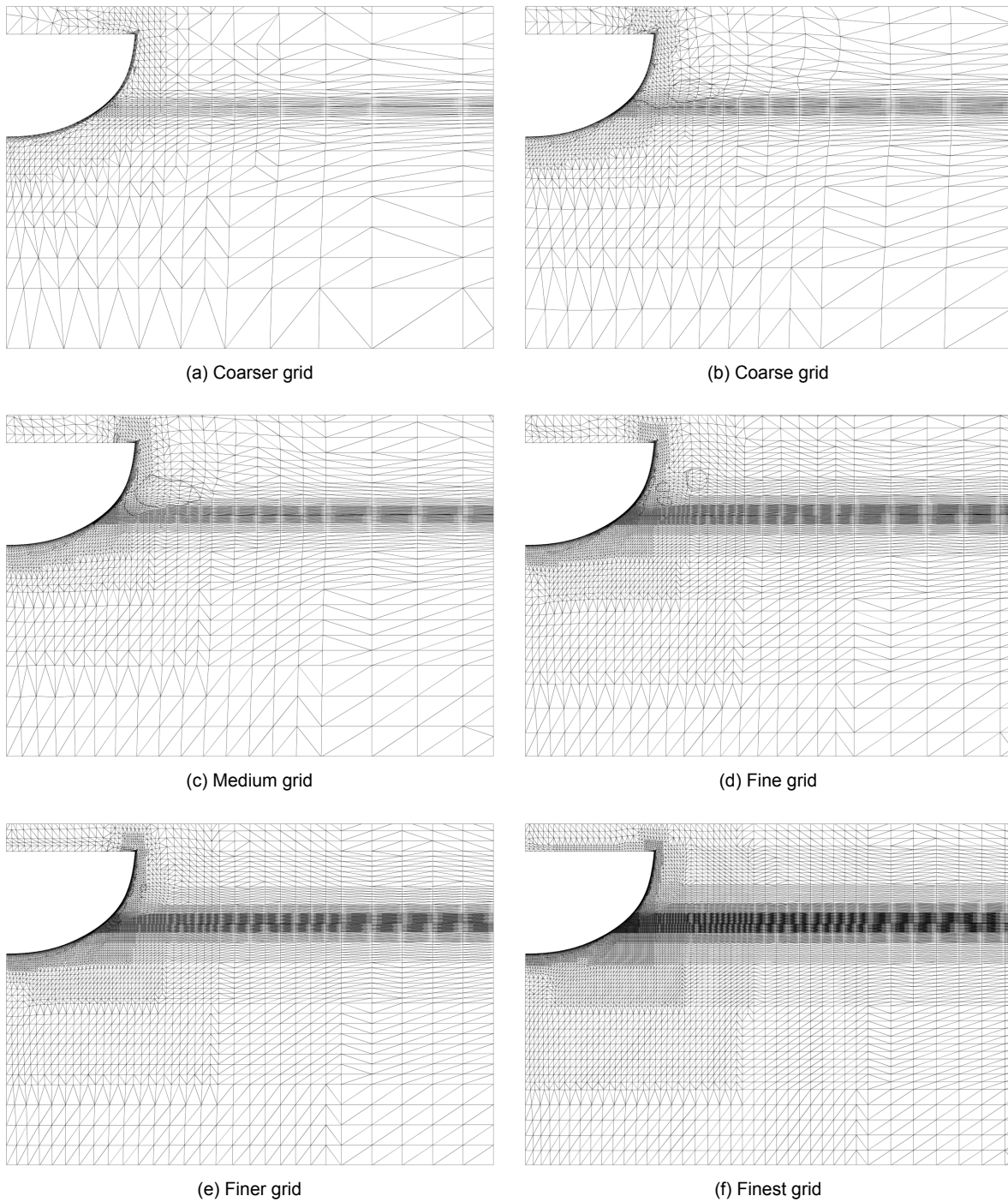
Figure 7.1: The different high-speed grids used in the refinement study. For every grid, a part of the cross section of the grid at midship is depicted. The grids for the low-speed grid are visually completely similar, since only the wall-normal cell size in the viscous layers is different between the low-speed grid and the high-speed grid.

[10,6], makes it difficult to apply the power series expansion of the error, used in the established methods, to the dataset. According to Eça and Hoekstra [9], other sources of scatter in the dataset are flux limiters, which are commonly used in the discretization of convective terms to avoid spurious oscillations in the solution around discontinuities in the grid, and damping functions used in turbulence models. These sources contribute to differences in discretization of the governing equations between the grids.

To avoid those limitations often accounted in practical ship hydromechanics applications, the numerical uncertainty estimation procedure proposed by Eça and Hoekstra [9] is used for the present refinement study. In this procedure, the error is estimated with truncated power series expansions, as function of the typical cell size. Non-weighted least-squares minimizations and weighted least-squares minimizations are used to fit error estimators to the dataset. Different error estimators are used to establish a reliable error estimate. Classifying one of the different error estimators as the most reliable one is done by means of the grid-convergence behaviour, the observed order of grid convergence and the standard deviations of the fits. The Eça and Hoekstra procedure was thoroughly tested for a variety of cases [7,8,9,30]. The method is discussed in this section.

7.3.1. Grid-convergence behaviour

Establishing the grid-convergence behaviour gives insight in, but no conclusive answer on, which numerical uncertainty estimator to use. A simple way to estimate the apparent grid-convergence behaviour is to use the discrimination ratio, or convergence ratio. The grid-convergence behaviour for equal grid refinement ratios between successively coarsened grid, i.e. $h_{i+1}/h_i = h_{i+2}/h_{i+1}$, can be estimated with the convergence ratio, R_k, as proposed by Roache [43,44]:

$$R_k = \frac{\phi_i - \phi_{i+1}}{\phi_{i+1} - \phi_{i+2}},$$

(7.4)

where the subscript k indicates a particular grid triplet, ϕ_i is any integral or other functional of the local flow quantity under consideration, and the subscripts i, $i+1$ and $i+2$ represent three successively coarsened grids in that grid triplet, respectively. Based on the convergence ratio, Roache identifies four types of convergence behaviour:

- Monotonic convergence for $0 < R_k < 1$;
- Monotonic divergence for $R_k > 1$;
- Oscillatory convergence for $R_k < 0$ and $|R_k| < 1$;
- Oscillatory divergence for $R_k < 0$ and $|R_k| > 1$.

These four types of grid-convergence behaviour can be used to obtain insight in the uncertainty estimation procedures to use, but it gives no conclusive answer. An indication of divergent behaviour probably yields no sufficient numerical uncertainty estimation. However, undertaking an effort with the numerical uncertainty estimation procedure described further on in this section can still give satisfactory results, because the convergence ratio is not that accurately defined for a series of more than three grids. An indication of convergent behaviour probably yields a sufficient numerical uncertainty estimation, but both types of convergence behaviour need a different approach to establish the numerical uncertainty.

From Table 7.2, it follows that for the present refinement study, the only grid triplet satisfying $h_{i+1}/h_i = h_{i+2}/h_{i+1}$ is the triplet of the fine, medium and coarse grid. Therefore, the convergence ratio, R, for this refinement study can only be defined by

$$R = \frac{\phi_3 - \phi_4}{\phi_4 - \phi_5},$$

(7.5)

where subscripts 3, 4 and 5 stand for the fine grid, the medium grid and the coarse grid, respectively.

7.3.2. Different error estimators

Eça and Hoekstra focus on estimating the discretization error with truncated power series expansions. Following Roache [43,44] and others, the basic equation for the estimation of the discretization error with the Eça and Hoekstra procedure is

$$\epsilon_\phi \simeq \delta_{RE} = \phi_i - \phi_0 = \alpha h_i{}^p,$$

(7.6)

where ϵ_ϕ is the discretization error, δ_{RE} is an estimate of the discretization error, ϕ_i is any integral or other functional of the local flow quantity under consideration, ϕ_0 is the estimate of the exact solution, α is a constant, h_i is the typical cell size defined by Equation (7.1), and p is the observed order of grid convergence. Obvious restrictions of this numerical error estimator on the dataset are the necessities of no scatter in the dataset, monotonic convergence behaviour and data within the asymptotic range, i.e. the range of grids should be wide and fine enough to give a single dominant term in the power series expansion. Due to these restrictions and the limitations encountered in practical ship hydromechanics applications, broader applicable error estimators are necessary.

Therefore, the Eça and Hoekstra procedure [9] gives three alternative error estimators that fix the observed order of grid convergence to first order, second order or a combination of both. These alternative error estimators are

$$\epsilon_\phi \simeq \delta_1 \ = \phi_i - \phi_0 = \alpha h_i, \tag{7.7}$$

$$\epsilon_\phi \simeq \delta_2 \ = \phi_i - \phi_0 = \alpha h_i{}^2, \tag{7.8}$$

$$\epsilon_\phi \simeq \delta_{12} = \phi_i - \phi_0 = \alpha_1 h_i + \alpha_2 h_i{}^2, \tag{7.9}$$

where δ_1, δ_2 and δ_{12} are alternative estimators of the discretization error; and α, α_1 and α_2 are constants. These three alternatives are only used when the error estimation with Equation (7.6) is found impossible or deemed unreliable. The procedure for selecting a reliable error estimator is discussed in Subsection 7.3.3.

Non-weighted least-squares minimizations and weighted least-squares minimizations are used to fit the four error estimators to the dataset. The standard deviations of these least-squares fits provide good information on the quality of the four error estimators; a low standard deviation implies good agreement of the data with the fit of the error estimator, and hence, it implies a reasonable estimate of the discretization error. The weighted least-squares minimization makes it possible to express more confidence in the results computed on the finer grids than in the results computed on the coarser grids. This is very desirable, since the best result — smallest discretization error — is expected on the finest grid.

The non-weighted least-squares minimization and the weighted least-squares minimization for error estimator δ_{RE} can be determined from the minimums of

$$S_{RE}(\phi_0, \alpha, p) = \sqrt{\sum_{i=1}^{n_g} \left(\phi_i - (\phi_0 + \alpha h_i{}^p) \right)^2}, \tag{7.10a}$$

$$S_{RE}^W(\phi_0, \alpha, p) = \sqrt{\sum_{i=1}^{n_g} w_i \left(\phi_i - (\phi_0 + \alpha h_i{}^p) \right)^2}, \tag{7.10b}$$

respectively, where n_g is the number of grids in the dataset, and w_i are the weights defined by

$$w_i = \frac{1/h_i}{\sum_{i=1}^{n_g} 1/h_i}. \tag{7.11}$$

The sum of the weights is equal to one. The minimums of Equations (7.10a) and (7.10b) can be obtained from

$$\frac{\partial S}{\partial \phi_0} = 0, \qquad \frac{\partial S}{\partial \alpha} = 0, \qquad \frac{\partial S}{\partial p} = 0, \tag{7.12}$$

where S stands for either S_{RE} or S_{RE}^W. This least-squares minimization leads to a system of non-linear equations for ϕ_0, α, and p. For error estimators (7.7), (7.8) and (7.9), similar least-squares minimizations can be derived. These minimizations lead to systems of linear equations. For a complete description of all the least-squares minimizations and the corresponding systems of equations, the reader is

referred to Eça and Hoekstra [9].

The standard deviations of the non-weighted least-squares minimization and the weighted least-squares minimization for error estimator (7.6) are given by

$$\sigma_{RE} = \sqrt{\frac{\sum\limits_{i=1}^{n_g}\left(\phi_i - (\phi_0 + \alpha h_i{}^p)\right)^2}{n_g - 3}}, \qquad \sigma_{RE}^{W} = \sqrt{\frac{\sum\limits_{i=1}^{n_g} n_g w_i\left(\phi_i - (\phi_0 + \alpha h_i{}^p)\right)^2}{n_g - 3}}, \qquad (7.13)$$

respectively. For the other three error estimators, similar standard deviations can be derived. The standard deviations are used to asses the quality of the four different error estimators.

7.3.3. Procedure for error estimation

The procedure for the estimation of the discretization error proposed by Eça and Hoekstra [9] is summarized in this subsection. The procedure starts with determining the error estimator δ_{RE} with the non-weighted least-squares minimization and the weighted least-squares minimization. Based on the observed order of grid convergence, p, and the standard deviations of both fits, the following steps are used to obtain the best estimate of the discretization error:

1. If for one of the two fits $0.5 \leq p \leq 2$, then that particular fit is used for the estimation of the error. If both fits satisfy this constraint on the observed order of grid convergence, then the fit with the smallest standard deviation is the best estimate of the discretization error. If this step is inconclusive, steps 2 and 3 are used.
2. If for one of the two fits $p > 2$, then the non-weighted and weighted least-squares minimizations of δ_1 and δ_2 are solved and the standard deviations of the four fits is determined. The error estimate is obtained from the fit with the smallest standard deviation.
3. If the order of grid convergence is impossible to establish for both fits of δ_{RE} or for one of the two fits of δ_{RE} the observed order of grid convergence satisfies $p < 0.5$, the non-weighted and weighted least-squares minimizations of δ_1, δ_2 and δ_{12} are solved and the standard deviations of the resulting six fits are determined. The error estimate is obtained from the fit with the smallest standard deviation.

For a second-order accurate discretization method, the constraint on the observed order of grid convergence, $0.5 \leq p \leq 2$, is empirically defined as an acceptable range by Eça and Hoekstra [9].

The finite-volume discretization methods used on the three-dimensional unstructured meshes in the FINE™/Marine flow solver are limited to third-order accuracy for the turbulence equations and the momentum equations, and to second-order accuracy for the volume fraction equation. Probably, they produce an order between one and two due to the various combinations of the first-order accurate upwind and downwind differencing schemes, the second-order central differencing scheme and the third-order QUICK scheme, used for the discretization of these equations. Hence, the constraint on the observed order of grid convergence, $0.5 \leq p \leq 2$, empirically defined by Eça and Hoekstra, is applicable to the present grid refinement study.

7.4. Discretization uncertainty estimation

Following Roache [43,44], the ITTC [15], and Eça and Hoekstra [9], the discretization uncertainty is estimated as the absolute value of the discretization error estimator multiplied by a factor of safety. Following the Grid Convergence Index (GCI) procedure from Roache [43,44], the safety factor F_S is either 1.25 if the error estimate is deemed to be reliable, or 3 otherwise. In the Eça and Hoekstra procedure, the reliability of an error estimator is assessed with its standard deviation, σ, and the data range parameter,

$$\Delta_\phi = \frac{\max(\phi_i) - \min(\phi_i)}{n_g - 1}. \qquad (7.14)$$

The error estimator is deemed to be reliable if the observed order of convergence is in the acceptable range and the standard deviation is smaller than the data range parameter; i.e. if $0.5 \leq p \leq 2$ and

$\sigma < \Delta_\phi$, then $F_S = 1.25$. Else the larger safety factor, $F_S = 3$, is adopted to express the lower confidence in the dataset and the least-squares fit.

Eça and Hoekstra [9] use a slightly different expression to estimate the discretization uncertainty than the absolute value of the discretization error estimator ϵ_ϕ multiplied by a factor of safety as used in the GCI procedure. Eça and Hoekstra add two additional terms to the expression of the discretization uncertainty estimator from the GCI procedure, namely, the standard deviation of the fit and the absolute difference between the value of the real data point and its value estimated with the least-squares fit. These two terms are added to deal with possible scatter in the dataset and to give a more reliable uncertainty estimate. Without any scatter in the dataset, this approach reduces to the GCI procedure.

For any ϕ_i from the dataset, i.e. for every grid i in the dataset, the discretization uncertainty can be estimated with

$$U_\phi(\phi_i) = \begin{cases} F_S \epsilon_\phi(\phi_i) + \sigma + |\phi_i - \phi_{LS}| & \text{for } \sigma < \Delta_\phi \\ 3\frac{\sigma}{\Delta_\phi}\big(\epsilon_\phi(\phi_i) + \sigma + |\phi_i - \phi_{LS}|\big) & \text{for } \sigma \geq \Delta_\phi \end{cases}, \tag{7.15}$$

where U_ϕ is the estimate of the discretization uncertainty, ϕ_{LS} is the discrete value of the least-squares fit corresponding to ϕ_i, and

$$F_S = \begin{cases} 1.25 & \text{for } 0.5 \leq p \leq 2 \\ 3 & \text{otherwise} \end{cases}. \tag{7.16}$$

Note that U_ϕ and ϵ_ϕ are both functions of ϕ_i. This formulation of the discretization uncertainty, as formulated by Eça and Hoekstra [9], defines another category of grid quality, namely, one for fits with $\sigma \geq \Delta_\phi$. The error estimators of these fits are deemed to have a poor reliability. Therefore, a safety factor larger than three that depends on the ratio of the standard deviation to the data range parameter, is adopted.

The estimate of the discretization uncertainty, U_ϕ, is meant to provide a 95-percent confidence interval about the exact solution, according to

$$\phi_i - U_\phi \leq \phi_{exact} \leq \phi_i + U_\phi, \tag{7.17}$$

where ϕ_{exact} is the exact solution; i.e. the discretization uncertainty provides an interval about the exact solution having a confidence level of 95 percent.

7.5. Discretization uncertainty and solving ship motions

As discussed in Section 6.5, the quasi-static approach is used to obtain the equilibrium position of a ship in a simulation. With this approach, ship motions are imposed rather than solved. There is no direct coupling between the motion equations and the governing equations. This uncoupling greatly reduces computation time. However, this uncoupling may contaminate the estimation of the numerical uncertainty with grid refinement studies, because the motions are not directly coupled to the computational grid, but they still influence the solution. The influence of the motions on the solution might be erratic due to this uncoupling.

The uncoupling of motion solving from the grid-dependent governing equations results in questionable dependency of the motions on the grid refinement. This may lead to unwanted scatter in the dataset. This scatter can result in unexpected or strange order of convergence and unreliable uncertainty estimates. The scatter in flow quantities between the grids can also be the result of a decrease in geometric similarity between the grids due to ship motions. Different ship motions between the various grids are likely to occur due to slight differences in flow quantities. Since a weighted deformation method is used to translate the rigid-body motion into deformation of the grid cells, these different motions lead to different mesh deformations, which contribute to the loss of geometric similarity between the grids. Furthermore, the difference in resistance between the grids results in different trimming moments of the driving force. These different moments are likely to increase the scatter in flow quantities between the grids, because they influence the trim, the sinkage and the computed resistance, and

thereby influencing themselves again, leading to a virtuous circle.

To accurately and reliably establish the observed order of grid convergence and the numerical uncertainty of the governing equations, two cases are investigated: one excluding motion solving and thereby excluding the trimming moment of the driving force, and one including motion solving and thereby including the trimming moment of the driving force. The numerical uncertainty is determined for Sysser 85 on the low-speed grid at Froude number 0.45 and on the high-speed grid at Froude number 0.85, including and excluding the influence of motion solving. No trimming moment of the crew's weight is applied, i.e. the crew CoG position is used. The case of excluding motion solving is discussed in the following section. The case of including motion solving is discussed in Section 7.7. A comparison between both cases is given in Section 7.8.

7.6. Numerical uncertainty excluding solving ship motions

The numerical uncertainty of the computed resistance, excluding the influence of solving ship motions, is determined in this section. On all the grids, the heave and the pitch are fixed at the values computed on the medium grid for the crew CoG position. The influence of the trimming moment of the driving force on the resistance is thereby excluded. The results of the grid refinement study, excluding the influence of motion solving, are depicted in Figure 7.2. For Froude numbers 0.45 and 0.85, the computed resistance, the least-squares fit of the error estimator and the uncertainty intervals are plotted as function of the typical cell size, h_i. Plots of the discretization error, as function of the typical cell size, are also given. The discretization uncertainty for the medium grid and the finest grid, the estimated exact solution and the observed order of grid convergence are listed in Table 7.3a. The properties of the fits and the dataset are given in Table 7.3b.

For Froude number 0.45, error estimator δ_1, Equation (7.7), is found to be the best estimator of the discretization error, and hence, the observed order of grid convergence is set to 1. According to the Eça and Hoekstra procedure discussed in Section 7.4, a safety factor of 3 should now be chosen for this error estimate. However, the fixed order of 1 is very close to the observed order of grid convergence at Froude number 0.85. Therefore, the error estimator δ_1 is deemed to be reliable in this case. Hence, following the GCI procedure of Roache [43,44], the safety factor is chosen as 1.25 at Froude number 0.45.

The weighted least-squares fit of δ_1 yields an accurate fit with a coefficient of determination R^2, defined by Equation (10.6), of 0.976 and a standard deviation of 4.49 millinewton, which is only 0.54‰ of the estimated exact solution. The relative discretization uncertainties are 3.55% and 1.76% for the medium grid and the finest grid, respectively.

For Froude number 0.85, error estimator δ_{RE}, Equation (7.6), is found to be the best estimator of the discretization error. The observed order of grid convergence is 1.1. An order of accuracy close to one was to be expected based on the various combinations of first-order, second-order and third-order accurate schemes used for the discretization of the turbulence equations, the momentum equations and the volume fraction equation. The weighted least-squares fit of δ_{RE} provides an excellent fit with a coefficient of determination of 0.997 and a standard deviation of 9.38 millinewton, which is only 0.34‰ of the estimated exact solution. The relative discretization uncertainties are 1.84% and 0.93% for the medium grid and the finest grid, respectively.

Since it is assumed that the round-off errors and the iterative errors are negligible compared to the discretization error, the numerical uncertainty consist solely of the discretization uncertainty. Therefore, the numerical uncertainties for the medium grid are 3.55% and 1.84% at Froude numbers 0.45 and 0.85, respectively. These uncertainties are used in the validation analysis discussed in Chapter 9. The numerical uncertainty is higher at Froude number 0.45 than at Froude number 0.85 as a result of the larger scatter in the data at the lower Froude number and the different error estimator used.

Table 7.3: Numerical uncertainty for Sysser 85 at Froude numbers 0.45 and 0.85, excluding the influence of motion solving.

(a) Discretization errors and uncertainties for the finest grid, denoted by subscript 1, and the medium grid, denoted subscript 4.

Fn [−]	p [−]	ϕ_0 [N]	ϵ_{ϕ_1} [N]	U_{ϕ_1} [N]	U_{ϕ_1} [%ϕ_1]	ϕ_4 [N]	ϵ_{ϕ_4} [N]	U_{ϕ_4} [N]	U_{ϕ_4} [%ϕ_4]
0.45	1	8.2623	0.1090	0.1470	1.76	8.4926	0.2303	0.3011	3.55
0.85	1.10	27.9018	0.2020	0.2624	0.93	28.3055	0.4037	0.5205	1.84

(b) Properties of the weighted least-squares fits and the dataset.

Fn [−]	Error estimator	R [−]	σ [mN]	R^2 [−]	Δ_ϕ [mN]	F_S [−]
0.45	δ_1	1.3	4.49	0.976	39.0	1.25
0.85	δ_{RE}	0.59	9.38	0.997	83.9	1.25

7.7. Numerical uncertainty including solving ship motions

The numerical uncertainty of the computed resistance, including the influence of solving ship motions, is determined in this section. The heave and the pitch are solved with the quasi-static approach. The trimming moment of the driving force is included in the simulations. The results of the grid refinement study, including the influence of motion solving, is depicted in Figure 7.2. For Froude numbers 0.45 and 0.85, the computed resistance, the least-squares fit of the error estimator and the uncertainty intervals are plotted as function of the typical cell size, h_i. Plots of the discretization error, as function of the typical cell size, are also given. The discretization uncertainty for the medium grid and the finest grid, the estimated exact solution and the observed order of grid convergence are listed in Table 7.4a. The properties of the fits and the dataset are given in Table 7.4b.

For Froude number 0.45, error estimator δ_1, Equation (7.7), is found to be the best estimator of the discretization error, and hence, the observed order of grid convergence is set to 1. According to the Eça and Hoekstra procedure, a safety factor of 3 should now be chosen for this error estimate. However, the fixed order of 1 is very close to the observed order of grid convergence for Froude number 0.85. Therefore, the error estimator δ_1 is deemed to be reliable in this case. Hence, following the GCI procedure, the safety factor is chosen as 1.25 at Froude number 0.45.

The weighted least-squares fit of δ_1 yields an accurate fit with a coefficient of determination of 0.964 and a standard deviation of 5.26 millinewton, which is only 0.64‰ of the estimated exact solution. The relative discretization uncertainties are 3.50% and 1.71% for the medium grid and the finest grid, respectively.

For Froude number 0.85, error estimator δ_{RE}, Equation (7.6), is found to be the best estimator of the discretization error. The observed order of grid convergence is 1.25. An order of accuracy close to one was to be expected. The weighted least-squares fit of δ_{RE} provides an excellent fit with a coefficient of determination of 0.996 and a standard deviation of 11.6 millinewton, which is only 0.41‰ of the estimated exact solution. The relative discretization uncertainties are 1.67% and 0.79% for the medium grid and the finest grid, respectively.

The heave and the pitch computed on the different grids are plotted in Figure 7.4. The pitch angle at both speeds follows more or less a linear grid convergence while the heave has a random distribution. The differences in pitch and in heave between the grids are very small. The computed flow field around the ship determines the resultant forces and moments acting on the ship. These forces and moments are used in the quasi-static motion-solving approach to impose ship motions. Slight differences between the flow fields of the various grids lead to minimally different motions. The influence of the minimal difference in motions on the computed resistance is very limited in this case, as a comparison of the computed resistance, excluding motion solving, and the computed resistance, including motion solving, illustrates.

Since it is assumed that the round-off errors and the iterative errors are negligible compared to the discretization error, the numerical uncertainty consist solely of the discretization uncertainty. Therefore, the numerical uncertainties for the medium grid are 3.50% and 1.67% at Froude numbers 0.45 and 0.85, respectively. These uncertainties are used in the validation analysis discussed in Chapter 9. The numerical uncertainty is higher at Froude number 0.45 than at Froude number 0.85 as a result of the larger scatter in the data at the lower Froude number and the different error estimator used.

Table 7.4: Numerical uncertainty for Sysser 85 at Froude numbers 0.45 and 0.85, including the influence of motion solving.

(a) Discretization errors and uncertainties for the finest grid, denoted by subscript 1, and the medium grid, denoted subscript 4.

Fn $[-]$	p $[-]$	ϕ_0 $[N]$	ϵ_{ϕ_1} $[N]$	U_{ϕ_1} $[N]$	U_{ϕ_1} $[\%\phi_1]$	ϕ_4 $[N]$	ϵ_{ϕ_4} $[N]$	U_{ϕ_4} $[N]$	U_{ϕ_4} $[\%\phi_4]$
0.45	1	8.2675	0.1045	0.1429	1.71	8.4928	0.2253	0.2976	3.50
0.85	1.25	27.9598	0.1673	0.2220	0.79	28.3251	0.3653	0.4741	1.67

(b) Properties of the weighted least-squares fits and the dataset.

Fn $[-]$	Error estimator	R $[-]$	σ $[mN]$	R^2 $[-]$	Δ_ϕ $[mN]$	F_S $[-]$
0.45	δ_1	1.6	5.26	0.964	37.3	1.25
0.85	δ_{RE}	0.57	11.6	0.996	84.1	1.25

7.8. Comparison of both cases

The results of the two refinement studies, excluding and including the influence of solving ship motions, are surprisingly similar. The relative comparison error of the estimated exact solution between both cases is 0.63‰ and 2.1‰ for Froude numbers 0.45 and 0.85, respectively. The observed order of grid convergence, the least-squares fits of the error estimators, the discretization errors and the numerical uncertainties are also very similar. This small difference is illustrated in Figure 7.5 by a comparison of the discretization errors including and excluding the influence of motion solving. The results of both cases are used in the validation analysis, discussed in Chapter 9.

The trim and the sinkage are not significantly affected by grid refinement. This contributes to a limited influence of the trimming moment of the driving force on the uncertainty estimation.
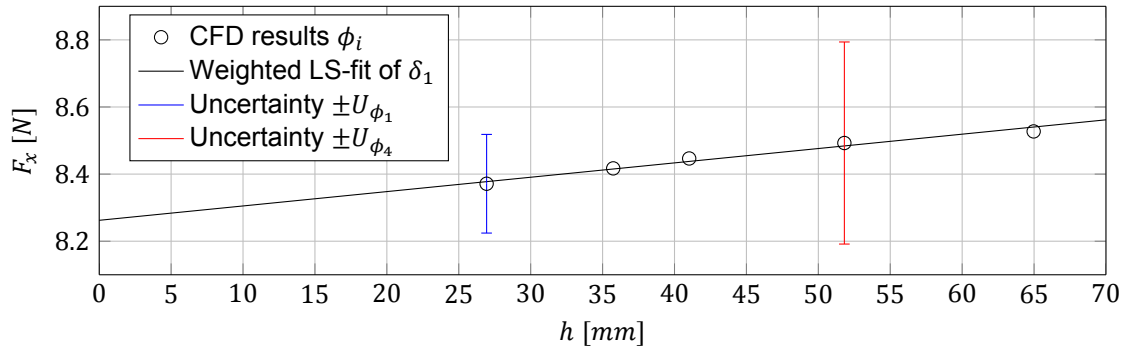
(a) The computed resistance, the weighted least-squares fit of error estimator δ_1, and the uncertainty intervals at $Fn = 0.45$.
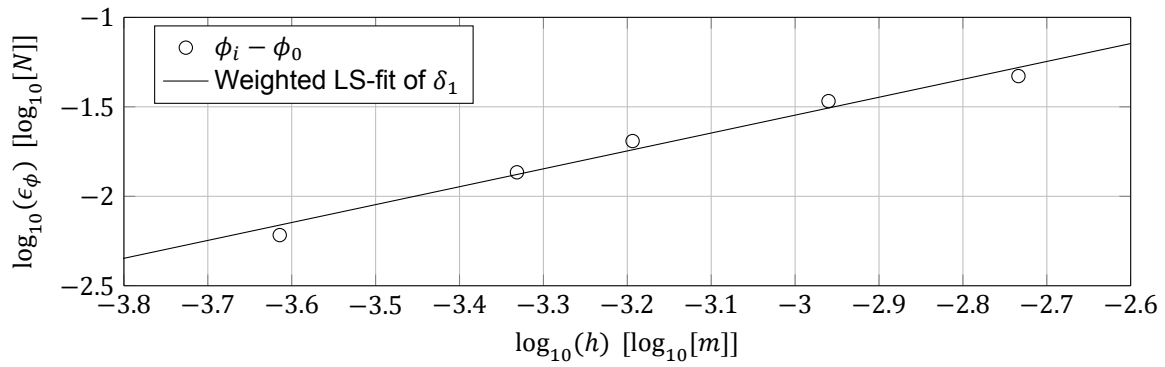
(b) The discretization error at $Fn = 0.45$, obtained with the weighted least-squares fit of error estimator δ_1.
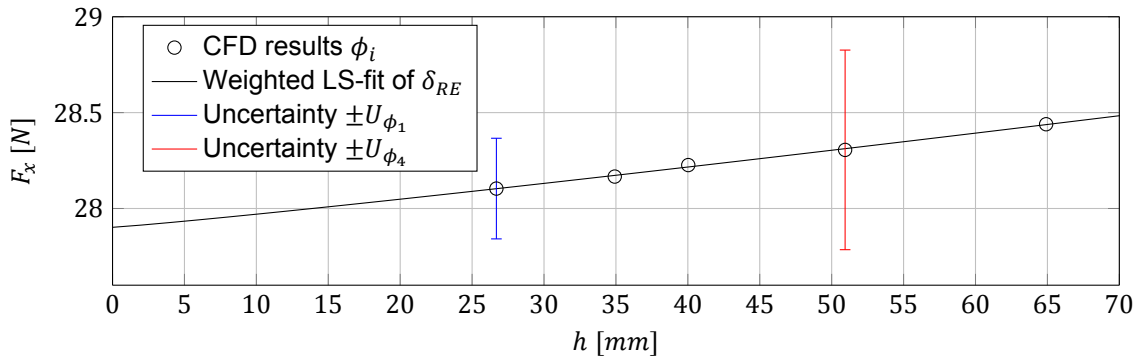
(c) The computed resistance, the weighted least-squares fit of error estimator δ_{RE}, and the uncertainty intervals at $Fn = 0.85$.
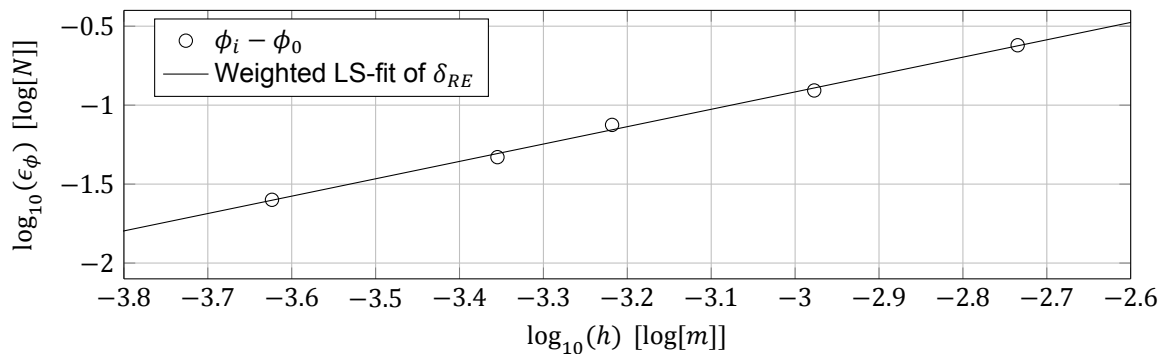
(d) The discretization error at $Fn = 0.85$, obtained with the weighted least-squares fit of error estimator δ_{RE}.

Figure 7.2: Results of the grid refinement study for Sysser 85 at Froude numbers 0.45 and 0.85, excluding the influence of motion solving.

(a) The computed resistance, the weighted least-squares fit of error estimator δ_1, and the uncertainty intervals at $Fn = 0.45$.
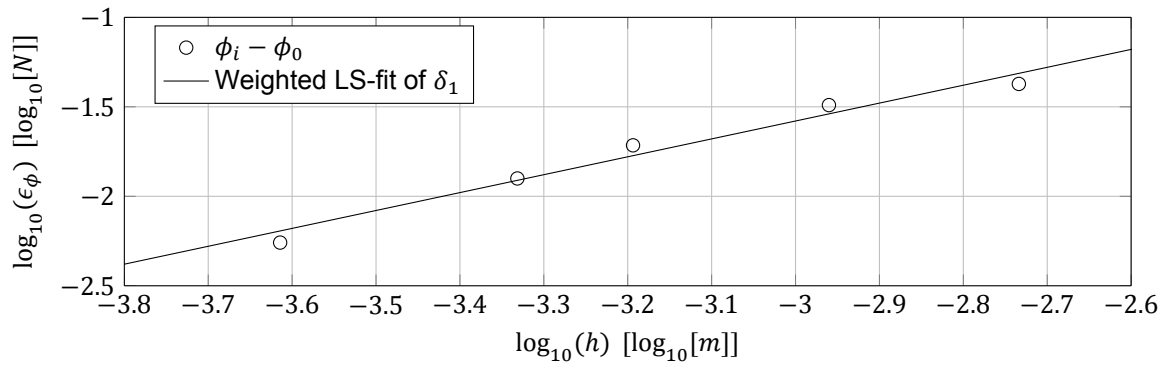
(b) The discretization error at $Fn = 0.45$, obtained with the weighted least-squares fit of error estimator δ_1.
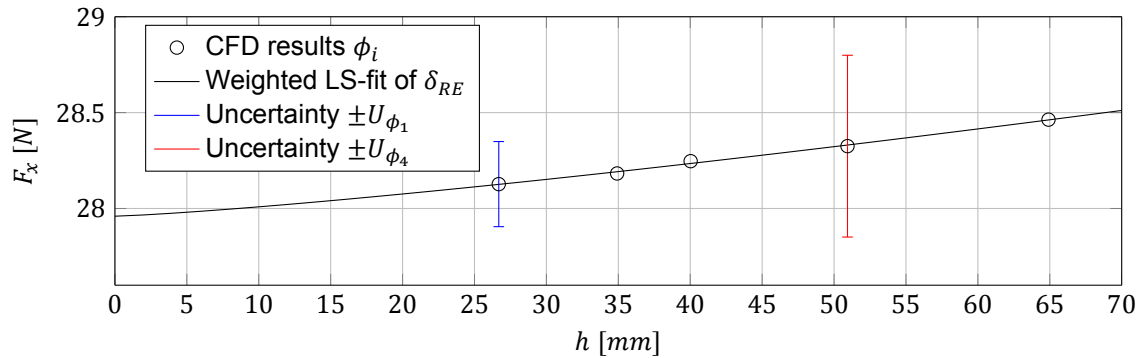
(c) The computed resistance, the weighted least-squares fit of error estimator δ_{RE}, and the uncertainty intervals at $Fn = 0.85$.
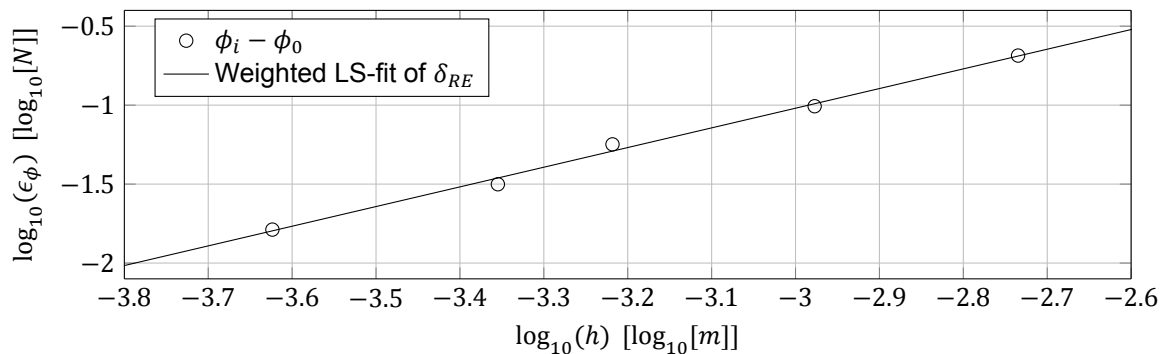
(d) The discretization error at $Fn = 0.85$, obtained with the weighted least-squares fit of error estimator δ_{RE}.

Figure 7.3: Results of the grid refinement study for Sysser 85 at Froude numbers 0.45 and 0.85, including the influence of motion solving.
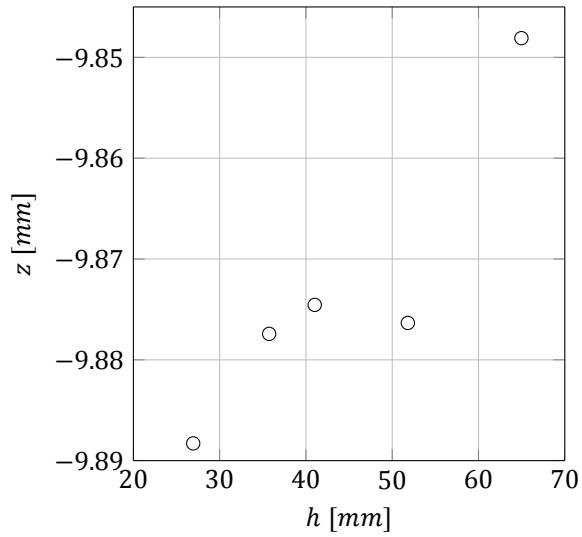
(a) Heave at $Fn = 0.45$.
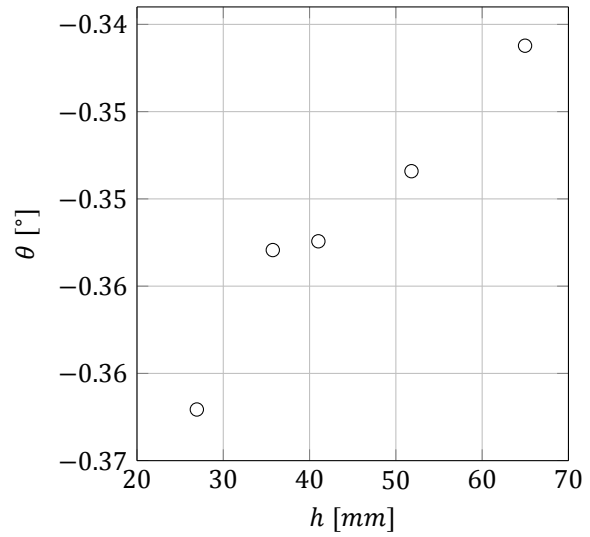
(b) Pitch at $Fn = 0.45$.
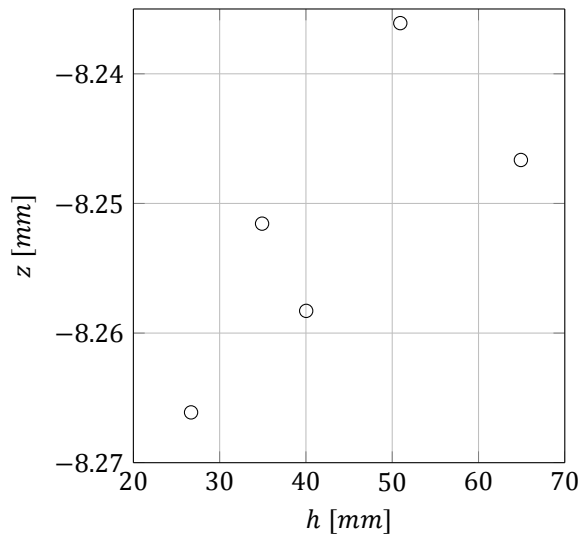
(c) Heave at $Fn = 0.85$.
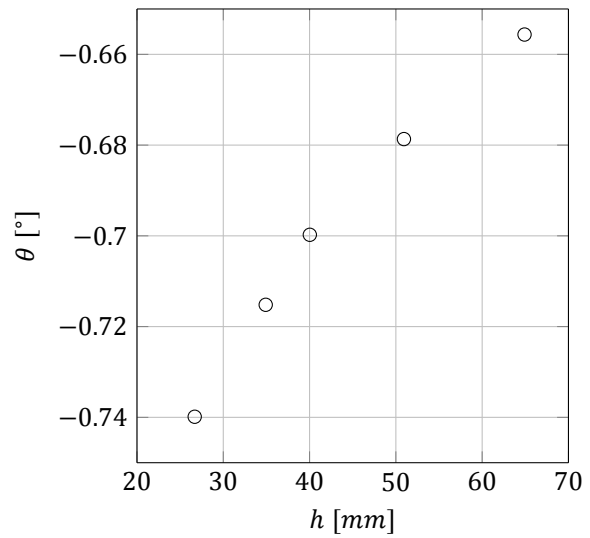
(d) Pitch at $Fn = 0.85$.

Figure 7.4: Heave and pitch for Sysser 85 at Froude numbers 0.45 and 0.85, computed on the different grids.
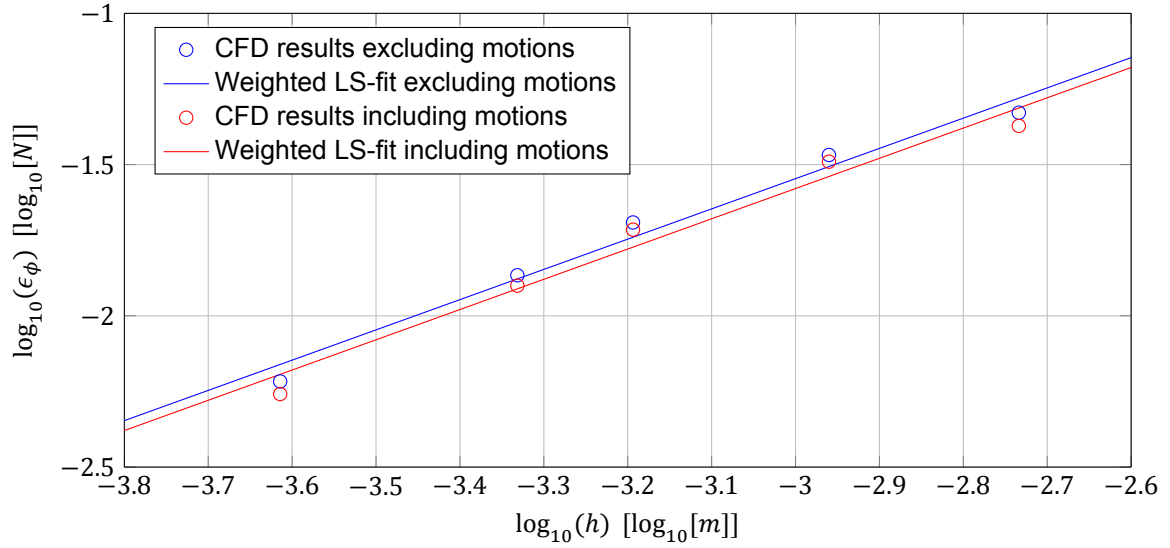
(a) Weighted least-squares fits of error estimator δ_1 at Froude number 0.45.
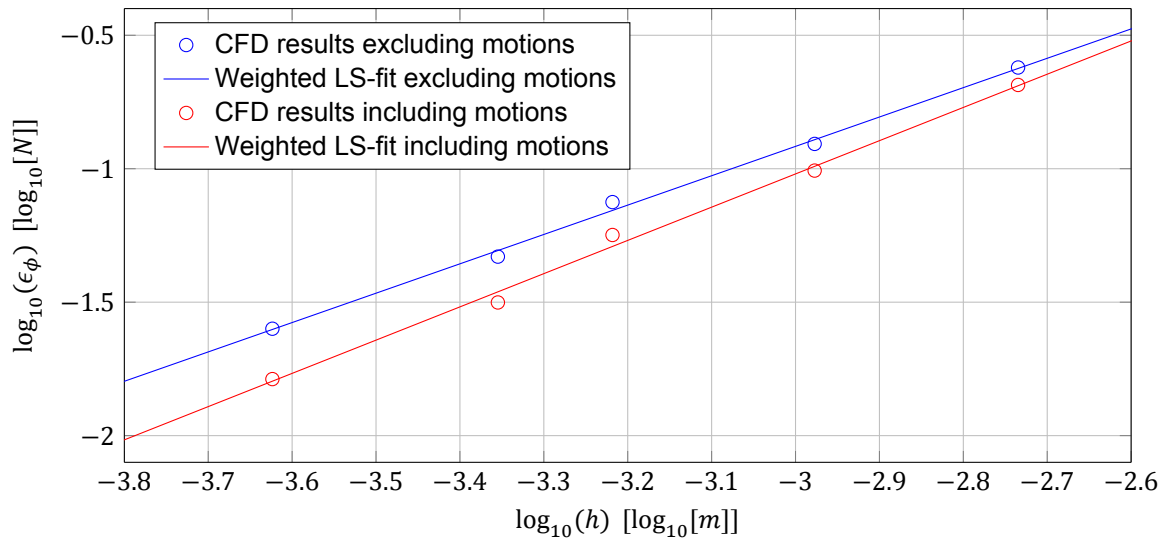
(b) Weighted least-squares fits of error estimator δ_{RE} at Froude number 0.85.

Figure 7.5: The discretization error, excluding and including the influence of solving ship motions.

8
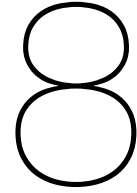
Experimental results

Experimental resistance measurements were conducted for validation of the numerical results. The parent model of the new systematic series, Sysser 85, was tested in the #1 towing tank of the Ship Hydromechanics Laboratory at the Delft University of Technology for various speeds and applied trimming moments. These resistance measurements for Sysser 85 were conducted according to the numerical test conditions. These measurements are not a part of this MSc thesis. They were conducted by the author as part of an additional thesis. The resistance measurements are thoroughly described by the author in [31]. For the sake of completeness, the experimental results and the experimental uncertainties, given in [31], are summarized in this chapter. The experimental results are presented in Section 8.1. The experimental uncertainties are given in Section 8.2.

The main objective of these resistance tests was to determine the upright trimmed resistance of the bare hull for the same test conditions as used for the numerical simulations. The upright trimmed resistance of Sysser 85 was measured for the crew CoG position at Froude numbers 0.25 up to 0.85 with increments of 0.10. For the crew back position, this resistance was measured at Froude numbers 0.25 up to 0.95 with increments of 0.10.

Sysser 85 was tested in the #1 towing tank of the Ship Hydromechanics Laboratory at the Delft University of Technology. This towing tank has a length of 142 metres, a width of 4.22 metres and a maximum water depth of 2.5 metres. For these experiments, a model with a waterline length of two metres was used. This waterline length is also used in the numerical computations to ensure a one-to-one comparison between the experimental results and the numerical results. This eliminates scale effects from the validation. The main dimensions of Sysser 85 at model scale are listed in Table 8.1.

A picture of the measurement set-up that was used for the resistance measurements is shown in Figure 8.1. The model was attached to the towing carriage by two balance arms at even positions fore and aft of the longitudinal position of the centre of gravity of the model. The balance arms allow the model to be free in heave, roll and pitch. The resistance of the model through the water was determined by measuring a horizontal tow force. The longitudinal trimming moment of the driving force and the crew's weight was exerted on the model by changing the longitudinal centre of gravity of the model prior to a measurement run with a longitudinally shiftable weight. Three iteration runs were carried out at each speed, in order to apply the right trimming moment corresponding to the measured resistance, i.e. to obtain a centre of effort (CoE) height of $0.60L_{WL}$ in the measurement run, and to satisfy Equation (4.5). All the final measurement runs satisfy $0.585L_{WL} \leq z_{CoE} \leq 0.60L_{WL}$. For the details of the measurement set-up and the measurement procedure used during the resistance measurements for Sysser 85, the reader is referred to Kleijweg [31].

Table 8.1: Main dimensions of the Sysser 85 model
used for the resistance measurements.

L_{WL}	$[m]$	2.000
B_{WL}	$[m]$	0.4094
T_c	$[m]$	0.0592
Δ_c	$[kg]$	17.98
LCB_{fp}	$[m]$	1.077
LCG_{fp}	$[m]$	1.077
S_c	$[m^2]$	0.5996
A_X	$[m^2]$	0.01657
α	$[-]$	5.00

Figure 8.1: A picture of the measurement set-up that was used for the resistance measurements. Figure from Kleijweg [31].

8.1. Experimental results

The bare hull upright trimmed resistance of Sysser 85 for the crew CoG and back positions, and corresponding heave, pitch and height of the CoE above the waterline are listed in Table 8.2. The given z_{CoE} is the height of the centre of effort simulated during the measurement of that particular resistance value. The upright trimmed resistance of Sysser 85 is plotted for the two crew positions in Figure 8.2. The resistance, heave and pitch curves and the differences between the two crew positions are very similar to those of the numerical results, shown in Figure 6.3. The upright untrimmed resistance of Sysser 85 is given in Table 8.3. The upright untrimmed resistance is also used in the validation analysis.

Table 8.2: The bare hull upright trimmed resistance of Sysser 85 for the crew CoG and back positions, determined by Kleijweg [31] with the experimental method.

Fn	Crew CoG				Crew back			
	R_t	z	θ	z_{CoE}	R_t	z	θ	z_{CoE}
$[-]$	$[N]$	$[mm]$	$[°]$	$[m]$	$[N]$	$[mm]$	$[°]$	$[m]$
0.25	1.75	-2.0	0.15	1.20	1.85	-0.62	-0.75	1.19
0.35	3.80	-5.4	0.26	1.17	4.13	-3.5	-0.81	1.18
0.45	8.91	-10.7	-0.28	1.20	8.92	-6.8	-1.41	1.18
0.55	14.31	-11.6	-0.90	1.19	14.08	-6.6	-1.96	1.19
0.65	19.41	-9.4	-1.26	1.18	19.01	-3.8	-2.27	1.18
0.75	24.51	-6.4	-1.14	1.17	23.27	-0.49	-2.17	1.18
0.85	30.56	-6.6	-0.72	1.18	28.25	-0.14	-1.92	1.18
0.95					35.64	-3.8	-1.66	1.18

Table 8.3: The bare hull upright untrimmed resistance of Sysser 85, determined by Kleijweg [31] with the experimental method.

Fn	R_t	z	θ
$[-]$	$[N]$	$[mm]$	$[°]$
0.25	1.80	-2.0	0.08
0.35	3.96	-5.1	0.02
0.45	8.97	-8.9	-0.85
0.55	14.12	-8.0	-1.73
0.65	19.08	-3.8	-2.31
0.75	23.11	0.75	-2.38

8.2. Experimental uncertainty

The reliability and the accuracy of the resistance measurements were assessed as well by Kleijweg [31]. The experimental uncertainties were determined for the measured resistance at Froude numbers 0.45 and 0.85 for the crew CoG position. These are also the conditions for which the numerical uncertainty was assessed in the previous chapter. The experimental uncertainties are briefly summarized below.

The uncertainty of the resistance measurements was determined, by Kleijweg [31], by following the ITTC recommended procedures and guidelines for uncertainty analysis in experimental hydrodynamics and resistance tests [19,20,21,22]. These recommended procedures and guidelines are based on the *Guide to the expression of uncertainty in measurement* [23] of the Joint Committee for Guides in Metrology (JCGM). Following these guidelines, uncertainties were classified into three categories: standard uncertainty, combined standard uncertainty and expanded uncertainty. Standard uncertainties cover all the possible elementary sources of experimental uncertainties like, for instance, repeatability, instrument calibration and environmental parameters.

Based on the ITTC [19,20,21,22], the following eight sources of standard uncertainties were identified and assessed for these resistance measurements: data acquisition, load cell calibration, repeata-
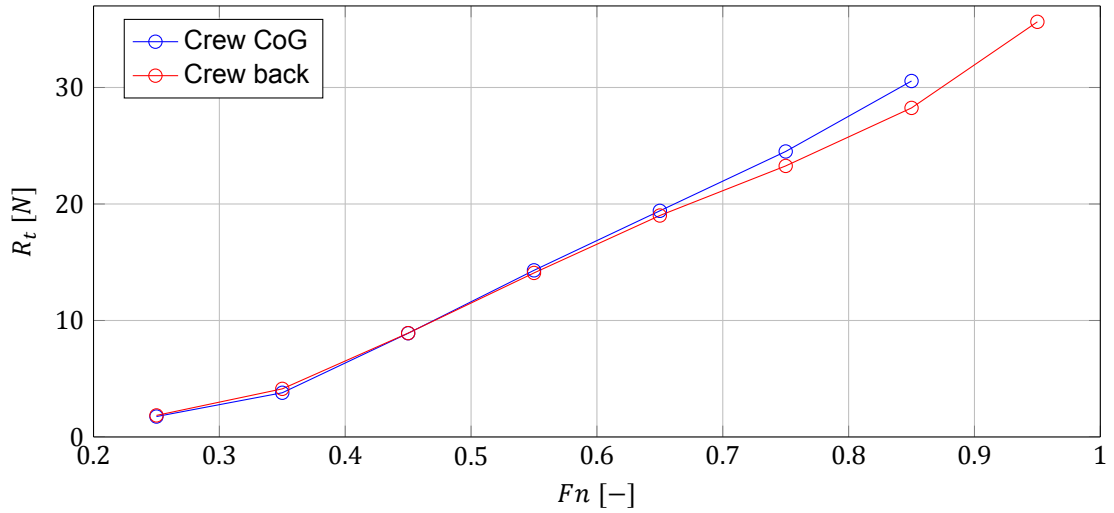
(a) Bare hull upright trimmed resistance for the crew CoG and back positions.
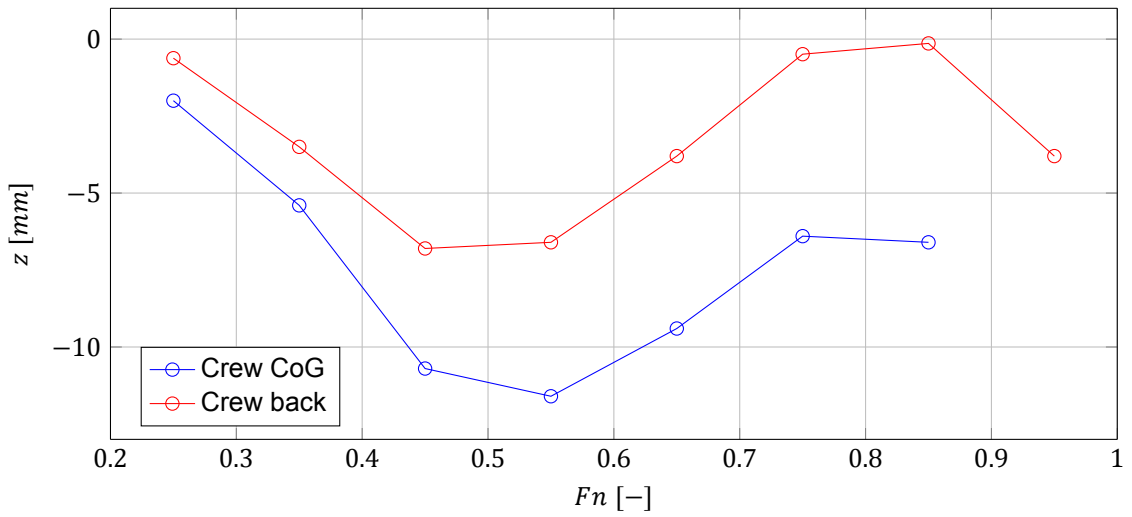
(b) Heave for the crew CoG and back positions.
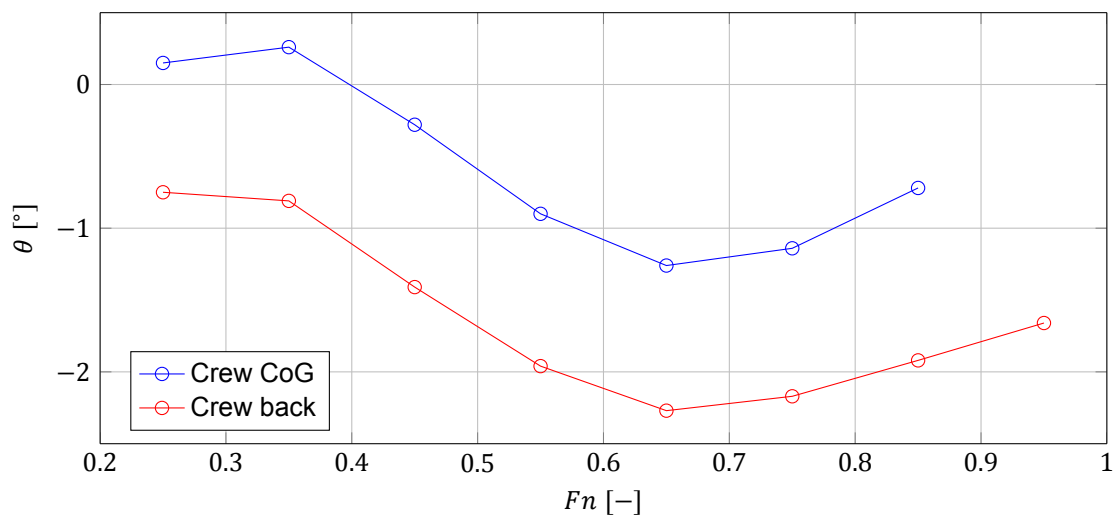
(c) Pitch for the crew CoG and back positions.

Figure 8.2: Experimental results of Sysser 85, determined by Kleijweg [31].

bility of the tests, the water temperature, ballasting of the model, the tow speed, the resistance of the turbulence-stimulating strips, and the trimming moment. The standard uncertainties and the estimated values at Froude numbers 0.45 and 0.85 for the crew CoG position are summarized in Table 8.5. The dominant standard uncertainties are related to the load cell calibration, the turbulence stimulators and the applied trimming moment. For a thorough discussion of the uncertainty components and their assessment, the reader is referred to Kleijweg [31].

All the standard uncertainties can be joined into one combined standard uncertainty. The combined standard uncertainty, u_c, is obtained with the root-sum-squares method as follows:

$$u_c(\bar{r}) = \sqrt{\sum_{i=1}^{8} u_i^2},$$

(8.1)

where u_i are the standard uncertainties, given in Table 8.5. At Froude numbers 0.45 and 0.85, the relative combined standard uncertainties are equal to 3.16 percent and 1.97 percent, respectively.

To asses the uncertainty of a measurement result, the combined standard uncertainty can be expanded to the expanded uncertainty, U_R, with

$$U_R = k u_c(\bar{r}),$$

(8.2)

where k is a coverage factor. The expanded uncertainty is meant to provide an interval about the exact solution with a level of confidence of 95 percent, according to

$$\bar{r} - U_R \leq R \leq \bar{r} + U_R,$$

(8.3)

where R is the exact solution, and $\bar{r}$ is the best estimate of the measurand — quantity intended to be measured — obtained from the average of the multiple measurement readings of the repeat tests.

According to the ITTC [21], a level of confidence of 95 percent is commonly used in experimental hydromechanics. This confidence level was also used for the numerical uncertainty determined in Chapter 7. To provide such an interval about the measurement result, an appropriate coverage factor has to be chosen. Based on the recommendations of the ITTC [21] and the JCGM [23], a coverage factor of 2.23 was used. The relative expanded uncertainty at Froude numbers 0.45 and 0.85 is equal to 7.04 percent and 4.38 percent, respectively. The experimental uncertainties of the resistance measurements for Sysser 85 at Froude numbers 0.45 and 0.85 for the crew CoG position are summarized in Table 8.5. The best estimate of the measurand is also given.

Table 8.4: Standard uncertainties of the resistance measurements for Sysser 85 at Froude numbers 0.45 and 0.85 for the crew CoG position, determined by Kleijweg [31]. These standard uncertainties were used to determine the relative combined standard uncertainty u_c and the relative expanded uncertainty U_R, given in Table 8.5.

Source	Uncertainty component	$Fn = 0.45$ u_i [%$\bar{r}$]	$Fn = 0.85$ u_i [%$\bar{r}$]
Data acquisition	Averaging signals	0.0677	0.194
Load cell	Calibration	2.60	0.769
Repeat tests	Repeatability	0.191	0.0890
Temperature	Viscosity	0.0959	0.0841
Ballasting	Wetted surface	0.107	0.107
Tow speed	Dynamic pressure	0.0502	0.0266
Turbulence stimulator	Resistance strips	0.854	0.898
Trimming moment	CoE height	1.55	1.55

Table 8.5: Uncertainty of the resistance measurements for Sysser 85 at Froude numbers 0.45 and 0.85 for the crew CoG position, determined by Kleijweg [31]. $R_t = \bar{r} - R_{t_{strip}}$, where $R_{t_{strip}}$ is the resistance of the turbulence-stimulating strips.

Fn [−]	$\bar{r}$ [N]	u_c [%$\bar{r}$]	k [−]	U_R [%$\bar{r}$]	U_R [N]	R_t [N]
0.45	9.4290	3.16	2.23	7.04	0.6635	8.9417
0.85	31.8458	1.97	2.23	4.38	1.3962	30.1072

9

Validation

To establish the reliability and the accuracy of the numerical results, a Verification & Validation (V&V) analysis is performed. With the numerical uncertainties and the experimental uncertainties, assessed in the previous two chapters, the validation analysis can be performed. Validation consists of a comparison of numerical results and experimental results, taking their corresponding uncertainties into account. The method used in the validation analysis is discussed in Section 9.1. The results of the validation analysis are presented and discussed in Section 9.2. Section 9.3 concludes the validation analysis with a qualitative comparison of numerical results and experimental results.

9.1. Validation method

Following the validation procedure described by the ITTC guidelines for uncertainty analysis in CFD [15], a comparison error, E, between the numerical result, F_x, and the experimental result, R_t, is defined by

$$E = F_x - R_t. \tag{9.1}$$

In order to determine if the numerical simulations are validated, this error is compared to the validation uncertainty. The validation uncertainty, U_V, is composed of the numerical uncertainty and the experimental uncertainty and is defined by

$$U_V = \sqrt{U_{\phi_4}{}^2 + U_R{}^2}, \tag{9.2}$$

where U_{ϕ_4} is the estimate of the numerical discretization uncertainty for the medium grid, determined in Chapter 7, and U_R is the expanded experimental uncertainty, given in Chapter 8.

The numerical results are not corrected for numerical errors in this validation analysis. For the uncorrected values, validation at the U_V level is achieved if $|E| < U_V$. Else the combination of all errors in the numerical simulations and the experimental tests is larger than the validation uncertainty, and therefore, the numerical simulations are not validated at the U_V level.

From a programmatic standpoint, validation of the numerical results is successful at the $|E|$ level if the absolute value of the comparison error is lower than the required uncertainty U_{reqd}, i.e. if $|E| < U_{reqd}$. Of course, the required uncertainty should be chosen carefully in order to fit the purpose of the numerical results.

For the purpose of deriving regressions for the upright trimmed resistance prediction in velocity prediction programs, validation at a level below 10 percent seems reasonable and acceptable. VPPs are used extensively for the design of sailing yachts and the determination of ratings for individual yachts. If the trends, i.e. the shapes of the resistance curves and the differences in resistance between the models, are captured correctly, it is very likely that an optimization of a yacht design or the determination of ratings for individual yachts yields the correct result. Furthermore, VPPs may contain other more dominant sources of errors.

9.2. Validation results

With the numerical uncertainties and the experimental uncertainties, assessed in the previous two chapters, the validation analysis can be performed. These uncertainties were assessed for Sysser 85 at Froude numbers 0.45 and 0.85 for the crew CoG position. The numerical uncertainties determined for the medium grid are used in the validation analysis. The numerical results on the medium grid are of interest, because medium grids are used to calculate the hydrodynamic forces acting on the models in the new systematic series. A distinction between including and excluding the influence of solving ship motions was made in the grid refinement study. The results of both cases are used in this validation analysis. The numerical results and uncertainties are listed in Tables 7.3 and 7.4. The experimental results and uncertainties are given in Table 8.5.

The validation of the numerical results for Sysser 85 at Froude numbers 0.45 and 0.85 for the crew CoG position on the medium grid, including and excluding the influence of solving ship motions, is summarized in Table 9.1. At Froude number 0.45, validation at the U_V level of 8.1 percent is achieved for both cases. The absolute value of the comparison error is smaller than the validation uncertainty at this speed. Unfortunately, at Froude number 0.85, no validation is achieved at the U_V level. The absolute value of the comparison error is larger than the validation uncertainty at this speed. Although validation is not achieved at the U_V level, confidence in the numerical results still exists, because the relative comparison errors are very similar at both speeds. Despite that the relative comparison errors are nearly the same, validation cannot be achieved due to the lower relative validation uncertainty at the higher Froude number.

From a programmatic standpoint, validation of the numerical results at Froude number 0.85 is still successful at the $|E|$ level if $|E| < U_{reqd}$. For the purpose of deriving regressions for the bare hull upright trimmed resistance prediction in VPPs, validation at the $|E|$ level of 6 percent is very reasonable. The numerical results, including and excluding the influence of motion solving, at Froude number 0.85 are therefore successfully validated from a programmatic standpoint at the $|E|$ level of 6 percent.

In order to asses the quality and the credibility of the numerical simulations for the entire speed range and the different crew positions, the validation analysis is extended to the numerical results of Sysser 85 computed on the medium grid for the crew CoG and back positions. These numerical results are depicted in Figure 6.3. Since no assessment of the experimental uncertainties and the numerical uncertainties is available at other Froude numbers than 0.45 and 0.85 for the crew CoG position, validation at the U_V level for the other Froude numbers and the crew back position is difficult and questionable. According to the ITTC [15], no good procedure exists for the estimation of the uncertainty at an arbitrary condition from the uncertainty level at a neighbouring validated condition.

Extending the validation results at Froude numbers 0.45 and 0.85 to neighbouring conditions is therefore deemed unreliable. Although validation cannot be achieved at the U_V level for the other Froude numbers and the crew back position, validation of the other numerical results is still successful from a programmatic standpoint at the $|E|$ level if $|E| < U_{reqd}$. For the intended purpose of the numerical results, the approach of validating the numerical results at the $|E|$ level below 10 percent is considered to be acceptable.

The experimental results, the numerical results and the comparison errors for Sysser 85, for both crew positions, are given in Table 9.2. Comparison errors are between -2.9 and -8.6 percent of the experimental results. Some exceptions excluded, the comparison error seems to slightly increase with increasing Froude number. The heave values, and also the pitch values, are very similar between the experimental method and the numerical method. The resistance, the heave and the pitch for the experimental results and the numerical results are plotted in Figures 9.1 and 9.2 for the crew CoG position and the crew back position, respectively. The curves of the numerical results are very similar to the curves of the experimental results. There is some difference in the absolute values of the data points, but the shape of the curves is nearly identical. Note that for the sake of illustration, the data points are connected with straight line segments. Fitting a cubic spline to the data points using a least-squares fit would provide smoother and more realistic curves, but distracts from the main goal: validation of the actual data points.

For the intended purpose of the numerical results, validation at the $|E|$ level between 2.9 and 8.6 percent is acceptable for the same reasons as mentioned before. For this purpose, confidence in the numerical results exists. Hence, for the resistance of Sysser 85 for the crew CoG and back positions computed on the medium grid, validation is successful from a programmatic standpoint at the $|E|$ level

between 2.9 and 8.6 percent.

It should be noted that the comparison errors of the resistance are influenced by the difference in applied longitudinal trimming moment between the experimental method and the numerical method. The goal in the experimental tests was to obtain the right CoE height of $0.60L_{WL}$ and not to apply the same longitudinal trimming moment used in the corresponding numerical simulation. For both methods, the longitudinal trimming moment is equal to the measured or computed resistance multiplied by nearly the same CoE height. This results in different applied trimming moments between the methods. The trimming moment applied in the numerical simulations is between 2 and 13 percent lower than the trimming moment applied in the experimental method. Note that the CoE height in the experimental tests satisfies $0.585L_{WL} \leq z_{CoE} \leq 0.60L_{WL}$ while the CoE height in the numerical simulations is always equal to $0.60L_{WL}$. Nevertheless, the applied trimming moment is always higher in the experimental method than in the corresponding numerical simulation.

   It is very likely that this difference in trimming moment increases the difference in resistance between both methods compared to the resistance measured or computed for the same longitudinal trimming moment. For experimental tests and numerical simulations with the same applied longitudinal trimming moment, the comparison errors are expected to be smaller than those listed in Table 9.2.

Table 9.1: Validation of the numerical results for Sysser 85 at Froude numbers 0.45 and 0.85 for the crew CoG position, computed on the medium grid. Numerical results and uncertainties from Tables 7.3 and 7.4. Experimental results and uncertainties from Table 8.5.

(a) Validation of the results of the grid refinement study excluding the influence of motion solving, given in Table 7.3.

Fn	R_t	U_R	$F_x = \phi_4$	U_{ϕ_4}	E	E	U_V	U_V	$|E| < U_V$
$[-]$	$[N]$	$[N]$	$[N]$	$[N]$	$[N]$	$[\%R_t]$	$[N]$	$[\%R_t]$	
0.45	8.9417	0.6635	8.4926	0.3011	-0.4491	-5.02	0.7286	8.15	✓
0.85	30.1072	1.3962	28.3055	0.5205	-1.8017	-5.98	1.4901	4.95	✗

(b) Validation of the results of the grid refinement study including the influence of motion solving, given in Table 7.4.

Fn	R_t	U_R	$F_x = \phi_4$	U_{ϕ_4}	E	E	U_V	U_V	$|E| < U_V$
$[-]$	$[N]$	$[N]$	$[N]$	$[N]$	$[N]$	$[\%R_t]$	$[N]$	$[\%R_t]$	
0.45	8.9417	0.6635	8.4928	0.2976	-0.4489	-5.02	0.7272	8.13	✓
0.85	30.1072	1.3962	28.3251	0.4741	-1.7821	-5.92	1.4745	4.90	✗

9.2.1. Validation of other numerical results

Additional numerical simulations are performed for Sysser 83, Sysser 84 and Sysser 85 to extend the validation effort and to illustrate the performance and the capabilities of the FINE™/Marine flow solver. The bare hull upright untrimmed resistance of these three models is computed with the numerical method described in Chapter 6.

   The lines plans and the hydrostatic parameters of Sysser 83 and Sysser 84 are given in Appendix C. Syssers 83 and 84 are more modern versions of Sysser 28. Nowadays, Sysser 83 and Sysser 84 are outdated designs. Syssers 83 and 84 were tested with the experimental method used for the DSYHS in the #1 towing tank of the Ship Hydromechanics Laboratory at the Delft University of Technology in the year 2010. The bare hull upright untrimmed resistance of these two models was measured for various speeds. These measured resistance values are used in this validation analysis. Since no assessment of the experimental uncertainties is available, no actual validation can be achieved. The comparison errors are given and discussed below. The experimental results for Sysser 85 were determined with the recent tests discussed in Chapter 8.

   The experimental upright untrimmed resistance and the numerical upright untrimmed resistance, and corresponding comparison errors for Syssers 83, 84 and 85 are listed in Table 9.3. Comparison errors are between -3.2 and -10.7 percent of the experimental results. These comparison errors are comparable to the errors given in Table 9.2. Again, the performance of the numerical flow solver and the accuracy of the numerical results are satisfying. A noticeable observation is that at every speed

Table 9.2: Experimental and numerical upright trimmed resistance, trim and sinkage of Sysser 85 for the crew CoG and back position. Numerical values are computed on the medium grid. Experimental results from Table 8.2.

(a) Crew CoG position.

Fn	Experimental			Numerical			
	R_t	z	θ	F_x	z	θ	E
$[-]$	$[N]$	$[mm]$	$[°]$	$[N]$	$[mm]$	$[°]$	$[\%R_t]$
0.25	1.75	-2.0	0.15	1.63	-1.9	0.13	-7.0
0.35	3.80	-5.4	0.26	3.62	-5.0	0.20	-4.8
0.45	8.91	-10.7	-0.28	8.49	-9.9	-0.35	-4.6
0.55	14.31	-11.6	-0.90	13.61	-10.5	-0.95	-4.8
0.65	19.41	-9.4	-1.26	18.11	-8.5	-1.23	-6.7
0.75	24.51	-6.4	-1.14	22.47	-6.9	-1.10	-8.3
0.85	30.56	-6.6	-0.72	28.31	-8.2	-0.68	-7.4

(b) Crew back position.

Fn	Experimental			Numerical			
	R_t	z	θ	F_x	z	θ	E
$[-]$	$[N]$	$[mm]$	$[°]$	$[N]$	$[mm]$	$[°]$	$[\%R_t]$
0.25	1.85	-0.62	-0.75	1.76	-0.36	-0.80	-4.8
0.35	4.13	-3.5	-0.81	3.86	-3.2	-0.87	-6.6
0.45	8.92	-6.8	-1.41	8.65	-6.1	-1.51	-2.9
0.55	14.08	-6.6	-1.96	13.24	-5.8	-1.99	-6.0
0.65	19.01	-3.8	-2.27	17.52	-3.0	-2.28	-7.9
0.75	23.27	-0.49	-2.17	21.27	-1.0	-2.15	-8.6
0.85	28.25	-0.14	-1.92	26.17	-1.4	-1.95	-7.4
0.95	35.64	-3.8	-1.66	32.87	-3.9	-1.74	-7.8

Table 9.3: Experimental and numerical upright untrimmed resistance for Syssers 83, 84 and 85. Experimental values for Sysser 85 are from Table 8.3. Experimental values for Syssers 83 and 84 are from tests in the year 2010. Numerical values are computed on the medium grid.

Fn	Sysser 83			Sysser 84			Sysser 85		
	R_t	F_x	E	R_t	F_x	E	R_t	F_x	E
$[-]$	$[N]$	$[N]$	$[\%R_t]$	$[N]$	$[N]$	$[\%R_t]$	$[N]$	$[N]$	$[\%R_t]$
0.25	1.63	1.53	-6.2	1.87	1.67	-10.7	1.80	1.64	-9.0
0.35	3.44	3.29	-4.3	3.88	3.65	-6.0	3.96	3.63	-8.5
0.45	7.97	7.72	-3.2	8.33	7.88	-5.4	8.97	8.40	-6.3
0.55	12.97	12.55	-3.2	13.45	12.70	-5.5	14.12	13.22	-6.4
0.65	17.61	16.48	-6.4	17.79	16.60	-6.7	19.08	17.53	-8.1
0.75	21.36	20.18	-5.5	22.09	20.39	-7.7	23.11	21.18	-8.3
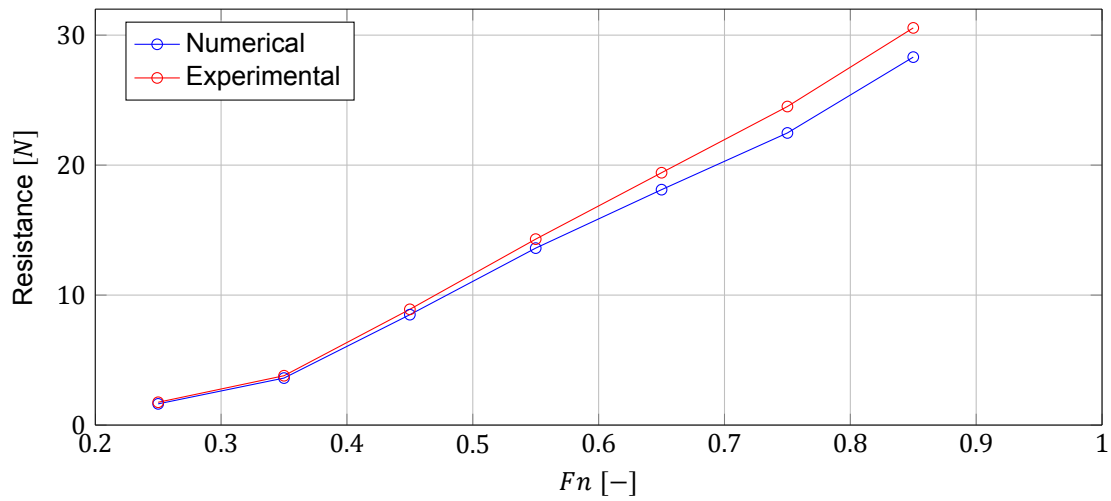
(a) Bare hull upright trimmed resistance.
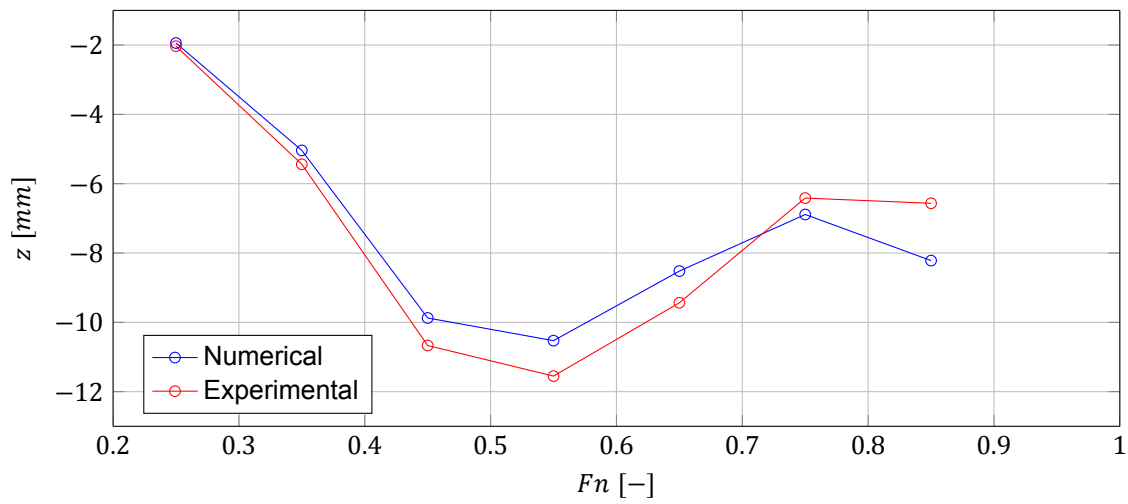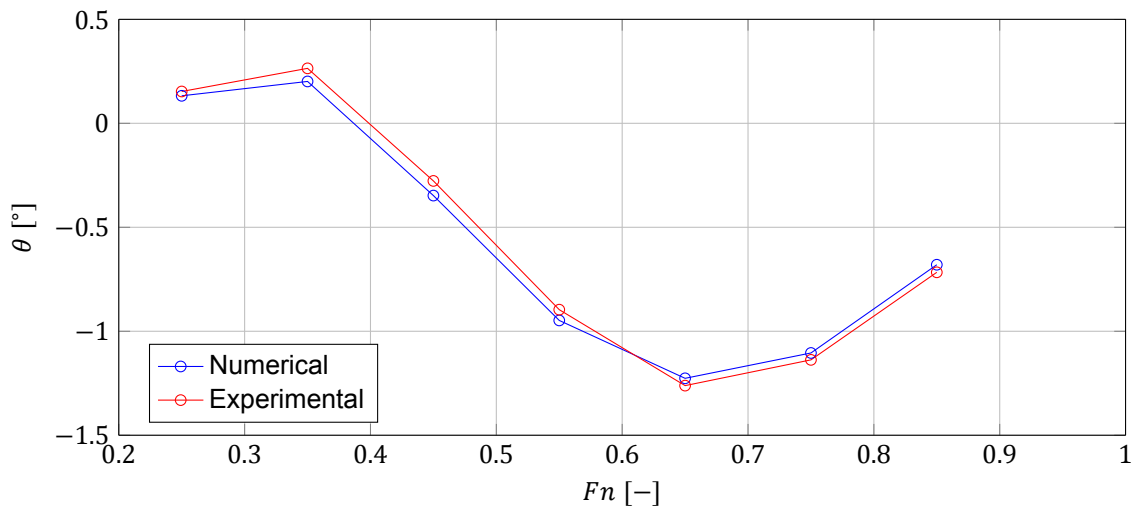
(b) Heave.

(c) Pitch.

Figure 9.1: Experimental and numerical upright trimmed resistance, heave and pitch of Sysser 85 for the crew CoG position. Numerical results from Figure 6.3. Experimental results from Table 8.2.
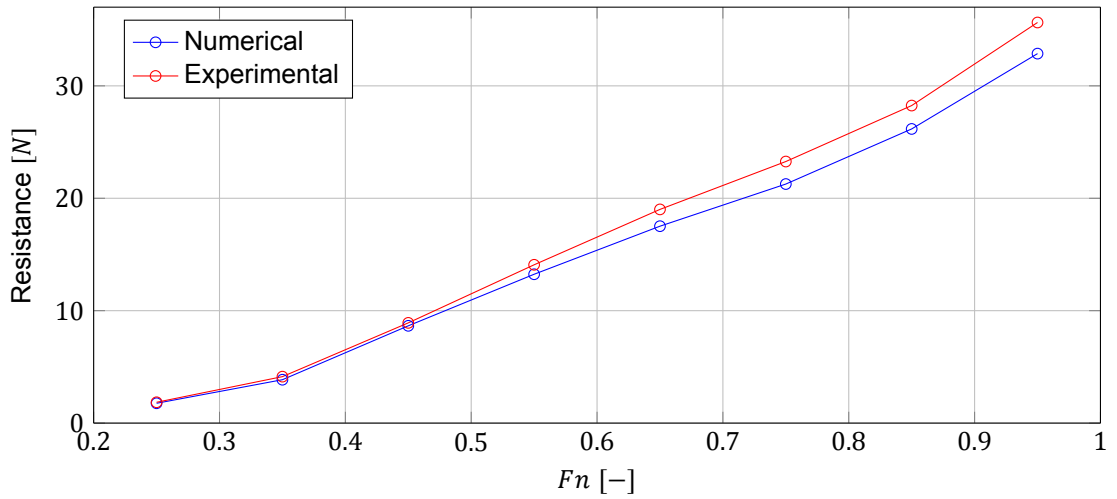
(a) Bare hull upright trimmed resistance.
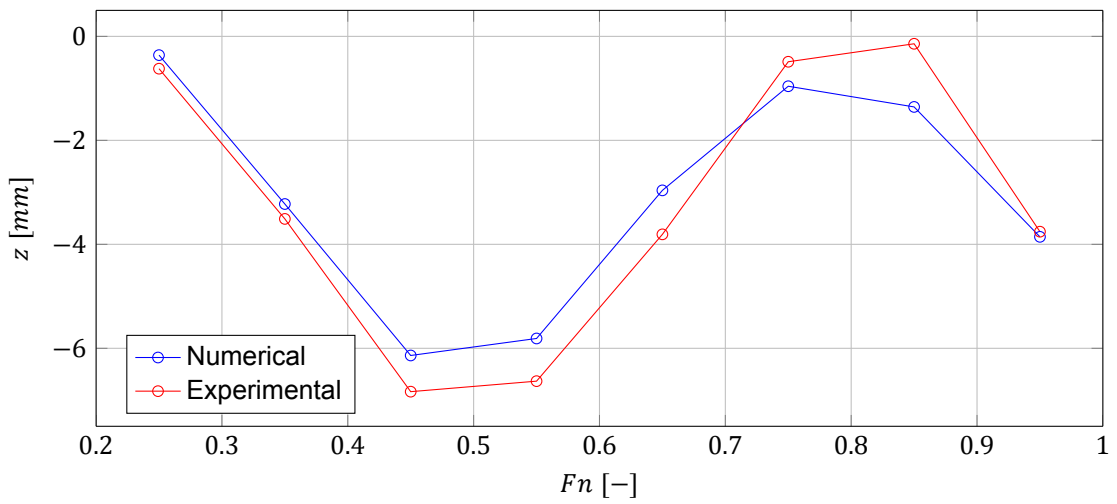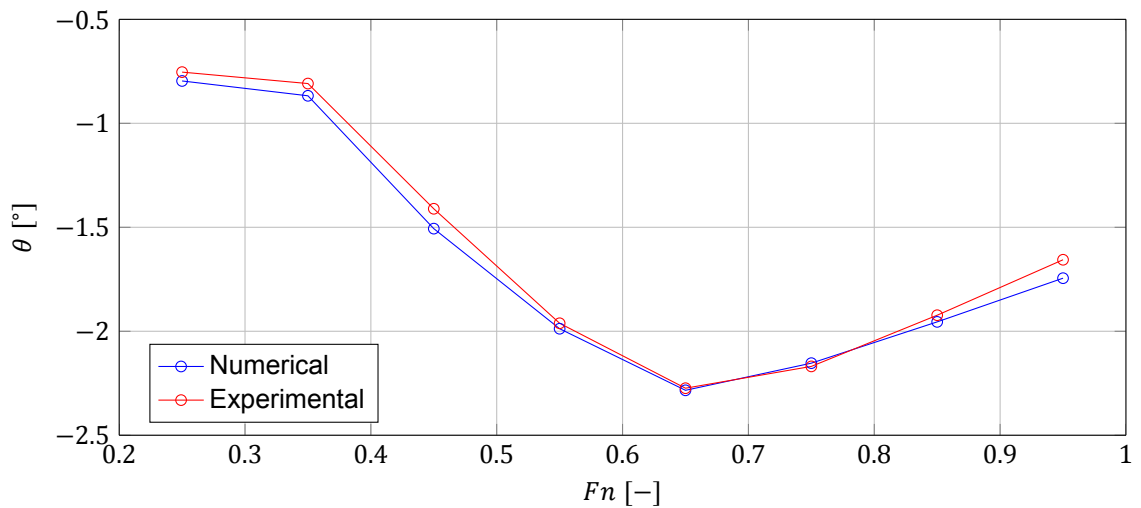
(b) Heave.

(c) Pitch.

Figure 9.2: Experimental and numerical upright trimmed resistance, heave and pitch of Sysser 85 for the crew back position. Numerical results from Figure 6.3. Experimental results from Table 8.2.

the comparison error of Sysser 83 is the lowest. It seems that for this more traditional hull shape with a narrow transom and a traditional waterline shape, i.e. gradually curved waterlines in the afterbody, the flow solver performs better. Apparently, the flow solver has more difficulties with the wide transoms and corresponding wide waterline shapes in the afterbodies of Sysser 84 and Sysser 85 than with the shapes of the more traditional Sysser 83. This is probably related to the increased flow separation associated with these wider transoms.

9.2.2. Conclusions from the validation effort

The validation analysis was performed for the numerical results of the grid refinement study for Sysser 85 at Froude numbers 0.45 and 0.85 for the crew CoG position computed on the medium grid. The numerical results on the medium grid are of interest, because medium grids are used to calculate the hydrodynamic forces acting on the models in the new systematic series. A distinction between including and excluding the influence of solving ship motions was made in the refinement study, discussed in Chapter 7. The results of the two refinement studies, excluding and including the influence of solving ship motions, were surprisingly similar. The results of the validation analysis for both cases are also very similar. For the validation of the numerical results of the new systematic series, the numerical results and uncertainties of the grid refinement study including the influence of solving ship motions and trimming moments of the driving force are the most appropriate.

At Froude number 0.45, validation at the U_V level of 8.1 percent was achieved for both cases. Unfortunately, at Froude number 0.85, no validation could be achieved at the U_V level. The absolute value of the comparison error is larger than the validation uncertainty at this speed. Although validation was not achieved at the U_V level, confidence in the numerical results still exists, because the relative comparison errors at both speeds are almost the same. From a programmatic standpoint, validation of the numerical results at Froude number 0.85 was successful at the $|E|$ level of 6 percent. For the purpose of deriving regressions for the upright trimmed resistance prediction in VPPs, the approach of validating the numerical results at the $|E|$ level below 10 percent is considered to be reasonable and acceptable.

In order to asses the quality and the credibility of the numerical simulations performed for the new systematic series, the validation analysis was extended to the numerical results computed for Sysser 85 on the medium grid for the crew CoG and back positions over the entire speed range. The corresponding comparison errors are between -2.9 and -8.6 percent of the experimental results. The heave values, and also the pitch values, are very similar between the experimental method and the numerical method. The trends in the resistance curves and the motion curves are captured perfectly by the numerical method. With the absence of reliable experimental and numerical uncertainty estimates for all the Froude numbers, validation could not be achieved at the U_V level. For the resistance of Sysser 85 computed on the medium grid for both crew positions, validation is successful from a programmatic standpoint at the $|E|$ level between 2.9 and 8.6 percent.

Since the other hull shapes in the new systematic series are all derived from Sysser 85 and the numerical simulations are performed with exactly the same settings on similar medium grids, similar comparison errors are expected for the other hull shapes in the systematic series. All the used grids are derived with exactly the same grid-generation settings. They all have similar mesh qualities and geometrical properties, like the orthogonality, the aspect ratio and the skewness of the grid cells.

Additional numerical simulations were performed for two models not belonging to the new systematic series to further extend the validation effort and to illustrate the performance and the capabilities of the FINE™/Marine flow solver. The found comparison errors are comparable to the errors of the numerical results for the new systematic series. Again, the performance of the numerical flow solver and the accuracy of the numerical results are satisfying. A noticeable observation is that at every speed the comparison error of the more traditional hull shape is the lowest. It seems that for this more traditional hull with a traditional narrow transom and a traditional waterline shape, the flow solver performs better. This is probably related to the increased flow separation associated with the wider transoms of the modern designs.

In general, the numerical method underpredicts the resistance compared to the experimental method for all the investigated cases, but yields satisfying results. The shape of the resistance curves, the

motions and the differences in resistance between the two crew positions are captured correctly by the numerical method compared to the experimental results.

9.3. Qualitative comparison

The validation analysis is concluded with a qualitative comparison of numerical results with experimental results. The wave system around a ship is one of the main contributors to the dissipation of energy and has therefore a large influence on the resistance. Consequently, an accurate computation of the wave system in the numerical simulations is necessary. Since no quantitative measurements of the wave field were or could be taken during the experimental tests, only a qualitative comparison from visual observations is given. The generated bow wave is compared visually for Sysser 85 at Froude numbers 0.45 and 0.85 for the crew CoG and back position. Photographs of the bow wave in the experimental method and corresponding visualisations of the bow wave in the numerical simulations at Froude numbers 0.45 and 0.85 are shown in Figures 9.3 and 9.4. Note the slight differences in camera angle between the figures of the numerical method and the experimental method.

The first thing that stands out from both figures is the good qualitative agreement between both methods. In general, the shape and the height of the bow wave seem to be similar between the experimental method and the numerical method. The bow waves seem more irregular in the experimental method than in the numerical method. This is probably a consequence of the turbulence stimulators used in the experimental method. At Froude number 0.45, the resemblance between both methods is striking. For instance, at Froude number 0.45 for the crew back position, the braking wave — wave tunnel near the middle turbulence stimulator — is captured perfectly by the numerical method.

At Froude number 0.85, the resemblance is less striking. The bow waves seem more irregular in the experimental method than in the numerical method. The bow waves in the experimental method seem to contain more elements of braking waves while these elements are less pronounced in the numerical method. This is probably again a consequence of the turbulence stimulators used in the experimental method. Wave breaking elements in the numerical method are mainly present between the highest contour line and the top of the bow wave. Some fading of colours and some irregular shapes can be observed there.

Overall, the shape and the height of the bow waves seem to be visually very similar between the experimental method and the numerical method at both Froude numbers. Although this is just a qualitative comparison of the bow wave and no actual validation of the wave system, the visual observations of the bow wave are encouraging and strengthen the confidence in the numerical results.
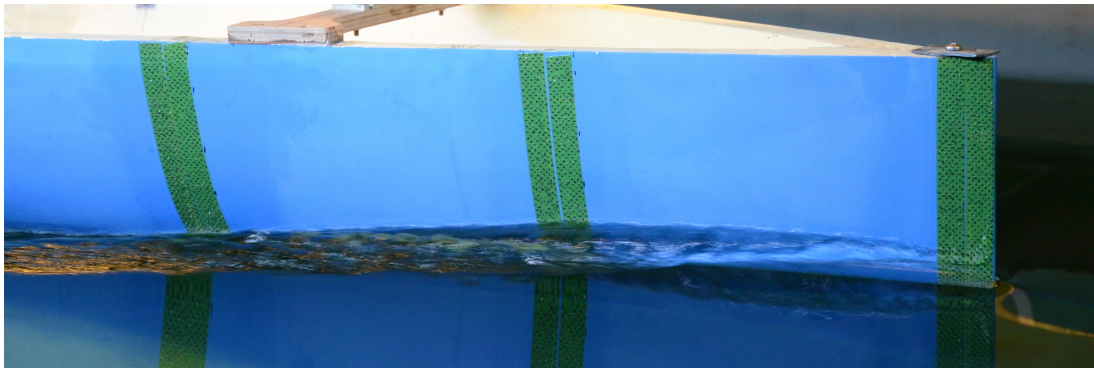
(a) Experimental method with the crew CoG position.
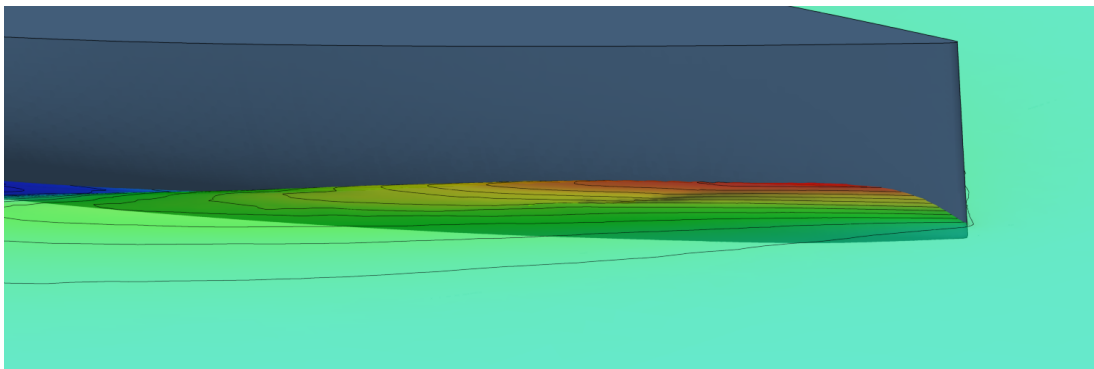
(b) Numerical method with the crew CoG position.
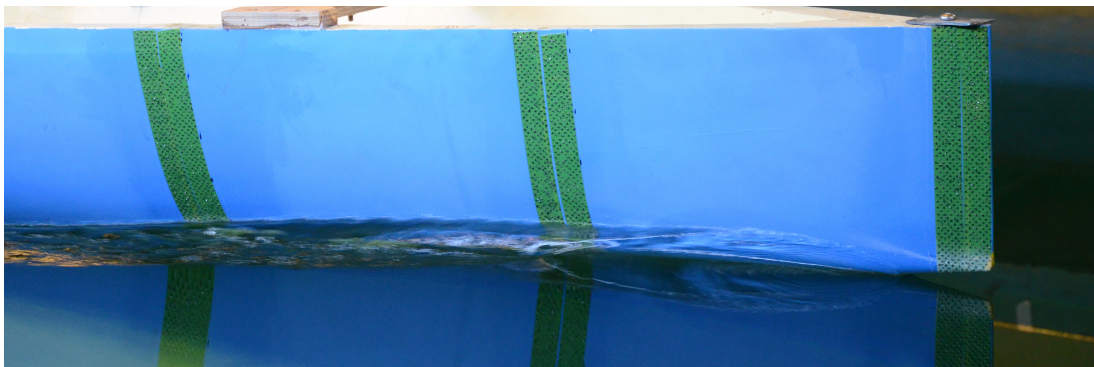
(c) Experimental method with the crew back position.
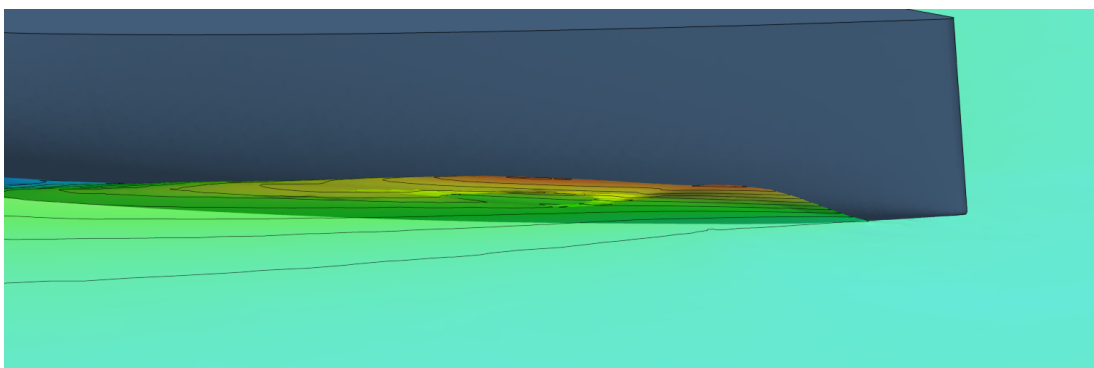
(d) Numerical method with the crew back position.

Figure 9.3: Bow waves of Sysser 85 at Froude number 0.45 for the crew CoG and back positions, determined with the experimental method and the numerical method.
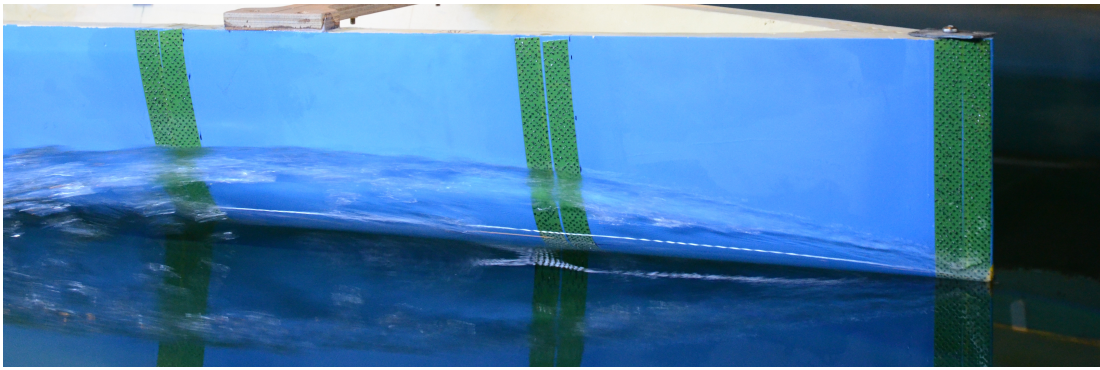
(a) Experimental method with the crew CoG position.
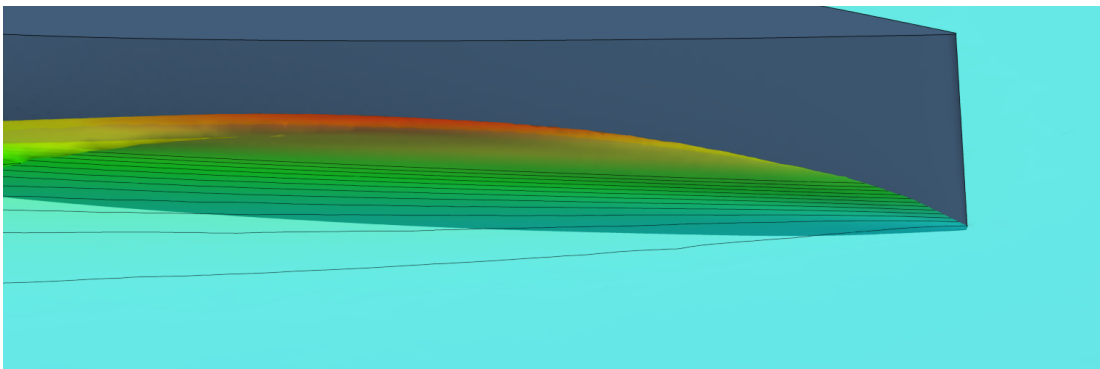
(b) Numerical method with the crew CoG position.

(c) Experimental method with the crew back position.
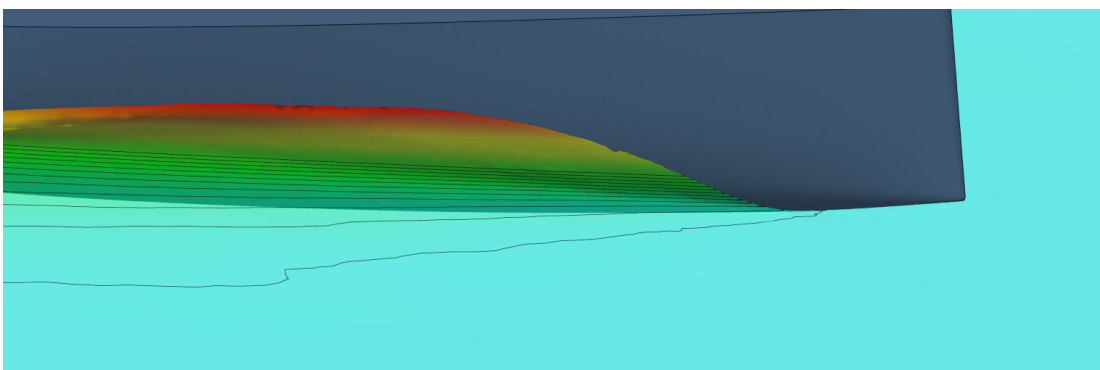
(d) Numerical method with the crew back position.

Figure 9.4: Bow waves of Sysser 85 at Froude number 0.85 for the crew CoG and back positions, determined with the experimental method and the numerical method.

10

Regression analysis

The hydrodynamic resistance forces acting on the hull shapes in the new systematic series are used to derive regressions for the estimation of the bare hull upright trimmed resistance. The dataset of the new systematic series, obtained with CFD simulations, contains the resistance values for various hull forms, speeds and trimming moments. A regression analysis is performed on this dataset to derive these regressions.

This analysis is performed for the resistance values extrapolated to prototype scale. In order to separate various physical effects and thereby to enhance the quality of the regression results, the resistance is decomposed into various components before the analysis. The decomposition and the extrapolation of the resistance are discussed in Section 10.1. Before discussing the regression analysis itself, a brief explanation of the for this analysis important statistical definitions is given in Section 10.2. The method followed in the regression analysis is explained in Section 10.3.

A clear distinction between dependent variables and independent variables is made throughout this analysis. The resistance is the dependent, or response, variable depending on the independent, or explanatory, variables. The independent variables are the hydrostatic parameters of a hull. All the independent variables that are assumed to be of influence on the dependent variable are given in Section 10.4. The resistance is made non-dimensional before the analysis. This scaling allows for removing some of the largest known physical relationships between the dependent variable and the independent variables. More subtle physical relationships between the dependent variable and the independent variables become thereby more apparent. The scaling of the resistance is discussed in Section 10.5.

The results of the regression analysis are presented and discussed in Section 10.6. An verification of the derived regressions is given in Section 10.7. The applicability of the derived regressions to the velocity prediction of modern high performance sailing yachts with existing VPPs is illustrated in Section 10.8. Section 10.9 concludes this chapter with a summary of the characteristics of the derived regression formulas. The bare hull upright trimmed resistance prediction based on the new formulations is summarized in Appendix G.

10.1. Resistance decomposition and extrapolation

In order to separate various physical effects and thereby to enhance the quality of the regression results, the resistance is decomposed into two components. These components require different treatment in the analysis. Two approaches for the decomposition are considered. The first one is to follow the decomposition of the resistance into a pressure resistance component and a frictional resistance component, as used in the numerical flow solver. The pressure resistance is equal to the horizontal component of the resultant force obtained with integration of the normal stresses over the wetted surface of the hull. Consequently, the pressure resistance consists of the wave-making resistance and the viscous pressure resistance. The frictional resistance is equal to the horizontal component of the resultant force obtained with integration of the shear stresses over the wetted surface of the hull. The decomposition into a pressure resistance and a frictional resistance makes it possible to perform a regression analysis on both resistance components.

Another possibility is to follow the extrapolation procedure discussed in Section 2.2, and to decompose the resistance into an estimated frictional resistance and a residuary resistance component. The frictional resistance is estimated with the friction coefficient calculated with the ITTC 1957 Model-Ship Correlation Line [16]. The residuary resistance is defined as the difference between the total resistance and the estimated frictional resistance. This decomposition is preferred over a decomposition into a pressure resistance component and a frictional resistance component, because it allows for easy extrapolation of the results to different waterline lengths with the standard extrapolation procedure used for resistance measurements in towing tanks. This offers more flexibility for the implementation of the derived regressions into velocity prediction programs and allows for an easier comparison of experimental and numerical resistance data. Furthermore, this same extrapolation procedure and decomposition is used to extrapolate the numerical resistance data from model scale to prototype scale. It seems to be a natural choice to follow this decomposition.

Therefore, only the decomposition into an estimated frictional resistance and a residuary resistance component is considered in this regression analysis. As a consequence of this estimation, the residuary resistance contains the wave-making resistance, the viscous pressure resistance and some frictional resistance. Only for the residuary resistance, a regression formula has to be derived.

In this regression analysis, the resistance is decomposed with the method described in Chapter 5. The bare hull upright trimmed resistance, $R_{T\theta_h}$, is decomposed as

$$R_{T\theta_h} = R_{F_h} + R_{R\theta_h}, \tag{5.2}$$

where $R_{R\theta_h}$ is the upright trimmed residuary resistance of the bare hull, and R_{F_h} is the frictional resistance of the bare hull. For the trimmed residuary resistance of the bare hull, $R_{R\theta_h}$, new regression formulas are derived in this chapter. The frictional resistance of the bare hull is computed with

$$R_{F_h} = \frac{1}{2}\rho V^2 S_c C_f, \tag{2.6}$$

where ρ is the density of water, V is the velocity, S_c is the wetted surface of the canoe body, and C_f is the friction coefficient. Following the procedure used for the DSYHS, no form factor is used for the frictional resistance. The friction coefficient is calculated with the ITTC 1957 Model-Ship Correlation Line [16]:

$$C_f = \frac{0.075}{(\log_{10} Re - 2)^2}. \tag{2.7}$$

$0.9L_{WL}$ is used as the characteristic length in the Reynolds number. Therefore, the Reynolds number is defined by

$$Re = \frac{0.9L_{WL} \cdot V}{\nu}. \tag{10.1}$$

Compared to the $0.7L_{WL}$ used for the DSYHS, a characteristic length of $0.9L_{WL}$ seems to be more appropriate for the modern hull shapes of the new systematic series. The results of a small number of numerical simulations at prototype scale were compared to the results of numerical simulations at model scale extrapolated to prototype scale with $0.7L_{WL}$, $0.8L_{WL}$ and $0.9L_{WL}$ used as the characteristic length in the Reynolds number. This small comparison suggested that $0.9L_{WL}$ was the most appropriate length. Furthermore, Keuning and Sonnenberg [27] already suggested that a characteristic length of $0.9L_{WL}$ seemed more appropriate for the more modern hull shapes in the DSYHS after Series 1. Nevertheless, for consistency, $0.7L_{WL}$ was used as the characteristic length throughout the entire DSYHS.

Unfortunately, time and resources were missing to thoroughly test the assumption of $0.9L_{WL}$ as the characteristic length in the Reynolds number. Moreover, the numerical simulation at prototype scale cannot be validated. This choice for the characteristic length remains therefore debatable. Nevertheless, the original choice for $0.7L_{WL}$, used in the DSYHS, was that as well.

Before applying a regression analysis to the resistance data of the new systematic series, the resistance is extrapolated from model scale, $L_{WL} = 2.00\ m$, to prototype scale, $L_{WL} = 10.00\ m$. For the

extrapolation of the resistance forces, the method described in Section 2.2 is used. In this case, a characteristic length of $0.9L_{WL}$ is used for the Reynolds number.

10.2. Statistical definitions

A brief explanation of the for this regression analysis important statistical definitions is given in this section. For a thorough discussion of statistics, the reader is referred to Dekking et al. [2]. In the regression analysis, the response variables and the explanatory variables are considered to be realizations of random variables. A random variable is a variable whose possible values are numerical outcomes of a random phenomenon. The expected value, or the mean, of random variable X is denoted by $\mathrm{E}[X]$. The expected squared deviation from the mean of random variable X, or simply the variance of X, is defined by

$$\mathrm{Var}(X) = \mathrm{E}[(X - \mathrm{E}[X])^2].$$ (10.2)

The standard deviation of random variable X is determined by $\sigma(X) = \sqrt{\mathrm{Var}(X)}$. The dependence, or relationship, between two random variables can be assessed with the covariance. The covariance between the two random variables X_1 and X_2 is defined by

$$\mathrm{Cov}(X_1, X_2) = \mathrm{E}[(X_1 - \mathrm{E}[X_1])(X_2 - \mathrm{E}[X_2])].$$ (10.3)

Two random variables can be positively correlated, negatively correlated or uncorrelated. The sign of the covariance determines if two variables are either positively or negatively correlated. The random variables are uncorrelated if the covariance between them is zero. The covariance gives an indication on how two random variables influence one another.

The dependence between two random variables X_1 and X_2 can also be determined with the correlation coefficient, $\rho(X_1, X_2)$. In contrast to the covariance, the correlation coefficient is dimensionless. The correlation coefficient of the two random variables X_1 and X_2 is defined by

$$\rho(X_1, X_2) = \frac{\mathrm{Cov}(X_1, X_2)}{\sqrt{\mathrm{Var}(X_1)\,\mathrm{Var}(X_2)}}.$$ (10.4)

In general, the correlation coefficient satisfies $-1 \le \rho(X_1, X_2) \le 1$. The two random variables are mostly correlated if $X_1 = X_2$ or $X_1 = -X_2$, corresponding to $\rho(X_1, X_2) = 1$ and $\rho(X_1, X_2) = -1$, respectively. The two random variables are uncorrelated if $\mathrm{Cov}(X_1, X_2) = 0$, and therefore, if $\rho(X_1, X_2) = 0$.

Note that if two random variables are uncorrelated, they are not necessarily independent. Two random variables that are independent are always uncorrelated. Statistical independence implies that the occurrence of one random variables does not affect the probability of the other. In this regression analysis, the interest lies not in the independence between explanatory variables, but in the correlation between explanatory variables. For stability of the regressions, it is important that the explanatory variables in the regression are not strongly correlated to each other.

For the assembling of the regressions, the dependence of the response variable on an explanatory variable has to be assessed; i.e. the probability of the response variable being independent from the explanatory variable has to determined. This is done with statistical hypothesis testing. In statistical hypothesis testing, a null hypothesis and an alternative hypothesis are proposed and compared to each other. A test statistic is used to decide whether to reject the null hypothesis. The strength of the evidence against the null hypothesis is quantified by a *p*-value. A *p*-value expresses the probability of obtaining a value of the test statistic at least as extreme as the value observed for the data under the assumptions that the null hypothesis is true. The smaller the *p*-value, the stronger the evidence that the observed value bears against the null hypothesis. In statistical hypothesis testing, an observed value is statistically significant if its *p*-value is less than the predefined significance level. Statistical significance implies that the observed value is unlikely to have occurred by chance. The determination of the *p*-value is complex and is not discussed here. The reader is referred to Dekking et al. [2] for more details.

In this present analysis, the null hypothesis proposes no relationship between the response variable and the explanatory variable. The alternative hypothesis proposes a relationship between the two

types of variables. The change in the sum of squared residuals is used as the test statistic. The *p*-value associated with an explanatory variable quantifies the probability of the response variable being independent from that explanatory variable. For independence, and therefore, for omitting the explanatory variable from the regression model, the *p*-value has to be larger than the predefined significance level. Significance levels of 5 percent and 5.5 percent are used for the inclusion and the exclusion of explanatory variables from the regression model, respectively.

Another important criteria in the building of regressions is the mean squared error, whereby the relative performance between two estimators can be assessed. The mean squared error of estimator T for parameter θ is defined by

$$\text{MSE}(T) = \text{E}[(T - \theta)^2]. \tag{10.5}$$

Let T_1 and T_2 be both estimators for the same parameter θ. Estimator T_1 performs better than estimator T_2 if $\text{MSE}(T_1) < \text{MSE}(T_2)$. The mean squared error is a good measure to compare the performance of different regression models with each other.

How well the regression formula represents the dataset can be expressed with the coefficient of determination R^2. The coefficient of determination is the ratio of the by the regression explained variation to the total variation. For the observed dataset, $y_1, y_2, ..., y_n$, and the with the regression formula predicted dataset, $f_1, f_2, ..., f_n$, the coefficient of determination is defined by

$$R^2 = 1 - \frac{\sum_{i=1}^{n}(y_i - f_i)^2}{\sum_{i=1}^{n}(y_i - \bar{y})^2}, \tag{10.6}$$

where $\bar{y}$ is the mean value of dataset y_i. The coefficient of determination is used to express how well the final regressions fit the database.

For the assembling process of regressions and for comparing regressions with different numbers of explanatory variables, the coefficient of determination has to be considered with care. Adding explanatory variables to a regression model automatically increases the coefficient of determination. In the assembling process, this coefficient acts as a spurious quality indicator. The adjusted coefficient of determination, denoted by $\bar{R}^2$, acts as a better quality indicator in the assembling process. It is also a better measure to compare regressions with different numbers of explanatory variables. This coefficient $\bar{R}^2$ adjusts the coefficient of determination, R^2, for the number of explanatory variables in the model relative to the size of the dataset. The adjusted coefficient of determination is defined by

$$\bar{R}^2 = 1 - (1 - R^2)\frac{n - 1}{n - m - 1}, \tag{10.7}$$

where n is the number of points in the dataset, and m is the number of explanatory variables in the regression model. The adjusted coefficient of determination is used as an additional measure in the assembling process of the regressions. The statistical significance of an explanatory variable is used as the dominant quality measure in the assembling process.

10.3. Regression analysis method

The regression analysis is based on a multiple linear regression that attempts to model the relationship between two or more independent variables and the dependent variable by fitting a linear equation to the observed data. A multiple linear regression has the following characteristic form:

$$Y = a_0 + a_1 X_1 + ... + a_N X_N, \tag{10.8}$$

where Y is the dependent variable or the response variable, X_i are the independent variables or the explanatory variables, a_i are the coefficients obtained with least-squares fitting, and N is the number of independent variables and is greater than or equal to two. The dependent variables and the independent variables are made non-dimensional in the analysis. One regression formula is derived for the entire speed range. The coefficients, a_i, are then determined at each Froude number individually to avoid fitting of the humps and hollows commonly present in speed-resistance curves for the wave-

making resistance and the residuary resistance. These humps and hollows are a result of interference between the wave system generated at the bow and the wave system generated at the stern.

For stability of the regression, it is important that the explanatory variables in the regression are not strongly correlated to each other. The correlation between two explanatory variables is determined with the correlation coefficient, defined by Equation (10.4). The goal is to keep the correlation coefficient between two explanatory variables as low as possible. The explanatory variable in the regression should have a high statistical significance, i.e. a low associated *p*-value, and should be (highly) correlated to the response variable. For stability and robustness of the regression, the number of explanatory variables in the regression should be low enough with respect to the database size. On the other hand, the number of variables should remain high enough to capture all the significant trends in the database and to ensure a high accuracy of the regression. An optimum number of explanatory variables in the regression model has to be found.

   The following rules of thumb for the quality of a final regression are used: adding an extra independent variable to the regression does not significantly improve the accuracy; removing an independent variable from the regression does significantly reduce the accuracy of the regression.

10.3.1. Database
The hydrodynamic resistance forces acting on the hull shapes in the new systematic series are used to derive regressions for the estimation of the bare hull upright trimmed resistance based on hydrostatic parameters of yacht hulls. The dataset of the new systematic series, obtained with numerical simulations, contains the resistance values for 21 hull shapes at eight different speeds for three crew positions. The resistance values calculated with CFD at model scale, $L_{WL} = 2.00\ m$, are extrapolated to prototype scale, $L_{WL} = 10.00\ m$. The resistance is extrapolated with the method described in Section 2.2. In this case, a characteristic length of $0.9 L_{WL}$ is used for the Reynolds number. The dataset at prototype scale is used in the regression analysis. The database of the DSYHS is not used in this regression analysis to avoid introducing errors and compatibility issues related to differences between the experimental results of the DSYHS and the numerical results of the new systematic series, and differences in test conditions — trimming moments and speeds — between both series.

   In this regression analysis, no results are classified as outlying, and therefore, no results are omitted from the database before the regression analysis is performed. The database for the crew CoG position contains resistance values for Froude numbers up to 0.85. The databases for the crew middle and back positions contain resistance values for Froude numbers up to 0.95. The databases of the crew CoG and back positions contain the resistance values of all the models at all the speeds previously defined. Only the database for the crew middle position contains no resistance values for Sysser 87 and Sysser 97 at Froude number 0.95.

   Convergence of the numerical simulation for these two models at that speed was impossible, because these models were trimming bow under as a results of the very high resistance and the related excessive trimming moment of the driving force. Of course, trimming bow under might be a result of numerical issues related to the excessive motions, the corresponding large grid deformations and the loss of accuracy. However, based on the hull shapes of these two models, it is likely that the resistance at that speed is indeed very high for both. Sysser 87 is shallow and very wide. Sysser 97 has the longitudinal centre of buoyancy relatively far forward. As a consequence of the very high resistance, the trimming moment is also very high, and the model trims bow down. The resistance and the trimming moment are likely to amplify each other. Based on the resistance curves of these two Syssers for the crew middle position up to Froude number 0.85, it is also expected that the resistance values are indeed very high for these two models at Froude number 0.95 for this crew position. The resistance is likely to be so high that it is doubtful that an actual sailing yacht close to those design characteristics would ever be capable of reaching such high speeds. Therefore, it is not an issue that these two resistance values are missing in the database.

10.3.2. Different regressions
The following five different regression formulas for the upright trimmed residuary resistance will be derived in this analysis:

   (i) A regression for the minimum upright trimmed residuary resistance;

  (ii) A regression for the upright trimmed residuary resistance with the crew CoG position;

  (iii) A regression for the upright trimmed residuary resistance with the crew middle position;

  (iv) A regression for the upright trimmed residuary resistance with the crew back position;

  (v) A regression for the upright trimmed residuary resistance covering the three crew positions.

The five different expressions have different application possibilities. Expression (i) gives the minimum resistance of the three crew positions in the database without any specification of the trimming moment of the crew's weight. Expressions (ii), (iii) and (iv) estimate the upright trimmed resistance for the crew CoG, middle and back positions, respectively. Expression (v) incorporates the influence of the trimming moment of the crew's weight on the resistance through either the effective centre of effort, defined by Equation (4.6), or the longitudinal centre of gravity, defined by Equation (4.4).

For a high performance sailing yacht with a full crew, expression (i) is preferred, because this regression simulates the optimum performance of the yacht. The other regressions can be used for different crew configurations. The derived regressions should be easily usable in existing velocity prediction programs.

10.3.3. Regression building

The multiple linear regressions are assembled by using a forward stepwise selection algorithm and a backward stepwise selection algorithm. Both algorithms produce different regressions, and therefore, they are both used. The starting model of the forward stepwise selection algorithm contains only a constant term. Explanatory variables are added to the model based on the order of their statistical significance with the response variable. The statistical significance of an explanatory variable with the response variable is determined with its corresponding p-value and the predefined significance levels. Significance levels of 5 percent and 5.5 percent are used for the inclusion and the exclusion of an explanatory variable from the regression model, respectively.

After adding a variable to the model in an iteration step, the statistical significance of each explanatory variable in the model with the response variable is determined. Based on their statistical significance with the response variable, every explanatory variable in the model can be either included or excluded from the regression model in this iteration step. In a following iteration step, earlier excluded variables may be reincluded. The iteration procedure stops when no explanatory variables can be added to or removed from the regression model based on their statistical significance with the response variable.

The backward stepwise selection algorithm uses a similar procedure. The starting model of this algorithm contains a constant term and all the explanatory variables considered in the regressions analysis. Explanatory variables are removed from the model based on the order of their statistical insignificance with the response variable. Based on their statistical significance with the response variable, every explanatory variable in the regression model can be either included or excluded from the model in this iteration step. In a following iteration step, earlier excluded variables may be reincluded. The iteration procedure stops when no explanatory variables can be added to or removed from the regression model based on their statistical significance with the response variable.

Both stepwise algorithms produce different regressions. The results of both methods are combined to form the 'optimum' regression. This regression is likely to contain too many and redundant variables. Therefore, another regression analysis is applied to the dataset with only the explanatory variables of the 'optimum' regression. This same iteration is applied again when necesarry. In the end, the algorithms produced regressions with five to nine explanatory variables, depending on how difficult it was to approximate the response variable. The resistance values at Froude numbers 0.35, 0.45 and 0.95 were the most difficult to approximate.

As a first step, a regression formula for each individual Froude number is determined to avoid fitting of the humps and hollows commonly present in speed-resistance curves. For each Froude number, a different regression formula containing different explanatory variables can be obtained. The explanatory variables of the regression formulas for the different Froude numbers are then combined into one final regression formula. The coefficients of the regression are then redetermined for each Froude number with least-squares fitting. The assembled regression formula is then again tested for its accuracy and

its robustness at each Froude number, and its fit for every hull shape in the database. If necesarry, it is adjusted and optimized.

A consequence of assembling the regression in this way is that some explanatory variables in the final regression formula can be redundant at a specific Froude number. These redundant variables can be artificially removed by fitting the regression model without these variables and setting their corresponding coefficients to zero in the assembled regression. This was not done. At every speed, all the explanatory variables of the assembled regression are used to fit the dataset. Consequently, one regression formula is used for the entire range of Froude numbers. At every Froude number, different coefficients are used.

The regressions analysis is applied to the minimum resistance. The used database contains for every hull shape at every speed, the minimum resistance of the three crew positions. The derived regression model is then used to fit the individual datasets of the crew CoG, middle and back positions separately. The three regressions for the individual crew positions have the same form as the regression model for the minimum resistance, but they all have different coefficients. As will be shown later on, the explanatory variables in the regression model for the minimum resistance are able to accurately describe the three individual databases of the three crew positions. Therefore, it is not necessary to derive different regression models for the individual crew positions.

Regression (v), which covers the three crew positions, is derived with an ad hoc approach. Since the explanatory variables contained within regression (i) are capable of accurately describing the three individual datasets of the three crew positions, these explanatory variables are permanently contained within the regression model covering the three crew positions. Only additional explanatory variables, facilitating a relation between the three individual databases of the three positions, can be added to the regression model. Additional explanatory variables that are considered for connecting the three datasets are the height of the effective CoE, and the longitudinal centre of gravity corresponding to a trimming moment of the crew's weight.

10.4. Explanatory variables

The following dimensionless explanatory variables are assumed to be of influence on the upright trimmed residuary resistance and are therefore considered in this regression analysis:

- C_b, block coefficient;

- C_p, prismatic coefficient;

- C_w, waterplane area coefficient;

- C_x, maximum sectional area coefficient;

- $\frac{\nabla_c}{A_W T_c}$, vertical prismatic coefficient;

- $\frac{B_{WL}}{L_{WL}}$, beam-to-length ratio;

- $\frac{T_c}{L_{WL}}$, draft-to-length ratio;

- $\frac{T_c}{B_{WL}}$, draft-to-beam ratio;

- $\frac{\nabla_c^{1/3}}{L_{WL}}$, displacement-to-length ratio;

- $\frac{\nabla_c^{2/3}}{A_W}$, displacement-to-waterplane area ratio;

- $\frac{\nabla_c^{2/3}}{S_c}$, displacement-to-wetted surface ratio;

- $\frac{A_X^{1/2}}{L_{WL}}$, maximum sectional area-to-length ratio;

- $\frac{A_W^{1/2}}{L_{WL}}$, waterplane area-to-length ratio;

- $\frac{S_c^{1/2}}{L_{WL}}$, wetted surface-to-length ratio;

- $\frac{LCB_{fp}}{L_{WL}}$, longitudinal centre of buoyancy-to-length ratio;

- $\frac{LCF_{fp}}{L_{WL}}$, longitudinal centre of flotation-to-length ratio;

- $\frac{LCB_{fp}}{LCF_{fp}}$, longitudinal centre of buoyancy-to-longitudinal centre of flotation ratio;

- $\frac{LCF_{fp}-LCB_{fp}}{L_{WL}}$, difference of longitudinal centre of flotation and longitudinal centre of buoyancy-to-length ratio;

- $\frac{A_X}{A_W}$, maximum sectional area-to-waterplane area ratio;

- $\frac{A_X}{S_c}$, maximum sectional area-to-wetted surface ratio;

- $\frac{A_W}{S_c}$, waterplane area-to-wetted surface ratio;

- $\frac{KM_L}{L_{WL}}$, longitudinal metacentric height-to-length ratio;

- $\frac{z_{CoE_{eff}}}{L_{WL}}$, centre of effort height-to-length ratio;

- $\frac{z_{CoE_{eff}}}{KM_L}$, centre of effort height-to-longitudinal metacentric height ratio;

- $\frac{LCG_{fp}}{L_{WL}}$, longitudinal centre of gravity-to-length ratio;

- $\frac{LCB_{fp}}{LCG_{fp}}$, longitudinal centre of buoyancy-to-longitudinal centre of gravity ratio;

- $\frac{LCF_{fp}}{LCG_{fp}}$, longitudinal centre of flotation-to-longitudinal centre of gravity ratio;

- $\frac{LCG_{fp}}{KM_L}$, longitudinal centre of gravity-to-longitudinal metacentric height ratio.

Only hydrostatic parameters are considered. Dynamic influences on the parameters are neglected, because this would overcomplicate the estimation of the resistance of an arbitrary sailing yacht for the purpose of velocity prediction with VPPs. Only parameters describing the hull as a whole are considered. No separate parameters for the forepart and the afterpart of the hull are defined. The six ratios including LCG_{fp} or $z_{CoE_{eff}}$ are considered for the derivation of regression (v) only. LCG_{fp} is defined by Equation (4.4), and $z_{CoE_{eff}}$ is defined by Equation (4.6).

Quadratic terms of the above-mentioned explanatory variables are also considered. For stability and robustness, quadratic terms are not preferred. In general, quadratic terms enhance instability when the regressions are extrapolated to (slightly) outside the range of the original database. No cross or interaction terms of the above-mentioned explanatory variables are considered.

10.5. Scaling of the residuary resistance
Scaling of the residuary resistance is used to make the residuary resistance non-dimensional. Scaling allows for removing some of the largest known physical relationships between the dependent variable and the independent variables. More subtle physical relationships between the dependent variable and the independent variables become thereby more apparent.

In this analysis, the residuary resistance is assumed to scale with the hydrostatic buoyancy, $\nabla_c \rho g$, and the displacement-to-length ratio according to

$$\widetilde{R_R} = \frac{R_{R\theta_h}}{\nabla_c \rho g}\left(\frac{L_{WL}}{\nabla_c^{1/3}}\right),\tag{10.9}$$

where $\widetilde{R_R}$ is the dimensionless residuary resistance used in this regression analysis. Consequently, all the explanatory variables and the constant term in the derived regression formula are coupled with the displacement-to-length ratio. The supposed contribution of the explanatory variables to the residuary resistance is assumed to follow a similar trend as the displacement-to-length ratio.

This scaling is very similar to the scaling of the residuary resistance used by Keuning et al. [27,25]. The only difference between the two scalings is the coupling of the constant term in the regression with the displacement-to-length ratio. The scaling used by Keuning et al., shown in Equation (2.9), couples only the explanatory variables with the displacement-to-length ratio, whereas the scaling used in this analysis, Equation (10.9), couples also the constant term of the derived regression formula with the displacement-to-length ratio. Compared to the scaling used by Keuning et al., this coupling of the constant produces marginally more accurate regressions in this regression analysis.

10.6. Regressions for the upright trimmed residuary resistance
The following five regressions for the bare hull upright trimmed residuary resistance, $R_{R\theta_h}$, have been derived in this regression analysis:

(i) The expression for the minimum upright trimmed residuary resistance:

$$\frac{R_{R\theta_h}}{\nabla_c \rho g}\left(\frac{L_{WL}}{\nabla_c^{1/3}}\right) = a_0 + a_1\frac{B_{WL}}{L_{WL}} + a_2\frac{T_c}{B_{WL}} + a_3\frac{LCB_{fp}}{L_{WL}} + a_4\frac{LCB_{fp}}{LCF_{fp}} + a_5C_p + a_6C_x$$
$$+ a_7C_p^2 + a_8\left(\frac{LCB_{fp}}{L_{WL}}\right)^2 + a_9\left(\frac{LCB_{fp}}{LCF_{fp}}\right)^2;\tag{10.10}$$

(ii) The expression for the upright trimmed residuary resistance with the crew CoG position:

$$\frac{R_{R\theta_h}}{\nabla_c \rho g}\left(\frac{L_{WL}}{\nabla_c^{1/3}}\right) = b_0 + b_1 \frac{B_{WL}}{L_{WL}} + b_2 \frac{T_c}{B_{WL}} + b_3 \frac{LCB_{fp}}{L_{WL}} + b_4 \frac{LCB_{fp}}{LCF_{fp}} + b_5 C_p + b_6 C_x$$
$$+ b_7 C_p{}^2 + b_8 \left(\frac{LCB_{fp}}{L_{WL}}\right)^2 + b_9 \left(\frac{LCB_{fp}}{LCF_{fp}}\right)^2 ; \tag{10.11}$$

(iii) The expression for the upright trimmed residuary resistance with the crew middle position:

$$\frac{R_{R\theta_h}}{\nabla_c \rho g}\left(\frac{L_{WL}}{\nabla_c^{1/3}}\right) = c_0 + c_1 \frac{B_{WL}}{L_{WL}} + c_2 \frac{T_c}{B_{WL}} + c_3 \frac{LCB_{fp}}{L_{WL}} + c_4 \frac{LCB_{fp}}{LCF_{fp}} + c_5 C_p + c_6 C_x$$
$$+ c_7 C_p{}^2 + c_8 \left(\frac{LCB_{fp}}{L_{WL}}\right)^2 + c_9 \left(\frac{LCB_{fp}}{LCF_{fp}}\right)^2 ; \tag{10.12}$$

(iv) The expression for the upright trimmed residuary resistance with the crew back position:

$$\frac{R_{R\theta_h}}{\nabla_c \rho g}\left(\frac{L_{WL}}{\nabla_c^{1/3}}\right) = d_0 + d_1 \frac{B_{WL}}{L_{WL}} + d_2 \frac{T_c}{B_{WL}} + d_3 \frac{LCB_{fp}}{L_{WL}} + d_4 \frac{LCB_{fp}}{LCF_{fp}} + d_5 C_p + d_6 C_x$$
$$+ d_7 C_p{}^2 + d_8 \left(\frac{LCB_{fp}}{L_{WL}}\right)^2 + d_9 \left(\frac{LCB_{fp}}{LCF_{fp}}\right)^2 ; \tag{10.13}$$

(v) The expression for the upright trimmed residuary resistance incorporating the influence of the trimming moment of the crew's weight through the longitudinal centre of gravity:

$$\frac{R_{R\theta_h}}{\nabla_c \rho g}\left(\frac{L_{WL}}{\nabla_c^{1/3}}\right) = e_0 + e_1 \frac{B_{WL}}{L_{WL}} + e_2 \frac{T_c}{B_{WL}} + e_3 \frac{LCB_{fp}}{L_{WL}} + e_4 \frac{LCB_{fp}}{LCF_{fp}} + e_5 C_p + e_6 C_x$$
$$+ e_7 C_p{}^2 + e_8 \left(\frac{LCB_{fp}}{L_{WL}}\right)^2 + e_9 \left(\frac{LCB_{fp}}{LCF_{fp}}\right)^2 \tag{10.14}$$
$$+ e_{10} \frac{LCG_{fp}}{L_{WL}} + e_{11} \left(\frac{LCG_{fp}}{L_{WL}}\right)^2 ;$$

where a_i, b_i, c_i, d_i and e_i are the coefficients of these five regressions. The derived regressions contain all the hydrostatic parameters whose variations were specifically introduced into the systematic series. The influence of each parameter on the residuary resistance seems to follow the expected behaviour discussed in Subsection 3.2.1.

All the coefficients have been determined with the least-squares method for Froude numbers 0.25 up to 0.95 with increments of 0.10 and are listed in Table G.2. The upright resistance at any speed can be determined by fitting a cubic spline to the estimated resistance values using a least-squares fit. The parameter range covered by these regressions for the bare hull upright trimmed residuary resistance is listed in Tables 3.3 and G.1. This range is prescribed by the hydrostatic parameters of the hull shapes in the systematic series and by the longitudinal centre of gravity, LCG_{fp}, corresponding to the three different trimming moments of the crew's weight.

The five different expressions have different application possibilities. Expression (i) gives the minimum residuary resistance of the three crew positions in the database without any specification of the trimming moments of the driving force and the crew's weight. Expressions (ii), (iii) and (iv) give the residuary resistance for the crew CoG, middle and back positions, respectively. Expression (v) incorporates the influence of the trimming moment of the crew's weight on the resistance through the longitudinal centre of gravity.

For a high performance sailing yacht with a full crew, expression (i) is preferred, because this regression simulates the optimum performance of the yacht. The other regressions can be used for different crew configurations or other ranges of trimming moments. Regression (v) can be used to calculate

the resistance of a yacht subjected to an 'arbitrary' trimming moment of the crew's weight or movable ballast. It can also be used to interpolate between the three crew positions to find, for instance, the 'optimum' crew configuration.

All the expressions can be easily implemented in existing VPPs, because they contain only hydrostatic parameters and no terms involving the trimming moment of the driving force. These terms would require an estimate of the trimming moment of the driving force. Such an estimate is not straightforward to derive, because the driving force is equal to the resistance while its trimming moment influences the resistance. The formulation for the minimum resistance, regression (i), will be used in an existing VPP in Section 10.8. This illustrates the applicability of the derived regressions to the velocity prediction of high performance yachts with existing VPPs. A velocity prediction calculated with the new regression is compared to a velocity prediction calculated with the regressions of the DSYHS.

Expression (v) incorporates the influence of the trimming moment of the crew's weight through the longitudinal centre of gravity-to-length ratio. The longitudinal centre of gravity, LCG_{fp}, corresponding to a trimming moment of the crew's weight is an ideal independent variable to cover the effects of the crew on the residuary resistance. Together with the longitudinal centre of buoyancy-to-length ratio, the longitudinal centre of gravity-to-length ratio determines the hydrostatic trim angle of the yacht. The hydrostatic trim angle influences the resistance in various ways. The longitudinal centre of gravity is preferred over the effective centre of effort, because it is less sensitive to variations in the input parameters and provides more accurate and stable regressions. Moreover, it is a less complicated parameter and it is easier to define for an arbitrary yacht.

The longitudinal centre of gravity is used to translate the trimming moment of the crew's weight into a corresponding longitudinal centre of gravity of the yacht with Equation (4.4). Applying a trimming moment about the 'original' longitudinal centre of gravity, which is located above the hydrostatic longitudinal centre of buoyancy, or using a shift in the longitudinal centre of gravity of the yacht to cover the effects of the trimming moment is, of course, equivalent. The range of the longitudinal centre of gravity-to-length ratio covered by the new regressions for the bare hull upright trimmed residuary resistance is listed in Table G.1.

Note that the trimming moment of the driving force is not incorporated in the definition of the longitudinal centre of gravity. No specific definition of the trimming moment of the driving force is contained within any of the regressions. The trimming moment of the driving force corresponding to an estimated resistance is simply obtained from multiplying this resistance with $0.6L_{WL}$.

10.6.1. Similarity with the regression of the DSYHS

The derived regressions have a similar form as the regression of the DSYHS for the upright untrimmed residuary resistance, given by Equation (2.9). The new formulations contain additional quadratic terms, lack the displacement-to-waterplane area ratio and use a slightly different scaling of the residuary resistance. It is not surprising that the derived regressions contain similar parameters as the regression of the DSYHS, since the variations introduced into the new systematic series were based on the DSYHS regression.

In general, for smooth hulls with an almost constant draft-to-beam ratio over the entire waterline length, the draft-to-beam ratio is highly correlated with the displacement-to-waterplane area ratio. Compared to the regression of the DSYHS, the displacement-to-waterplane area ratio is removed from the new regressions, because it is indeed highly correlated to the draft-to-beam ratio for the new systematic series. The correlation coefficient between the two was 0.97, which implies that the two ratios are almost correlated. As a consequence, these two ratios are (almost) interchangeable in the regressions, without significantly affecting the accuracy of the regressions. Obviously, the coefficients of the regressions should be redetermined if the ratios are interchanged. Only one of these two ratios should be used in the regressions to avoid multicollinearity between the explanatory variables in the regressions. The draft-to-beam ratio is preferred over the displacement-to-waterplane area, because variations in this ratio were specifically introduced into the systematic series.

Multicollinearity should be avoided, because a linear relationship between two or more explanatory variables may result in erratic changes of the coefficients associated with the collinear variables in response to small changes in the dataset or the regression model. Within the dataset of the regression, multicollinearity does not necessarily affect the accuracy and the reliability of the regression model as a whole, but it may lead to misleading and invalid predictions of the effects of any explanatory variable

on the response variable. This makes it probably very difficult to identify redundant variables.

Two additional dimensionless forms of the waterplane area, namely, the waterplane area coefficient and the vertical prismatic coefficient, were considered as substitutions of the displacement-to-waterplane area ratio, but they did not improve the formulations. The waterplane area coefficient was highly correlated to the prismatic coefficient, and the vertical prismatic coefficient had no significant influence on the residuary resistance. Therefore, the waterplane area is not included in the new regressions.

10.6.2. Accuracy
The regressions are fitted to the database with the least-squares method for Froude numbers 0.25 up to 0.95 with increments of 0.10. The coefficient of determination, R^2, for every regression at every Froude number is given in Table G.2. In general, the coefficient of determination is larger than 0.995 for every Froude number, which is considered to be very good. The noteworthy exceptions are: regression (ii), Froude number 0.85 with a R^2 of 0.977; regression (iii), Froude number 0.25 with a R^2 of 0.987; regression (iv), Froude number 0.25 with a R^2 of 0.898; and regression (v), Froude numbers 0.25, 0.85 and 0.95 with a R^2 of 0.955, 0.967, and 0.988, respectively. With the exception of regression (iv) at Froude number 0.25, the regressions produce accurate and adequate predictions.

An illustration of the accuracy of the fit of regression (i) to the database is depicted in Figure 10.1 for three of the eight speeds. The predicted values are plotted against their observed values. The relative residuals are also depicted. In general, the predicted values fall closely against the target line $y = x$. Some exceptions excluded, the residuals are between plus or minus 1 percent of the corresponding observed value, which is considered to be good. The other regressions have similar fits to the database. Some have slightly higher residuals, which is of course related to the slightly worse coefficient of determination for some regressions and some speeds.

For every model itself, the regressions produce accurate predictions with a coefficient of determination above 0.998. For the sake of illustration, the resistance predicted with regression (i) and the resistance in the database of some of the models in the new systematic series are plotted in Figure 10.2. The fits are satisfactory over the entire speed range. Regressions (ii), (iii) and (iv) produce similar fits. Note that no cubic spline is fitted to the estimated resistance values, because this would distract from the main goal: illustrating the estimation of the actual data points. The estimated data points are simply connected with straight line segments in all the figures presented in this chapter. Fitting a cubic spline to the estimated data points using a least-squares fit would provide smoother and more realistic curves.

For the sake of illustration, the residuary resistance predicted with regression (v) and the resistance in the database of some of the models are plotted in Figure 10.4. In general, the regression incorporating the influence of the trimming moment of the crew's weight produces accurate predictions. Only for Syssers 86 and 94, the prediction is a bit worse, but it still captures the trends of the speed-resistance curves and the differences between the crew positions nicely. The prediction for Sysser 94 is plotted in Figure 10.4c.

The residuary resistance values predicted with the five regressions have been compared against the database. For prediction f_i of resistance value y_i from the database, a relative comparison error, η, is defined by

$$\eta = \frac{|f_i - y_i|}{y_i} \cdot 100\%. \tag{10.15}$$

The maximum, minimum and mean values of the relative comparison errors for every Froude number and every regression are listed in Table G.2. In general, the maximum error is very reasonable and the average relative comparison error is below 1 percent, which is considered to be very good. The noteworthy exceptions are: regression (iv), Froude number 0.25 with a maximum error of 10% and an average error of 2%; and regression (v), Froude numbers 0.25 and 0.85 with maximum errors of 31% and 10%, respectively, and average errors of 6% and 2%, respectively.

For stability of the regressions, it is important that the explanatory variables in the regression are not strongly correlated to each other. The correlation between two explanatory variables X_1 and X_2 is de-

termined with the correlation coefficient, $\rho(X_1, X_2)$, defined by Equation (10.4). The correlation between the independent variables in the final regressions is given in Table 10.1. The correlation between the explanatory variables is low, which contributes to the stability of the regressions.

Table 10.1: Correlation between the explanatory variables in the final regressions, expressed as the correlation coefficient defined by Equation (10.4).

	$\frac{\nabla_c^{1/3}}{L_{WL}}$	$\frac{B_{WL}}{L_{WL}}$	$\frac{T_c}{B_{WL}}$	$\frac{LCB_{fp}}{L_{WL}}$	$\frac{LCB_{fp}}{LCF_{fp}}$	C_p	C_x	$\frac{LCG_{fp}}{L_{WL}}$
$\frac{\nabla_c^{1/3}}{L_{WL}}$	1.00	0.28	0.28	0.00	0.00	-0.04	0.26	-0.09
$\frac{B_{WL}}{L_{WL}}$	0.28	1.00	-0.80	0.04	0.05	-0.44	0.05	-0.01
$\frac{T_c}{B_{WL}}$	0.28	-0.80	1.00	-0.05	-0.04	0.25	-0.02	-0.04
$\frac{LCB_{fp}}{L_{WL}}$	0.00	0.04	-0.05	1.00	0.71	0.03	-0.04	0.32
$\frac{LCB_{fp}}{LCF_{fp}}$	0.00	0.05	-0.04	0.71	1.00	-0.11	0.06	0.23
C_p	-0.04	-0.44	0.25	0.03	-0.11	1.00	-0.20	0.01
C_x	0.26	0.05	-0.02	-0.04	0.06	-0.20	1.00	-0.04
$\frac{LCG_{fp}}{L_{WL}}$	-0.09	-0.01	-0.04	0.32	0.23	0.01	-0.04	1.00

10.6.3. Alternative regressions

Quadratic terms generally enhance instability when the regressions are extrapolated to (slightly) outside the range of the original explanatory variables. Therefore, alternative formulations of the five regressions are also given. These alternative formulations contain the same parameters as Equations (10.10) up to (10.14), but exclude the quadratic terms with the exception of the $(LCG_{fp}/L_{WL})^2$ term in Equation (10.14). This quadratic term is needed, because there is a distinctive non-linear relationship between the resistance values of the three crew positions at every speed as can been seen in Figure 10.4. These alternative formulations provide more stability and robustness at the expense of accuracy.

All the coefficients have been redetermined for the alternative regressions with the least-squares method and are listed in Table G.3. The coefficient of determination R^2 and the relative comparison errors for every regression and every Froude number are also given in this table. The accuracy of the alternative formulations is indeed a bit lower, but still very acceptable.

For the sake of illustration, the resistance predicted with regression (i) and the resistance predicted with regression (v) are depicted for some of the models with their corresponding resistance values in the database in Figures 10.3 and 10.5, respectively. These predictions are very similar to the predictions including the quadratic terms, plotted in Figures 10.2 and 10.4, but have a lower accuracy as can been seen in these four figures.

For the prediction of the resistance of an arbitrary sailing yacht whose hydrostatic parameters clearly satisfy the parameter range covered by the systematic series, it is advisable to use the full regressions, including the quadratic terms, because these regressions produce the most accurate results in that range. For predictions outside the parameter range covered by the new systematic series, it is advisable to use the full regressions and the alternative regressions in parallel. The results of both methods should be checked for credibility. The one seeming to have the largest credibility can then be used as the prediction of the resistance. It should be noted that extrapolation to outside any database with any regression will always introduce errors. Extrapolation should always be used with caution. It is up to the user to decide which formulation of the regressions is the most appropriate one for the job at hand.
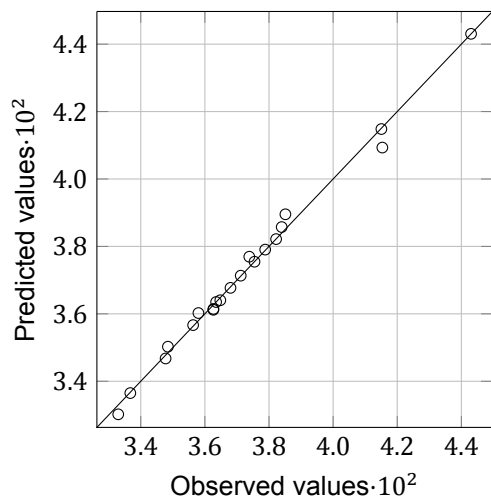
(a) Predicted versus observed values at $Fn = 0.35$.
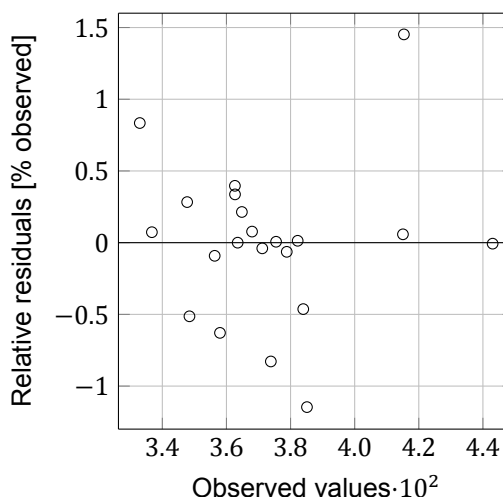
(b) Relative residuals at $Fn = 0.35$.
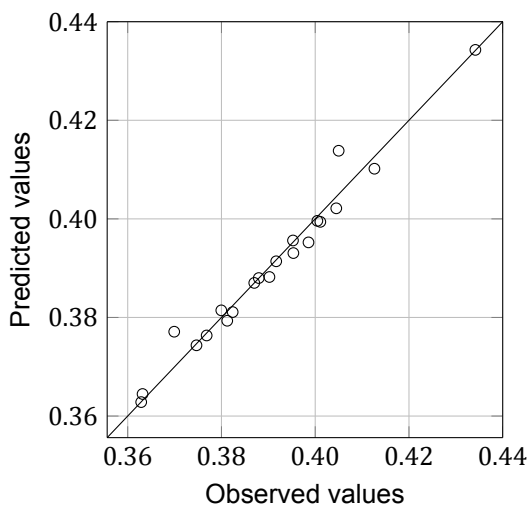
(c) Predicted versus observed values at $Fn = 0.65$.
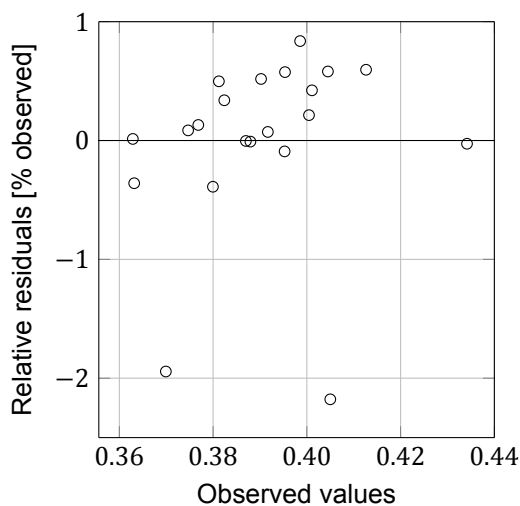
(d) Relative residuals at $Fn = 0.65$.
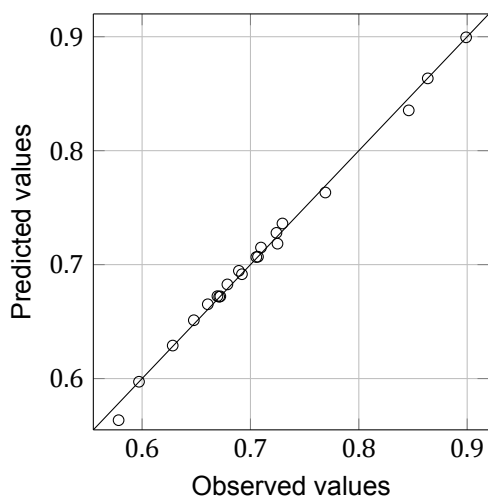
(e) Predicted versus observed values at $Fn = 0.95$.
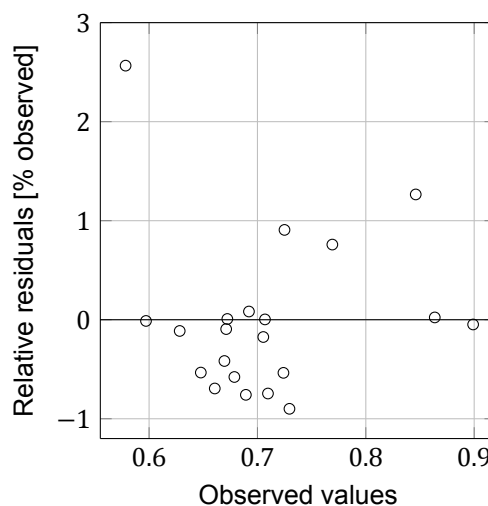
(f) Relative residuals at $Fn = 0.95$.

Figure 10.1: Illustration of the accuracy of the fit of regression (i) to the database.
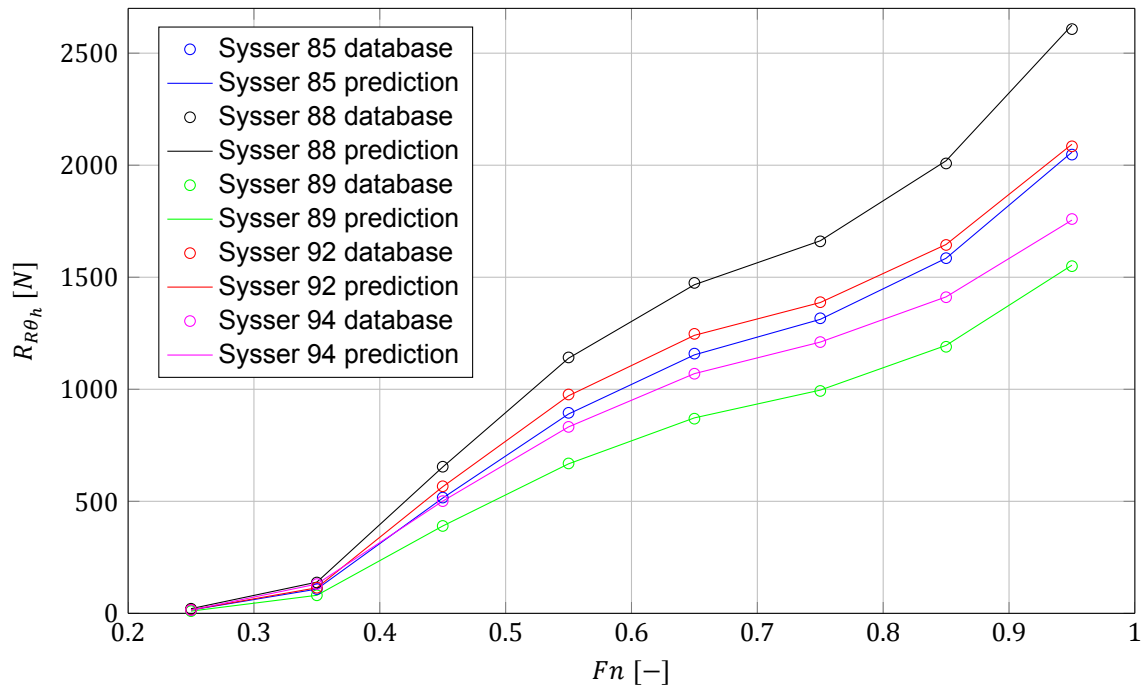
(a) Bare hull upright trimmed residuary resistance $R_{R\theta_h}$.
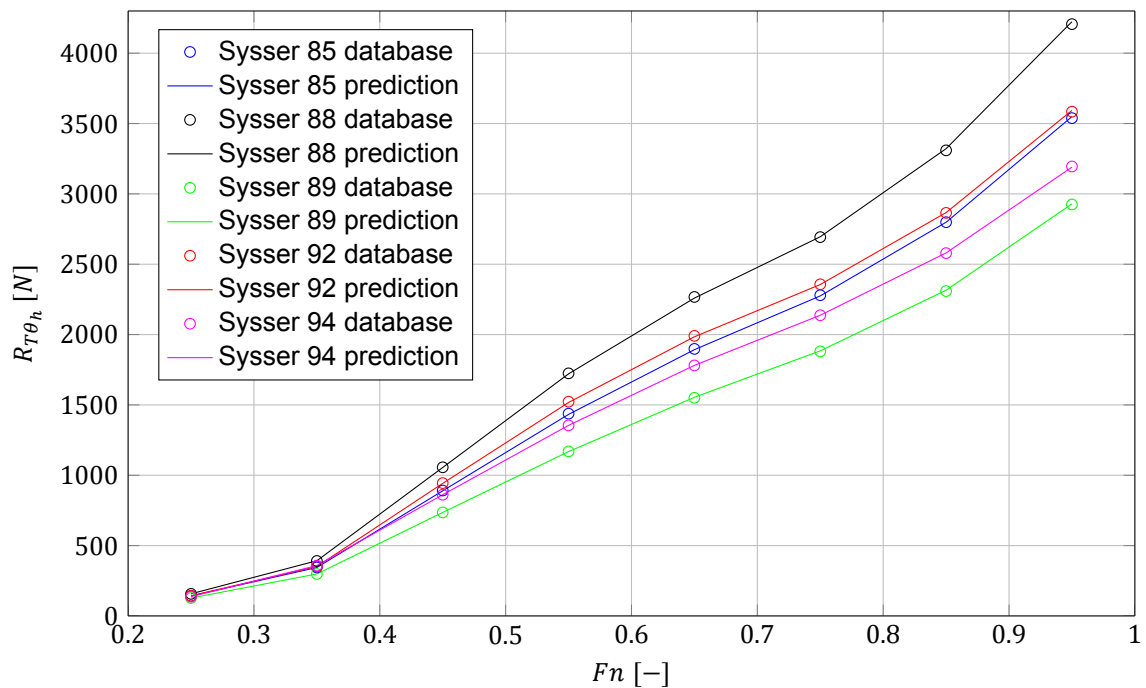
(b) Bare hull upright trimmed resistance $R_{T\theta_h}$.

Figure 10.2: The resistance predicted with regression (i), including the quadratic terms, and the resistance in the database.
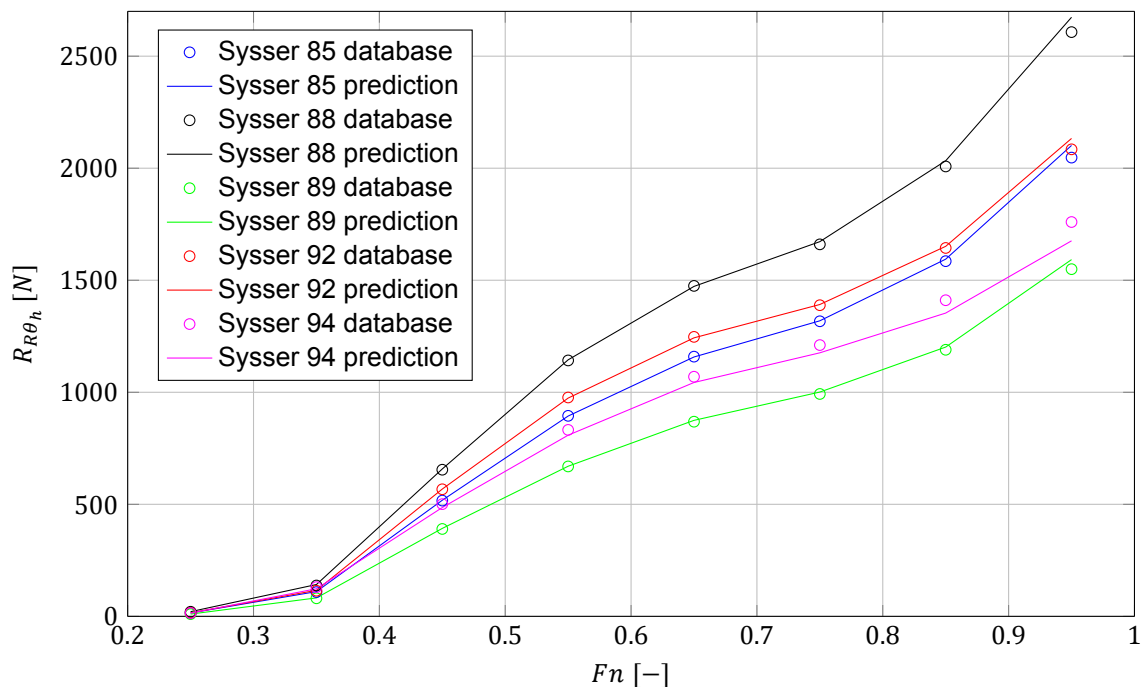
(a) Bare hull upright trimmed residuary resistance $R_{R\theta_h}$.
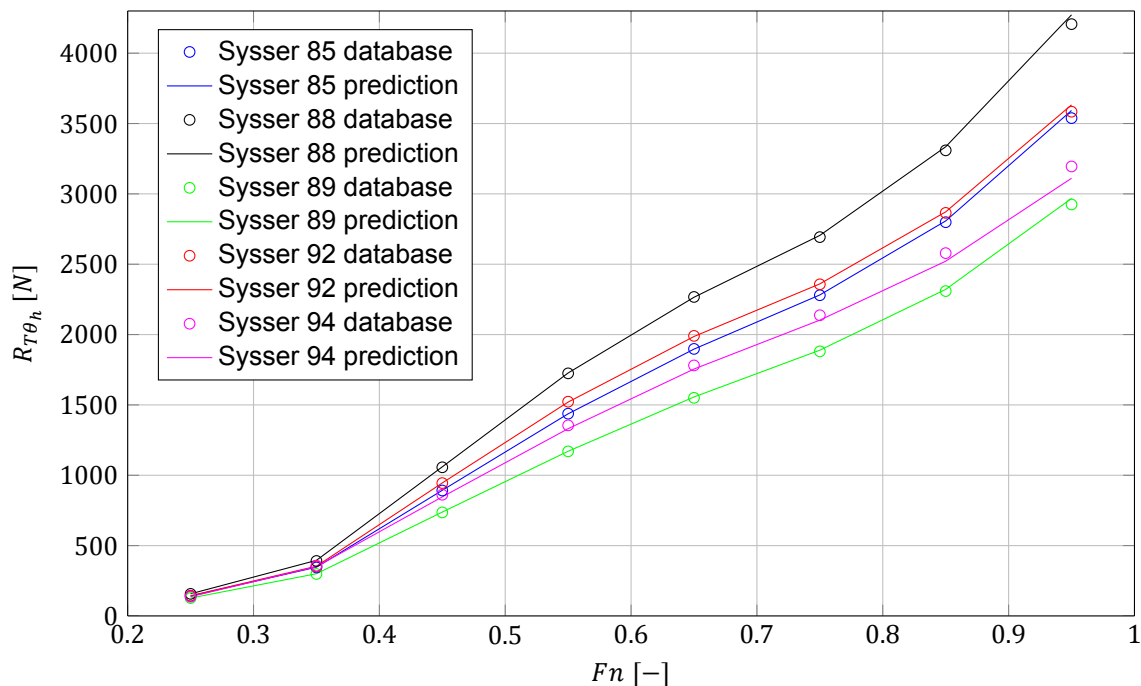
(b) Bare hull upright trimmed resistance $R_{T\theta_h}$.

Figure 10.3: The resistance predicted with regression (i), excluding the quadratic terms, and the resistance in the database.
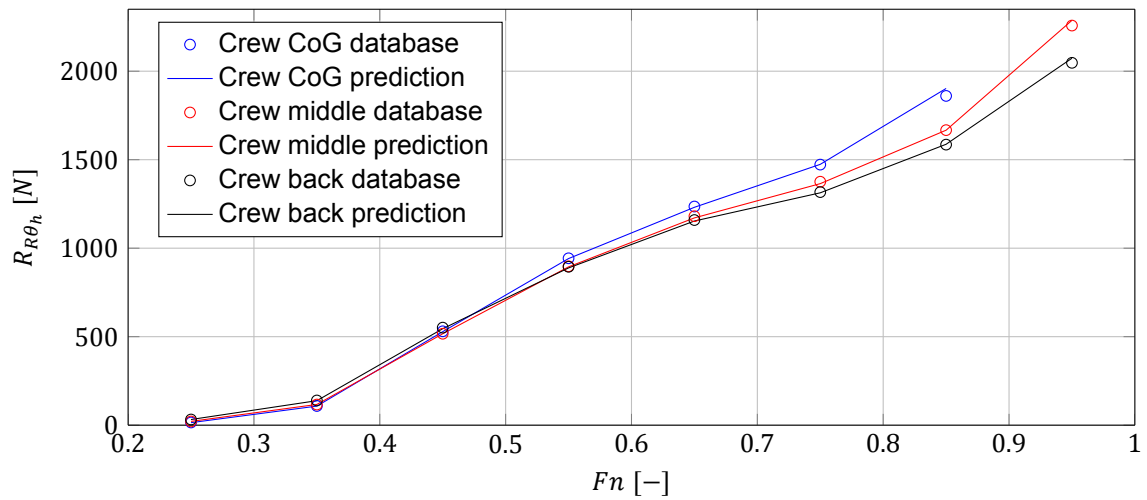
(a) Bare hull upright trimmed residuary resistance of Sysser 85 for the three crew positions.
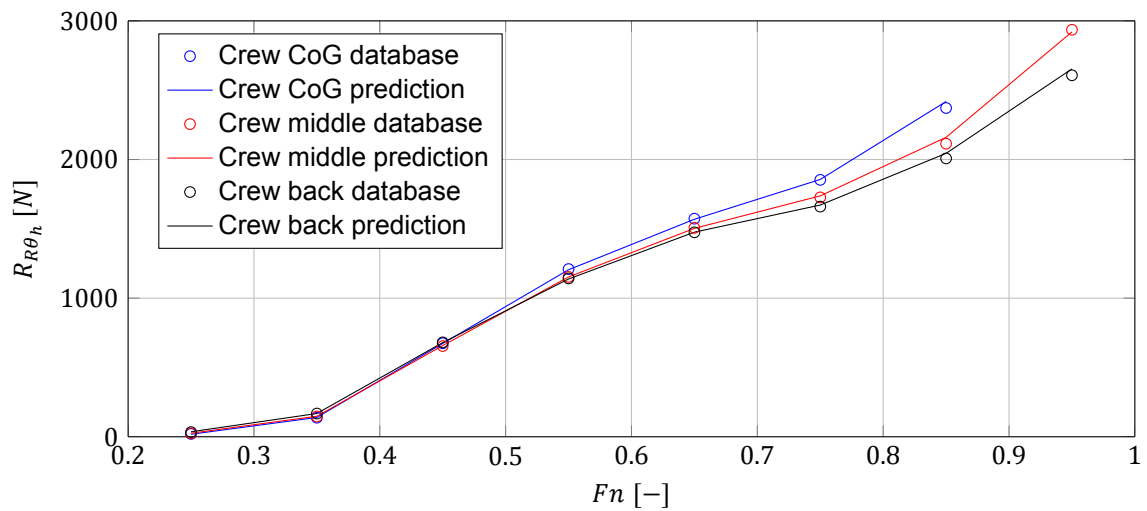
(b) Bare hull upright trimmed residuary resistance of Sysser 88 for the three crew positions.
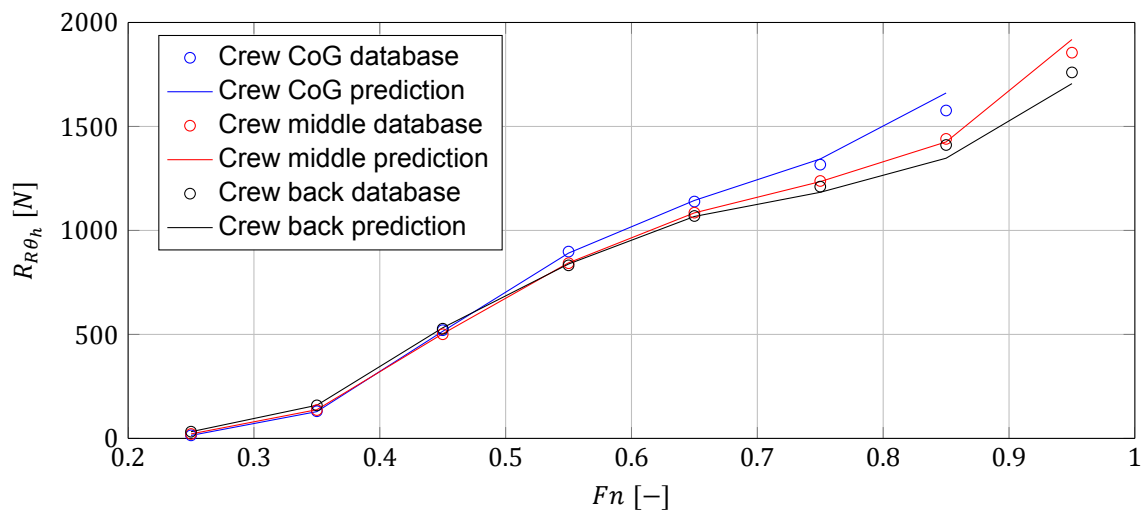
(c) Bare hull upright trimmed residuary resistance of Sysser 94 for the three crew positions.

Figure 10.4: The resistance predicted with regression (v), including the quadratic terms, and the resistance in the database.
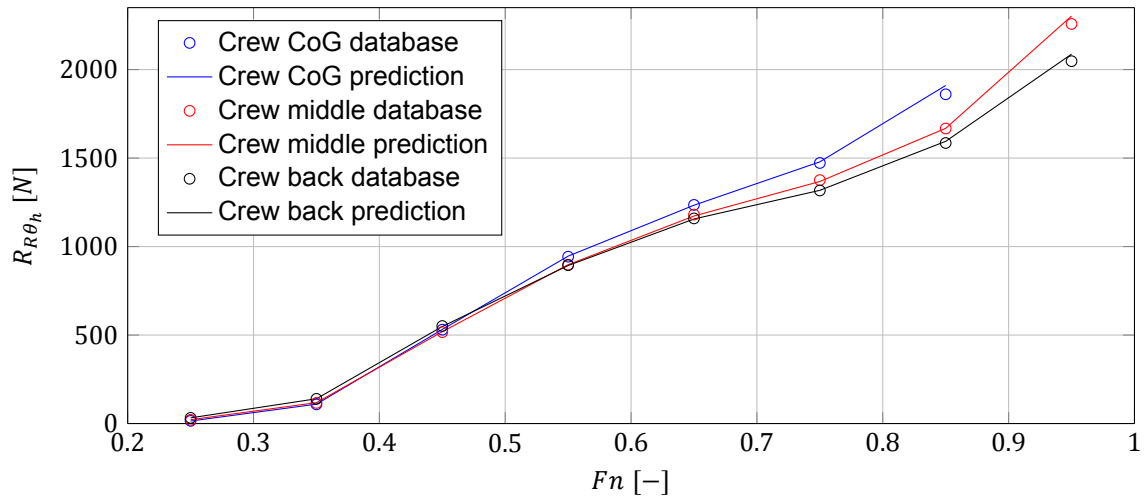
(a) Bare hull upright trimmed residuary resistance of Sysser 85 for the three crew positions.
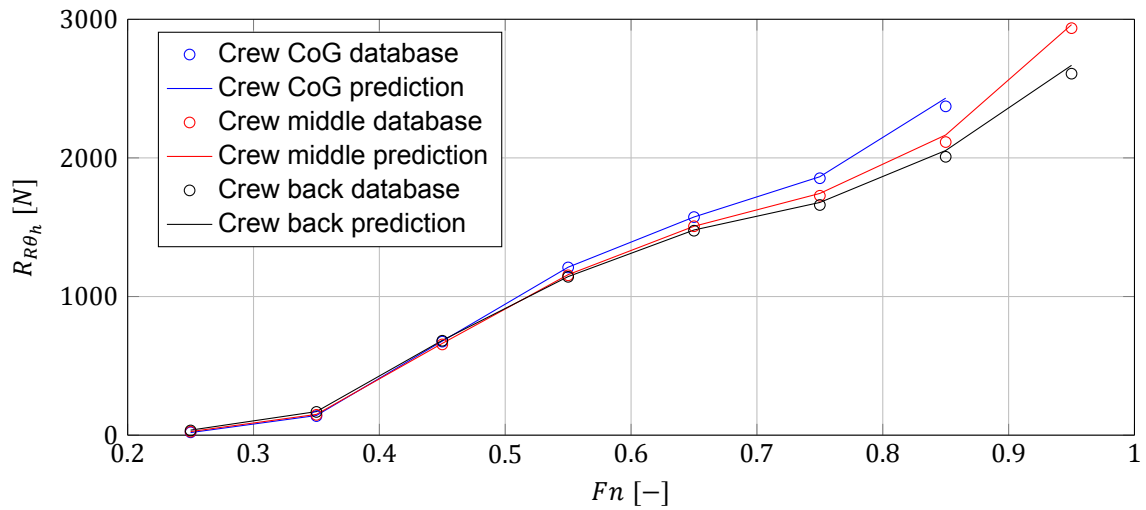
(b) Bare hull upright trimmed residuary resistance of Sysser 88 for the three crew positions.
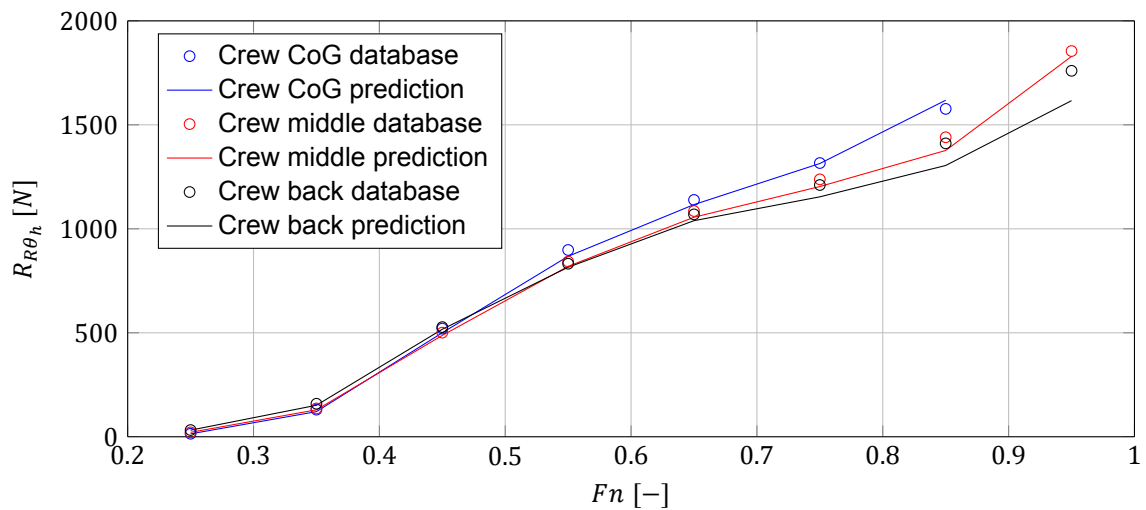
(c) Bare hull upright trimmed residuary resistance of Sysser 94 for the three crew positions.

Figure 10.5: The resistance predicted with regression (v), excluding the quadratic terms with the exception of $(LCG_{fp}/L_{WL})^2$, and the resistance in the database.

10.6.4. Sensitivity
The derived regressions should not be too sensitive to variations in the input parameters. The sensitivity of the five regressions to variations in the input parameters have been checked by altering the value of each parameter, one at a time, by 1 percent. The effects of these variations on the resistance have been calculated and compared to the situation with no variation. The sensitivity is defined as the absolute percentage change from the situation with no variation. In general, the regressions seem to be most sensitive to variations in the longitudinal centre of buoyancy-to-length ratio and the longitudinal centre of buoyancy-to-longitudinal centre of flotation ratio. This is not surprising, since small variations in the location of the longitudinal centre of buoyancy generally have a relatively large influence on the residuary resistance. Furthermore, these are also the quadratic terms contained within the regression models. The alternative regressions are slightly less sensitive to variations in these two ratios.

For illustration, the maximum and the average sensitivity of regression (i), including the quadratic terms, to variations in the input parameters are listed in Table G.4. In general, the sensitivity is very reasonable. For speeds above Froude number 0.35, the maximum impact on the predicted resistance is 3 percent for all the models, which is considered to be good. For Froude numbers 0.25, 0.35 and 0.95, the maximum sensitivities are 11%, 6% and 7%, respectively, and are all related to variations in the longitudinal centre of buoyancy-to-length ratio or the longitudinal centre of buoyancy-to-longitudinal centre of flotation ratio. In general, the average sensitivity over all the models in the series is very reasonable with values about 1 percent. The noteworthy exceptions are again related to variations in the longitudinal centre of buoyancy-to-length ratio or the longitudinal centre of buoyancy-to-longitudinal centre of flotation ratio at Froude numbers 0.25, 0.35 and 0.95. Regressions (ii), (iii) and (iv) have a similar sensitivity as regression (i).

The maximum and the average sensitivity of regression (v), including the quadratic terms, to variations in the input parameters are given in Table G.5. The sensitivity of this regression is similar to the sensitivity of regression (i). Again, for speeds above Froude number 0.35, the maximum impact on the predicted resistance is 3 percent. The noteworthy exceptions are Froude numbers 0.25, 0.35, 0.85 and 0.95, again related to variations in the longitudinal centre of buoyancy-to-length ratio or the longitudinal centre of buoyancy-to-longitudinal centre of flotation ratio. Another noteworthy exception is the longitudinal centre of gravity-to-length ratio for Froude numbers 0.25 and 0.35 with maximum variations of 14 percent and 6 percent, respectively. This is not unexpected, since the trim angle of a yacht is related to this ratio. At the lower speeds, small changes in trim angle give relatively large differences in resistance due to, for instance, immersed transom effects. Nevertheless, the sensitivity seems to be too high to be explained by only the physics involved. It seems to be a small defect in the regressions.

In conclusion, the sensitivity of all the regressions is very reasonable. Only for Froude numbers 0.25 and 0.35, the regressions seem to be a bit too sensitive to variations in some of the parameters. All the regressions are the most sensitive to variations in the longitudinal centre of buoyancy-to-length ratio, the longitudinal centre of buoyancy-to-longitudinal centre of flotation ratio and the longitudinal centre of gravity-to-length ratio. The alternative regressions excluding the quadratic terms, with the exception of the quadratic term of the longitudinal centre of gravity-to-length ratio, are slightly less sensitive to variations in these first two ratios.

10.7. Verification of the regressions
In order to give a verification of the regression formulas, the regressions are tested on three models not belonging to the systematic series. A comparison of the predicted resistance with numerical results is given for two models. For the other model, the predicted resistance is compared with experimental data.

10.7.1. Syssers 83 and 84
Additional numerical simulations were performed for Syssers 83 and 84 to illustrate the applicability of the regressions to other models not belonging to the systematic series. The numerical simulations for these two models were performed only for the crew CoG position in exactly the same way as the numerical simulations for the models in the systematic series. The resistance values of these two models are calculated with CFD at model scale and extrapolated to prototype scale. For the extrapolation of

the resistance forces, the method described in Section 2.2 is used. A characteristic length of $0.9L_{WL}$ is used for the Reynolds number. This length is also used for the models in the systematic series.

The lines plans and the hydrostatic parameters of Syssers 83 and 84 are given in Appendix C. The hydrostatic ratios and the hydrostatic coefficients of these models are compared to the parameter range of the systematic series in Table 10.2. For Sysser 83, its maximum sectional area coefficient falls slightly outside the range of the series. For Sysser 84, its longitudinal centre of buoyancy-to-longitudinal centre of flotation ratio falls slightly outside the range of the series. Both models do not comply with all the design characteristics of the modern hull shapes in the systematic series. The hull shapes in this series distinguish themselves from the more 'traditional' hull shapes by their straight vertical bows, the wide transoms and the very long waterlines compared to the overall length. Syssers 83 and 84 have no straight vertical bows and have relatively short waterlines compared to their overall length. Sysser 83 has a 'traditional' narrow transom shape. Sysser 84 has a 'modern' wide transom shape at the waterline, but it still has a long overhang aft. Syssers 83 and 84 are outdated designs.

The residuary resistance predicted with the regression for the upright trimmed residuary resistance with the crew CoG position, regression (ii), including and excluding the quadratic terms, and the with CFD computed resistance are plotted in Figure 10.7. The relative comparison errors of the prediction of the residuary resistance with respect to the CFD results is given in Table 10.4. In general, the comparison is considered to be good; especially, if it is taken into consideration that the hull shapes of these two models differ from the characteristic hull shapes in the systematic series. Only for Froude number 0.25, the prediction is unreasonable with a relative comparison error of -36 percent for the prediction of the residuary resistance. For Froude 0.35, the prediction is reasonable. After Froude number 0.45, the prediction is quite accurate. A noticeable observation is that the resistance of Sysser 84 is better predicted than the resistance of Sysser 83. This is probably related to the similar wide transom shape of Sysser 84 compared to the models in the systematic series while Sysser 83 has a more traditional narrow transom shape.

Again, there is a small difference between the prediction including the quadratic terms and the prediction excluding those terms in the regression. For Sysser 83, the prediction excluding the quadratic terms is more accurate. For Sysser 84, the prediction including the quadratic terms is more accurate. This illustrates that for predictions (slightly) outside the parameter range covered by the systematic series and for yachts with different design characteristics, it is advisable to use the full regressions and the alternative regressions in parallel.

10.7.2. The SYRF Wide Light Project

As a part of the Sailing Yacht Research Foundation (SYRF) Wide Light Project [38], one modern high performance sailing yacht design was tested by the Wolfson Unit in the QinetiQ #2 towing tank at the Haslar Marine Technology Park, Gosport, United Kingdom. This towing tank has a length of 270 metres, a width of 12 metres and a water depth of 5.5 metres. The model tested has an overall length of 4.88 metres and a displacement of 197 kilograms. The lines plan of the Wide Light yacht is depicted in Figure 10.6. The hydrostatic parameters of this yacht are compared to the parameter range of the systematic series in Table 10.2. For this yacht, the displacement-to-length ratio falls slightly outside the range of the series. Its maximum sectional area coefficient falls also outside the range of the series.

The experimental results of this model provide a good possibility for the verification of the derived regressions. For the sake of comparison, the experimental results are extrapolated to a waterline length of ten metres with the method described in Section 2.2. A characteristic length of $0.9L_{WL}$ is used for the Reynolds number. This length is also used for the models in the systematic series.

The Wide Light yacht was tested for a predetermined longitudinal centre of gravity to incorporate the effects of representative trimming moments of the driving force. A different position of the longitudinal centre of gravity was used at every speed to cover the increase in trimming moment of the driving force with speed. In the present study, a different definition of the longitudinal centre of gravity is used in the regressions. The longitudinal centre of gravity-to-length ratio is used in the regressions to incorporate only the trimming moment of the crew's weight. The trimming moment of the driving force is not explicitly contained within the regressions.

For the purpose of comparing the experimental results with the regressions, the longitudinal centre of gravity used during the resistance measurement has to be transformed into the definition of the longitudinal centre of gravity as used in the regressions; i.e. the trimming moment applied during the measurement run has to be converted into a trimming moment of the driving force and a trimming mo-

ment of the crew's weight. The moment applied during the measurement run is equal to the difference of the hydrostatic LCB_{fp} and the LCG_{fp} used during the measurement run, multiplied by the weight of the model. The following procedure is used for this transformation: the measured resistance is multiplied with $0.60L_{WL}$ to obtain the trimming moment of the driving force; this moment is subtracted from the moment applied during the measurement run; the difference in trimming moment is attributed to a trimming moment of the crew's weight; the corresponding LCG_{fp} is calculated with Equation (4.4). With this definition of the longitudinal centre of gravity, the experimental results can be compared with the resistance predicted with regression (v). The corresponding LCG_{fp}-to-L_{WL} ratios are listed in Table 10.3.

The residuary resistance predicted with regression (v), including and excluding the quadratic terms, and the measured resistance values are plotted in Figure 10.8. The total bare hull resistance values are also given. A cubic spline is fitted to the estimated resistance values using a least-squares fit. This fit is used to estimate the resistance values at the intermediate Froude numbers 0.3, 0.4, 0.5, and so on. The resistance is underpredicted at every speed compared to experimental results. Nevertheless, the trends of the speed-resistance curve are captured perfectly and the underprediction is not that large.

The relative comparison errors of the prediction of the residuary resistance with respect to the experimental results is listed in Table 10.4. For Froude numbers 0.25 and 0.35, the prediction of the residuary resistance is unreasonable with relative comparison errors of -66 percent and -35 percent, respectively. After Froude number 0.35, the prediction is quite accurate. There is almost no difference between the prediction including the quadratic terms and the prediction excluding those terms. In general, the comparison is considered to be good; especially, if it is taken into consideration that the midship sectional area falls outside the range of the series and that a comparison with experimental results is made while the database of the series contains only numerical results. Based on the validation analysis discussed in the previous chapter, the experimental resistance values are likely to be higher than the numerical resistance values computed with CFD.

This difference between the experimental results and the numerical results contributes to the comparison error between the predicted resistance, which is based on a database of numerical results, and the measured resistance. Hence, it is likely that the regressions underpredict the resistance compared to the experimental results. As a part of the Wide Light Project, CFD computations were conducted for the Wide Light yacht according to the experimental test conditions with the FINE™/Marine flow solver. Similar comparison errors between the computed resistance and the measured resistance were found as those of the numerical simulations for the new systematic series, listed in Table 9.2.

10.8. Velocity prediction

For the velocity prediction of sailing yachts, velocity prediction programs (VPPs) are used. A VPP predicts the velocity of a yacht for various wind strengths and wind directions by balancing hydrodynamic forces acting on the hull and aerodynamic forces acting on the sails. A detailed description of the structure of a VPP and the formulations involved is given by the Offshore Racing Congress [36]. VPPs are used extensively for the design of yachts and the determination of ratings for individual yachts. These ratings allow yachts of different sizes and with different characteristics to race each other with an equal chance to win.

The velocity prediction with a VPP relies on a set of expressions, as function of the hydrostatic parameters of yacht hulls, for the estimation of the hydrodynamic forces acting on yachts. The regression formulas of the DSYHS, given in Chapter 2, are used in VPPs for the estimation of the hydrodynamic forces. Even for modern yachts, the regressions of the DSYHS are the most accurate prediction method as was shown by Raymond [40]. Nevertheless, as discussed in Section 2.5, the DSYHS regressions are less applicable to modern high performance yacht designs due to the range of parameters contained within the DSYHS and the limited speed range of the DSYHS. The accuracy of the performance prediction for modern yachts suffers from this in some extent.

To improve the velocity prediction, new regressions were derived to more accurately predicted the bare hull upright trimmed resistance of high performance yachts. The applicability of the derived regressions to the velocity prediction of high performance yachts with existing VPPs is illustrated in this section. The regression for the minimum bare hull upright trimmed resistance is used in an existing VPP to calculate a velocity prediction of a TP52-design. This velocity prediction is compared with a

Table 10.2: Hydrostatic parameters of Sysser 83, Sysser 84 and the Wide Light yacht. The maximums and the minimums of the parameter range covered by the new regression are also listed. Parameters outside this range are highlighted in red.

	$\frac{\nabla_c^{1/3}}{L_{WL}}$	$\frac{B_{WL}}{L_{WL}}$	$\frac{T_c}{B_{WL}}$	$\frac{LCB_{fp}}{L_{WL}}$	$\frac{LCB_{fp}}{LCF_{fp}}$	C_p	C_x
Sysser 83	0.131	0.189	0.157	0.521	0.931	0.546	0.730
Sysser 84	0.130	0.187	0.155	0.532	0.914	0.578	0.711
Wide Light	0.123	0.192	0.119	0.526	0.923	0.562	0.751
Maximum	0.137	0.239	0.195	0.560	0.957	0.603	0.726
Minimum	0.124	0.175	0.106	0.515	0.919	0.497	0.633

Table 10.3: The longitudinal centre of gravity-to-length ratios used for the resistance measurements of the Wide Light yacht, converted into the definition of the longitudinal centre of gravity-to-length ratio as used in regression (10.14).

$Fn\ [-]$	0.25	0.35	0.45	0.55	0.65	0.75
$\frac{LCG_{fp}}{L_{WL}}$	0.5249	0.5259	0.5273	0.5280	0.5304	0.5325

Table 10.4: Relative comparison errors of the prediction of the residuary resistance with respect to either CFD results or experimental results for Sysser 83, Sysser 84 and the Wide Light yacht. Errors are given as a percentage of either numerical or experimental results.

(a) Prediction with regressions including the quadratic terms.

$Fn\ [-]$	0.25	0.35	0.45	0.55	0.65	0.75	0.85
Sysser 83	-36.1	12.1	10.6	3.0	-1.4	-2.6	8.6
Sysser 84	-35.8	-7.0	0.9	-2.5	-3.9	-4.3	0.0
Wide Light	-66.1	-34.9	-8.5	-5.0	-8.5	-11.0	

(b) Prediction with regressions excluding the quadratic terms with the exception of $(LCG_{fp}/L_{WL})^2$.

$Fn\ [-]$	0.25	0.35	0.45	0.55	0.65	0.75	0.85
Sysser 83	-35.4	10.3	9.5	2.0	-1.8	-4.5	2.7
Sysser 84	-37.8	-11.1	-0.5	-4.1	-4.7	-2.9	3.4
Wide Light	-66.5	-35.1	-8.4	-5.1	-8.6	-10.8	
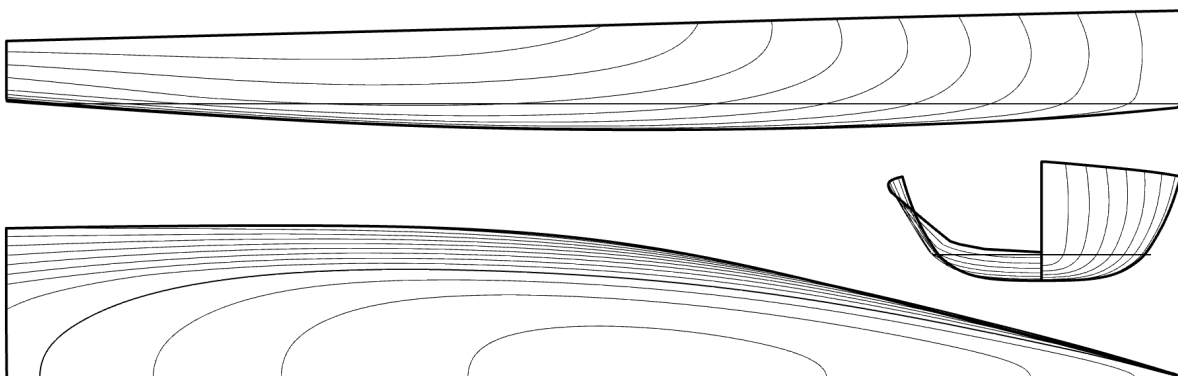
Figure 10.6: Lines plan of the SYRF Wide Light yacht [38].
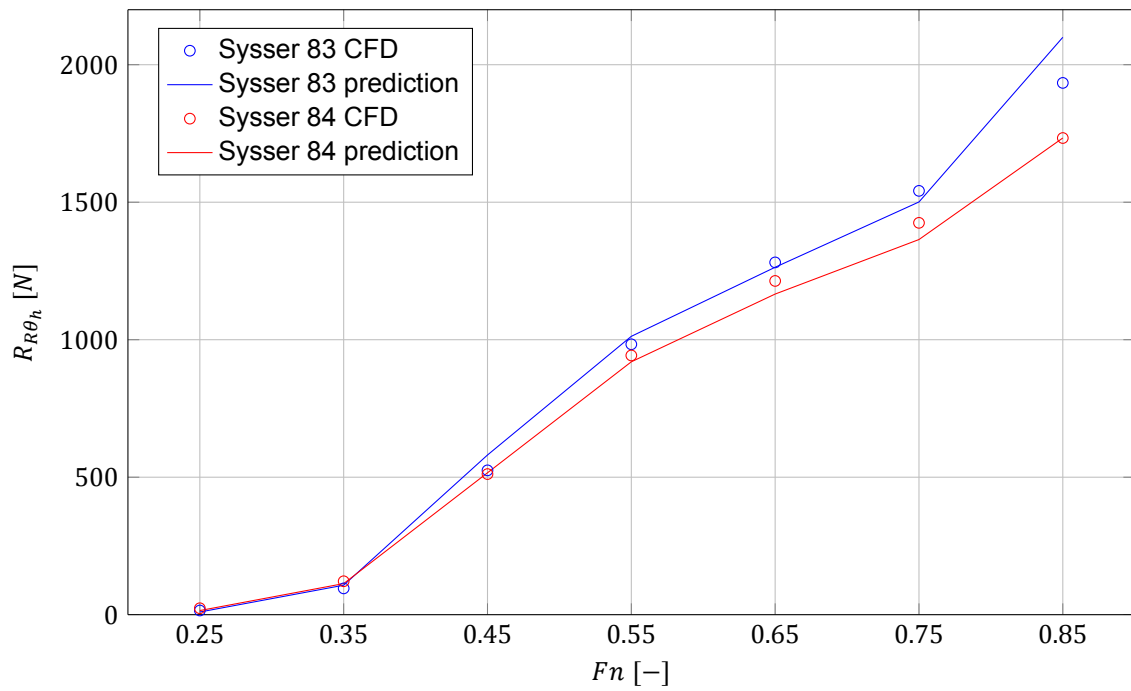
(a) Prediction of the upright trimmed residuary resistance, $R_{R\theta_h}$, including the quadratic terms in the regression.
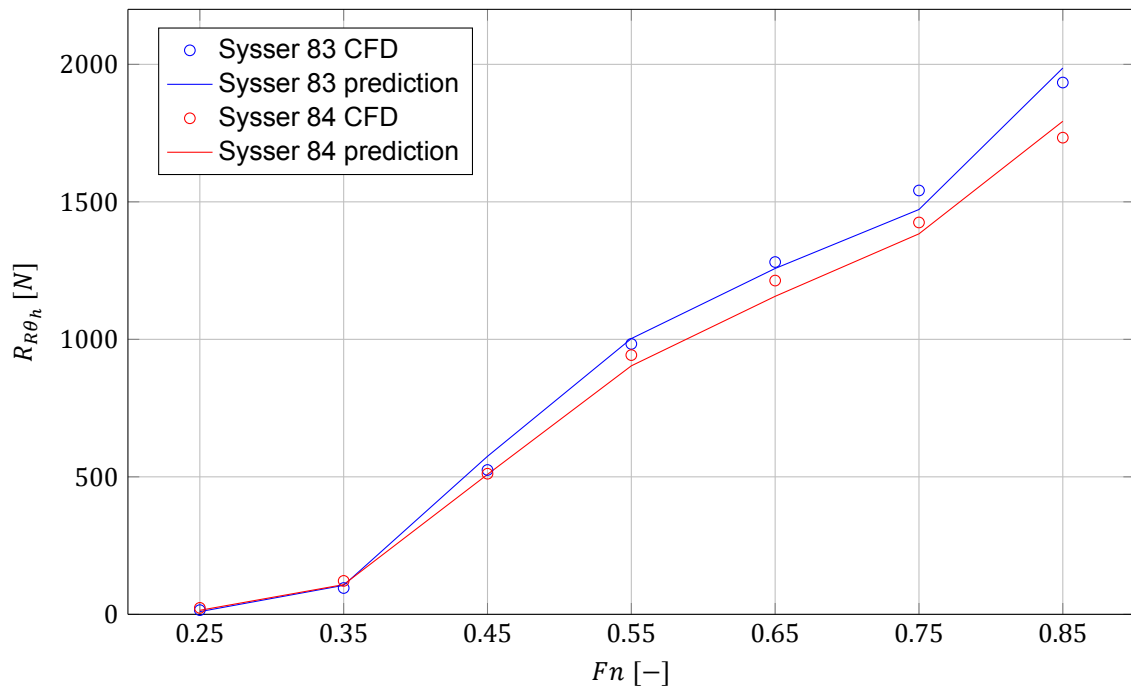
(b) Prediction of the upright trimmed residuary resistance, $R_{R\theta_h}$, excluding the quadratic terms in the regression.

Figure 10.7: The resistance of Sysser 83 and Sysser 84 predicted with regression (ii) and calculated with CFD for the crew CoG position.
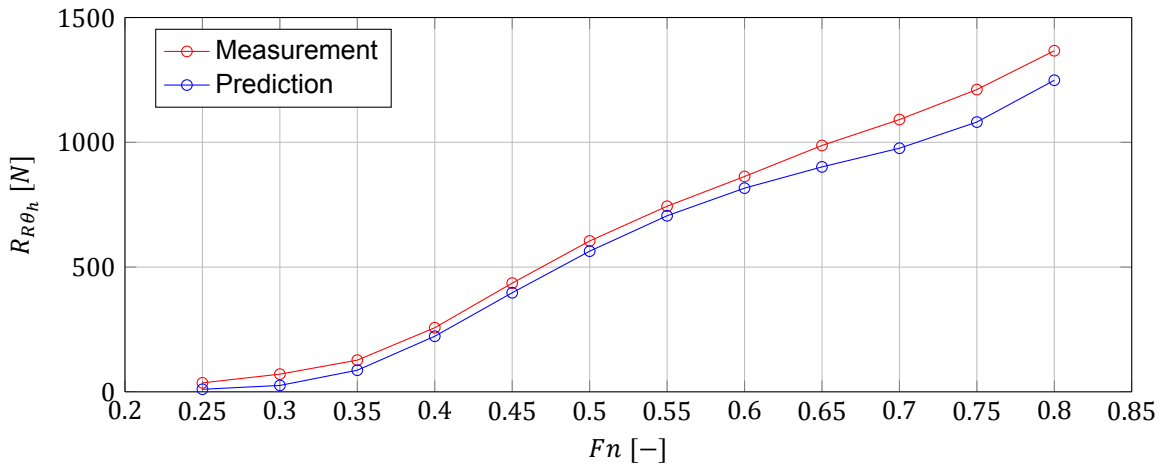
(a) Bare hull upright trimmed residuary resistance $R_{R\theta_h}$. Resistance predicted with regression (v), including the quadratic terms.
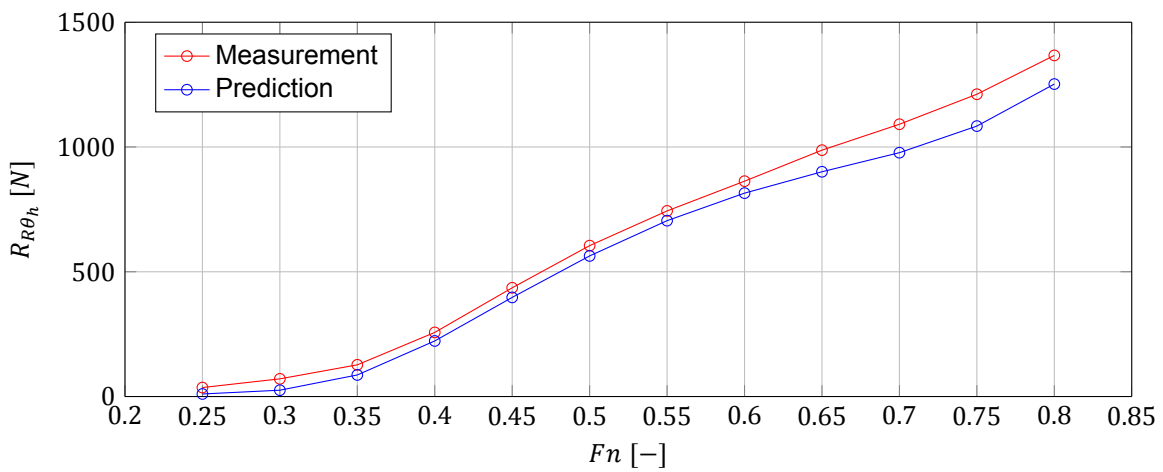
(b) Bare hull upright trimmed residuary resistance $R_{R\theta_h}$. Resistance predicted with regression (v), excluding the quadratic terms with the exception of $(LCG_{fp}/L_{WL})^2$.
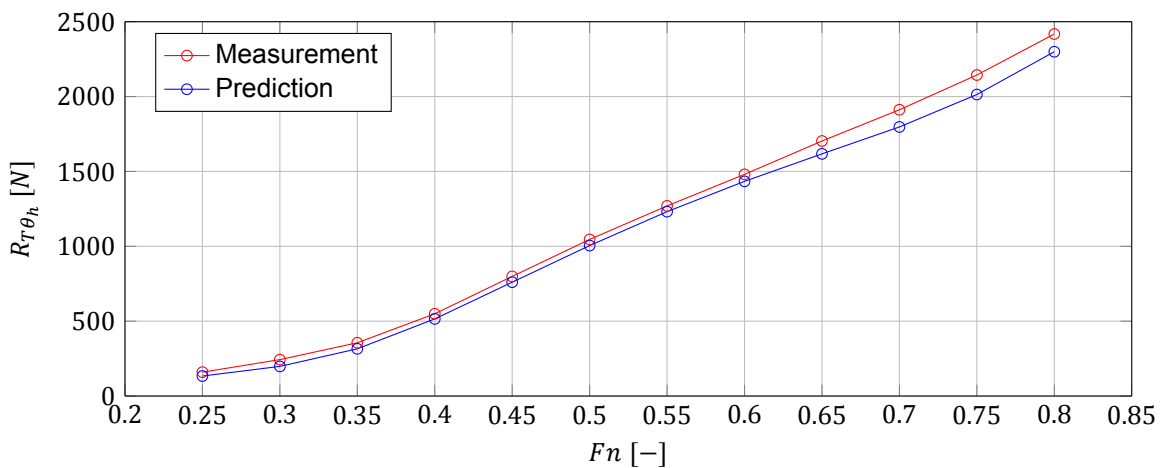
(c) Bare hull upright trimmed resistance $R_{T\theta_h}$. Residuary resistance predicted with regression (v), including the quadratic terms.

Figure 10.8: The measured resistance and the predicted resistance of the Wide Light yacht. A cubic spline is fitted to the predicted resistance values using a least-squares fit. This fit is used to estimate the resistance values at the intermediate Froude numbers 0.3, 0.4, 0.5, and so on.

velocity prediction calculated with the regressions of the DSYHS.

For the velocity prediction of high performance yachts, a new resistance decomposition was proposed in Chapter 5. This decomposition, depicted in Figure 5.1, uses the upright trimmed condition for the reference resistance. The resistance decomposition of the DSYHS, depicted in Figure 2.1, uses the upright untrimmed condition for the reference resistance. Delta resistance components for heel and leeway are defined with respect to the reference resistance. In the new resistance decomposition, the upright untrimmed resistance is omitted and is replaced by the upright trimmed resistance. At least for the higher speeds, this decomposition has a closer resemblance with the physics involved in real-life sailing conditions, because a sailing yacht always experiences a trimming moment of the driving force while sailing.

From this new resistance decomposition method, the need arises to update the regressions for all the resistance components, because there is a small difference in their definitions between the method of the DSYHS and the new method. Updating the regressions for the other resistance components is also preferable, because these regressions are also less applicable to modern sailing yachts. However, updating all the regressions is outside the scope of the present study. For now, it is assumed that between the method of the DSYHS and the new method, the values of the delta resistance components, the resistance of the keel and the rudder, and the induced resistance are not changed significantly. In that way, the regressions of the DSYHS can be used to estimate the resistance components other than the upright trimmed bare hull resistance.

The existing WinDesign VPP, developed by the Wolfson Unit MTIA, is used to calculate the velocity prediction of a full-scale TP52 based on Sysser 85. The 2015 release of WinDesign VPP version 4.0 is used. WinDesign VPP incorporates the regressions of the DSYHS for the estimation of the hydrodynamic forces acting on a sailing yacht. It also allows the user to use its own data for the hydrodynamic forces of a specific yacht through the experimental data input available in the software. This input requires the upright resistance of the hull with its appendages, the resistance under heel of the hull with its appendages, the effective draft and the lift curve slope, at different speeds and heel angles. The effective draft, also called the effective span of the hull with its appendages, is used to describe the relation between the induced resistance and the generated side force. The lift curve slope describes the relation between the generated side force and the leeway angle. With these two parameters, the generated side force and the corresponding induced resistance can be calculated. The experimental data input method in WinDesign VPP is used to calculate the velocity prediction of a full-scale TP52 based on Sysser 85 with the regressions of the DSYHS and the new regression for the upright trimmed resistance.

For the velocity prediction with the Delft method, the original regressions of the DSYHS as described in Chapter 2 are used. For the new method, the regression for the minimum upright trimmed resistance, Equation (10.10), is used. This regression is preferred for a high performance yacht with a full crew, because it simulates the optimum performance of the yacht. The new method uses the same delta resistance components for heel, the same effective draft and the same lift curve slope. Both methods have therefore only a different bare hull upright resistance. The upright resistance of the bare hull predicted with both methods is plotted in Figure 10.9. Both methods produce a similar resistance curve. The bare hull upright resistance predicted by the new method is between 4 and 15 percent lower than the resistance predicted by the DSYHS. The input used in WinDesign VPP is given in Appendix H.

The bare hull upright resistance prediction of the DSYHS stops after Froude number 0.75. For the other resistance components, the reliable hydrodynamic force prediction stops at lower Froude numbers. WinDesign VPP uses an extrapolation procedure to come up with the resistance values at the higher speeds. The accuracy of this procedure is questionable.

The polar diagram for the full-scale TP52 based on Sysser 85 and the TP52 class rules [45] is depicted in Figure 10.10. A polar diagram visualizes the velocity of a yacht, given on the vertical axis, at different true wind angles for different true wind speeds — the coloured numbers printed next to the curves. Both methods produce similar realistic velocity predictions. The predicted velocity seems to be a bit low for both. The prediction of the new method is slightly higher than that of the Delft method. The difference between both methods is very limited due to the fact that the bare hull resistance, which is the only difference between both methods, makes up only a part of the total resistance.

Despite that the difference between both methods is limited, it shows that the new resistance decomposition with the new bare hull upright trimmed resistance prediction is able to produce realistic velocity predictions compared to the original velocity prediction with the regressions of the DSYHS. The new regressions for the upright trimmed resistance are considered to be a good first step to improve the velocity prediction of modern high performance sailing yachts. For accurate velocity predictions of these yachts, it is necessary to improve the prediction of the other resistance components as well. The motivation is still that the DSYHS regressions are less applicable to modern high performance yacht designs due to the range of parameters contained within the DSYHS and the limited speed range of the DSYHS. Of course, the applicability of the aerodynamic models used in VPPs to high performance yachts need to be assessed as well and improved if necesarry.
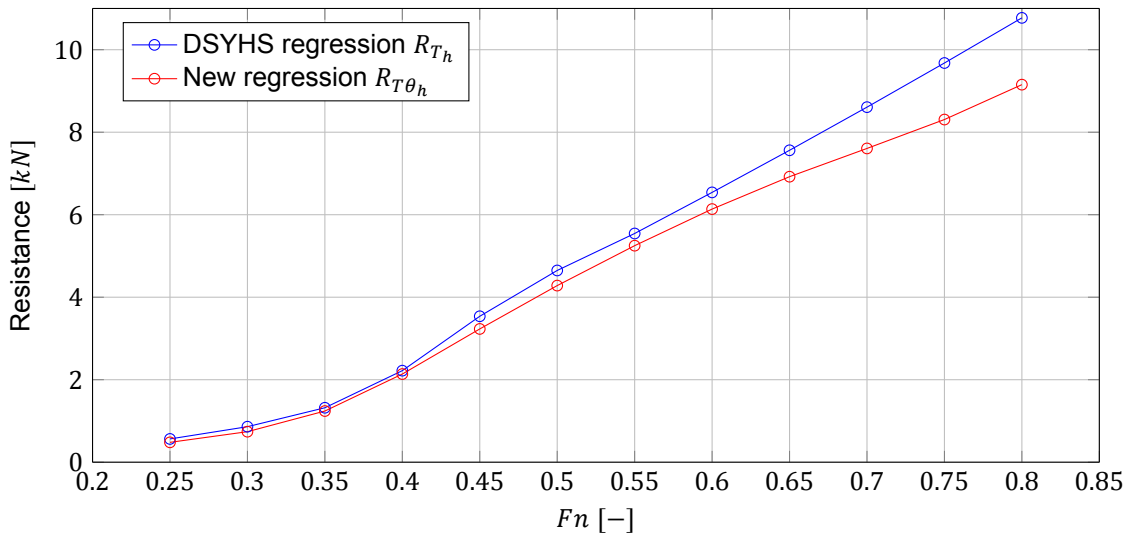
Figure 10.9: Bare hull upright resistance of a full-scale TP52 based on Sysser 85, calculated with the regression of the DSYHS and the new regression.

10.9. Summary

In this regression analysis, five different regressions for the upright trimmed residuary resistance of the bare hull were derived: a regression for the minimum resistance, three regressions for the resistance of each individual crew position, and a regression incorporating the influence of the trimming moment of the crew's weight on the resistance. All the expressions can be easily implemented in existing VPPs, because they contain only hydrostatic parameters and no terms involving the trimming moment of the driving force. For a high performance sailing yacht with a full crew, regression (i) is preferred, because it represents the optimum performance of the yacht. The other regressions can be used for different crew configurations or other ranges of trimming moments. Regression (v) can be used to calculate the resistance of a yacht subjected to an 'arbitrary' trimming moment of the crew's weight or movable ballast. The bare hull upright trimmed resistance prediction based on the new formulations is summarized in Appendix G. The parameter range covered by these regressions is listed in Tables 3.3 and G.1.

In general, quadratic terms enhance instability when the regressions are extrapolated to (slightly) outside the range of the original database. Therefore, alternative formulations of the five regressions are also given. These alternative formulations contain the same parameters as the original regressions, but exclude the quadratic terms with the exception of the $(LCG_{fp}/L_{WL})^2$ term. This quadratic term is needed, because there is a distinctive non-linear relationship between the resistance values of the three crew positions at every speed. The alternative formulations provide more stability and robustness at the expense of accuracy. The accuracy of the alternative formulations is still very acceptable.

In general, the ten regressions fit the database accurately at every Froude number. With the exception of regression (iv) at Froude number 0.25, the regressions produce accurate and adequate fits. For every model in the database, the regressions produce accurate predictions. The corresponding fits are satisfactory over the entire speed range. In general, the maximum comparison error is very
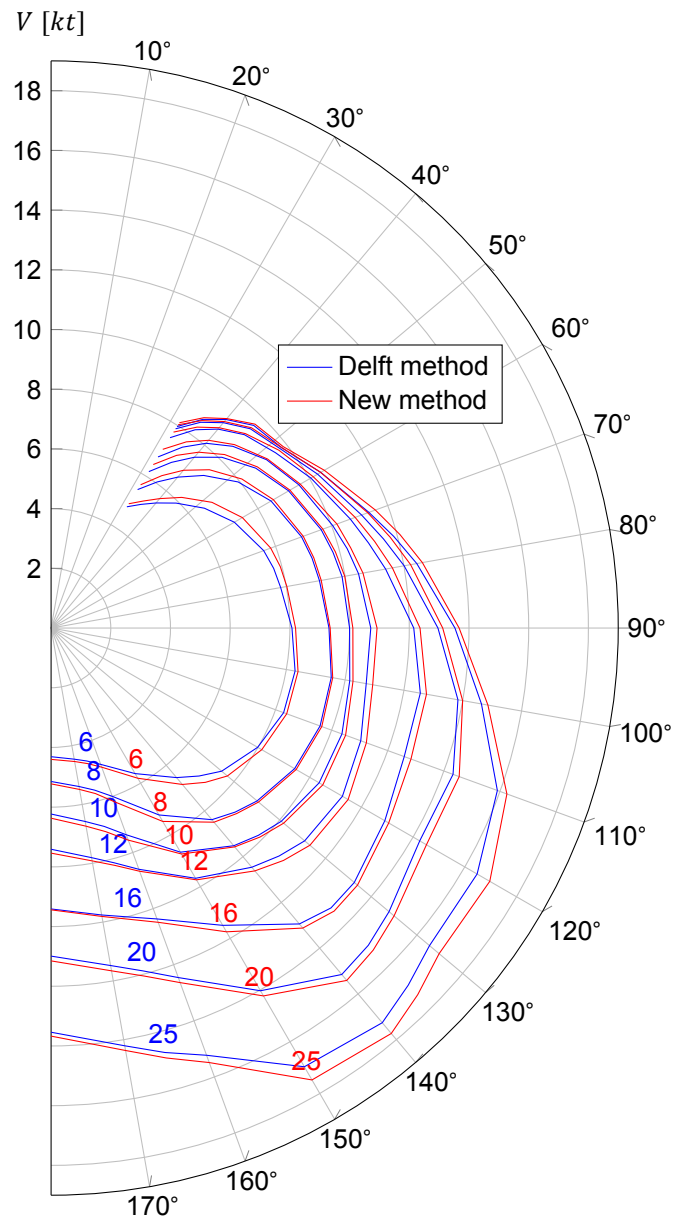
Figure 10.10: Polar diagram of a full-scale TP52 based on Sysser 85, calculated with WinDesign VPP. True wind speeds are given in knots. The input used in WinDesign VPP is given in Appendix H.

reasonable and the average relative comparison error is mostly below 1 percent, which is considered to be very good.

The correlation between the independent variables in the regressions is low, which contributes to the stability of the regressions. The number of variables in the regressions seems reasonable compared to the database size. This contributes to the stability and the robustness of the regressions.

The sensitivity of the regressions to variations in the input parameters is very reasonable. Only for Froude numbers 0.25 and 0.35, the regressions seems to be a bit too sensitive to variations in some of the parameters. All the regressions are the most sensitive to variations in the longitudinal centre of buoyancy-to-length ratio, the longitudinal centre of buoyancy-to-longitudinal centre of flotation ratio, and the longitudinal centre of gravity-to-length ratio. The alternative regressions excluding the quadratic terms are slightly less sensitive to variations in these first two ratios.

For the prediction of the resistance of an arbitrary sailing yacht whose hydrostatic parameters clearly satisfy the parameter range covered by the new systematic series, it is advisable to use the full regressions, including the quadratic terms, because these regressions produce the most accurate results in that range. For predictions outside the parameter range covered by the series, it is advisable to use the full regressions and the alternative regressions in parallel. The results of both methods should be checked for credibility.

The derived regressions have a similar form as the regression of the DSYHS for the bare hull upright untrimmed resistance, given by Equation (2.9). The new formulations contain additional quadratic terms, lack the displacement-to-waterplane area ratio and use a slightly different scaling of the residuary resistance. It is not surprising that the derived regressions contain similar parameters as the regression of the DSYHS, since this regression was used to introduce the variations into the new systematic series. Compared to the regression of the DSYHS, the displacement-to-waterplane area ratio is removed from the new regressions, because it is highly correlated to the draft-to-beam ratio for the new systematic series.

The derived regressions are tested for their applicability to predict the resistance of models not belonging to the systematic series and that have parameters or design characteristics not fully covered by the systematic series. For the three models used in this comparison, the resistance is quite accurately predicted; especially, if it is taken into consideration that some of the parameters falls outside the range covered by the series and that the hull shapes of two of these models differ from the characteristic hull shapes of the systematic series. Only for Froude number 0.25, the prediction seems unreasonable with relative comparison error above 35 percent. For one of the models, the prediction for Froude number 0.35 seems also unreasonable. After Froude number 0.45, the prediction is quite accurate.

For one of the models, the predicted resistance was compared with measured resistance values. For Froude numbers after 0.35, the prediction is quite accurate; especially, if it is taken into consideration that the regressions are based on a database of numerical results. The resistance is underpredicted at every speed compared to experimental results, but the trends of the speed-resistance curve are captured perfectly and the underprediction is not that large. The measured resistance values are likely to be higher than corresponding numerical resistance values. Hence, it is likely that the regressions underpredict the resistance compared to experimental results.

The regression for the minimum upright trimmed residuary resistance of the bare hull together with the new resistance decomposition have been used in an existing VPP to calculate the velocity prediction of a full-scale TP52 based on Sysser 85. This showed that the new resistance decomposition with the new bare hull upright trimmed resistance prediction is able to produce realistic velocity predictions.

In conclusion, the derived regressions provide an accurate resistance prediction for models covered by the new systematic series. Even for models (slightly) outside the parameter range covered by the series or for models with different design characteristics than the hull shapes in the new systematic series, the prediction can be quite accurate. The regressions seem to be stable, robust and not too sensitive to variations in the input parameters.

$$11$$

Conclusions

Velocity prediction programs (VPPs) are used extensively for the design of sailing yachts. VPPs generally rely on the regressions derived from the Delft Systematic Yacht Hull Series (DSYHS) for the estimation of the hydrodynamic forces and moments acting on yacht hulls. After the last extension of the DSYHS more than ten years ago, the most pronounced developments in yacht design are the straight vertical bows, the wide transoms, the very small overhangs aft and the very light displacement hulls. Furthermore, the contemporary designs carry above the waterline their maximum beam all the way aft. These developments contribute to the ever increasing speed potential of the newer designs.

As a results of these developments, the DSYHS is no longer representative of today's high performance yacht designs. The regression formulas derived from the DSYHS are therefore less applicable to recent hull shapes. The accuracy of the velocity prediction of modern high performance yachts suffers from this in some extent. The developments in yacht design and the limitations of the regressions of the DSYHS for the velocity prediction of contemporary high performance yachts formed the motivation for the present study.

The aim of the present study was to improve the velocity prediction of modern high performance sailing yachts from a hydrodynamic perspective. Improving the prediction of the bare hull upright trimmed resistance was considered to be a promising method to realize this. To this end, a new systematic series of contemporary high performance yacht hulls has been created. The new series is representative of a wide range of today's high performance yachts. The regressions derived from this new series cover a wider speed range and a different range of hydrostatic parameters than those of the DSYHS.

The bare hull upright trimmed resistance forces acting on the models in the new systematic series have been determined with computational fluid dynamics (CFD) for eight speeds, from Froude number 0.25 up to 0.95, one centre of effort height and three different trimming moments of the crew's weight. The used trimming moments correspond to typical crew configurations during sailing.

A grid refinement study has been performed to assess the uncertainty of the numerical results for the parent hull of the systematic series at Froude numbers 0.45 and 0.85 for the crew CoG position. For validation, the numerical results for the parent hull have been compared to the results of resistance measurements. At Froude number 0.45, validation was achieved. Unfortunately, at Froude number 0.85, no validation could be achieved. The absolute value of the comparison error was larger than the validation uncertainty at this speed. Although validation was not achieved, confidence in the numerical results still exists, because the relative comparison errors at both speeds are almost the same. From a programmatic standpoint, validation of the numerical results at Froude number 0.85 was still successful at a level of 6 percent. For the purpose of deriving regressions for resistance prediction in VPPs, the approach of validating numerical results at a level below 10 percent is considered to be reasonable and acceptable.

In order to asses the quality and the credibility of the numerical simulations performed for the new systematic series, the validation analysis was extended to the numerical results computed for the parent hull on the medium grid for the crew CoG and back positions over the entire speed range. The corresponding comparison errors are between -2.9 and -8.6 percent of the experimental results. Validation was successful from a programmatic standpoint. The heave values, and also the pitch values,

are very similar between the experimental method and the numerical method. The trends in the resistance curves and the motion curves are captured perfectly by the numerical method. The performance of the numerical flow solver and the accuracy of the numerical results are satisfying.

Since the other hull shapes in the new systematic series have been derived from the parent hull and the numerical simulations have been performed with exactly the same settings on similar grids, similar comparison errors are expected for the other hull shapes in the systematic series. Confidence in the numerical results of the systematic series therefore exists.

The hydrodynamic resistance forces acting on the models in the new systematic series have been used to derive new regression formulas for the estimation of the bare hull upright trimmed resistance forces based on hydrostatic parameters of yacht hulls. Five different regressions for the upright trimmed residuary resistance of the bare hull have been derived, all with a different application. The derived formulations can be easily used in existing VPPs. The derived regressions provide an accurate resistance prediction for models covered by the systematic series. Even for models (slightly) outside the parameter range covered by the series or for models with different design characteristics than the characteristic hull shapes in the series, the prediction can be quite accurate. The regressions seem to be stable, robust and not too sensitive to variations in the input parameters. The applicability of the derived regressions to the velocity prediction of modern high performance sailing yachts with existing VPPs has been illustrated. The obtained polar diagram seemed very reasonable.

The new regressions for the upright trimmed resistance are a good first step to improve the velocity prediction of modern high performance sailing yachts. For accurate velocity predictions of these yachts, it is still necessary to improve the prediction of the other resistance components as well. The motivation is still that the regressions of the DSYHS are less applicable to modern high performance yacht designs due to the range of parameters contained within the DSYHS and the limited speed range of the DSYHS.

Based on the insights gained during this thesis, the following recommendations are made for further research on resistance prediction for high performance yachts and associated topics:

- The derived regressions have been tested for three additional models not belonging to the new systematic series. To strengthen the confidence in the resistance prediction with these regressions for 'arbitrary' yachts, a more elaborate verification study should be performed against numerical resistance data and experimental resistance data.

- One parent hull, a TP52-design, was used for the new systematic series. Contemporary high performance yacht designs are diverse and do not share all the same design characteristics and hydrostatic parameters. For instance, some designs exhibit (hard) chines in the aft sections while others have none. Some designs also carry their chine far forward. More recent developments are the slightly immersed transoms and the (slightly) inverted bows of, for instance, the Volvo Ocean 65. To cover a larger range of possible yacht designs and to improve the resistance prediction of 'arbitrary' yachts, the database of hydrodynamics of yacht hulls should be expanded with additional systematic series having different parent hulls. To keep up with the developments in yacht design, extension of the database is necesarry anyway in the foreseeable future.

- The regressions of the DSYHS seemed less applicable to modern high performance yacht designs due to the range of parameters contained within the DSYHS and the limited speed range of the DSYHS. New regressions for the bare hull upright resistance have been derived in this thesis. The prediction of the other resistance components should be improved as well. This is necessary for accurate velocity predictions of modern yachts.

- The applicability of the aerodynamic models used in VPPs to modern high performance yachts should be assessed and improved if necesarry.

- To assess the numerical uncertainty, it is not necessary to do one grid refinement study excluding the influence of solving ship motions and one grid refinement study including the influence of solving ship motions, as long as the quasi-static method of the FINE™/Marine flow solver is correctly used. The advise is to perform a grid refinement study including the influence of motion solving, because the numerical uncertainty including this influence is the most appropriate one

for the validation of the numerical results of the systematic series. If this study does not produce reasonable and expected results, an additional grid refinement study excluding the influence of motion solving should be performed, and the use of the quasi-static method should be questioned.

Bibliography

[1] American Society of Mechanical Engineers (ASME). Standard for Verification and Validation in Computational Fluid Dynamics and Heat Transfer. *ASME V&V 20-2009*, New York, NY, USA, 2009.

[2] F.M. Dekking, C. KraaiKamp, H.P. Lopuhaä, and L.E. Meester. *A Modern Introduction to Probability and Statistics: Understanding Why and How*. London: Springer-Verlag London, 2005.

[3] G.B. Deng, P. Queutey, and M. Visonneau. A Code Verification Exercise for the Unstructered Finite-Volume CFD Solver ISIS-CFD. In E. Onate P. Wesseling and J. Periaux, editors, *European Conference on Computational Fluid Dynamics 2006 (ECCOMAS CFD 2006)*, Egmond aan Zee, Netherlands, September 2006. Delft University of Technology, 2006.

[4] G.B. Deng, A. Leroyer, E. Guilmineau, P. Queutey, M. Visonneau, J. Wackers, and A. del Toro Llorens. Verification and Validation of Resistance and Propulsion Computation. In *Tokyo 2015 - A Workshop on CFD in Ship Hydrodynamics*, Tokyo, Japan, 2015.

[5] L. Eça and M. Hoekstra. On the Influence of the Iterative Error in the Numerical Uncertainty of Ship Viscous Flow Calculations. In *26th Symposium on Naval Hydrodynamics*, Rome, Italy, September 2006.

[6] L. Eça and M. Hoekstra. Error estimation based on grid refinement studies: a challenge for grid generation. In *Congreso de Métodos Numéricos en Ingeniería 2009*, Barcelona, Spain, 2009. SEMNI.

[7] L. Eça and M. Hoekstra. Evaluation of numerical error estimation based on grid refinement studies with the method of the manufactured solutions. *Computers and Fluids*, 38:1580–1591, 2009.

[8] L. Eça and M. Hoekstra. Verification and Validation for Marine Applications of CFD. *International Shipbuilding Progress*, 60(1-4):107–141, 2013. Proceedings of the 29th Symposium on Naval Hydrodynamics.

[9] L. Eça and M. Hoekstra. A Procedure for the Estimation of the Numerical Uncertainty of CFD Calculations based on Grid Refinement Studies. *Journal of Computational Physics*, 262:104–130, April 2014.

[10] L. Eça and M.Hoekstra. An evaluation of verification procedures for CFD applications. In *24th Symposium on Naval Hydrodynamics*, Fukuoka, Japan, July 2002.

[11] Ecole Centrale de Nantes. Theoretical Manual: ISIS-CFD v3.1. Technical report, Equipe Dynamique des Systèmes Propulsifs Marins, Laboratoire de recherche en Hydrodynamqie, Energétique et Environnement Atmosphérique, CNRS-UMR 6598, Ecole Centrale de Nantes, Nantes, France, July 2014.

[12] T.B. Gatski and C.G. Speziale. On explicit algebraic stress models for complex turbulent flows. *Journal of Fluid Mechanics*, 254:59–78, 1993.

[13] J. Gerritsma and G. Moeyes. The seakeeping performance and steering properties of sailing yachts. In *3rd HISWA Symposium of Yacht Design and Yacht Construction*, Amsterdam, Netherlands, 1973.

[14] L. Huetz. *Systematic Study of the Hydrodynamic Behaviour of Sailing Yacht Hulls using CFD and Parametric Design*. PhD thesis, Ecole Centrale de Nantes, Nantes, France, 2012.

[15] International Towing Tank Conference (ITTC). ITTC - Recommended Procedures and Guidelines: Uncertainty Analysis in CFD Verification and Validation Methodology and Procedures 7.5-03-01-01. In *25th International Towing Tank Conference*, Fukuoka, Japan, 2008.

[16] International Towing Tank Conference (ITTC). ITTC - Recommended Procedures and Guidelines: Resistance Test 7.5-02-02-01. In *26th International Towing Tank Conference*, Rio de Janeiro, Brazil, 2011.

[17] International Towing Tank Conference (ITTC). ITTC - Recommended Procedures: Fresh Water and Seawater Properties 7.5-02-01-03. In *26th International Towing Tank Conference*, Rio de Janeiro, Brazil, 2011.

[18] International Towing Tank Conference (ITTC). ITTC - Recommended Procedures and Guidelines: Practical Guidelines for Ship CFD Applications 7.5-03-02-03. In *27th International Towing Tank Conference*, Copenhagen, Denmark, 2014.

[19] International Towing Tank Conference (ITTC). ITTC - Recommended Procedures and Guidelines: Example for Uncertainty Analysis of Resistance Tests in Towing Tanks 7.5-02-02-02.1. In *27th International Towing Tank Conference*, Copenhagen, Denmark, 2014.

[20] International Towing Tank Conference (ITTC). ITTC - Recommended Procedures and Guidelines: Practical Guide for Uncertainty Analysis of Resistance Measurements in Routine Tests 7.5-02-02-02.2. In *27th International Towing Tank Conference*, Copenhagen, Denmark, 2014.

[21] International Towing Tank Conference (ITTC). ITTC - Recommended Procedures: Guide to the Expression of Uncertainty in Experimental Hydrodynamics 7.5-02-01-01. In *27th International Towing Tank Conference*, Copenhagen, Denmark, 2014.

[22] International Towing Tank Conference (ITTC). ITTC - Recommended Procedures: General Guideline for Uncertainty Analysis in Resistance Tests 7.5-02-02-02. In *27th International Towing Tank Conference*, Copenhagen, Denmark, 2014.

[23] Joint Committee for Guides in Metrology (JCGM). Evaluation of measurement data - Guide to the expression of uncertainty in measurement. *JCGM 100:2008 GUM 1995 with minor corrections*, September 2008.

[24] M. Katgert and J. den Ouden. Manual DSYHS.tudelft.nl: A User Manual for the Delft Systematic Yacht Hull Series Database website. Technical report, Ship Hydromechanics Laboratory of the Delft University of Technology, Delft, Netherlands, n.d.

[25] J.A. Keuning and M. Katgert. A Bare Hull Resistance Prediction Method derived from the Results of the Delft Systematic Yacht Hull Series extended to Higher Speeds. In *International Conference on Innovation in High Perfromance Sailing Yachts (INNOV'SAIL 2008)*, Lorient, France, 2008. Royal Institution of Naval Architects (RINA).

[26] J.A. Keuning and M. Katgert. The Influence of Heel on the Bare Hull Resistance of a Sailing Yacht. In *2nd International Conference on Innovation in High Performance Sailing Yachts (INNOV'SAIL 2010)*, Lorient, France, 2010. Royal Institution of Naval Architects (RINA).

[27] J.A. Keuning and U.B. Sonnenberg. Approximation of the Hydrodynamic Forces on a Sailing Yacht based on the 'Delft Systematic Yacht Hull Series'. In *15th HISWA Symposium of Yacht Design and Yacht Construction*, Amsterdam, Netherlands, 1998.

[28] J.A. Keuning and B. Verwerft. A new Method for the Prediction of the Side Force on Keel and Rudder of a Sailing Yacht based on the Results of the Delft Systematic Yacht Hull Series. In *19th Chesapeake Sailing Yacht Symposium*, Annapolis, Maryland, USA, 2009.

[29] J.A. Keuning, K.J. Vermeulen, and H.P. ten Have. An Approximation Method for the Added Resistance in Waves of a Sailing Yacht. In *2nd International Symposium on Design and Production of Motor and Sail Yachts (MDY06)*, Madrid, Spain, 2006.

[30] C.M. Klaij, G. Vaz, and L. Eça. Numerical Uncertainty Estimation in Maritime CFD Applications. In *6th European Conference on Computational Fluid Dynamics (ECFD VI)*, Barcelona, Spain, July 2014.

[31] N. Kleijweg. *Upright Bare Hull Resistance Measurements for Sysser 85*. Additional MSc thesis, Delft University of Technology, Delft, Netherlands, 2016.

[32] B. Leonard. A stable and accurate convective modelling procedure based on quadratic upstream interpolation. *Computer Methods in Applied Mechanics and Engineering*, 19(1):59–98, 1979.

[33] McLube. Mclubemarine.com, n.d. URL `http://www.mclubemarine.com/images/slider_imgs/lg_oetking_1.jpg`. Accessed 10 May 2016.

[34] F.R. Menter. Two-Equation Eddy-Viscosity Turbulence Models for Engineering Applications. *AIAA Journal*, 32(8):1598–1605, August 1994.

[35] NUMECA International. User Manual: FINE™/Marine v3 (including ISIS-CFD) - Flow Integrated Environement for Marine Hydrodynamics. Technical report, NUMECA International, Brussels, Belgium, July 2014.

[36] Offshore Racing Congress. ORC VPP Documenation 2015. Technical report, Offshore Racing Congress, Milan, Italy, 2015.

[37] S.B. Pope. *Turbulent Flows*. Cambridge: Cambridge University Press, 2000.

[38] M. Prince and A. Claughton. The SYRF Wide Light Project. In *22nd Chesapeake Sailing Yacht Symposium*, Annapolis, Maryland, USA, March 2016.

[39] V. Pržulj and B. Basara. Bounded convection schemes for unstructured grids. In *15th AIAA Computational Fluid Dynamics Conference, AIAA 2001-2593*, Anaheim, CA, USA, 2001.

[40] J. Raymond. *Estimation Des Performances Des Voiliers au Planing et en Manoeuvre (Estimated Performance of Sailing Yachts in Planing and Manoeuvring)*. PhD thesis, Ecole Centrale de Nantes, Nantes, France, 2009.

[41] O. Reynolds. On the Dynamical Theory of Incompressible Viscous Fluids and the Determination of the Criterion. *Philosophical Transactions of the Royal Society of London. A*, 186:123–164, 1895.

[42] L. F. Richardson. *Weather Prediction by Numerical Process*. Cambridge: Cambridge University Press, 1922.

[43] P.J. Roache. *Verification and Validation in Computational Science and Engineering*. Albuquerque, New Mexico: Hermosa Publishers, 1998.

[44] P.J. Roache. *Fundamentals of Verification and Validation*. Albuquerque, New Mexico: Hermosa Publishers, 2009.

[45] Transpac 52 Class. TRANSPAC 52 RULE (TP52 RULE) - 2015. Technical report, Transpac 52 Class, 2015.

[46] P. Wesseling. *Principles of Computational Fluid Dynamics*. Berlin: Springer-Verlag Berlin Heidelberg, 2001.

[47] F.M. White. *Viscous Fluid Flow* . New York, NY: McGraw-Hill, third edition, international edition, 2006.

[48] D.C. Wilcox. *Turbulence Modeling for CFD*. La Cañada Flintridge, CA: DCW Industries, 1993.

A
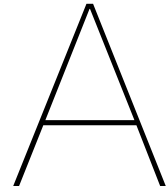
Hydrostatic coefficients

Prismatic coefficient

The prismatic coefficient, C_p, is defined by

$$C_p = \frac{\nabla_c}{A_X L_{WL}},$$ (3.1)

where ∇_c is the volume of displacement of the canoe body, A_X is the maximum sectional area, and L_{WL} is the length of the waterline.

Maximum sectional area coefficient

The maximum sectional area coefficient, C_x, is defined by

$$C_x = \frac{A_X}{B_{WL} T_c},$$ (3.2)

where B_{WL} is the beam of the waterline, and T_c is the draft of the canoe body.

Block coefficient

The block coefficient, C_b, is defined by

$$C_b = \frac{\nabla_c}{L_{WL} B_{WL} T_c} = C_x \cdot C_p.$$ (A.1)

Waterplane area coefficient

The waterplane area coefficient, C_w, is defined by

$$C_w = \frac{A_W}{L_{WL} B_{WL}},$$ (A.2)

where A_W is the waterplane area.

B

Delft Systematic Yacht Hull Series

B.1. Parameter range

Table B.1: The parameters of the models in Series 1 up to 4, 6 and 7 of the DSYHS. The parameter range contained within the DSYHS is listed at the bottom of this table. The maximum, minimum and mean values, and the standard deviation of the parameters are listed there. Table adapted from Keuning and Katgert [25].

	Sysser	$\frac{LCB_{fp}}{L_{WL}}$	C_p	$\frac{\nabla_c^{2/3}}{A_W}$	$\frac{B_{WL}}{L_{WL}}$	$\frac{LCB_{fp}}{LCF_{fp}}$	$\frac{\nabla_c^{1/3}}{L_{WL}}$	C_x	$\frac{B_{WL}}{T_c}$
Series 1	1	0.523	0.564	0.201	0.317	0.980	0.210	0.646	3.99
	2	0.523	0.567	0.230	0.276	0.981	0.210	0.646	3.04
	3	0.523	0.572	0.173	0.364	0.981	0.210	0.647	5.35
	4	0.523	0.568	0.195	0.285	0.980	0.200	0.646	3.95
	5	0.524	0.559	0.212	0.364	0.981	0.230	0.647	3.96
	6	0.524	0.561	0.244	0.317	0.981	0.230	0.646	2.98
	7	0.523	0.561	0.174	0.317	0.980	0.190	0.646	4.95
	8	0.524	0.586	0.203	0.305	0.983	0.210	0.647	3.84
	9	0.522	0.546	0.199	0.328	0.979	0.210	0.646	4.13
	10	0.500	0.564	0.199	0.317	0.963	0.210	0.646	3.99
	11	0.550	0.565	0.203	0.317	1.000	0.210	0.646	3.99
	12	0.500	0.564	0.194	0.285	0.963	0.200	0.647	3.94
	13	0.550	0.564	0.198	0.285	1.000	0.200	0.646	3.94
	14	0.523	0.529	0.205	0.285	0.978	0.200	0.646	3.69
	15	0.523	0.530	0.212	0.316	0.978	0.210	0.646	3.68
	16	0.523	0.529	0.255	0.317	0.978	0.230	0.646	2.81
	17	0.500	0.598	0.191	0.317	0.966	0.210	0.647	4.24
	18	0.550	0.599	0.194	0.317	1.002	0.210	0.647	4.24
	19	0.500	0.530	0.208	0.317	0.960	0.210	0.646	3.75
	20	0.550	0.530	0.212	0.317	0.998	0.210	0.646	3.75
	21	0.523	0.598	0.188	0.285	0.983	0.200	0.647	4.17
	22	0.523	0.599	0.202	0.366	0.983	0.230	0.647	4.23
Series 2	23	0.519	0.547	0.206	0.288	0.938	0.200	0.721	4.09
	24	0.521	0.543	0.109	0.286	0.933	0.140	0.739	10.96
	25	0.520	0.548	0.165	0.250	0.936	0.170	0.727	5.39
	26	0.521	0.543	0.093	0.250	0.924	0.130	0.749	12.91
	27	0.519	0.546	0.265	0.222	0.939	0.200	0.724	2.46

		$\frac{LCB_{fp}}{L_{WL}}$	C_p	$\frac{\nabla_c^{2/3}}{A_W}$	$\frac{B_{WL}}{L_{WL}}$	$\frac{LCB_{fp}}{LCF_{fp}}$	$\frac{\nabla_c^{1/3}}{L_{WL}}$	C_x	$\frac{B_{WL}}{T_c}$
	28	0.521	0.544	0.137	0.222	0.930	0.140	0.736	6.75
Series 3	29	0.546	0.549	0.106	0.250	0.947	0.130	0.751	10.87
	30	0.546	0.549	0.141	0.250	0.946	0.150	0.751	7.08
	31	0.545	0.548	0.082	0.250	0.943	0.120	0.752	15.82
	32	0.521	0.549	0.104	0.250	0.927	0.130	0.751	10.87
	33	0.566	0.549	0.108	0.250	0.963	0.130	0.751	10.87
	34	0.544	0.522	0.110	0.250	0.945	0.130	0.757	10.37
	35	0.545	0.580	0.103	0.250	0.946	0.130	0.758	11.47
	36	0.544	0.551	0.108	0.250	0.949	0.130	0.707	10.16
	37	0.544	0.552	0.110	0.250	0.956	0.130	0.657	9.43
	38	0.545	0.547	0.079	0.333	0.942	0.130	0.755	19.38
	39	0.546	0.549	0.133	0.200	0.948	0.130	0.753	6.97
	41	0.582	0.540	0.175	0.250	0.977	0.170	0.741	5.21
Series 4	42	0.533	0.554	0.224	0.301	0.945	0.210	0.711	3.71
	43	0.533	0.553	0.167	0.359	0.943	0.200	0.712	6.29
	44	0.533	0.554	0.200	0.301	0.947	0.200	0.712	4.42
	45	0.533	0.554	0.252	0.240	0.947	0.200	0.711	2.79
	46	0.533	0.553	0.172	0.301	0.947	0.190	0.712	5.57
	47	0.560	0.548	0.159	0.300	0.959	0.180	0.749	6.04
	48	0.507	0.557	0.164	0.300	0.920	0.180	0.725	5.80
	49	0.563	0.566	0.157	0.298	0.964	0.180	0.743	6.31
	50	0.579	0.539	0.159	0.300	0.979	0.180	0.777	6.34
Series 6	60	0.546	0.541	0.158	0.256	0.955	0.170	0.747	5.74
	61	0.546	0.542	0.149	0.269	0.952	0.170	0.790	6.70
	62	0.545	0.541	0.167	0.243	0.958	0.170	0.676	4.71
Series 7	71	0.560	0.519	0.218	0.200	0.969	0.170	0.754	3.39
	72	0.560	0.521	0.146	0.170	0.971	0.130	0.745	5.67
	73	0.561	0.521	0.159	0.200	0.967	0.140	0.757	5.41

	$\frac{LCB_{fp}}{L_{WL}}$	C_p	$\frac{\nabla_c^{2/3}}{A_W}$	$\frac{B_{WL}}{L_{WL}}$	$\frac{LCB_{fp}}{LCF_{fp}}$	$\frac{\nabla_c^{1/3}}{L_{WL}}$	C_x	$\frac{B_{WL}}{T_c}$
Maximum	0.582	0.599	0.265	0.366	1.002	0.230	0.790	19.38
Minimum	0.500	0.519	0.079	0.170	0.920	0.120	0.646	2.46
Mean	0.535	0.553	0.172	0.282	0.962	0.180	0.700	6.12
σ	0.019	0.019	0.046	0.044	0.021	0.034	0.049	3.45
σ [%Mean]	3.58	3.49	26.8	15.6	2.15	19.0	7.00	56.5

B.2. Coefficients of the DSYHS regressions

Table B.2: The coefficients, a_i, of the regression for the bare hull residuary resistance, R_{R_h}, Equation (2.9). Coefficients taken from Keuning and Katgert [25]. All the coefficients are dimensionless.

Fn	a_0	a_1	a_2	a_3	a_4	a_5	a_6	a_7
0.15	-0.0005	0.0023	-0.0086	-0.0015	0.0061	0.0010	0.0001	0.0052
0.20	-0.0003	0.0059	-0.0064	0.0070	0.0014	0.0013	0.0005	-0.0020
0.25	-0.0002	-0.0156	0.0031	-0.0021	-0.0070	0.0148	0.0010	-0.0043
0.30	-0.0009	0.0016	0.0337	-0.0285	-0.0367	0.0218	0.0015	-0.0172
0.35	-0.0026	-0.0567	0.0446	-0.1091	-0.0707	0.0914	0.0021	-0.0078
0.40	-0.0064	-0.4034	-0.1250	0.0273	-0.1341	0.3578	0.0045	0.1115
0.45	-0.0218	-0.5261	-0.2945	0.2485	-0.2428	0.6293	0.0081	0.2086
0.50	-0.0388	-0.5986	-0.3038	0.6033	-0.0430	0.8332	0.0106	0.1336
0.55	-0.0347	-0.4764	-0.2361	0.8726	0.4219	0.8990	0.0096	-0.2272
0.60	-0.0361	0.0037	-0.2960	0.9661	0.6123	0.7534	0.0100	-0.3352
0.65	0.0008	0.3728	-0.3667	1.3957	1.0343	0.3230	0.0072	-0.4632
0.70	0.0108	-0.1238	-0.2026	1.1282	1.1836	0.4973	0.0038	-0.4477
0.75	0.1023	0.7726	0.5040	1.7867	2.1934	-1.5479	-0.0115	-0.0977

Table B.3: The coefficients, b_i, of the regression for the change in bare hull residuary resistance due to heel, $\Delta R_{R\phi_h}$, Equation (2.12). Coefficients taken from Keuning and Katgert [26]. All the coefficients are multiplied by 10^3 and are dimensionless.

Fn	b_0	b_1	b_2	b_3
0.15	-1.850	-0.032	1.037	1.781
0.20	-1.032	0.000	0.731	0.996
0.25	2.061	-0.024	0.451	-2.046
0.30	10.881	-0.163	-0.431	-10.773
0.35	26.984	-0.494	-2.208	-26.780
0.40	48.633	-1.062	-4.344	-48.397
0.45	73.015	-1.795	-6.432	-72.799

Table B.4: The coefficients, T_i, of the regression for the change in residuary resistance of the bare hull due to the trimming moment of the driving force, $\Delta R_{R\theta_h}$, Equation (2.14). Coefficients taken from Keuning and Sonnenberg [27]. All the coefficients are multiplied by 10^3 and are dimensionless.

Fn	T_0	T_1	T_2	T_3	T_4	T_5
0.15	0	0	0	0	0	0
0.20	0	0	0	0	0	0
0.25	1.91	1.42	3.60	-3.96	-0.35	0.68
0.30	1.50	0.85	2.70	-3.00	0.16	0.01
0.35	2.55	2.66	5.49	-6.63	0.37	0.04
0.40	1.88	2.91	5.83	-6.87	1.10	-0.31
0.45	6.96	3.34	7.38	-8.94	1.65	-0.50
0.50	6.28	2.90	7.21	-8.02	1.33	-0.24
0.55	2.62	3.33	7.36	-7.56	1.78	-0.44
0.60	-4.58	3.70	7.23	-6.54	1.72	-0.66

B.3. Comparison of the regressions with experimental results

Table B.5: Comparison errors E of the bare hull resistance computed with the DSYHS regressions and the measured resistance. E.g. $E(R_{T_h})$ indicates the comparison error of R_{T_h} with corresponding experimental result R_t; $E(R_{T_h}) = R_{T_h} - R_t$. Comparison errors are given as a percentage of the experimental results, R_t. Note that for every column, R_t is different. $R_{T20_h} = \left(R_{T\phi_h}\right)_{\phi=20°}$, and $R_{T30_h} = \left(R_{T\phi_h}\right)_{\phi=30°}$.

(a) Models from Series 2 of the DSYHS.

Fn	Sysser 25			Sysser 28		
	$E(R_{T_h})$	$E(R_{T\theta_h})$	$E(R_{T20_h})$	$E(R_{T_h})$	$E(R_{T\theta_h})$	$E(R_{T20_h})$
$[-]$	$[\%R_t]$	$[\%R_t]$	$[\%R_t]$	$[\%R_t]$	$[\%R_t]$	$[\%R_t]$
0.25	-4.3	-5.7	-4.4	-2.2	-2.2	0.6
0.30	-2.2	-5.4	-2.9	-1.9	-0.8	3.6
0.35	-5.8	-7.0	-6.4	1.3	2.2	5.4
0.40	-1.8	-6.1	-4.3	0.8	-0.6	-0.9
0.45	-2.2	-5.9	-3.9	-3.0	-0.9	-4.4
0.50	-0.1	-2.8		-3.3	-0.9	
0.55	-0.2	-3.0		-5.0	0.5	
0.60	-0.5	-1.1		-5.0	1.3	
0.65	-0.6			-4.1		
0.70	0.9			-2.6		
0.75	-0.2			0.2		

(b) Models from Series 3 of the DSYHS.

Fn	Sysser 33			Sysser 39		
	$E(R_{T_h})$	$E(R_{T\theta_h})$	$E(R_{T20_h})$	$E(R_{T_h})$	$E(R_{T\theta_h})$	$E(R_{T20_h})$
$[-]$	$[\%R_t]$	$[\%R_t]$	$[\%R_t]$	$[\%R_t]$	$[\%R_t]$	$[\%R_t]$
0.25	5.9	11.1	8.5	-4.7	-2.2	5.9
0.30	6.6	7.6	9.3	-0.8	-4.3	5.1
0.35	1.5	9.1	11.8	1.0	0.0	6.5
0.40	0.2	12.3	7.1	0.4	-1.0	0.5
0.45	3.1	12.4	2.5	1.2	2.2	-0.4
0.50	3.9	16.3		-2.3	1.0	
0.55	2.5	17.4		-5.2	-0.7	
0.60	2.2	20.6		-4.2	1.9	
0.65	-0.7			-3.6		
0.70	-1.4			-4.3		
0.75	-0.1			0.4		

(c) Models from Series 4 of the DSYHS.

Fn	Sysser 44			Sysser 47		
	$E(R_{T_h})$	$E(R_{T\theta_h})$	$E(R_{T20_h})$	$E(R_{T_h})$	$E(R_{T\theta_h})$	$E(R_{T20_h})$
$[-]$	$[\%R_t]$	$[\%R_t]$	$[\%R_t]$	$[\%R_t]$	$[\%R_t]$	$[\%R_t]$
0.25	5.2	2.7	3.8	6.1	4.8	6.4
0.30	0.0	0.0	0.0	6.2	4.2	1.6
0.35	7.4	6.5	5.8	9.0	6.5	7.6
0.40	5.1	0.8	1.6	11.8	7.8	12.1
0.45	-0.5	-1.8	0.2	8.2	5.0	9.1
0.50	-1.6	-4.1		7.0	1.9	
0.55	1.3	-2.8		8.1	0.5	
0.60	1.5	-5.0		7.2	1.1	
0.65	0.9			4.8		
0.70	2.6			2.9		
0.75	-2.1					

(d) Models from Series 6 of the DSYHS.

Fn	Sysser 61			Sysser 62		
	$E(R_{T_h})$	$E(R_{T\theta_h})$	$E(R_{T20_h})$	$E(R_{T_h})$	$E(R_{T\theta_h})$	$E(R_{T20_h})$
$[-]$	$[\%R_t]$	$[\%R_t]$	$[\%R_t]$	$[\%R_t]$	$[\%R_t]$	$[\%R_t]$
0.25	4.4	4.4	5.8	3.5	5.1	5.2
0.30	5.7	3.6	7.8	15.5	3.9	16.6
0.35	7.6	8.1	18.4	11.8	4.1	10.4
0.40	5.0	4.2	15.5	-2.9	-7.8	-0.9
0.45	1.5	8.8	8.2	-7.1	-12.4	-8.5
0.50	-0.2	6.0		-3.3	-7.6	
0.55	-4.6	1.5		1.3	-4.0	
0.60	-5.4	2.3		0.7	-2.8	

(e) Models from Series 7 of the DSYHS.

Fn	Sysser 72		Sysser 73	
	$E(R_{T_h})$	$E(R_{T\theta_h})$	$E(R_{T_h})$	$E(R_{T\theta_h})$
$[-]$	$[\%R_t]$	$[\%R_t]$	$[\%R_t]$	$[\%R_t]$
0.25	14.9	13.8	4.1	13.4
0.30	9.8	3.0	-0.1	-1.8
0.35	1.9	2.4	4.5	2.7
0.40	13.4	8.0	8.7	1.5
0.45	16.8	12.1	11.5	9.0
0.50	10.5	8.4	9.4	7.2
0.55	5.1	3.7	4.2	3.8
0.60	4.8	7.8	5.0	6.6
0.65	8.8		5.1	
0.70	7.7		2.1	
0.75	11.4		2.2	

(f) A model not belonging to the DSYHS.

Fn	Sysser 85			
	$E(R_{T_h})$	$E(R_{T\theta_h})$	$E(R_{T20_h})$	$E(R_{T30_h})$
$[-]$	$[\%R_t]$	$[\%R_t]$	$[\%R_t]$	$[\%R_t]$
0.25	-0.7	-11.5	-4.4	-6.6
0.30	-3.7	-1.0	-3.0	-3.9
0.35	-3.7	-8.3	-3.4	-5.5
0.40	-11.3	-14.7	-13.3	-14.8
0.45	-10.2	-15.9	-12.4	-14.9
0.50	-9.3	-14.4		
0.55	-6.5	-11.2		
0.60	-6.4	-7.4		
0.65	-3.2			
0.70	-1.8			
0.75	1.9			

Table B.6: Comparison errors E of the residuary resistance of the bare hull computed with the DSYHS regressions and the residuary resistance derived from resistance measurements. E.g. $E(R_{R_h})$ indicates the comparison error of R_{R_h} with corresponding experimental result R_t; $E(R_{R_h}) = R_{R_h} - R_t$. Comparison errors are given as a percentage of the experimental results, R_t. Note that for every column, R_t is different. $R_{R\theta_h} = R_{R_h} + \Delta R_{R\theta_h}$, $R_{R20_h} = R_{R_h} + \left(\Delta R_{R\phi_h}\right)_{\phi=20°}$, and $R_{R30_h} = R_{R_h} + \left(\Delta R_{R\phi_h}\right)_{\phi=30°}$.

Fn	Sysser 85			
	$E(R_{R_h})$	$E(R_{R\theta_h})$	$E(R_{R20_h})$	$E(R_{R30_h})$
$[-]$	$[\%R_t]$	$[\%R_t]$	$[\%R_t]$	$[\%R_t]$
0.25	-4.4	-100.5	-28.9	-41.7
0.30	-15.8	-4.4	-11.7	-14.4
0.35	-11.6	-28.9	-9.8	-15.3
0.40	-28.4	-39.7	-32.2	-34.8
0.45	-20.5	-34.8	-24.4	-29.3
0.50	-17.4	-28.2		
0.55	-11.3	-20.1		
0.60	-11.1	-12.3		
0.65	-5.4			
0.70	-3.0			
0.75	3.1			

C
Syssers

C.1. Syssers belonging to the DSYHS
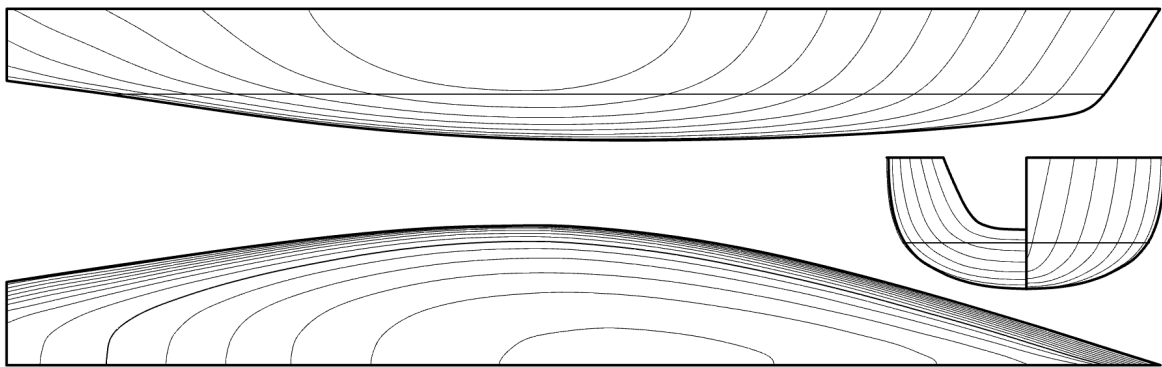
Figure C.1: Lines plan of Sysser 25.
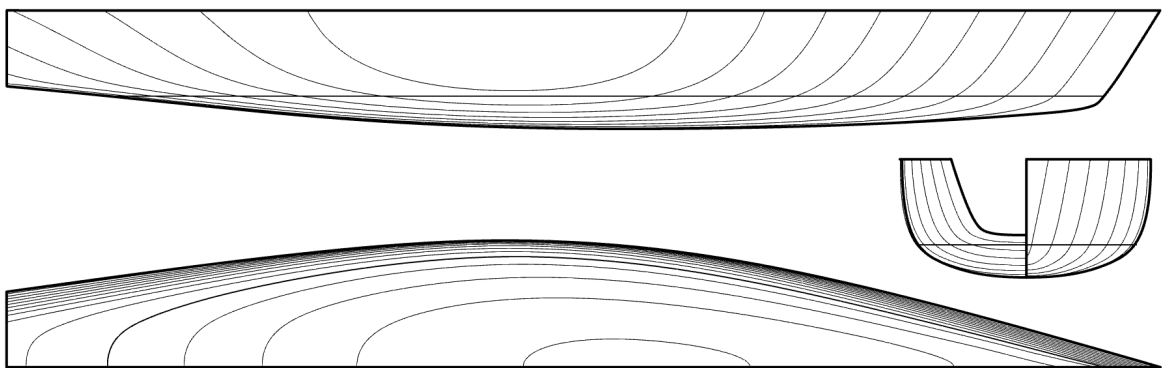
Figure C.2: Lines plan of Sysser 28.
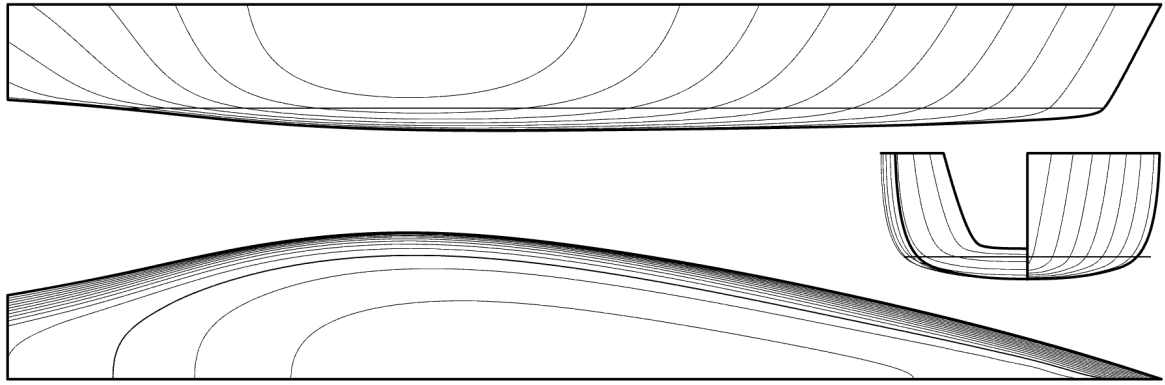
Figure C.3: Lines plan of Sysser 33.
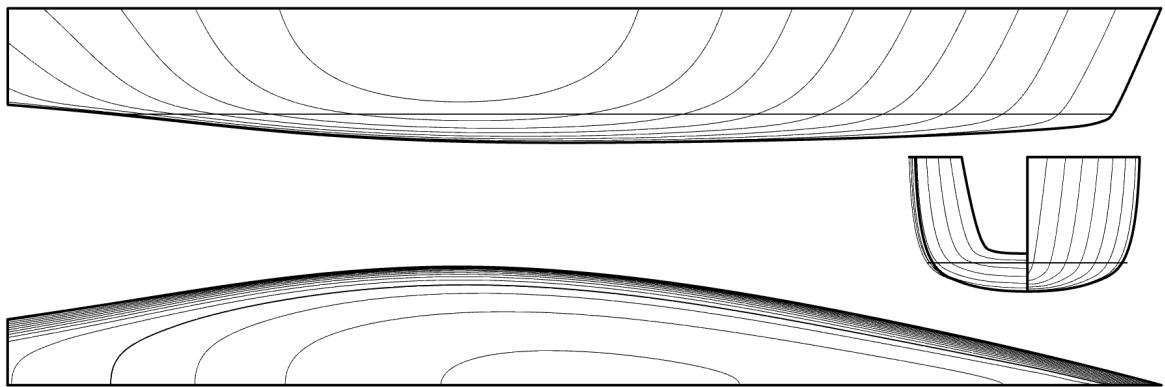
Figure C.4: Lines plan of Sysser 39.
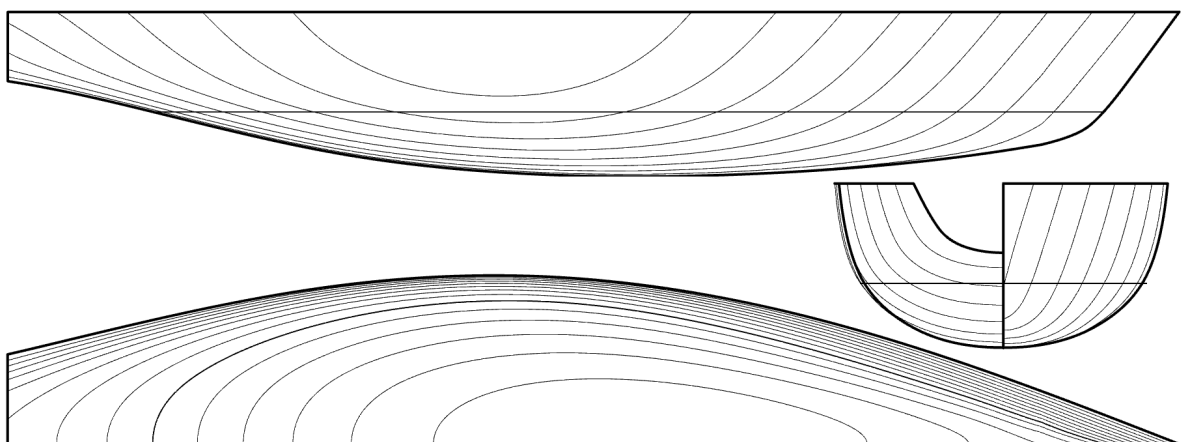
Figure C.5: Lines plan of Sysser 44.
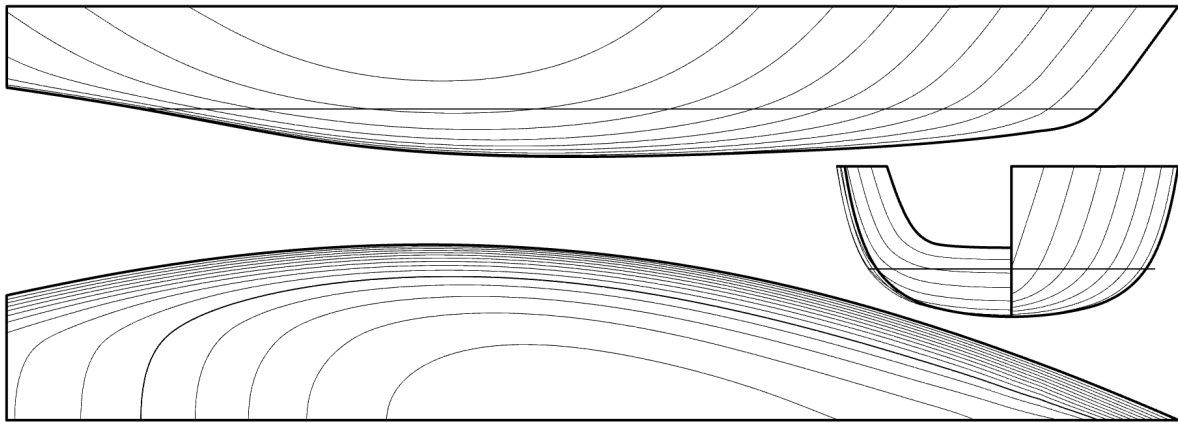
Figure C.6: Lines plan of Sysser 47.
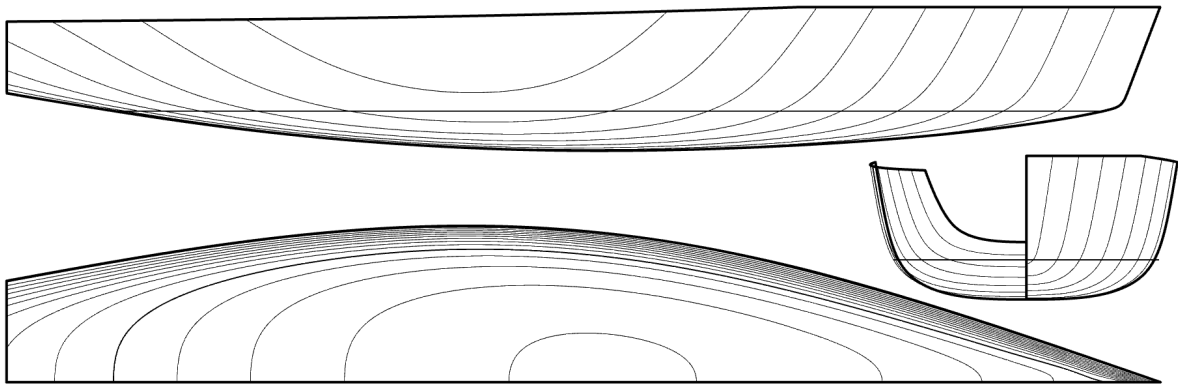
Figure C.7: Lines plan of Sysser 61.
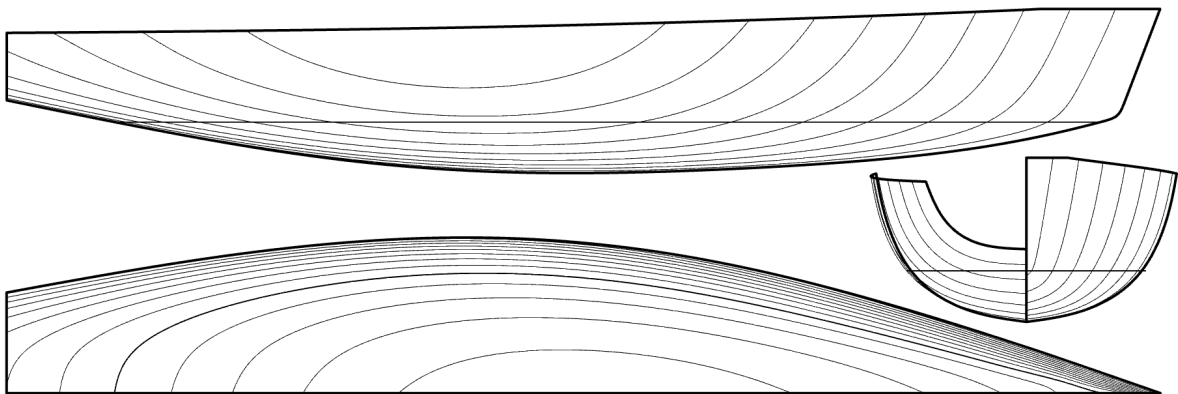
Figure C.8: Lines plan of Sysser 62.
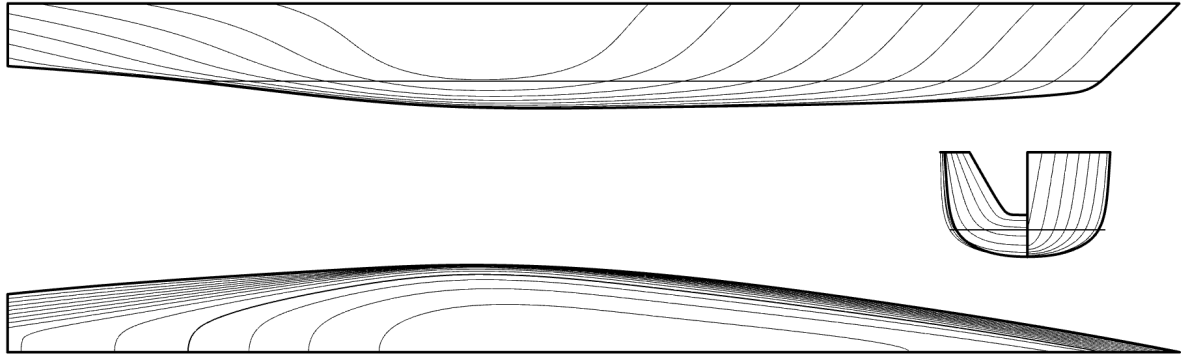
Figure C.9: Lines plan of Sysser 72.
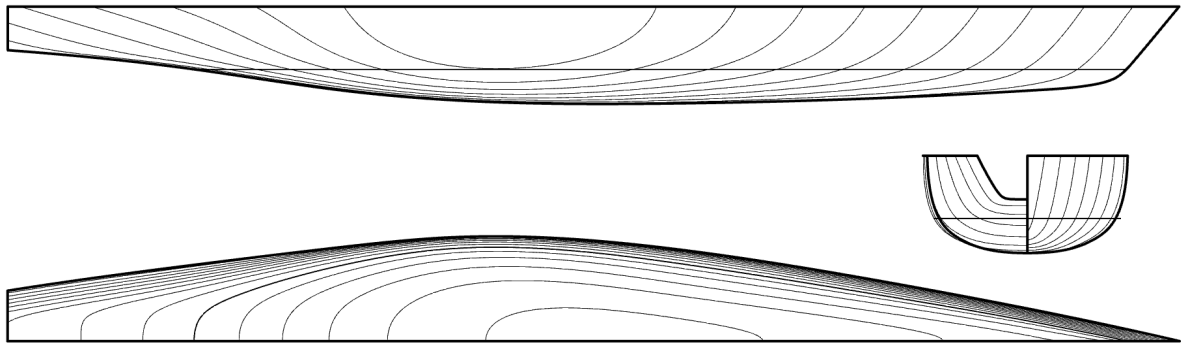
Figure C.10: Lines plan of Sysser 73.

Table C.1: Hydrostatic parameters of Syssers belonging to the DSYHS.

	L_{WL} [m]	$L_{WL_{20}}$ [m]	B_{WL} [m]	$B_{WL_{20}}$ [m]	T_c [m]	$T_{c_{20}}$ [m]	∇_c [m^3]	LCB_{fp} [m]	LCF_{fp} [m]	KM_L [m]
Sysser 25	10.00	10.26	2.500	2.310	0.4640	0.5330	4.623	-5.199	-5.554	19.54
Sysser 28	10.00	10.31	2.222	1.945	0.3290	0.4130	2.925	-5.205	-5.595	27.02
Sysser 33	10.00	10.35	2.500	1.877	0.2300	0.3720	2.372	-5.655	-5.873	37.52
Sysser 39	10.00	10.45	2.000	1.746	0.2870	0.3730	2.371	-5.455	-5.754	30.33
Sysser 44	10.00	10.15	3.013	2.890	0.6810	0.7260	8.087	-5.329	-5.625	13.77
Sysser 47	10.00	10.67	2.997	2.736	0.4960	0.6000	6.096	-5.602	-5.840	19.37
Sysser 61	10.00	10.39	2.687	2.402	0.4010	0.5510	4.619	-5.454	-5.727	22.18
Sysser 62	10.00	10.13	2.434	2.352	0.5170	0.5250	4.609	-5.448	-5.688	19.38
Sysser 72	10.04	10.37	1.710	1.557	0.3000	0.3630	2.014	-5.619	-5.835	29.08
Sysser 73	10.00	10.31	2.012	1.862	0.3700	0.4440	2.912	-5.613	-5.820	23.27

	A_W [m^2]	A_X [m^2]	$A_{X_{20}}$ [m^2]	S_c [m^2]	$S_{c_{20}}$ [m^2]	C_b [−]	C_p [−]	C_w [−]	C_x [−]	$C_{x_{20}}$ [−]
Sysser 25	16.78	0.8430	0.8530	18.86	18.23	0.399	0.548	0.671	0.727	0.693
Sysser 28	14.94	0.5380	0.5450	16.12	14.96	0.400	0.544	0.672	0.736	0.678
Sysser 33	16.48	0.4320	0.4430	16.80	14.17	0.413	0.549	0.659	0.751	0.634
Sysser 39	13.40	0.4320	0.4350	14.52	13.55	0.413	0.549	0.670	0.753	0.668
Sysser 44	20.13	1.4600	1.4550	23.83	23.56	0.394	0.554	0.668	0.712	0.693
Sysser 47	20.95	1.1130	1.0770	23.14	22.04	0.410	0.548	0.699	0.749	0.656
Sysser 61	18.67	0.8520	0.8430	20.37	18.95	0.429	0.542	0.695	0.791	0.637
Sysser 62	16.57	0.8510	0.8570	18.63	18.24	0.366	0.542	0.681	0.676	0.694
Sysser 72	10.99	0.3870	0.3860	12.51	12.03	0.391	0.518	0.640	0.754	0.683
Sysser 73	12.88	0.5610	0.5580	14.79	14.32	0.391	0.519	0.640	0.754	0.675

C.2. Syssers not belonging to the DSYHS or the new systematic series
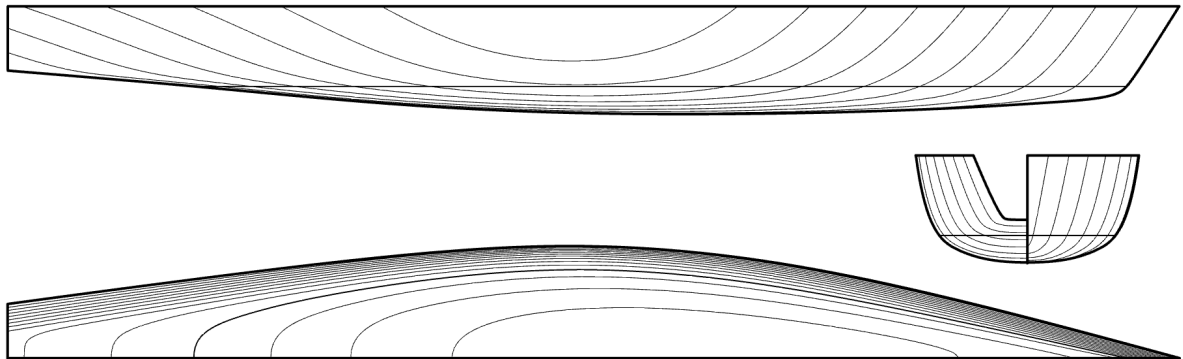
Figure C.11: Lines plan of Sysser 83.
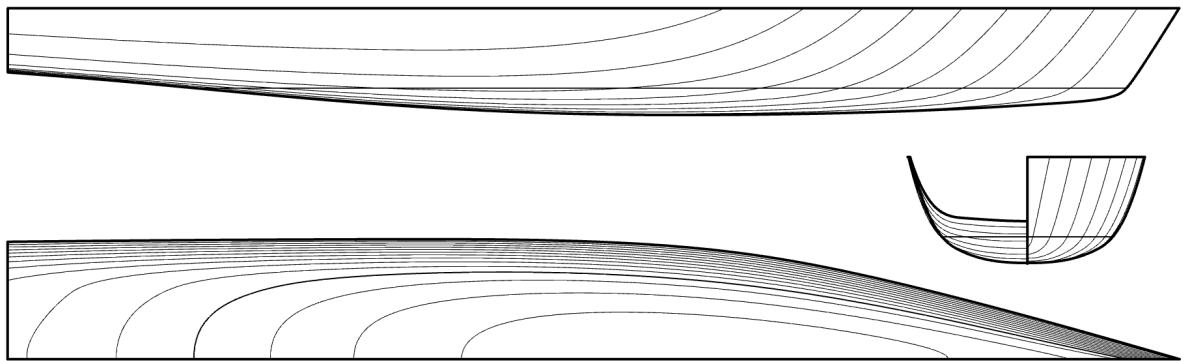
Figure C.12: Lines plan of Sysser 84.

Table C.2: Hydrostatic parameters of Syssers not belonging to the DSYHS or the new systematic series.

	L_{WL} [m]	$L_{WL_{20}}$ [m]	B_{WL} [m]	$B_{WL_{20}}$ [m]	T_c [m]	$T_{c_{20}}$ [m]	∇_c [m^3]	LCB_{fp} [m]	LCF_{fp} [m]	KM_L [m]
Sysser 83	10.01	10.26	1.894	1.722	0.2972	0.3616	2.246	-5.212	-5.595	29.95
Sysser 84	10.01	11.10	1.870	1.674	0.2892	0.3367	2.224	-5.320	-5.818	34.16

	A_W [m^2]	A_X [m^2]	$A_{X_{20}}$ [m^2]	S_c [m^2]	$S_{c_{20}}$ [m^2]	C_b [$-$]	C_p [$-$]	C_w [$-$]	C_x [$-$]	$C_{x_{20}}$ [$-$]
Sysser 83	12.74	0.4110	0.4201	14.01	13.06	0.399	0.546	0.672	0.730	0.675
Sysser 84	13.53	0.3848	0.3748	14.72	13.91	0.411	0.578	0.723	0.711	0.665

C.3. Syssers belonging to the new systematic series
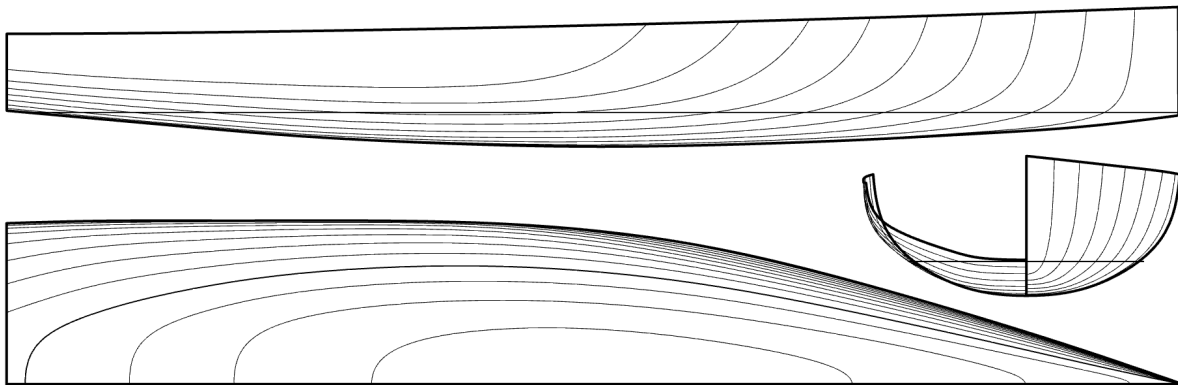
Figure C.13: Lines plan of Sysser 85.
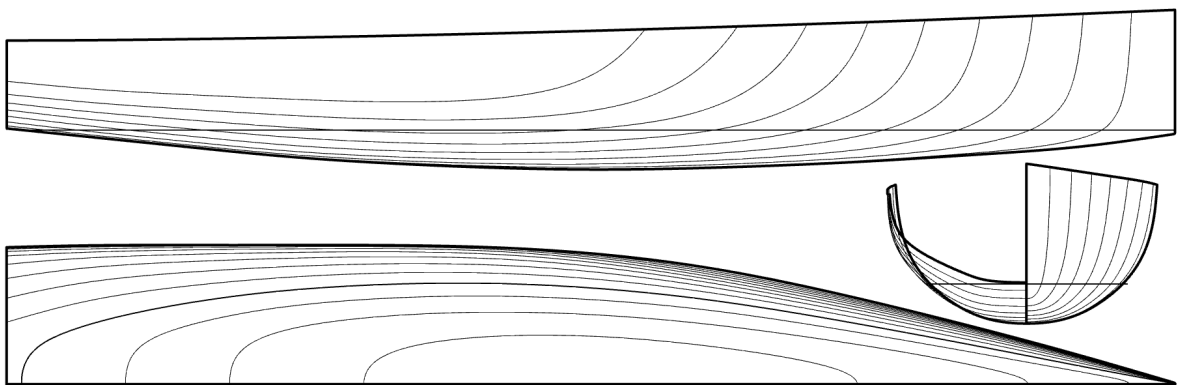
Figure C.14: Lines plan of Sysser 86.
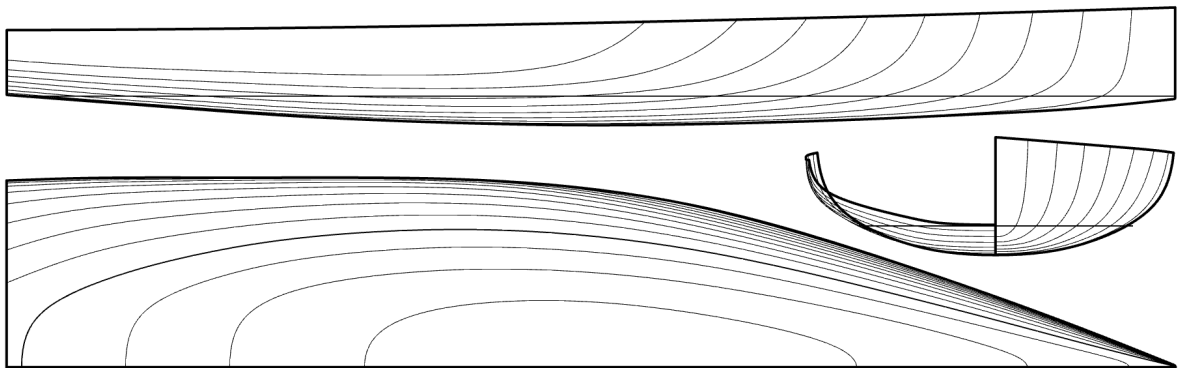
Figure C.15: Lines plan of Sysser 87.
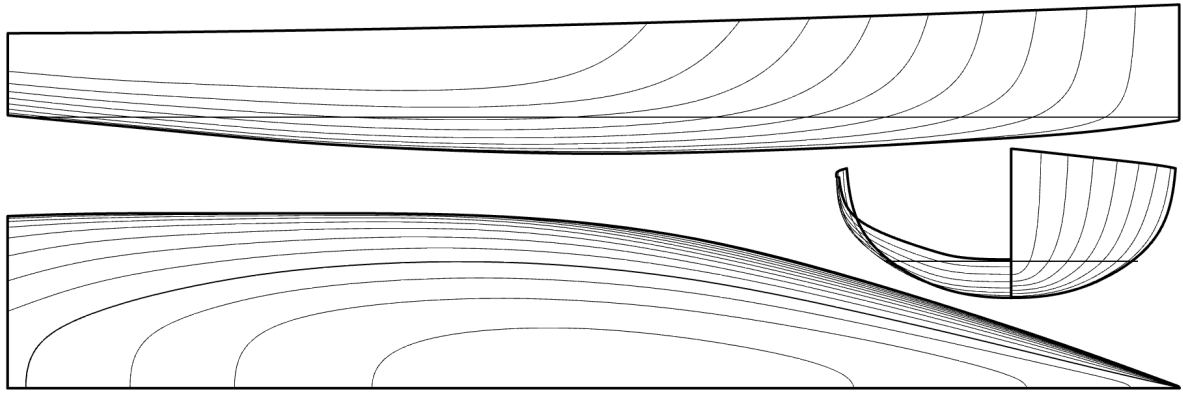
Figure C.16: Lines plan of Sysser 88.
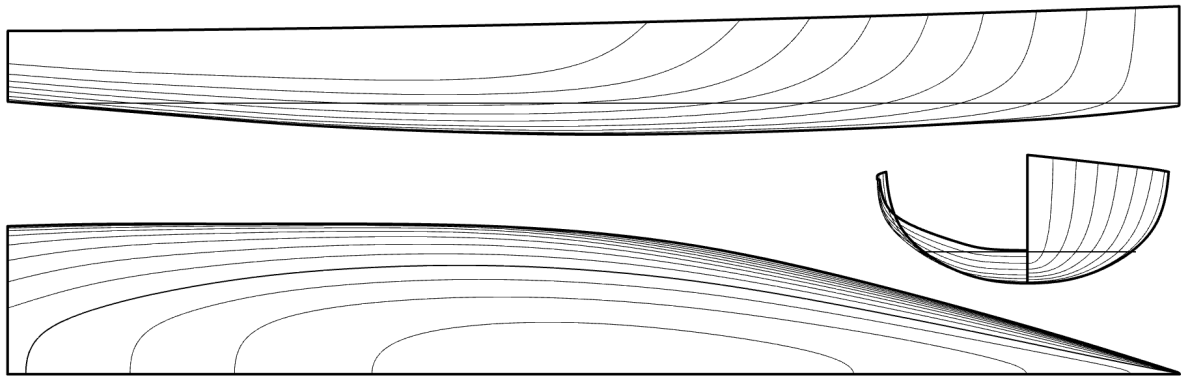
Figure C.17: Lines plan of Sysser 89.
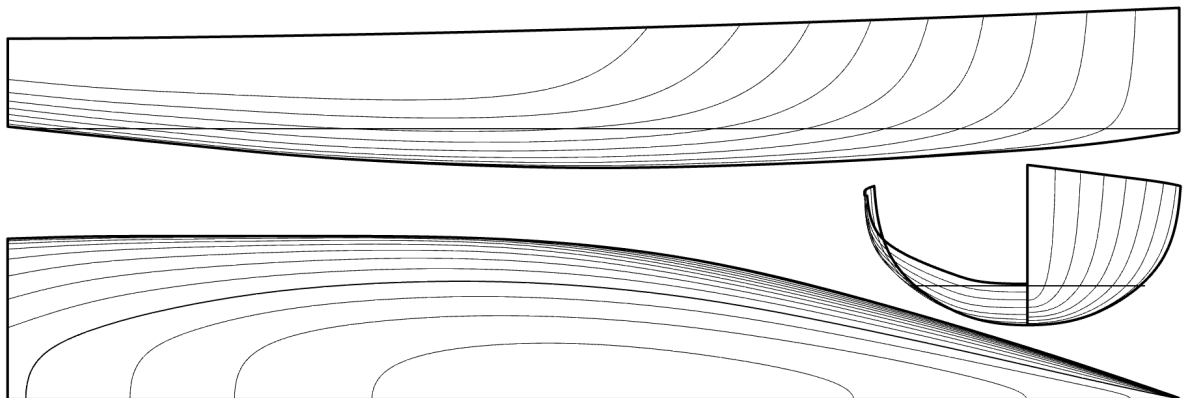
Figure C.18: Lines plan of Sysser 90.
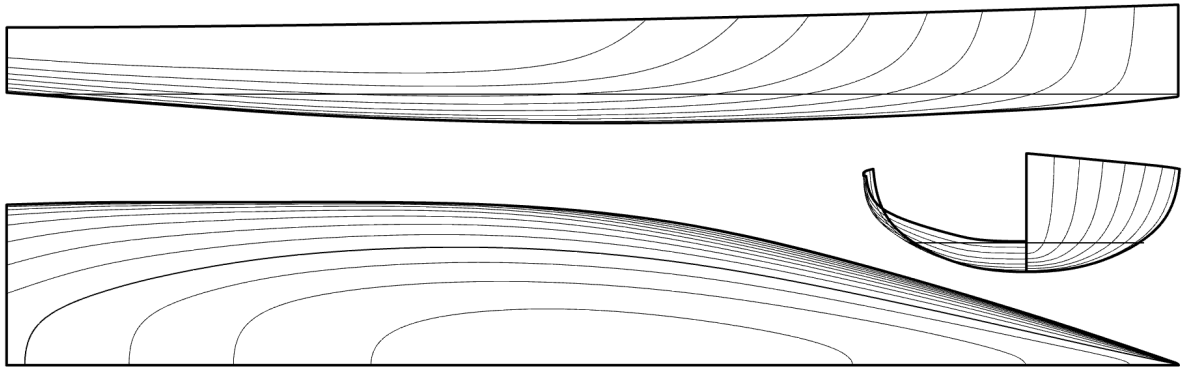
Figure C.19: Lines plan of Sysser 91.
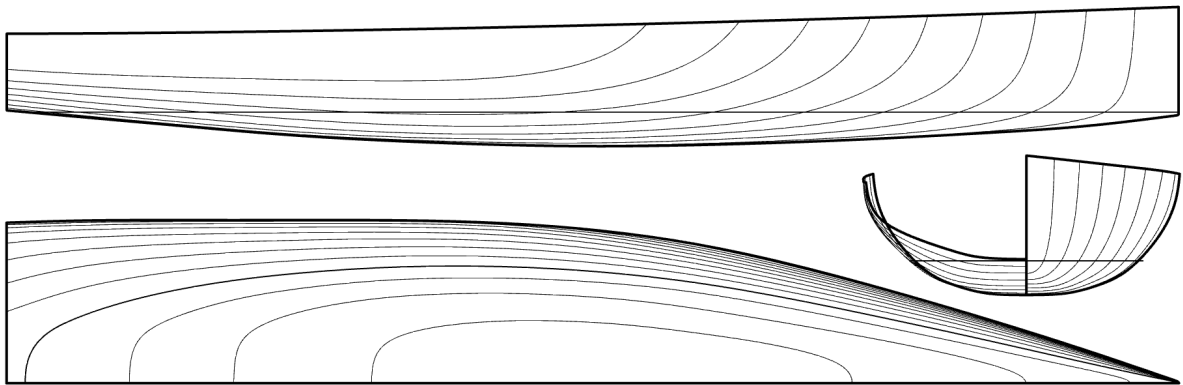
Figure C.20: Lines plan of Sysser 92.
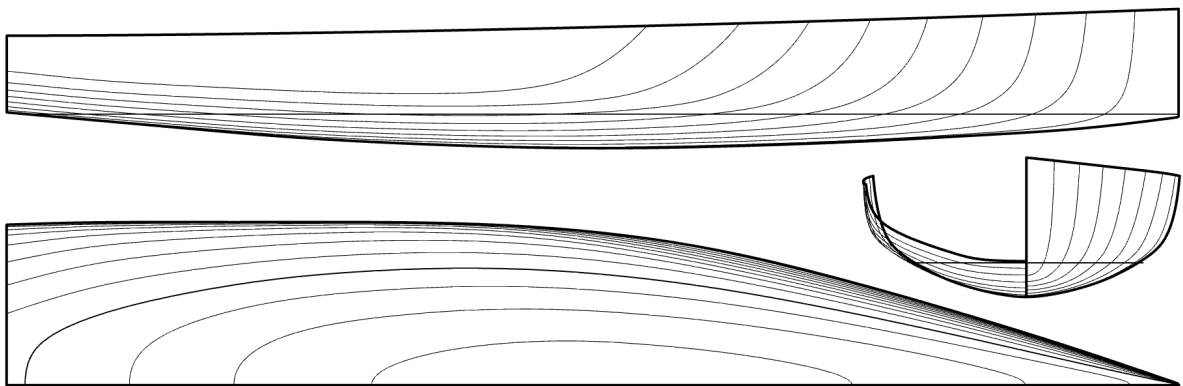
Figure C.21: Lines plan of Sysser 93.
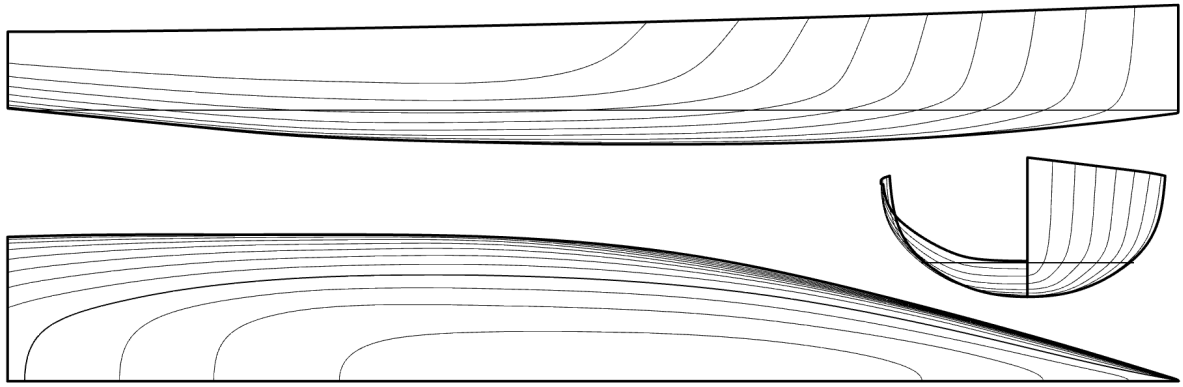
Figure C.22: Lines plan of Sysser 94.
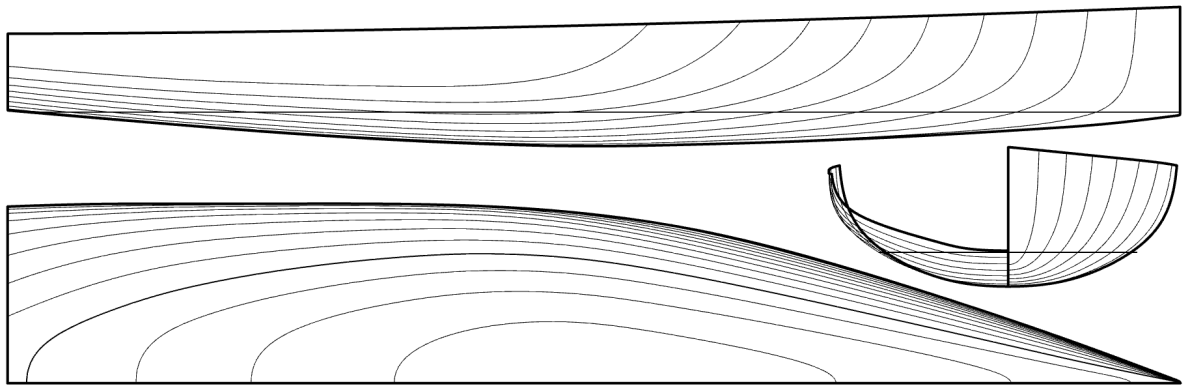
Figure C.23: Lines plan of Sysser 95.
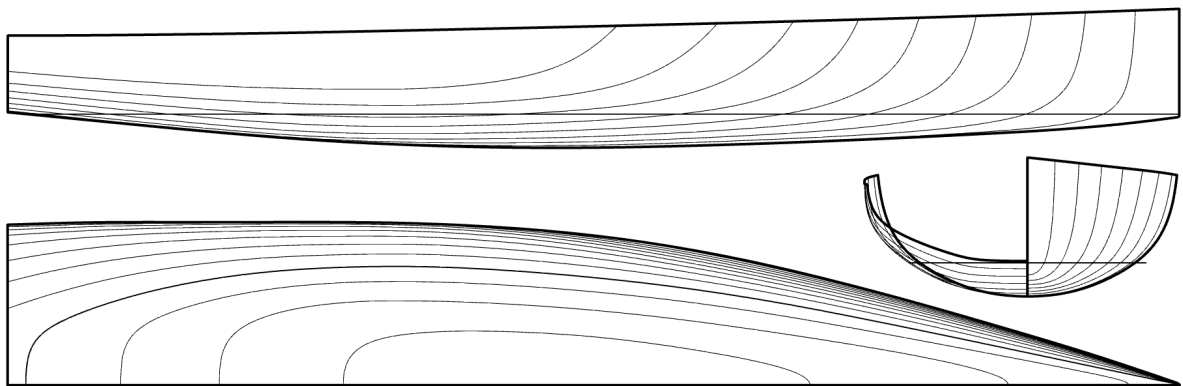
Figure C.24: Lines plan of Sysser 96.
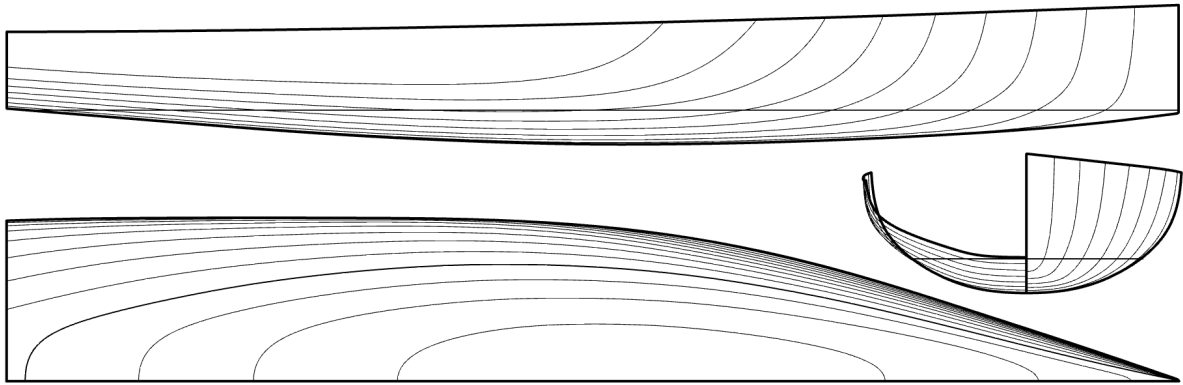
Figure C.25: Lines plan of Sysser 97.
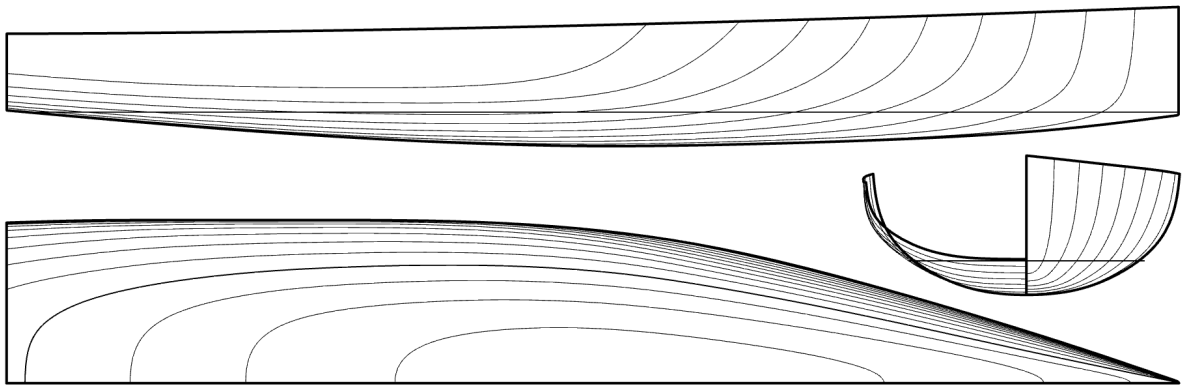
Figure C.26: Lines plan of Sysser 98.
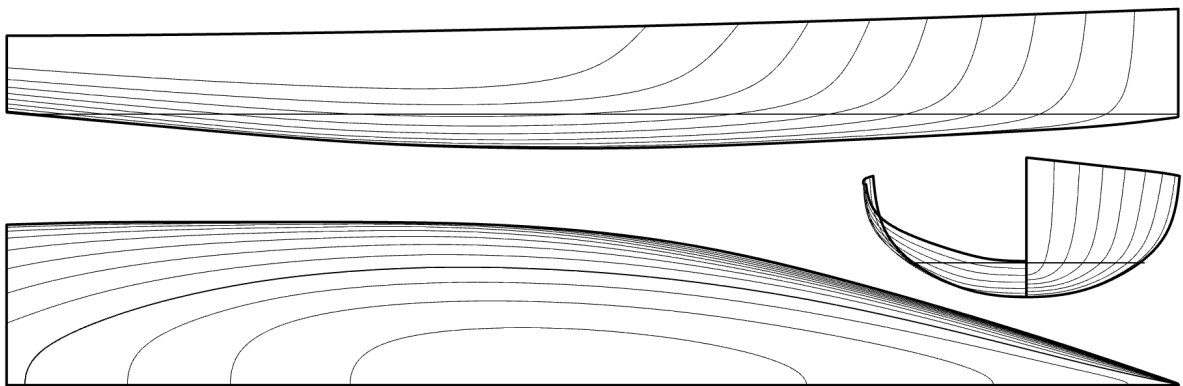
Figure C.27: Lines plan of Sysser 99.
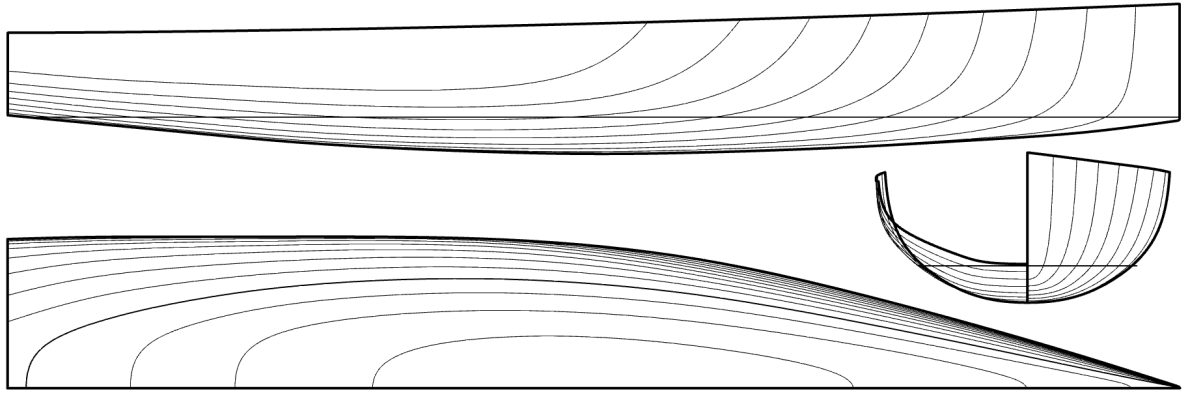
Figure C.28: Lines plan of Sysser 100.
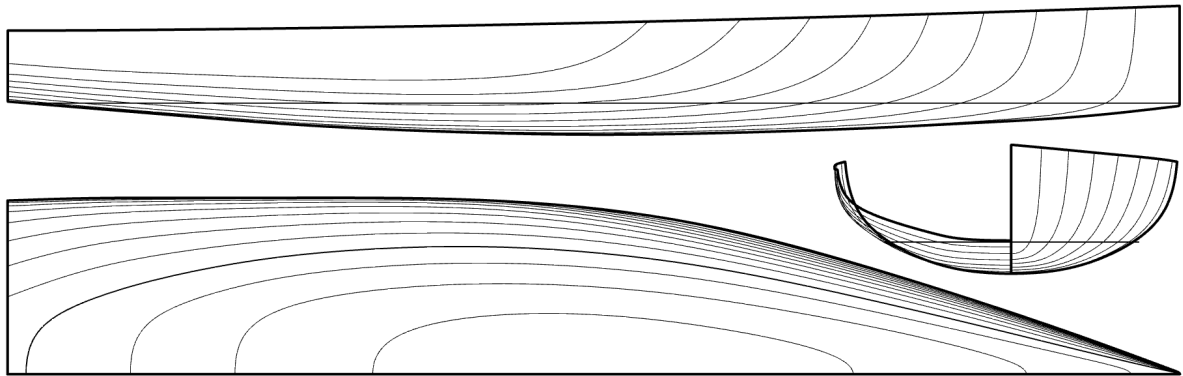
Figure C.29: Lines plan of Sysser 101.
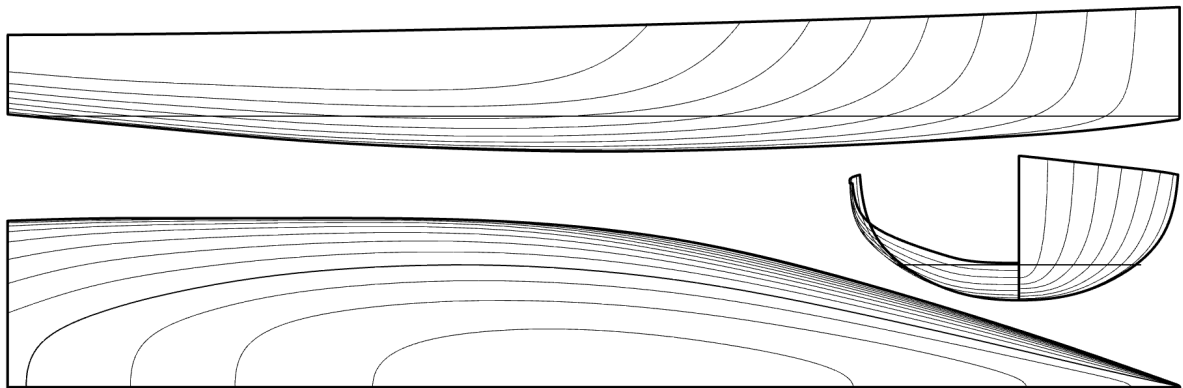
Figure C.30: Lines plan of Sysser 102.
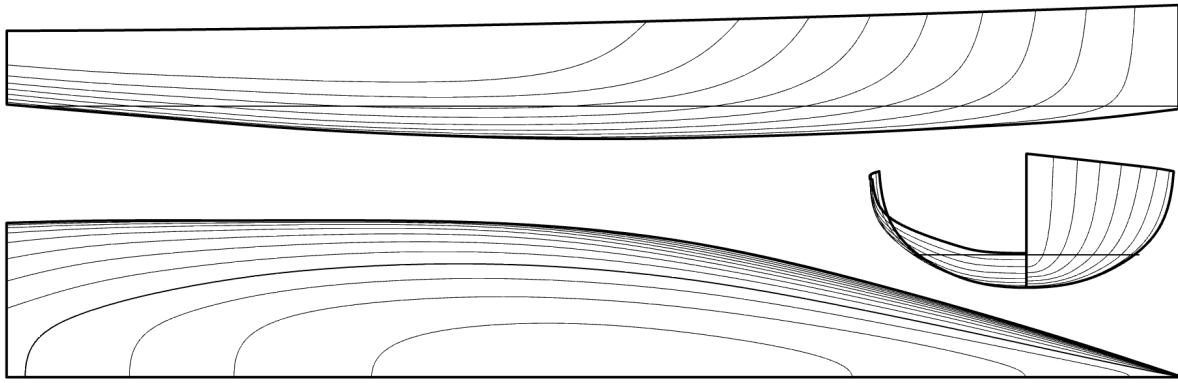
Figure C.31: Lines plan of Sysser 103.
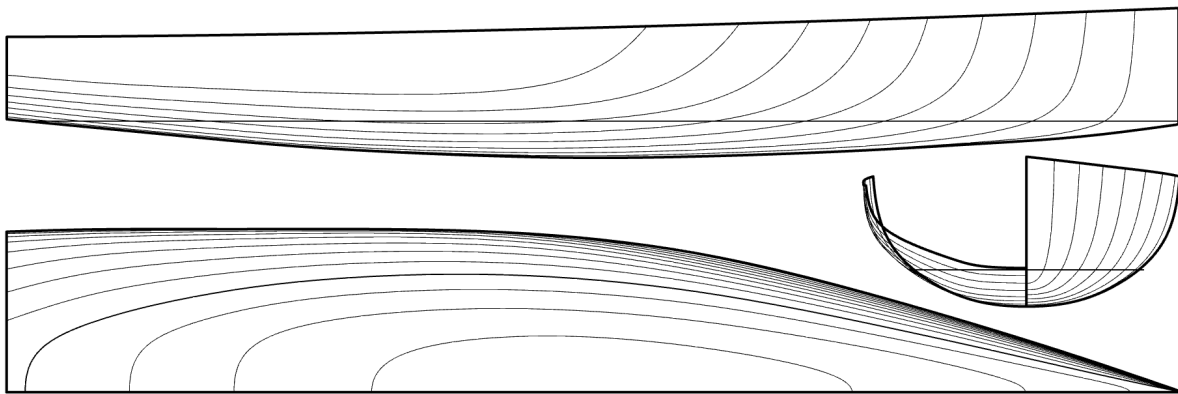
Figure C.32: Lines plan of Sysser 104.
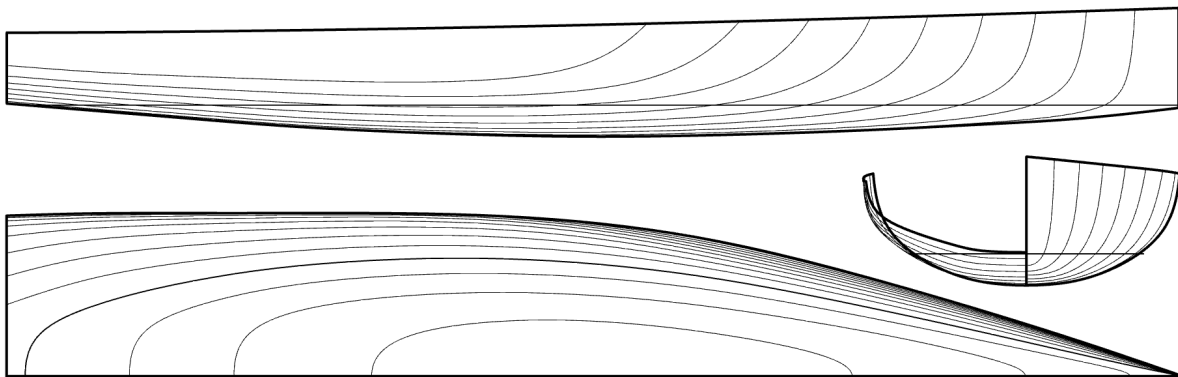
Figure C.33: Lines plan of Sysser 105.

Table C.3: Hydrostatic parameters of the hull shapes belonging to the new systematic series.

	L_{WL} [m]	$L_{WL_{20}}$ [m]	B_{WL} [m]	$B_{WL_{20}}$ [m]	T_c [m]	$T_{c_{20}}$ [m]	∇_c [m^3]	LCB_{fp} [m]	LCF_{fp} [m]	KM_L [m]
Sysser 85	10.00	10.13	2.047	1.905	0.2960	0.3259	2.252	-5.387	-5.734	33.38
Sysser 86	10.00	10.13	1.754	1.737	0.3428	0.3573	2.236	-5.375	-5.728	28.88
Sysser 87	10.00	10.13	2.389	2.006	0.2524	0.3038	2.242	-5.377	-5.729	39.09
Sysser 88	10.00	10.13	2.196	2.042	0.3171	0.3492	2.587	-5.386	-5.733	31.19
Sysser 89	10.00	10.13	1.888	1.757	0.2728	0.3004	1.914	-5.386	-5.733	36.18
Sysser 90	10.00	10.11	2.047	1.970	0.3404	0.3644	2.590	-5.386	-5.733	29.08
Sysser 91	10.00	10.16	2.047	1.816	0.2519	0.2886	1.917	-5.386	-5.733	39.16
Sysser 92	10.00	10.16	2.032	1.924	0.2960	0.3500	2.356	-5.402	-5.743	32.04
Sysser 93	10.00	10.03	2.030	1.853	0.2960	0.2944	2.086	-5.355	-5.716	35.61
Sysser 94	10.00	10.15	1.845	1.766	0.2972	0.3206	2.239	-5.386	-5.739	33.17
Sysser 95	10.00	9.935	2.245	2.032	0.2960	0.3305	2.263	-5.387	-5.727	33.06
Sysser 96	10.00	10.16	2.061	1.895	0.2926	0.3149	2.225	-5.596	-5.850	34.26
Sysser 97	10.00	10.07	2.026	1.904	0.2974	0.3340	2.254	-5.155	-5.609	32.84
Sysser 98	10.00	10.16	2.048	1.890	0.2955	0.3235	2.260	-5.399	-5.861	34.68
Sysser 99	10.00	10.00	2.048	1.920	0.2968	0.3269	2.251	-5.387	-5.628	33.05
Sysser 100	10.00	10.12	1.901	1.833	0.3188	0.3406	2.252	-5.387	-5.734	31.03
Sysser 101	10.00	10.16	2.214	1.967	0.2737	0.3131	2.252	-5.387	-5.734	36.08
Sysser 102	10.00	10.13	2.122	1.975	0.3068	0.3378	2.419	-5.387	-5.734	32.22
Sysser 103	10.00	10.13	1.967	1.831	0.2845	0.3131	2.079	-5.387	-5.734	34.72
Sysser 104	10.00	10.12	2.047	1.940	0.3182	0.3450	2.421	-5.387	-5.734	31.08
Sysser 105	10.00	10.15	2.047	1.863	0.2734	0.3065	2.080	-5.387	-5.734	36.11

	A_W [m^2]	A_X [m^2]	$A_{X_{20}}$ [m^2]	S_c [m^2]	$S_{c_{20}}$ [m^2]	C_b [$-$]	C_p [$-$]	C_w [$-$]	C_x [$-$]	$C_{x_{20}}$ [$-$]
Sysser 85	14.06	0.4143	0.4194	15.00	14.25	0.371	0.543	0.687	0.683	0.675
Sysser 86	12.05	0.4111	0.4146	13.43	13.32	0.372	0.544	0.687	0.684	0.668
Sysser 87	16.41	0.4123	0.4204	17.03	14.91	0.372	0.544	0.687	0.684	0.690
Sysser 88	15.08	0.4760	0.4818	16.08	15.28	0.372	0.544	0.687	0.684	0.676
Sysser 89	12.97	0.3522	0.3565	13.83	13.14	0.371	0.544	0.687	0.683	0.675
Sysser 90	14.06	0.4765	0.4815	15.27	14.86	0.371	0.543	0.687	0.683	0.670
Sysser 91	14.06	0.3527	0.3580	14.76	13.53	0.371	0.544	0.687	0.683	0.683
Sysser 92	14.05	0.4371	0.4362	15.08	14.51	0.392	0.539	0.691	0.726	0.648
Sysser 93	13.91	0.3806	0.3910	14.75	13.82	0.347	0.548	0.685	0.633	0.716
Sysser 94	13.34	0.3712	0.3793	14.43	13.78	0.408	0.603	0.723	0.677	0.670
Sysser 95	14.64	0.4549	0.4586	15.46	14.48	0.341	0.497	0.652	0.685	0.682
Sysser 96	14.08	0.4080	0.4067	15.00	14.15	0.369	0.545	0.683	0.677	0.681
Sysser 97	13.93	0.4164	0.4235	14.91	14.31	0.374	0.541	0.687	0.690	0.666
Sysser 98	14.38	0.4110	0.4120	15.36	14.27	0.373	0.550	0.702	0.679	0.674
Sysser 99	14.05	0.4207	0.4259	14.93	14.17	0.370	0.535	0.686	0.692	0.678
Sysser 100	13.06	0.4143	0.4186	14.19	13.83	0.372	0.543	0.687	0.684	0.670
Sysser 101	15.21	0.4143	0.4206	15.97	14.65	0.372	0.543	0.687	0.684	0.683
Sysser 102	14.57	0.4451	0.4506	15.54	14.77	0.372	0.543	0.687	0.684	0.676
Sysser 103	13.51	0.3826	0.3872	14.41	13.70	0.371	0.543	0.687	0.683	0.676
Sysser 104	14.06	0.4454	0.4504	15.13	14.57	0.372	0.543	0.687	0.684	0.672
Sysser 105	14.06	0.3827	0.3879	14.87	13.90	0.371	0.543	0.687	0.683	0.679

D
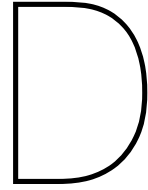
Upright resistance for fixed pitch angles

Table D.1: Upright resistance of Sysser 85 for three fixed pitch angles, computed with the numerical method on the medium grid. The model is free to heave. $\Delta_\% = (F_x - F_x^*)/F_x^* \cdot 100$.

	$\theta = -1°$		$\theta = 0°$	$\theta = +1°$	
Fn	F_x	$\Delta_\%$	F_x^*	F_x	$\Delta_\%$
$[-]$	$[N]$	$[\%]$	$[N]$	$[N]$	$[\%]$
0.25	1.82	11.7	1.63	1.69	3.9
0.35	3.94	8.9	3.62	3.80	5.0
0.45	8.42	-3.3	8.71	9.67	11.0
0.55	13.60	-8.7	14.91	17.01	14.1
0.65	18.46	-8.1	20.08	22.16	10.4
0.75	22.66	-8.1	24.65	27.09	9.9
0.85	27.58	-9.4	30.43	33.47	10.0
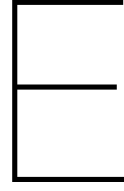
Computational fluid dynamics

The hydrodynamic forces acting on the models in the new systematic series are determined with computational fluid dynamics (CFD). The numerical simulations are performed using the ISIS-CFD flow solver [11] implemented in the commercial FINE™/Marine software package of NUMECA International [35]. This flow solver solves the unsteady incompressible RANS equations with a finite-volume method (FVM). The theoretical background and the simulation settings were discussed in Chapter 6. For the interested reader, a more elaborate explanation of (computational) fluid dynamics is given in this appendix. For a thorough discussion of the physics involved in fluid dynamics, the reader is referred to White [47] and Pope [37]. For a thorough discussion of all the mathematical details of CFD, the reader is referred to Wesseling [46].

E.1. Governing equations

The governing equations of fluid dynamics are based on the following three fundamental physical principles: conservation of mass, conservation of energy and Newton's second law of motion. From these principles, the continuity equation, the energy equation and the momentum equations can be derived, respectively. Computational fluid dynamics (CFD) is based on these equations. With the assumption of incompressible flow under isothermal conditions, the governing equations are the incompressible Navier-Stokes equations. The incompressible Navier-Stokes equations in Cartesian coordinates, in an Eulerian formulation, are given by

$$\frac{\partial u_i}{\partial x_i} = 0, \tag{E.1a}$$

$$\frac{\partial u_i}{\partial t} + u_j \frac{\partial u_i}{\partial x_j} = -\frac{1}{\rho} \frac{\partial p}{\partial x_i} + v \frac{\partial^2 u_i}{\partial x_j^2} + g_i, \tag{E.1b}$$

where u_i are the Cartesian velocity components, x_i are the Cartesian coordinates, t is the time, ρ is the density, p is the pressure, v is the kinematic viscosity, and g_i is the gravitational acceleration. Subscripts i and j can have values 1, 2 or 3 and denote one of the three Cartesian coordinates, x_1, x_2 and x_3, and corresponding velocity components, u_1, u_2 and u_3. Note that as a consequence of Einstein notation, or Einstein summation convention, summation over the repeated index in a term is implied.

Equation (E.1a) is the conservation of mass equation, or the continuity equation. This equation is transformed into a pressure equation from which the pressure field is extracted in the ISIS-CFD flow solver. The reader is referred to Wesseling [46] for the mathematical details.

Equation (E.1b) is one of the three momentum equations. The two terms on the left-hand side of the momentum equation arise from the inertia of fluid particles and form the material derivative, or particle derivative. The first term is the local derivative, which describes the local temporal rate of change of momentum. The second term is the convective derivative, which describes the rate of change of momentum as a result of the movement of fluid particles.

The first two terms on the right-hand side of the momentum equation are surface forces acting on fluid particles and originate from the normal stresses and the shear stresses acting on these particles.

The normal stress acting on a fluid particle is the pressure, p. The shear stress acting on a fluid particle is $\mu(\partial u_i/\partial x_j + \partial u_j/\partial x_i)$. The first term on the right-hand side is the pressure term and represents the pressure force that acts on the fluid particles. The second term is the viscous term and represents the friction force. The third term is the body force acting on the fluid particles.

E.1.1. Reynolds-averaged Navier-Stokes equations

The flow field around a ship is likely to be partly or fully turbulent. A turbulent flow contains a very wide range of length scales of turbulent motion. Solving the Navier-Stokes equations for a turbulent flow requires capturing of all the length scales — eddy sizes — of turbulent motion, because different physical processes occur at these scales. According the energy-cascade concept of Richardson [42], turbulent kinetic energy is produced at the largest scale and dissipated at the smallest scale by viscous dissipation. Large eddies are unstable and break up into successively smaller and smaller eddies. They transfer thereby their turbulent kinetic energy to smaller and smaller scales, until the turbulent kinetic energy is dissipated at the smallest scale. All the scales of turbulent motion should be captured, because the physical processes occurring at each scale are very import.

In general, for turbulent flows in ship hydromechanics applications, the full Navier-Stokes equations are too complex to solve by direct numerical simulation (DNS) due to this very wide range of length scales of turbulent motion. By using modelling approaches, e.g. large-eddy simulation (LES) or the Reynolds-averaged Navier-Stokes (RANS) equations, solving turbulent motion can be greatly simplified by modelling instead of resolving all the scales of turbulent motion. For practical ship hydromechanics applications, LES is still too costly. For the present study, the RANS equations are used, because they produce sufficiently accurate results for an acceptable required computation time.

To derive the RANS equations, Reynolds-averaging is applied to the Navier-Stokes equations to obtain the mean, or time-averaged, equations of fluid motion. Following Reynolds [41], any flow quantity f is decomposed into a mean value, $\overline{f}$, and a fluctuating value, f', in order to capture the randomly unsteady turbulent state of the flow; i.e. $f = \overline{f} + f'$. The mean value is defined by

$$\overline{f} = \frac{1}{T} \int_{t_0}^{t_0+T} f\, dt, \tag{E.2}$$

where the time period of length T is large compared to the relevant period of the turbulent fluctuations. The mean value of a flow quantity may vary 'slowly' with time. If this is the case, the flow is classified as an unsteady turbulent flow. From Equation (E.2), the following rules of averaging can be derived for any two flow quantities f and g:

$$\overline{f+g} = \overline{f} + \overline{g}, \qquad \overline{cf} = c\overline{f}, \qquad \overline{\overline{f}} = \overline{f}, \qquad \overline{f'} = 0, \qquad \overline{\frac{\partial f}{\partial s}} = \frac{\partial \overline{f}}{\partial s}, \qquad \overline{\overline{f}g} = \overline{f} \cdot \overline{g}, \tag{E.3}$$

where c is some arbitrary constant, and s is any time or spatial coordinate. For incompressible turbulent flow, fluctuations in the velocities and the pressure are expected; hence, $u_i = \overline{u}_i + u'_i$, and $p = \overline{p} + p'$. Substitution of these Reynolds decompositions into the Navier-Stokes equations (E.1), applying time averaging to the resulting equations, and rewriting with the rules of averaging (E.3) yields the RANS equations:

$$\frac{\partial \overline{u}_i}{\partial x_i} = 0, \tag{6.1a}$$

$$\frac{\partial \overline{u}_i}{\partial t} + \overline{u}_j \frac{\partial \overline{u}_i}{\partial x_j} = -\frac{1}{\rho}\frac{\partial \overline{p}}{\partial x_i} + \nu \frac{\partial^2 \overline{u}_i}{\partial x_j^2} + g_i - \frac{\partial \overline{u'_i u'_j}}{\partial x_j}, \tag{6.1b}$$

where the last term in the Reynolds-averaged momentum equation is the Reynolds stress, or turbulent stress, term. This term originates from the transport of mean momentum by turbulent fluctuations. The turbulent fluctuations seem to act on the mean flow as if they induce an additional stress on the fluid particles; therefore, it is called a stress. The Reynolds stress, or turbulent stress, is defined as $\rho\overline{u'_i u'_j}$. The first two terms on the right-hand side of the mean momentum equation represent together the

surface forces originating from the mean molecular stress acting on a fluid particle.

The Reynolds stress term poses a problem: there are now ten unknowns — three mean-velocity components, the mean pressure and the six Reynolds stresses — while there are only four equations — one mean continuity equation and three mean momentum equations. An additional closure model or turbulence model is needed for the modelling of the Reynolds stress term in the RANS equations.

E.1.2. Turbulence models

As a consequence of Reynolds-averaging the Navier-Stokes equations, an additional turbulence model is necessary to close the resulting equations. Many turbulence models were developed and proposed over the years. Selecting an appropriate turbulence model is all about balancing the desired accuracy against the computation time. For the present study, the large systemic series requires small computation times while keeping a sufficiently high accuracy.

According to the ITTC [18], $k - \omega$ two-equation turbulence models have shown to be able to yield accurate predictions in ship hydromechanics. They are by far the most applied turbulence models in this scientific field. A $k - \omega$ turbulence model is also used for the present study, because it produces sufficiently accurate results for an acceptable required computation time.

$k - \omega$ two-equation turbulence models use a transport equation for the turbulent kinetic energy, k, and a transport equation for the specific turbulence dissipation rate, ω, to model the conservation of these two turbulence quantities. In general, a transport equation describes the conservation of a particular flow quantity as the rate of change of that flow quantity as function of convection, diffusion, production and dissipation of that flow quantity. The turbulent kinetic energy is defined by $k = \overline{u'_i u'_i}/2$. The specific turbulence dissipation rate, or turbulence frequency, ω, is defined as the dissipation rate of turbulent kinetic energy, ϵ, divided by the turbulent kinetic energy, k; i.e. $\omega = \epsilon/k$. The turbulent kinetic energy and the specific turbulence dissipation rate calculated from the two transport equations are used to determine the Reynolds stresses.

Various $k - \omega$ two-equation turbulence models were developed and proposed over the years. For an accurate determination of the hydrodynamic forces in ship hydromechanics, two good options for turbulence modelling are the EASM $k - \omega$ two-equation turbulence model, Gatski and Speziale [12], and the SST $k - \omega$ two-equation turbulence model, developed by Menter [34]. Over the years, several changes were made to both turbulence models; therefore, various variations of both models exist. The principles of both models have not changed and are discussed in this subsection. The EASM and the SST $k - \omega$ two-equation turbulence model are both implemented in the ISIS-CFD flow solver. The specific details of the turbulence models implemented in this flow solver are given in its theoretical manual [11].

The EASM $k - \omega$ turbulence model and the SST $k - \omega$ turbulence model differ in the way the Reynolds stress term is modelled. The SST $k - \omega$ model is a linear eddy-viscosity model and follows the Boussinesq hypothesis, or Boussinesq eddy-viscosity assumption. This hypothesis models the turbulent stress analogous to the mean molecular stress as a turbulent normal stress and a turbulent shear stress. The turbulent normal stress, also called the turbulent pressure, is assumed to be proportional to the turbulent kinetic energy. The turbulent shear stress is assumed to have a similar formulation as the mean viscous shear stress, $\mu(\partial \overline{u}_i/\partial x_j + \partial \overline{u}_j/\partial x_i)$, only the dynamic viscosity, μ, is replaced by the turbulent viscosity, or eddy viscosity, μ_t; i.e. the turbulent shear stress is modelled as $\mu_t(\partial \overline{u}_i/\partial x_j + \partial \overline{u}_j/\partial x_i)$. The eddy viscosity is determined with an empirical formulation from the turbulent kinetic energy and the specific turbulence dissipation rate.

The shear stress transport $k - \omega$ model, developed by Menter [34], combines the best performance of $k - \omega$ turbulence models and $k - \epsilon$ turbulence models. According to Wilcox [48], $k - \omega$ models are superior to $k - \epsilon$ models for boundary layer flows. On the other hand, for free-stream flows, $k - \epsilon$ models are superior.

The shear stress transport model rewrites the transport equation for ϵ into a non-standard transport equation for ω. Multiplication of some terms in this equation for ω with a 'blending function' combines the standard formulations of $k - \omega$ models and $k - \epsilon$ models. The resulting non-standard transport equation for ω and the standard transport equation for k are used to form the SST $k - \omega$ two-equation turbulence model. The specific turbulence dissipation rate, ω, and the turbulence dissipation rate, ϵ, are closely related to each other by $\omega = \epsilon/k$.

Close to a solid wall, the blending function is zero, whereas far in the free-stream flow, the blending

function is unity. The result is that close to the solid wall, the standard transport equation for ω is used, whereas far away from the solid wall, in the free-stream flow, the non-standard transport equation for ω reduces to a formulation for ω that corresponds to the standard transport equation of ϵ. In between these two locations, a combination of $k - \omega$ models and $k - \epsilon$ models is captured by the non-standard transport equation for ω.

For complex turbulent flows characterized by intense vortices, the isotropic description of turbulence in the Boussinesq hypothesis probably results in inaccurate results. The EASM $k - \omega$ model uses a different approach for the modelling of the Reynolds stresses. Algebraic stress models are derived from the six Reynolds stress equations. A Reynolds stress equation, or Reynolds stress transport equation, is a conservation equation for a single Reynolds stress component and describes the rate of change of that Reynolds stress as function of the convection, production, diffusion and dissipation of that stress. It also incorporates pressure-strain effects. For the derivation of the Reynolds stress equations, the reader is referred to Pope [37] and White [47].

Reynolds stress equations are extremely complex differential equations. From the six Reynolds stress equations, simpler algebraic equations can be derived with modelling assumptions to obtain an algebraic stress model (ASM). Algebraic stress models implicitly determine the Reynolds stresses as function of the turbulent kinetic energy, the turbulence frequency and the mean-velocity gradients. This requires an iterative procedure to solve all the involved equations numerically.

Explicit analytical solutions of the algebraic equations for the Reynolds stresses used in ASMs can generally be derived. These solutions form then an explicit algebraic stress model (EASM). The Reynolds stresses can now be explicitly determined from the turbulent kinetic energy, the turbulence frequency and the mean-velocity gradients. For the mathematical background and the derivation of the EASM model, the reader is referred to Gatski and Speziale [12].

Compared to linear eddy-viscosity models, the Reynolds stresses in EASMs are modelled with additional (non-linear) terms that can include powers of the mean-velocity gradients or combinations of the mean strain-rate tensor and the mean rotation-rate tensor. This allows for an anisotropic description of turbulence. This anisotropic description enhances the modelling of vortices significantly compared to linear eddy-viscosity models.

In the EASM $k - \omega$ two-equation turbulence model, the turbulent kinetic energy and the specific turbulence dissipation rate determined with the two transport equations are used in the explicit algebraic expressions for the Reynolds stress components and in an empirical formulation for the eddy viscosity. The EASM model and the SST model use different empirical formulations for the eddy viscosity.

E.2. Boundary layer

Viscous fluid flow over a solid surface produces a boundary layer as a result of the no-slip condition between the wall and the fluid. The flow field around a ship is likely to be partly or fully turbulent, and therefore, turbulent boundary layers are discussed. Following White [47] and Pope [37], in order to account for the complex physical effects in turbulent boundary layers separately, the mean-velocity profile normal to the solid wall in a turbulent boundary layer is thought to consist of an inner layer, an overlap region and an outer layer. In the inner layer, the mean-velocity profile does not explicitly depend on free-stream conditions. In the outer layer, the flow does not explicitly depend on wall conditions; direct effects of viscosity on the mean velocity are negligible. The overlap region is defined as the intermediate region between the two layers. For the sake of illustration, a typical mean-velocity profile in a turbulent boundary layer over a smooth curved surface with a mild adverse pressure gradient is depicted in Figure E.1. The shape of the mean-velocity profile depends on the Reynolds number of the flow and the magnitude of the pressure gradient.

These three layers are subdivided into other regions and layers. With increasing distance from the wall, the following layers were defined [37,47]: the viscous sublayer, the buffer layer, the log-law region and the velocity-defect layer. The range of each region or layer depends on the Reynolds number of the flow. For the sake of illustration, a sketch of the various wall regions and layers for a turbulent channel flow is shown in Figure E.2. Laws exist to describe the mean-velocity profile in some of the layers. In the log-law region, the log-law holds. The log-law states that the mean velocity at a certain point in the turbulent boundary layer is proportional to the logarithm of the distance from that point to the wall, i.e. $u^+ \propto \ln y^+$.

An illustration of a log-law fitted to a typical mean-velocity profile is shown in Figure E.1. For the depicted mean-velocity profile, the log-law holds for approximately $30 \leq y^+ \leq 200$. Before $y^+ = 30$, a part of the velocity profile in the buffer layer is depicted. After $y^+ = 200$, the velocity profile in the velocity-defect layer for a mild adverse pressure gradient is depicted. The shape of the velocity profile in this layer depends heavily on the strength and the direction of the pressure gradient. A stronger adverse pressure gradient results in a steeper profile. A strong favourable pressure gradient results in a velocity profile very close to the depicted log-law.

The total shear stress in a turbulent flow consists of the viscous shear stress and the turbulent shear stress. Turbulent shear stress dominates in the turbulent boundary layer except for the region close to the solid wall. The viscous contribution to the total shear stress is significant in the viscous wall region. The viscous wall region ends where the overlap region and the outer layer begin. In the viscous wall region, high velocity gradients as a result of the no-slip condition are present. Very close to the wall, in the viscous sublayer, the turbulent shear stress is negligible, and the viscous shear stress dominates. The viscous sublayer is a part of the viscous wall region. The buffer layer, which is also a part of the viscous wall region, is defined as the region between the viscous sublayer and the log-law region. For the specific details of each layer and region, the reader is referred to Pope [37] and White [47].

The range of these regions is typically defined with the distance from the wall expressed in viscous lengths, or wall units. This wall coordinate, y^+, is defined by

$$y^+ = \frac{y u_\tau}{\nu}, \tag{E.5}$$

where y is the normal distance to the wall, and u_τ is the wall-friction velocity defined by

$$u_\tau = \sqrt{\frac{\tau_W}{\rho}}. \tag{E.6}$$

The wall shear stress, τ_W, consists solely of the viscous shear stress and is defined for two-dimensional flows as

$$\tau_W = \mu \left(\frac{\partial \overline{u}}{\partial y} \right)_{y=0}. \tag{E.7}$$

The wall shear stress can also be determined by

$$\tau_W = \frac{1}{2} \rho V_{ref}^2 C_f, \tag{E.8}$$

where V_{ref} is the reference velocity, and C_f is the calculated or estimated friction coefficient.
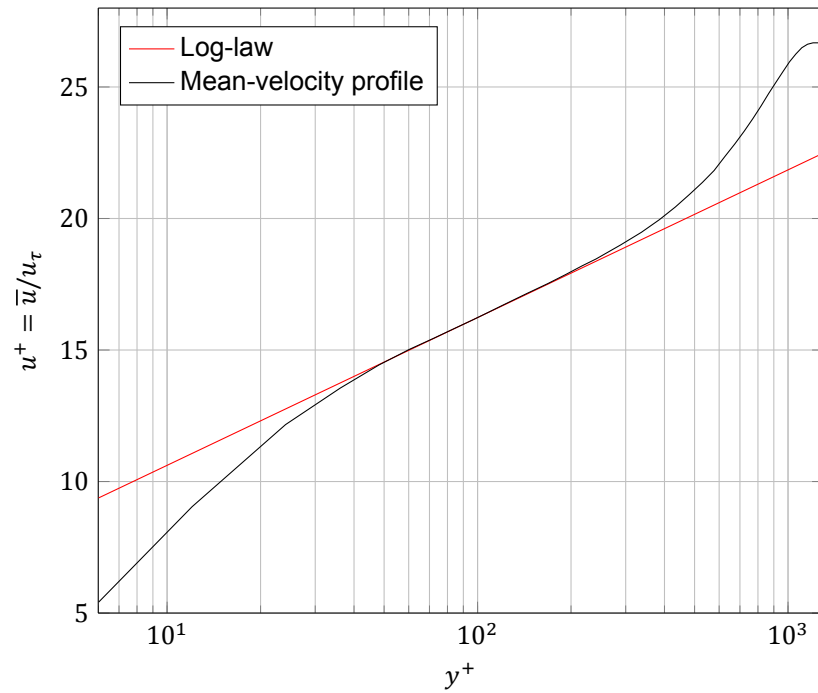
Figure E.1: A typical measured mean-velocity profile in a turbulent boundary layer over a smooth curved surface with a mild adverse pressure gradient. A fitted log-law is also depicted.
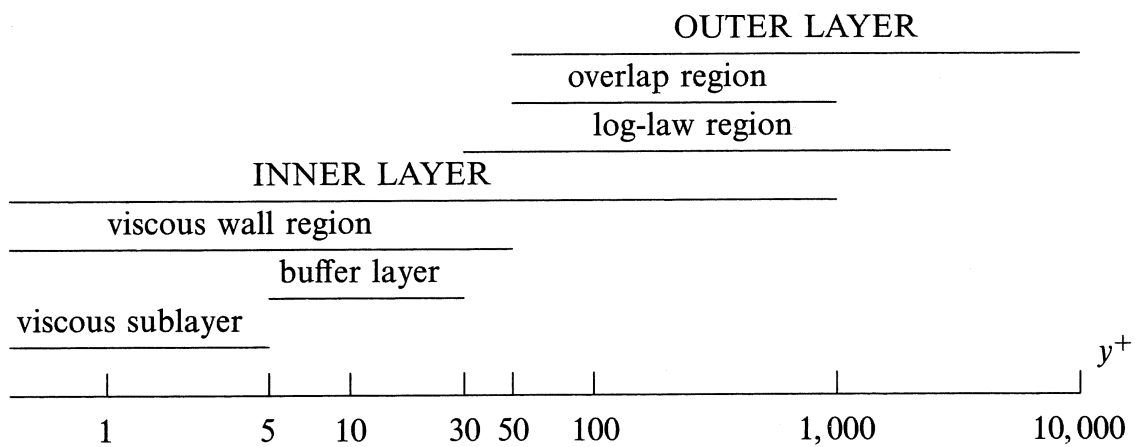
Figure E.2: A sketch of the various wall regions and layers for a turbulent channel flow at $Re = 10^4$. Figure from Pope [37].
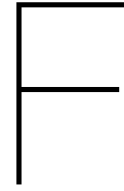
Numerical tests

The results of the computational tests performed with the FINE™/Marine CFD solver in Chapter 6.

Turbulence models

Table F.1: Resistance of Sysser 85 for the crew CoG position, computed with two different turbulence models on the medium grid. The computation time is also listed. $\Delta_{\%} = (F_x - F_x{}^*)/F_x{}^* \cdot 100$.

	SST $k - \omega$ model		EASM $k - \omega$ model		
Fn	$F_x{}^*$	Computation time	F_x	Computation time	$\Delta_{\%}$
$[-]$	$[N]$	$[min]$	$[N]$	$[min]$	$[\%]$
0.45	8.4926	735	8.5587	620	0.78
0.85	28.3616	851	28.5426	931	0.64

Height of the grid refinement around the initial free surface

Table F.2: Resistance of Sysser 85 for the crew CoG position, computed on the medium grid and on a grid with a 25-percent thicker grid refinement around the initial free surface. The cell sizes in the refinement region are the same for both grids. They differ in the height of the grid refinement only. The number of grid cells, N_i, is also listed. $\Delta_{\%} = (F_x - F_x{}^*)/F_x{}^* \cdot 1000$.

	Medium grid		Thicker refinement		
Fn	N_i	$F_x{}^*$	N_i	F_x	$\Delta_{\%}$
$[-]$	$[-]$	$[N]$	$[-]$	$[N]$	$[\permil]$
0.45	862875	8.4925	1072127	8.4918	-0.076
0.85	908136	28.3094	1122809	28.3073	-0.072

Grid refinement at the hull and the transom curve

Table F.3: Resistance of Sysser 85 for the crew CoG position, computed on three different grids: the medium grid, a grid with additional refinement of the hull compared to the medium grid, and a grid with additional refinement of the transom curve compared to the medium grid. The number of grid cells, N_i, is also listed. $\Delta_{\%} = (F_x - F_x{}^*)/F_x{}^* \cdot 1000$.

	Medium grid		Additional refinement hull			Additional refinement transom curve		
Fn	N_i	$F_x{}^*$	N_i	F_x	$\Delta_{\%}$	N_i	F_x	$\Delta_{\%}$
$[-]$	$[-]$	$[N]$	$[-]$	$[N]$	$[\permil]$	$[-]$	$[N]$	$[\permil]$
0.45	862875	8.4925	1424832	8.4839	-1.0	924438	8.4868	-0.67
0.85	908136	28.3094	1586049	28.3165	0.25	977027	28.3108	0.051

Convergence

Table F.4: The converged solution of Sysser 85 for the crew CoG position and the solution after a doubling of the number of time steps in the simulation. $\Delta_{\%} = (F_x - F_x{}^*)/F_x{}^* \cdot 1000$.

Fn	Converged solution			Double number of time steps			
	$F_x{}^*$	z	θ	F_x	z	θ	$\Delta_{\%}$
$[-]$	$[N]$	$[m]$	$[°]$	$[N]$	$[m]$	$[°]$	$[‰]$
0.45	8.4925	-9.8745	-0.3484	8.4928	-9.8741	-0.3475	0.042
0.85	28.3094	-8.2183	-0.6801	28.3226	-8.2330	-0.6790	0.47

G

Bare hull upright trimmed resistance prediction

From the dataset of the new systematic series, which contains the bare hull upright trimmed resistance values obtained with CFD for various hull forms, speeds and trimming moments, new expressions for the estimation of the bare hull upright trimmed resistance from hydrostatic parameters of the hull have been derived. The bare hull upright trimmed resistance prediction is summarized below. The parameter range covered by these regression formulas is listed in Tables 3.3 and G.1. This range is prescribed by the hydrostatic parameters of the hull shapes in the systematic series, listed in Table C.3, and by the longitudinal centre of gravity, LCG_{fp}, defined by Equation (4.4).

1. The frictional resistance of the bare hull, R_{F_h}, is defined by

$$R_{F_h} = \frac{1}{2}\rho V^2 S_c C_f, \tag{2.6}$$

where ρ is the density of water, V is the velocity of the hull, S_c is the wetted surface of the canoe body, and C_f is the friction coefficient calculated with the ITTC 1957 Model-Ship Correlation Line [16]:

$$C_f = \frac{0.075}{(log(Re) - 2)^2}, \tag{2.7}$$

in which the Reynolds number, Re, is defined by

$$Re = \frac{0.9L_{WL} \cdot V}{\nu}, \tag{10.1}$$

where L_{WL} is the length of the waterline, $0.9L_{WL}$ is the characteristic length in the Reynolds number, and ν is the kinematic viscosity of water. No form factor is used in the formulation for the frictional resistance of the bare hull.

2. The upright trimmed residuary resistance of the bare hull, $R_{R\theta_h}$, can be determined by either one of the following five regressions:

(i) The expression for the minimum upright trimmed residuary resistance:

$$\frac{R_{R\theta_h}}{\nabla_c \rho g}\left(\frac{L_{WL}}{\nabla_c^{1/3}}\right) = a_0 + a_1\frac{B_{WL}}{L_{WL}} + a_2\frac{T_c}{B_{WL}} + a_3\frac{LCB_{fp}}{L_{WL}} + a_4\frac{LCB_{fp}}{LCF_{fp}} + a_5C_p + a_6C_x$$

$$+ a_7C_p{}^2 + a_8\left(\frac{LCB_{fp}}{L_{WL}}\right)^2 + a_9\left(\frac{LCB_{fp}}{LCF_{fp}}\right)^2; \tag{10.10}$$

155

(ii) The expression for the upright trimmed residuary resistance with the crew CoG position:

$$\frac{R_{R\theta_h}}{\nabla_c \rho g}\left(\frac{L_{WL}}{\nabla_c^{1/3}}\right) = b_0 + b_1\frac{B_{WL}}{L_{WL}} + b_2\frac{T_c}{B_{WL}} + b_3\frac{LCB_{fp}}{L_{WL}} + b_4\frac{LCB_{fp}}{LCF_{fp}} + b_5 C_p + b_6 C_x$$
$$+ b_7 C_p{}^2 + b_8\left(\frac{LCB_{fp}}{L_{WL}}\right)^2 + b_9\left(\frac{LCB_{fp}}{LCF_{fp}}\right)^2;$$

(10.11)

(iii) The expression for the upright trimmed residuary resistance with the crew middle position:

$$\frac{R_{R\theta_h}}{\nabla_c \rho g}\left(\frac{L_{WL}}{\nabla_c^{1/3}}\right) = c_0 + c_1\frac{B_{WL}}{L_{WL}} + c_2\frac{T_c}{B_{WL}} + c_3\frac{LCB_{fp}}{L_{WL}} + c_4\frac{LCB_{fp}}{LCF_{fp}} + c_5 C_p + c_6 C_x$$
$$+ c_7 C_p{}^2 + c_8\left(\frac{LCB_{fp}}{L_{WL}}\right)^2 + c_9\left(\frac{LCB_{fp}}{LCF_{fp}}\right)^2;$$

(10.12)

(iv) The expression for the upright trimmed residuary resistance with the crew back position:

$$\frac{R_{R\theta_h}}{\nabla_c \rho g}\left(\frac{L_{WL}}{\nabla_c^{1/3}}\right) = d_0 + d_1\frac{B_{WL}}{L_{WL}} + d_2\frac{T_c}{B_{WL}} + d_3\frac{LCB_{fp}}{L_{WL}} + d_4\frac{LCB_{fp}}{LCF_{fp}} + d_5 C_p + d_6 C_x$$
$$+ d_7 C_p{}^2 + d_8\left(\frac{LCB_{fp}}{L_{WL}}\right)^2 + d_9\left(\frac{LCB_{fp}}{LCF_{fp}}\right)^2;$$

(10.13)

(v) The expression for the upright trimmed residuary resistance covering the influence of the trimming moment of the crew's weight through the longitudinal centre of gravity:

$$\frac{R_{R\theta_h}}{\nabla_c \rho g}\left(\frac{L_{WL}}{\nabla_c^{1/3}}\right) = e_0 + e_1\frac{B_{WL}}{L_{WL}} + e_2\frac{T_c}{B_{WL}} + e_3\frac{LCB_{fp}}{L_{WL}} + e_4\frac{LCB_{fp}}{LCF_{fp}} + e_5 C_p + e_6 C_x$$
$$+ e_7 C_p{}^2 + e_8\left(\frac{LCB_{fp}}{L_{WL}}\right)^2 + e_9\left(\frac{LCB_{fp}}{LCF_{fp}}\right)^2$$
$$+ e_{10}\frac{LCG_{fp}}{L_{WL}} + e_{11}\left(\frac{LCG_{fp}}{L_{WL}}\right)^2;$$

(10.14)

where a_i, b_i, c_i, d_i and e_i are the coefficients of the five regressions. The longitudinal centre of gravity is defined by Equation (4.4). All the coefficients have been determined for Froude numbers 0.25 up to 0.95 with increments of 0.10 and are listed in Table G.2. Alternative formulations, excluding the quadratic terms in the regressions, can also be used. The coefficients of the alternative regressions are listed in Table G.3. The upright resistance at any speed can be determined by fitting a cubic spline to the estimated resistance values using a least-squares fit.

3. The upright trimmed resistance of the bare hull, $R_{T\theta_h}$, can be determined by

$$R_{T\theta_h} = R_{F_h} + R_{R\theta_h}.$$

(5.2)

4. The total resistance with appendages under heel and leeway can now be computed by following the procedure described in Chapter 5 and Figure 5.1. The regression formulas of the DSYHS, described in Chapter 2, are used for the remaining resistance components.

Table G.1: The longitudinal centre of gravity-to-length ratio range covered by
the new regressions for the bare hull upright trimmed residuary resistance.
The longitudinal centre of gravity is defined by Equation (4.4).

	Crew CoG	Crew middle	Crew back
	$\frac{LCG_{fp}}{L_{WL}} = \frac{LCB_{fp}}{L_{WL}}$	$\frac{LCG_{fp}}{L_{WL}}$	$\frac{LCG_{fp}}{L_{WL}}$
Sysser 85	0.539	0.563	0.588
Sysser 86	0.538	0.562	0.587
Sysser 87	0.538	0.562	0.587
Sysser 88	0.539	0.560	0.581
Sysser 89	0.539	0.567	0.596
Sysser 90	0.539	0.560	0.581
Sysser 91	0.539	0.567	0.596
Sysser 92	0.540	0.564	0.587
Sysser 93	0.536	0.562	0.589
Sysser 94	0.539	0.563	0.588
Sysser 95	0.539	0.563	0.588
Sysser 96	0.560	0.584	0.609
Sysser 97	0.515	0.540	0.565
Sysser 98	0.540	0.564	0.589
Sysser 99	0.539	0.563	0.588
Sysser 100	0.539	0.563	0.588
Sysser 101	0.539	0.563	0.588
Sysser 102	0.539	0.562	0.584
Sysser 103	0.539	0.565	0.592
Sysser 104	0.539	0.562	0.584
Sysser 105	0.539	0.565	0.592
Maximum	0.560	0.584	0.609
Minimum	0.515	0.540	0.565
Mean	0.538	0.563	0.588

Table G.2: The coefficients of the five regressions for the upright trimmed residuary resistance of the bare hull, $R_{R\theta_h}$, Equations (10.10) up to (10.14). All the coefficients are multiplied by 100 and are dimensionless. The relative comparison error, η, is defined by Equation (10.15) and is given as a percentage.

(a) Coefficients a_i of Equation (10.10).

Fn	0.25	0.35	0.45	0.55	0.65	0.75	0.85	0.95
a_0	23.919	423.42	583.43	337.16	106.99	290.66	171.44	5546.7
a_1	5.37	17.231	63.958	128.58	148.51	158.7	212.79	277.41
a_2	1.6124	3.3971	42.38	68.881	64.262	45.156	-4.1476	-107.88
a_3	11.69	-562.82	-735.6	-836.22	-1713.2	-2960.9	-5466	-22459
a_4	-60.023	-517.71	-686.15	-19.537	1045.5	1543.9	3603.8	2769.9
a_5	-0.97182	-135.32	-292.96	-451.47	-497.2	-681.47	-1127.7	-1950.2
a_6	-0.11358	0.62106	14.268	19.469	10.471	-6.7194	-27.266	-58.331
a_7	1.8952	134.06	261.28	392.32	425.76	583.65	964.37	1658.6
a_8	-3.6824	522.84	645.39	749.78	1615.3	2809.2	5072.8	20530
a_9	29.979	280.49	385.85	27.111	-564.93	-853.8	-1957.4	-1552.3
R^2	0.997	0.998	0.999	0.999	0.997	1.000	0.999	0.998
max(η)	1.72	1.41	1.08	1.28	2.22	0.38	1.23	2.85
min(η)	0.00	0.02	0.00	0.00	0.03	0.00	0.02	0.06
mean(η)	0.68	0.36	0.25	0.33	0.46	0.13	0.35	0.55

(b) Coefficients b_i of Equation (10.11).

Fn	0.25	0.35	0.45	0.55	0.65	0.75	0.85
b_0	23.919	450.83	1027.3	1601.4	1087.2	320.56	2053.7
b_1	5.37	17.219	72.289	140.4	179.77	174.94	323.15
b_2	1.6124	3.385	42.42	66.89	54.5	5.6176	-84.177
b_3	11.69	-649.85	-1894.4	-2495.9	-2004.8	-4980.1	-17873
b_4	-60.023	-525.14	-977	-1772.9	-857.25	2656.6	6740.4
b_5	-0.97182	-135.6	-239.33	-360.69	-466.83	-512.55	-594.43
b_6	-0.11358	0.71205	14.828	24.141	18.708	-3.9163	-36.941
b_7	1.8952	134.31	219.9	325.62	409.16	423.83	481.08
b_8	-3.6824	602.14	1680.9	2200.1	1751.4	4506.2	16118
b_9	29.979	284.4	538.25	959.5	460.72	-1441.4	-3647.4
R^2	0.997	0.998	0.999	0.999	0.999	0.999	0.977
max(η)	1.72	1.61	0.71	1.00	0.85	0.87	6.21
min(η)	0.00	0.13	0.05	0.03	0.01	0.02	0.11
mean(η)	0.68	0.44	0.39	0.26	0.27	0.32	1.59

(c) Coefficients c_i of Equation (10.12).

Fn	0.25	0.35	0.45	0.55	0.65	0.75	0.85	0.95
c_0	59.305	392.32	839.13	1193.7	645.33	91.915	528.17	23833
c_1	0.74681	14.462	64.071	135.69	174.7	170.35	230.03	357.57
c_2	-1.9106	3.2792	42.48	69.413	67.255	37.156	-31.273	-152.4
c_3	28.511	-599.18	-1806.4	-1866.1	-2180.2	-4137.7	-9352.6	-88996
c_4	-134.69	-434.28	-624.85	-1243.9	174.45	2613.7	5043.4	2684.1
c_5	-7.358	-133	-291.38	-443.5	-517.16	-552.49	-827.15	-1532.4
c_6	-0.84893	0.019508	13.67	23.148	15.485	-3.9139	-28.798	-9.0483
c_7	7.1788	129.98	259.84	390.5	449.7	462.89	680.84	1269.5
c_8	-17.446	569.27	1651.6	1679.8	1995	3841.7	8551.8	80959
c_9	68.233	235.21	353.58	673.98	-93.014	-1429	-2750.6	-1605.7
R^2	0.987	0.996	0.999	0.999	0.998	1.000	0.996	0.995
max(η)	3.12	2.35	1.18	1.33	1.46	0.62	2.65	3.09
min(η)	0.05	0.11	0.05	0.01	0.01	0.03	0.00	0.09
mean(η)	1.04	0.55	0.28	0.32	0.37	0.22	0.56	0.76

(d) Coefficients d_i of Equation (10.13).

Fn	0.25	0.35	0.45	0.55	0.65	0.75	0.85	0.95
d_0	102.83	313.3	181.99	517.85	236.29	290.66	171.44	5546.7
d_1	-9.5558	0.20992	40.507	128.64	148.61	158.7	212.79	277.41
d_2	-10.907	-5.1471	27.736	69.796	64.352	45.156	-4.1476	-107.88
d_3	54.603	-611.2	-1447.1	-1741	-2302.3	-2960.9	-5466	-22459
d_4	-229.02	-246.56	592.53	139.32	1100.5	1543.9	3603.8	2769.9
d_5	-4.612	-137.22	-320.46	-506.64	-495.64	-681.47	-1127.7	-1950.2
d_6	-2.1854	-1.8922	8.8716	18.286	9.9025	-6.7194	-27.266	-58.331
d_7	3.3174	130.84	277.85	439.98	424.33	583.65	964.37	1658.6
d_8	-40.013	591.61	1355.6	1607.3	2173.1	2809.2	5072.8	20530
d_9	115.78	134.31	-294.95	-57.656	-593.9	-853.8	-1957.4	-1552.3
R^2	0.898	0.993	1.000	0.999	0.997	1.000	0.999	0.998
max(η)	10.03	2.54	0.62	0.96	2.19	0.38	1.23	2.85
min(η)	0.07	0.02	0.00	0.02	0.02	0.00	0.02	0.06
mean(η)	1.96	0.60	0.21	0.32	0.46	0.13	0.35	0.55

(e) Coefficients e_i of Equation (10.14).

Fn	0.25	0.35	0.45	0.55	0.65	0.75	0.85	0.95
e_0	82.941	436.11	787.77	1157.5	694.14	243.52	1036.4	4706.9
e_1	2.373	18.098	70.515	135.62	164.85	155.39	240.36	214.83
e_2	-1.2514	5.7772	45.709	69.208	60.038	20.429	-50.393	-180.74
e_3	120.57	-270.48	-487.64	-751.27	-819.12	-2173.1	-5913.6	-16023
e_4	-186.88	-504.8	-521.12	-1015.4	123.49	2354	5123.8	5250.8
e_5	-3.9805	-134.96	-284.91	-439.96	-496.94	-588.66	-864.27	-1779.4
e_6	-0.51446	0.73107	14.115	21.833	14.117	-6.9935	-33.84	-83.507
e_7	4.4141	132.67	255.53	388.22	430.63	493.91	719.42	1474.1
e_8	-114.24	243.79	411.95	671.6	775.38	2100.7	5487.6	14731
e_9	95.618	272.7	297.27	555.22	-67.006	-1285.4	-2782.2	-2908.2
e_{10}	-90.1	-356.65	-1259.1	-1319.9	-1383.3	-1911.9	-5134.1	-6910.3
e_{11}	90.827	335.24	1127.9	1139.5	1180.8	1599.3	4365.7	5748.6
R^2	0.955	0.994	0.996	0.998	0.996	0.995	0.967	0.988
$\max(\eta)$	31.13	3.28	2.12	1.87	3.93	3.12	10.38	5.54
$\min(\eta)$	0.15	0.03	0.01	0.03	0.01	0.01	0.02	0.05
$\text{mean}(\eta)$	6.15	0.97	0.57	0.49	0.54	0.67	1.98	1.25

Table G.3: The coefficients of the five alternative regressions for the upright trimmed residuary resistance of the bare hull, $R_{R\theta_h}$, Equations (10.10) up to (10.14) without the quadratic terms. All the coefficients are multiplied by 100 and are dimensionless. The relative comparison error, η, is defined by Equation (10.15) and is given as a percentage.

(a) Coefficients a_i of Equation (10.10). Coefficients a_7 up to a_9 are zero.

Fn	0.25	0.35	0.45	0.55	0.65	0.75	0.85	0.95
a_0	-1.9836	-15.628	-23.488	-25.462	5.8399	50.853	132.08	491.65
a_1	5.3494	17.29	64.68	130.61	150.61	161.04	216.89	269.51
a_2	1.5956	3.2217	42.463	69.654	65.009	45.795	-2.9428	-116.38
a_3	7.6779	-2.3557	-44.812	-34.16	19.765	54.567	-19.522	-400.09
a_4	-3.7342	9.6253	40.282	35.094	-11.667	-55.036	-64.54	-149.55
a_5	1.1135	12.912	-3.8191	-16.935	-25.588	-35.137	-59.64	-118.48
a_6	-0.10094	0.80337	14.516	19.579	10.418	-6.7646	-27.532	-56.783
R^2	0.996	0.920	0.989	0.993	0.992	0.990	0.981	0.922
max(η)	2.14	8.50	3.40	3.04	2.67	3.02	4.06	12.29
min(η)	0.20	0.41	0.09	0.02	0.01	0.16	0.14	0.41
mean(η)	1.09	2.93	1.01	0.77	0.82	0.92	1.35	3.03

(b) Coefficients b_i of Equation (10.11). Coefficients b_7 up to b_9 are zero.

Fn	0.25	0.35	0.45	0.55	0.65	0.75	0.85
b_0	-1.9836	-14.521	1.8871	23.021	50.146	160.21	479.03
b_1	5.3494	17.19	71.406	139.19	180.3	175.05	314.06
b_2	1.5956	3.1466	41.437	65.513	54.19	4.9196	-91.597
b_3	7.6779	-4.1231	-89.95	-134.75	-126.35	-137.74	-543.97
b_4	-3.7342	9.4393	33.628	28.908	10.044	-49.207	-119.45
b_5	1.1135	12.886	3.4856	-1.129	-14.235	-43.642	-65.105
b_6	-0.10094	0.90428	15.246	24.8	19.11	-4.0475	-36.816
R^2	0.996	0.911	0.982	0.988	0.994	0.990	0.940
max(η)	2.14	8.40	4.91	3.84	2.14	3.24	10.98
min(η)	0.20	0.29	0.06	0.11	0.01	0.18	0.11
mean(η)	1.09	3.07	1.35	1.11	0.77	1.00	2.96

(c) Coefficients c_i of Equation (10.12). Coefficients c_7 up to c_9 are zero.

Fn	0.25	0.35	0.45	0.55	0.65	0.75	0.85	0.95
c_0	2.0538	-18.962	-28.047	-4.4687	12.536	99.306	275.89	519.46
c_1	0.73062	14.5	63.746	135.88	175.96	171.44	229.36	360.94
c_2	-1.9318	3.0937	41.819	68.907	67.385	37.09	-33.015	-134.2
c_3	9.6012	11.297	-33.735	-64.772	-39.7	-10.143	-161.46	-238.36
c_4	-6.5304	7.9718	39.721	23.524	2.7393	-67.557	-121.38	-240.16
c_5	0.56716	10.733	-4.1904	-11.674	-19.417	-40.06	-74.139	-136.51
c_6	-0.82095	0.1869	14.008	23.633	15.676	-4.1065	-29.06	-100.06
R^2	0.976	0.923	0.981	0.989	0.992	0.991	0.976	0.984
max(η)	3.40	7.60	4.28	2.77	2.54	2.62	5.44	3.75
min(η)	0.30	0.03	0.03	0.00	0.05	0.13	0.17	0.16
mean(η)	1.69	2.70	1.39	1.05	0.88	0.93	1.73	1.59

(d) Coefficients d_i of Equation (10.13). Coefficients d_7 up to d_9 are zero.

Fn	0.25	0.35	0.45	0.55	0.65	0.75	0.85	0.95
d_0	11.465	-15.939	-35.48	-31.608	0.7957	50.853	132.08	491.65
d_1	-9.6368	0.35937	41.46	130.2	150.14	161.04	216.89	269.51
d_2	-10.966	-5.2587	27.929	70.156	64.694	45.795	-2.9428	-116.38
d_3	11.416	23.401	7.9626	-17.245	30.438	54.567	-19.522	-400.09
d_4	-11.646	6.3114	40.597	34.339	-11.734	-55.036	-64.54	-149.55
d_5	-0.98464	7.5061	-12.838	-19.544	-25.8	-35.137	-59.64	-118.48
d_6	-2.1394	-1.766	8.9	18.451	9.8948	-6.7646	-27.532	-56.783
R^2	0.883	0.923	0.986	0.990	0.991	0.990	0.981	0.922
max(η)	9.19	6.58	3.48	3.30	2.70	3.02	4.06	12.29
min(η)	0.24	0.16	0.11	0.08	0.03	0.16	0.14	0.41
mean(η)	2.63	2.34	1.09	0.99	0.89	0.92	1.35	3.03

(e) Coefficients e_i of Equation (10.14). Coefficients e_7 up to e_9 are zero.

Fn	0.25	0.35	0.45	0.55	0.65	0.75	0.85	0.95
e_0	28.44	95.185	341.74	379.15	409.86	646.99	1786.6	3663
e_1	2.3525	18.755	71.954	137.72	167.67	159.3	246.31	235.63
e_2	-1.2697	6.0277	46.307	70.062	61.307	22.316	-47.502	-173.24
e_3	-2.43	-9.9359	-47.566	-33.584	10.298	82.161	-16.71	-166.29
e_4	-7.2373	8.2898	39.355	30.491	1.9768	-54.907	-95.518	-200.5
e_5	0.89007	11.907	-1.9295	-10.089	-19.806	-41.108	-66.761	-143.38
e_6	-0.49095	0.9153	14.345	22.243	14.241	-7.1978	-34.083	-83.369
e_{10}	-83.392	-395.38	-1310.3	-1410.7	-1437.8	-2027.9	-5520.6	-10828
e_{11}	84.873	369.58	1173.3	1220	1229	1702.2	4708.6	9150.7
R^2	0.953	0.964	0.989	0.992	0.992	0.990	0.960	0.962
max(η)	33.89	8.17	4.86	4.37	4.42	4.62	9.86	8.12
min(η)	0.11	0.01	0.03	0.03	0.03	0.01	0.07	0.00
mean(η)	6.33	2.24	0.97	0.85	0.74	0.97	2.35	2.34

Table G.4: The sensitivity of regression (10.10), including the quadratic terms, to variations in the input parameters. The sensitivities are given as an absolute percentage change from the situation with no variation.

(a) Maximum sensitivity of all the models in the systematic series.

Fn		0.25	0.35	0.45	0.55	0.65	0.75	0.85	0.95
B_{WL}/L_{WL}	+1%	2.7	1.0	0.9	1.0	0.9	0.8	0.8	0.9
T_c/B_{WL}	+1%	0.7	0.2	0.5	0.5	0.3	0.2	0.0	0.4
LCB_{fp}/L_{WL}	+1%	10.1	3.4	1.9	1.0	1.5	2.4	2.5	6.8
LCB_{fp}/LCF_{fp}	+1%	10.7	5.5	3.1	1.1	1.0	2.2	3.0	3.1
C_p	+1%	1.6	3.7	0.8	0.9	0.8	1.0	1.3	1.7
C_x	+1%	0.2	0.1	0.6	0.5	0.2	0.1	0.4	0.7
All parameters	+1%	8.5	11.0	4.2	2.8	1.6	1.1	3.2	8.7
B_{WL}/L_{WL}	-1%	2.7	1.0	0.9	1.0	0.9	0.8	0.8	0.9
T_c/B_{WL}	-1%	0.7	0.2	0.5	0.5	0.3	0.2	0.0	0.4
LCB_{fp}/L_{WL}	-1%	10.2	3.6	2.1	1.1	1.2	2.1	2.4	8.0
LCB_{fp}/LCF_{fp}	-1%	11.9	4.2	2.7	1.0	0.8	1.8	2.3	2.7
C_p	-1%	1.6	3.5	0.9	0.9	0.9	1.0	1.4	1.8
C_x	-1%	0.2	0.1	0.6	0.5	0.2	0.1	0.4	0.7
All parameters	-1%	7.3	8.8	3.5	2.5	1.5	1.1	3.2	9.7

(b) Average sensitivity over all the models in the systematic series.

Fn		0.25	0.35	0.45	0.55	0.65	0.75	0.85	0.95
B_{WL}/L_{WL}	+1%	2.2	0.9	0.7	0.9	0.8	0.7	0.8	0.8
T_c/B_{WL}	+1%	0.5	0.1	0.4	0.3	0.2	0.1	0.0	0.2
LCB_{fp}/L_{WL}	+1%	8.3	0.7	1.1	0.5	0.5	1.0	0.4	2.2
LCB_{fp}/LCF_{fp}	+1%	6.4	3.0	2.3	1.0	0.5	1.4	1.6	2.2
C_p	+1%	1.2	1.7	0.3	0.4	0.5	0.6	0.8	1.1
C_x	+1%	0.2	0.1	0.6	0.4	0.2	0.1	0.3	0.6
All parameters	+1%	5.5	6.3	2.6	1.8	0.8	0.4	1.6	5.0
B_{WL}/L_{WL}	-1%	2.2	0.9	0.7	0.9	0.8	0.7	0.8	0.8
T_c/B_{WL}	-1%	0.5	0.1	0.4	0.3	0.2	0.1	0.0	0.2
LCB_{fp}/L_{WL}	-1%	8.3	0.6	1.4	0.6	0.3	0.7	0.5	3.8
LCB_{fp}/LCF_{fp}	-1%	7.5	1.8	1.9	1.0	0.3	1.1	1.0	1.8
C_p	-1%	1.2	1.5	0.4	0.5	0.5	0.6	0.9	1.2
C_x	-1%	0.2	0.1	0.6	0.4	0.2	0.1	0.3	0.6
All parameters	-1%	4.5	4.1	1.9	1.6	0.7	0.5	1.6	6.4

Table G.5: The sensitivity of regression (10.14), including the quadratic terms, to variations in the input parameters. The sensitivities are given as an absolute percentage change from the situation with no variation.

(a) Maximum sensitivity of all the models in the systematic series.

Fn		0.25	0.35	0.45	0.55	0.65	0.75	0.85	0.95
B_{WL}/L_{WL}	+1%	1.3	1.1	0.9	1.0	0.9	0.8	1.0	0.7
T_c/B_{WL}	+1%	0.7	0.3	0.5	0.5	0.3	0.1	0.2	0.6
LCB_{fp}/L_{WL}	+1%	9.0	2.4	1.7	0.9	0.8	2.3	2.7	4.4
LCB_{fp}/LCF_{fp}	+1%	18.1	5.0	2.8	1.7	0.1	2.6	4.3	5.0
C_p	+1%	1.7	3.6	0.9	0.8	0.8	0.9	1.1	1.7
C_x	+1%	1.0	0.1	0.6	0.5	0.3	0.1	0.5	1.0
LCG_{fp}/L_{WL}	+1%	13.6	5.7	3.7	2.0	1.8	2.4	4.1	3.7
All parameters	+1%	11.2	11.3	6.8	4.6	2.5	3.2	7.3	10.5
B_{WL}/L_{WL}	-1%	1.3	1.1	0.9	1.0	0.9	0.8	1.0	0.7
T_c/B_{WL}	-1%	0.7	0.3	0.5	0.5	0.3	0.1	0.2	0.6
LCB_{fp}/L_{WL}	-1%	7.5	2.7	1.9	1.0	0.6	2.0	2.5	5.2
LCB_{fp}/LCF_{fp}	-1%	22.5	3.7	2.5	1.3	0.1	2.1	3.3	4.2
C_p	-1%	1.6	3.3	0.8	0.8	0.8	1.0	1.2	1.8
C_x	-1%	1.0	0.1	0.6	0.5	0.3	0.1	0.5	1.0
LCG_{fp}/L_{WL}	-1%	12.5	5.2	3.3	2.2	2.0	2.6	4.5	4.3
All parameters	-1%	14.2	9.4	5.9	3.8	2.2	3.3	7.5	11.8

(b) Average sensitivity over all the models in the systematic series.

Fn		0.25	0.35	0.45	0.55	0.65	0.75	0.85	0.95
$B_{WL}L_{WL}$	+1%	0.7	0.9	0.8	0.9	0.8	0.7	0.9	0.6
T_cB_{WL}	+1%	0.3	0.2	0.4	0.3	0.2	0.1	0.1	0.4
$LCB_{fp}L_{WL}$	+1%	2.6	0.9	1.2	0.4	0.3	1.2	0.4	0.9
$LCB_{fp}LCF_{fp}$	+1%	8.7	2.3	2.1	1.0	0.1	1.5	2.1	3.2
C_p	+1%	0.7	1.4	0.2	0.3	0.4	0.6	0.7	1.2
C_x	+1%	0.5	0.1	0.5	0.5	0.2	0.1	0.4	0.8
$LCG_{fp}L_{WL}$	+1%	9.5	3.0	1.4	0.9	0.8	1.2	1.9	1.9
All parameters	+1%	3.2	7.0	3.0	1.6	0.8	1.4	3.9	7.2
$B_{WL}L_{WL}$	-1%	0.7	0.9	0.8	0.9	0.8	0.7	0.9	0.6
T_cB_{WL}	-1%	0.3	0.2	0.4	0.3	0.2	0.1	0.1	0.4
$LCB_{fp}L_{WL}$	-1%	1.7	1.2	1.4	0.6	0.2	0.9	0.5	1.9
$LCB_{fp}LCF_{fp}$	-1%	11.2	1.3	1.8	0.7	0.0	1.0	1.3	2.4
C_p	-1%	0.6	1.2	0.3	0.4	0.4	0.6	0.8	1.3
C_x	-1%	0.5	0.1	0.5	0.5	0.2	0.1	0.4	0.8
$LCG_{fp}L_{WL}$	-1%	8.7	2.5	1.2	0.9	0.8	1.4	2.3	2.4
All parameters	-1%	4.4	4.9	2.2	1.1	0.6	1.5	4.2	8.4

Input WinDesign VPP

The input used in WinDesign VPP to calculate a velocity prediction of a full-scale Transpac 52 (TP52) based on Sysser 85 with the Delft method and the new method. The polar diagram is given in Figure 10.10.

DELFT Flotation Input Data for Condition Sailing (MONOHULL)
Sailing Condition

Basics		Heel Functions					Appendages			
Dspl	9200.0	Heel	WSc	ra	lwl			ws	cm	tc
Dsplc	8780.0	0	36.510	0.000	15.602		Fin	2.972	0.550	0.082
Lwl	15.602	2	36.493	0.093	15.653		Bulb	3.505	3.000	0.400
Lsunk	15.850	10	36.060	0.458	15.848		Rud	1.284	0.300	0.045
Bwl	3.194	25	33.806	1.025	15.853		Other	0.000	0.000	0.000
Bmax	4.414	40	31.813	1.388	15.869					
Tc	0.462									
Tmax	3.500				Factors					
Trud	2.664									
Ax	1.009		Wing/CB Eff	0.333						
Cp	0.543		Apndg Cd2	On						
Awp	34.23		Biplane Hyd	On						
LCB	-3.86		FwdCL Apndg	No						
LCF	-7.33		Set Angle	0.000						
GYR	0.25		Canoe Form	0.100						
Ad+/-	0.000		Vt Grad	0.100				Crew Wt	1130.0	
PIPA	0.000							Crew Arm	1.900	
HBI,f	1.300							KEEL CANT	0.0	
ProjA	0.000									
M,Long	52.048									
KeelVCB	1.210		vcg shift	0.000						
KeelTaper	0.874		RudLoadFract	0.100						
			TabLimit	0.000						
			TabRatio	0.000						
			KeelCantRamp(d)	5.000						

Model: Delft

Figure H.1: Flotation input in WinDesign VPP for a full-scale TP52 based on Sysser 85.

Rig and Sail Plan Dimensions

	Main		Fore		Spin
P	20.400	IG	19.720	SPL	9.000
E	7.400	J	6.188	SMW	14.000
BAD	2.100	LP	6.300	SLU	25.500
		HBI	1.300	SLE	23.000
				ISP	22.400

Sail Inventory

Name	Area	Span	BaseHt	AFx	Aero	Base
Jib	65.590	19.720	0.000	1.000	Jib_0	HEAD
Main	97.810	20.400	0.800	1.000	Main_0	MAIN
Spin	269.590	22.400	0.000	0.750	ASpin_0	SPIN

Windage Elements

Name	Ax	Ay	Cdx	Cdy	Ht	Type
MainRigging	1.914	1.914	1.000	1.000	9.354	other
MastBare	3.191	5.450	0.800	1.100	9.354	mast bare
MastSail	3.191	5.268	0.400	1.000	9.354	mast w/sail
Hull	3.943	20.101	0.400	0.900	-0.520	hull

Sail Sets and Member Sails

Upwind [Up]	Downwind [Dn]
Jib	Spin
Main	Main

Opsets

Name	Flotation	SailSet	TWS-Lo	TWS-Hi	TWA-Lo	TWA-Hi	AWS-Lim	FlatMin	UpOpt
Ops_Down	Sailing	Downwind	4.0	25.0	80.0	180.0	99.0	1.0	
Ops_Upwind	Sailing	Upwind	4.0	25.0	0.0	130.0	99.0	1.0	*

Figure H.2: Rig and sail-plan input in WinDesign VPP for a full-scale TP52 based on Sysser 85.

Experimental data input for the Delft method

```
1.0
Sailing Condition
15
6.01 0.766
7.21 1.165
8.42 1.721
9.62 2.777
10.82 4.453
12.02 5.861
13.23 7.172
14.43 8.707
15.63 10.383
16.83 12.208
18.04 14.190
19.24 16.338
20.44 18.660
21.64 21.165
22.85 23.861
10
6.01
```

```
0 0 0 0
0 0 0
0 0.766 0 0 2.11 0 57.982 1.5
15 0.839 0 0 1.868 0 38.533 1.5
22.5 0.867 0 0 1.791 0 21.599 1.5
30 0.897 0 0 1.571 0 5.397 1.5
7.21
0 0 0 0
0 0 0
0 1.165 0 0 2.037 0 57.933 1.5
15 1.271 0 0 1.745 0 38.535 1.5
22.5 1.313 0 0 1.672 0 21.634 1.5
30 1.356 0 0 1.478 0 5.400 1.5
8.42
0 0 0 0
0 0 0
0 1.721 0 0 1.964 0 57.650 1.5
15 1.877 0 0 1.622 0 38.445 1.5
22.5 1.945 0 0 1.552 0 21.591 1.5
30 2.019 0 0 1.384 0 5.398 1.5
9.62
0 0 0 0
0 0 0
0 2.777 0 0 1.891 0 57.735 1.5
15 3.069 0 0 1.499 0 38.332 1.5
22.5 3.246 0 0 1.432 0 21.644 1.5
30 3.453 0 0 1.291 0 5.397 1.5
10.82
0 0 0 0
0 0 0
0 4.453 0 0 1.819 0 58.090 1.5
15 4.872 0 0 1.376 0 38.430 1.5
22.5 5.145 0 0 1.313 0 21.639 1.5
30 5.468 0 0 1.198 0 5.400 1.5
12.02
0 0 0 0
0 0 0
0 5.861 0 0 1.746 0 57.854 1.5
15 6.362 0 0 1.253 0 38.622 1.5
22.5 6.683 0 0 1.193 0 21.633 1.5
30 7.061 0 0 1.105 0 5.397 1.5
13.23
0 0 0 0
0 0 0
0 7.172 0 0 1.673 0 57.609 1.5
15 7.808 0 0 1.129 0 38.706 1.5
22.5 8.226 0 0 1.074 0 21.566 1.5
30 8.721 0 0 1.012 0 5.391 1.5
14.43
0 0 0 0
0 0 0
0 8.707 0 0 1.6 0 57.685 1.5
15 9.484 0 0 1.006 0 38.809 1.5
22.5 10.002 0 0 0.954 0 21.678 1.5
30 10.616 0 0 0.918 0 5.403 1.5
15.63
0 0 0 0
0 0 0
0 10.383 0 0 1.527 0 57.076 1.5
15 11.214 0 0 0.883 0 38.088 1.5
22.5 11.742 0 0 0.834 0 21.527 1.5
30 12.362 0 0 0.825 0 5.392 1.5
16.83
0 0 0 0
0 0 0
0 12.208 0 0 1.454 0 59.620 1.5
15 13.028 0 0 0.76 0 38.886 1.5
22.5 13.542 0 0 0.732 0 21.748 1.5
30 14.150 0 0 0.715 0 5.409 1.5
```

Experimental data input for the new method

```
1.0
Sailing Condition
15
6.01 0.683
7.21 1.043
8.42 1.642
9.62 2.695
10.82 4.146
12.02 5.494
13.23 6.876
14.43 8.303
15.63 9.743
16.83 11.207
18.04 12.819
19.24 14.718
20.44 16.985
21.64 19.653
22.85 22.627
10
6.01
0 0 0 0
0 0 0
0 0.683 0 0 2.11 0 57.982 1.5
15 0.756 0 0 1.868 0 38.533 1.5
22.5 0.784 0 0 1.791 0 21.599 1.5
30 0.814 0 0 1.571 0 5.397 1.5
7.21
0 0 0 0
0 0 0
0 1.043 0 0 2.037 0 57.933 1.5
15 1.149 0 0 1.745 0 38.535 1.5
22.5 1.191 0 0 1.672 0 21.634 1.5
30 1.234 0 0 1.478 0 5.400 1.5
8.42
0 0 0 0
0 0 0
0 1.642 0 0 1.964 0 57.650 1.5
15 1.798 0 0 1.622 0 38.445 1.5
22.5 1.866 0 0 1.552 0 21.591 1.5
30 1.940 0 0 1.384 0 5.398 1.5
9.62
0 0 0 0
0 0 0
0 2.695 0 0 1.891 0 57.735 1.5
15 2.987 0 0 1.499 0 38.332 1.5
22.5 3.164 0 0 1.432 0 21.644 1.5
30 3.371 0 0 1.291 0 5.397 1.5
10.82
0 0 0 0
0 0 0
0 4.146 0 0 1.819 0 58.090 1.5
15 4.565 0 0 1.376 0 38.430 1.5
22.5 4.838 0 0 1.313 0 21.639 1.5
30 5.161 0 0 1.198 0 5.400 1.5
12.02
0 0 0 0
0 0 0
0 5.494 0 0 1.746 0 57.854 1.5
15 5.995 0 0 1.253 0 38.622 1.5
22.5 6.316 0 0 1.193 0 21.633 1.5
30 6.694 0 0 1.105 0 5.397 1.5
13.23
0 0 0 0
0 0 0
0 6.876 0 0 1.673 0 57.609 1.5
15 7.512 0 0 1.129 0 38.706 1.5
22.5 7.930 0 0 1.074 0 21.566 1.5
30 8.425 0 0 1.012 0 5.391 1.5
14.43
0 0 0 0
```

```
0 0 0
0 8.303 0 0 1.6 0 57.685 1.5
15 9.080 0 0 1.006 0 38.809 1.5
22.5 9.598 0 0 0.954 0 21.678 1.5
30 10.212 0 0 0.918 0 5.403 1.5
15.63
0 0 0 0
0 0 0
0 9.743 0 0 1.527 0 57.076 1.5
15 10.574 0 0 0.883 0 38.088 1.5
22.5 11.102 0 0 0.834 0 21.527 1.5
30 11.722 0 0 0.825 0 5.392 1.5
16.83
0 0 0 0
0 0 0
0 11.207 0 0 1.454 0 59.620 1.5
15 12.027 0 0 0.76 0 38.886 1.5
22.5 12.541 0 0 0.732 0 21.748 1.5
30 13.149 0 0 0.715 0 5.409 1.5
```